PHD Thesis

Modelling of tidally generated large scale bedforms

Giovanni Besio

University of Genoa
Department of Environmental Engineering

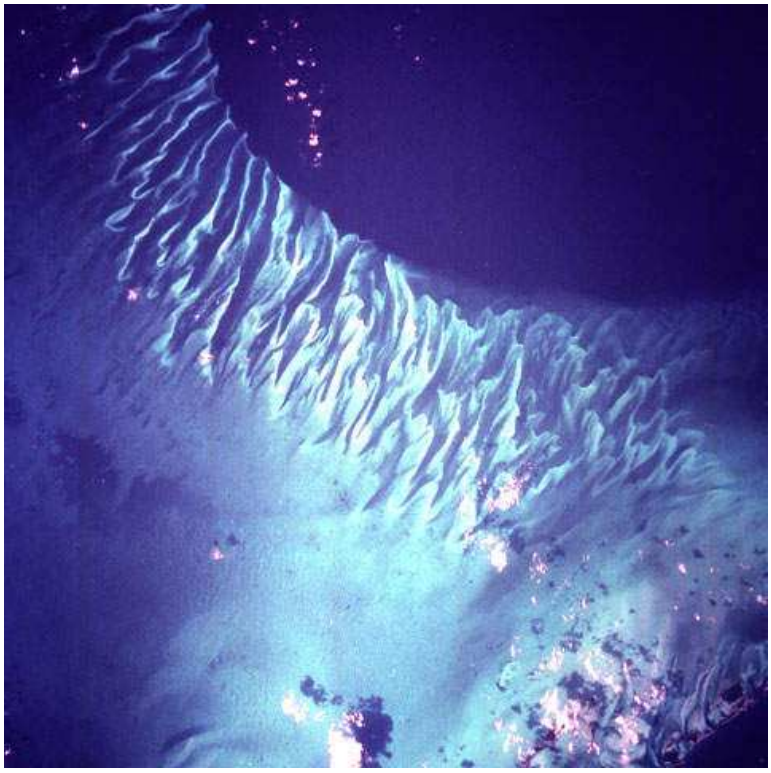

Dottorato di Ricerca in

Fluodinamica e Processi dell'Ingegneria Ambientale

XVI CICLO

Modelling of tidally generated large scale bedforms

Giovanni Besio

Università degli Studi di Genova
Dipertimento di Ingegneria Ambientale

Supervisore:
Prof. Paolo Blondeaux

Revisore:
Prof. Huib de Swart

Università degli Studi di Genova

Dottorato di Ricerca in

Fluodinamica e Processi dell'Ingegneria Ambientale

XVI CICLO

Coordinatore:
Prof. Giovanna Vittori - Università degli Studi di Genova

Commissione esaminatrice:
Prof. Alessandro Bottaro - Università degli Studi di Genova
Prof. Dino Zardi - Università degli Studi di Trento
Prof. Rodolfo Repetto - Università degli Studi dell'Aquila

Esame finale:
29 Maggio 2004

Acknowledgements

First and foremost, I wish to thank my supervisor Prof. Paolo Blondeaux for his continous guidance and support and for his precious advice for my future career. I am also indebted to Prof. Giovanna Vittori and Prof. Maurizio Brocchini for their support and scientific contribution during the three years of my PhD. A special thanks to Dr. Huib de Swart for accepting to read my work and giving invaluable advice which contributed to the improvement of my thesis. I am deeply grateful to Prof. Giovanni Seminara who introduced me to the world of research and for the fruitful discussions on science as well as on life. I would also like to acknowledge Marco Galiani and Tina D'Agostino who have been a special support and are an added value to the Department of Environmental Engineering of the University of Genoa. I want to thank all the young researchers with whom I shared my PhD experience, in particular Michele for his constant support, Nunzio for all the "ciarlatanate", Laura for her spaciness, Bianca, Alessandro and Nicoletta who are always ready to share good as well as bad moments.

Because life is not only science and work, I want to thank all of the people who have supported me and always show me the "Nerd way": Omar, Ciccio Bariletti, Fanaus, Matteo, Gigi, the VDCM Crew (Charlie, Pino, il Coinquilino, Marce, Stani, Vica, Ubbe, Lollo, Laura, Pablo, Mangiaxxxxx, Agnese, Sara, Cami), all the Torpedo Team and in particular Giovanni, Michelone, Conce, La Nonna and Dibba, Old Disco Club (Gian), Cetto, Taro and the people from ISF (Cristiano, Amedeo, Tommaso).

I want to dedicate a special thanks to my father and my mother for their patience, wisdom and encouragement throughout my studies. Thanks as well to my brother "Ciro" as well for his affection and friendship.

Last but not least, I want to thank Lauren and Cucis for putting up with me and for supporting me every day.

Contents

List of Figures

List of Tables

Abstract

The aim of this research thesis is to deepen the knowledge and understanding of sand wave dynamics, improving the description of the physics of the problem and introducing new elements to the analysis which were not taken into account in previous works. The first step followed in this work is the set-up of a two dimensional simple model focused on the study of the interaction between the topography of small bedforms and the surrounding flow field. In fact, the physical process leading to the formation and migration of sand waves in tide-dominated coastal areas has been investigated by means of a linear stability analysis of a flat sandy bottom subject to an oscillatory current of tidal origin. To perform the analysis the problem has been divided in to a basic state and a perturbed state. The former represents an undisturbed tidal current in absence of bedforms, while the latter takes into account the introduction of bottom perturbation which trigger the rise of a perturbed flow responsible of the growth or decay of the bedforms.

In a second stage a fully three-dimensional model for the generation and evolution of sand waves and tidal sand banks from bottom perturbations of a flat seabed subject to the action of tidal currents is proposed. A horizontally two-dimensional basic flow comprehensive of Coriolis effects, forced by the local tidal currents, is considered. The basic flow is completely resolved also in the vertical direction from the sea bed up to the free surface. The flow regime is assumed to be turbulent and a Boussinesq approach is adopted to model Reynolds stresses. The eddy viscosity depends on the distance from the bed and an accurate description of the flow close to the sea bed, where sediment motion is mainly confined, is obtained. Sediment transport is modelled in terms of both suspended load and bed load. Finally, the presence of wind waves is taken into account.

Introduction to Coastal Morphodynamics

Morphology and Morphodynamics

The morphology of different patterns and forms, which are present on the surface of the earth and on the bottom of the sea, is of great interest from a scientific point of view as well as for many practical reasons. The observation, investigation, and study of the appearance and evolution of these natural patterns arising in sedimentary environments for different time scales (depending on the physical processes involved) are the main subject of morphodynamics.

These features invariably arise from the mechanical interaction of the sediment with the motion of natural fluids and often show a spectacular surprisingly high degree of self-organisation. Rivers, coasts and deserts may be viewed as self-formed features triggered by this complex dynamic interaction between the fluid forces and the sediment present in the environment.

The study of the Earth's morphology has a strong multidisciplinary character. Relying on the understanding of the mechanics of sediment transport, morphodynamics is part of the branch of fluid mechanics dealing with two phase flows. However, the existence of quasi-equilibrium patterns and the dynamics whereby they evolve in response to change either of sediment inputs or of fluid motion, is of great practical interest to environmental engineers for the planning and design of fluvial and coastal structures. This is because they yield the knowledge of the major factors controlling the erosion and deposition processes acting in rivers, along the coastline and in the continental shelf. In these quasi-equilibrium patterns full equilibrium is not reached because the time scale of the climatic changes is much greater than the morphodynamic scale, for this reason nature tends to an equilibrium configuration that changes slowly. Finally, understanding the origin of the morphodynamical features of sedimentary structures is of interest to historical geology, contributing to the environmental interpretation of stratigraphic records. The

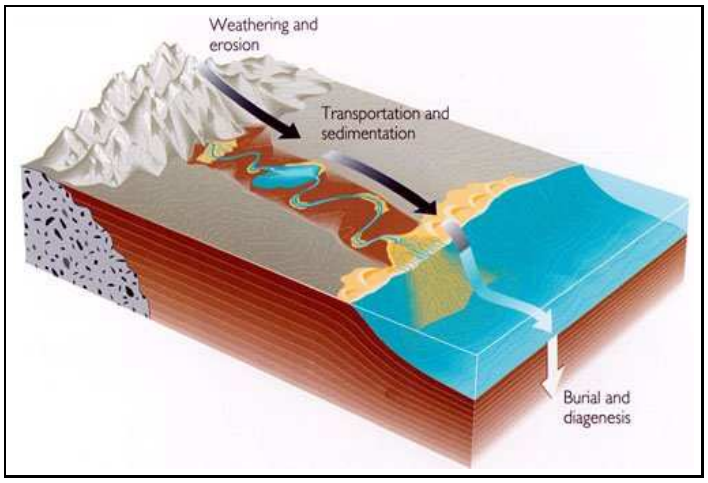

Figure 1: The sediment cycle from the mountains to the abyssal plains.

contribution of geomorphology to the description of physical processes plays a fundamental role in studying and understanding the phenomena. In fact, morphodynamics relies strongly on field observations, as the collection and analysis of observations is crucial for the identification and characterisation of morphological phenomena.

Observation of actual self-forming processes reveals their typical unsteadiness, being both the flow conditions and the production of sediment controlled by the climate. The self-adjusting character of such processes also implies that the evolving shape of the container produces a feedback on the flow field: states of coasts, deserts, and rivers may only be temporary. Nevertheless, the observation of evolving patterns clearly indicates the presence of different temporal and spatial scales characterising their dynamics. If the process is viewed at its proper temporal and spatial scale, an ideal quasi-equilibrium state can often be achieved such that the evolving pattern may be thought as a perturbed state relative to equilibrium. This point of view often allows to interpret a large number of morphodynamical processes.

The environments in which sedimentary patterns occur are all those involved in the sediment cycle comprised of the mountain regions to the abyssal plains (see figure **1**). Sediment particles typically travel downhill from a continental source to an oceanic sink under the action of a sequence of agents associated with the different sedimentary environments traversed by the paths of sediment particles. The most effective terrestrial transporting agents are definitely rivers, fed with the sediment by debris flows, rock avalanches, and other less-disruptive types of sediment motion occurring in mountain regions. Through alluvial fans and alluvial valleys the sediment is carried by the flow

to the coastal region which extends to the edge of the continental shelf. In this region, the transport of solid material is carried out by the action of tidal currents, waves, long-shore currents and other coastal flows.

Coastal Morphodynamics

This research work focuses attention on the study and understanding of coastal morphodynamics. Coastal morphodynamics investigates the appearance and development of the morphological patterns observed on the continental shelf, from its offshore edge up to the beach face. Its aim is to predict the motion and the time development of the interface comprised between the seabed, which is a granular medium at high concentration, and the flowing currents above it, consisting of a mixture of water and sediment.

The distinctive feature of coastal bedforms is the oscillatory character of the flow which drives the dynamics of the bottom interface. The oscillatory nature of the resulting flow is due to the presence of wind-generated waves and the propagation of tides.

In principle, to accurately describe coastal morphodynamics it would be necessary to use a very detailed model that can predict the motion of every particle and of the forcing flow, taking into account the interactions which are present between these two elements and the dynamics of inelastic collision between the sediment particles. Drawing up this kind of model presents many difficulties because of the limited analytical capability of solving differential equations and because of the high computational time required even for modern computers to solve a complete model.

Therefore the way to follow is to solve the problem separately, describing the motion of water, assuming that its dynamics is not affected by the presence of the solid phase (one-way coupling) and simplifying the physics of the phenomena obtaining an approximated model. This is justified if sediment concentrations are small.

Coastal and Offshore Bedforms

The main aim of this study is to understand the evolution of some of the bed patterns which appear in coastal seas, characterised by the presence of a sandy bed. In shallow sandy seas, like the North Sea, various types of regular bottom patterns exist. Most readers will be familiar with the small regular patterns that are visible on sandy beaches during low tide. These particular seabed features are called *ripples* (figure **2**) and they arise from

Figure 2: 2D ripple patterns appearing on sandy beaches subjected to tidal current and wind waves.

the interaction between the bottom waviness with the oscillatory current due to the presence of waves in the surf zone (Sleath, 1984; Blondeaux, 2001). Their appearance is very important to understand and study the mechanics of sediment transport in coastal environments: the presence of these bedforms has a strong influence on the value of the bed roughness and therefore on the bottom resistance and the mechanism through which sediment particles are picked up from the bed and then transported by the fluid motions.

These small scale seabed features, which can reach up to 0.5m of amplitude (*megaripples*), can be observed lying on larger bed forms which appear in deeper waters and are always completely covered by sea water. The wavelength of these larger features greatly exceeds the local water depth and in some case their amplitude can be up to 70% of the water depth. These characteristics give a prominent role to these large scale bedforms in the morphodynamics of the continental shelf. The overlapping of different types of bedforms can give rise to very complex morphological patterns. Nevertheless these large scale bottom patterns show a surprising regularity, considering the large amount of physical processes involved in their environment.

The two most important kinds of bedforms encountered in the offshore region consist of *tidal sand banks* and *tidal sand waves*. These two patterns have different spacial dimensions and are formed along different time scales. The former are associated with relatively strong tidal currents (0.9-1.2m/s), the latter with relatively weak tides (0.3-0.7m/s) (Belderson, 1986).

Tidal sand banks (figure **3**) are elongated sand bodies with wavelengths of a few kilometres and heights of tens of meters (Stride, 1982), which is a very large value compared to the water depth in shallow seas. Furthermore, they hardly move, and in the northern hemisphere their crests are oriented between 5° and 30° counter-clockwise with respect to the principal direction of the tidal current, even if sand banks having a clockwise orientation exist

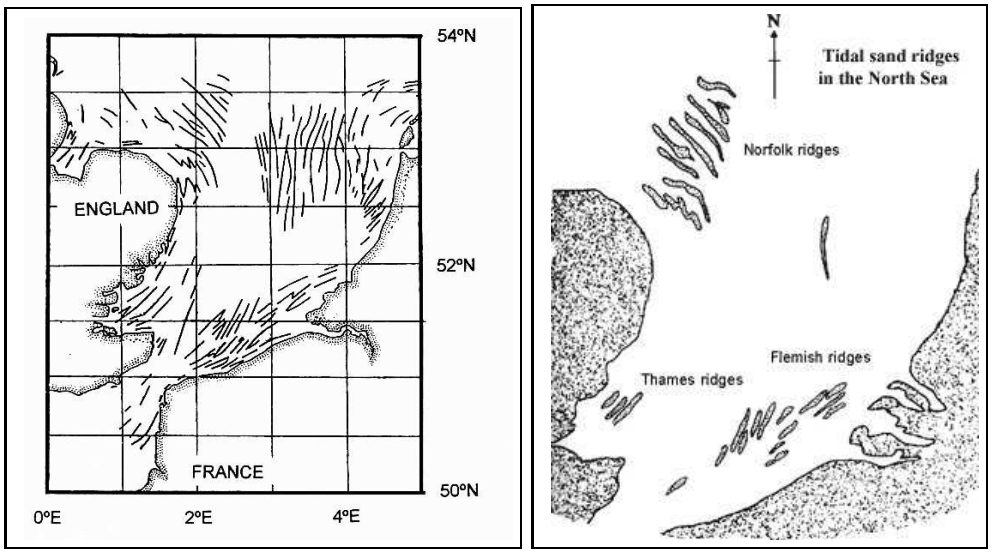

Figure 3: Patches of tidal sand banks (left panel, adapted from Dyer & Huntley, 1999) and of tidal sand ridges (right panel) present in the North Sea.

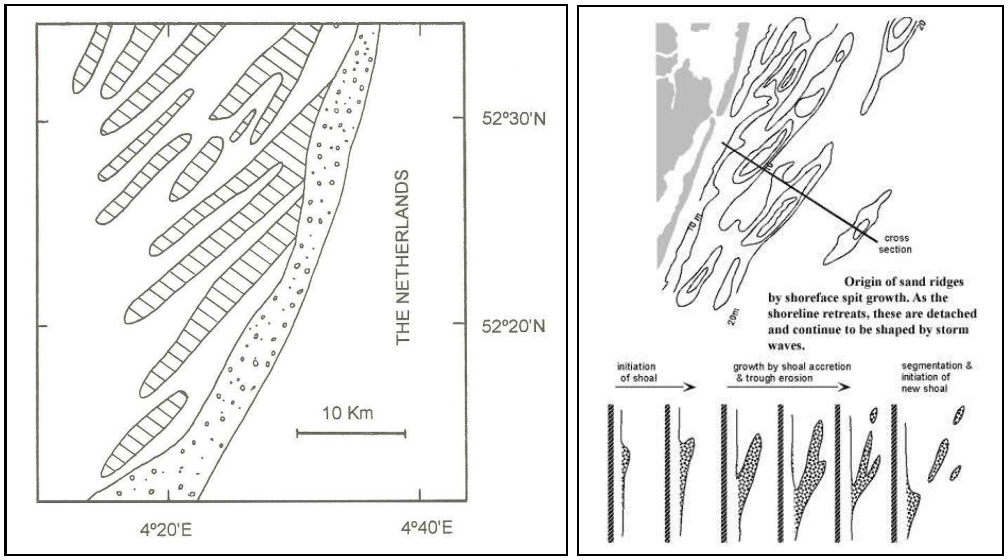

Figure 4: Shoreface-connected ridges along the central part of the Dutch coast (left panel, adapted form Van de Meene, 1994); origin of sand ridges by shoreface spit growth (right panel).

(Dyer & Huntley, 1999). Their typical evolution time has been estimated to be of a few hundreds of years.

Smaller bodies of sand, elongated and almost parallel to the main tidal

Figure 5: Longshore bar at low tide (left panel) and beach cusps (right panel) observed on sandy beaches.

current, have been recognised over large areas of continental shelves swept by tidal currents (Stride, 1982). The spacing of these bedforms (often called *sand ribbons,* longitudinal sand patches or *sand ridges*; see figure **3**) usually scales with the water depth.

Sometimes topographic rhythmic features are observed in the transition region between the continental shelf and the near-shore region. These kind of patterns usually start at the offshore end of the shore-face and extend seaward. They are quasi alongshore periodic with a spacing of several kilometres. They are oriented along the coastline, forming an angle of $20 - 35^{\circ}$ with it, and they are named *shoreface-connected ridges* (figure **4**).

Systematic studies, based on field surveys, have led to group beach morphologies in two-dimensional states and states showing varying degrees of three dimensionality. From the hydrodynamic point of view beaches are usually categorised as dissipative (gentle slope, breaking of waves well offshore) and reflective (steep slope, breaking of waves close to the shore). Wright & Short (1984) introduced a dimensionless parameter Ω which represents the state of the beach, taking into account both wave and sediment characteristics

$$\Omega = \frac{H_b}{w_s T} \tag{1}$$

where H_b is the breaker height, w_s is the sediment fall velocity and T is the wave period. Values of Ω smaller than 1 identify fully reflective beaches, while values greater than 6 represent fully dissipative beaches. A more detailed classification can be introduced, identifying intermediate states, represented by values of Ω comprised between 1 and 6.

Highly dissipative beaches are characterised by the presence of one or more longshore bars consisting of ridges of sediment running roughly parallel to the shore (figure **5**), which may have a considerable longshore extent, and

an inter-bar spacing of the order of 100 m. The generation and maintenance of these bars are commonly associated with the shoaling and breaking of high-frequency waves.

Field observations show that, for mild wave conditions, the longshore bars may take on a rhythmic crescentic shape. Large crescentic forms appear in the outer bar of a beach while the inner bars are segmented by more closely spaced periodic forms. The shape of the arcuate crescentic bar is generally symmetrical, but there are cases where it is skewed. Bottom patterns with a significant asymmetry are named welded or transverse bars.

Observing the shoreface at a smaller scale it can be noted that the beach face is seldom straight, but often contains seaward projections of sediment that are known as *beach cusps or* shoreline rhythms (figure **5**). A wide range of cusps spacings can be found on beaches, the cusps wavelength varying between 1 and 100m. The smaller values are found on beaches with small waves, while the largest values are generated by large storms.

Sand Waves

Among the many bedforms occurring in coastal regions, characterised by non-cohesive (sandy) deposits, sand waves are undoubtedly one of the most important for human activities. Sand waves typically occur in shallow seas, among which the North Sea is one of the most studied (Van Veen, 1935; Langeraar, 1966; Stride, 1970; Mc Cave, 1971; Terwindt, 1971; Huntley et al., 1993; Dyer and Huntley, 1999). These bedforms have been observed as well in the Japanese Sea (Knaapen et. al, 2002), in the Chinese Sea (Boggs, 1974) and in front of the North American coasts (Ludwick, 1972). Even in deeper waters, like the Strait of Messina in the Mediterranean Sea, field surveys revealed the presence of these kinds of sand bodies (Santoro et al., 2002). These bedforms have a typical wavelength ranging from 100m to 800m and heights of a few meters and their crests are almost orthogonal to the direction of propagation of the tidal wave. They are not static bedforms, in fact, they migrate at a rate which strongly depends on the tide characteristics and in particular on the intensity of the local residual currents, and can be of up to some tens of meters per year (Terwindt, 1971; Bokuniewicz et al., 1977; Fenster et al., 1990). The sawtooth-shaped profile of sand waves is similar, but less asymmetric, to that of desert sand dunes or that of dunes observed in fluvial environments. However, they differ from bedforms induced by steady currents since the basic flow in which sand waves evolve has an oscillatory nature. Even if their shape is asymmetric, flow separation does not occur in the neighbourhood of the crests.

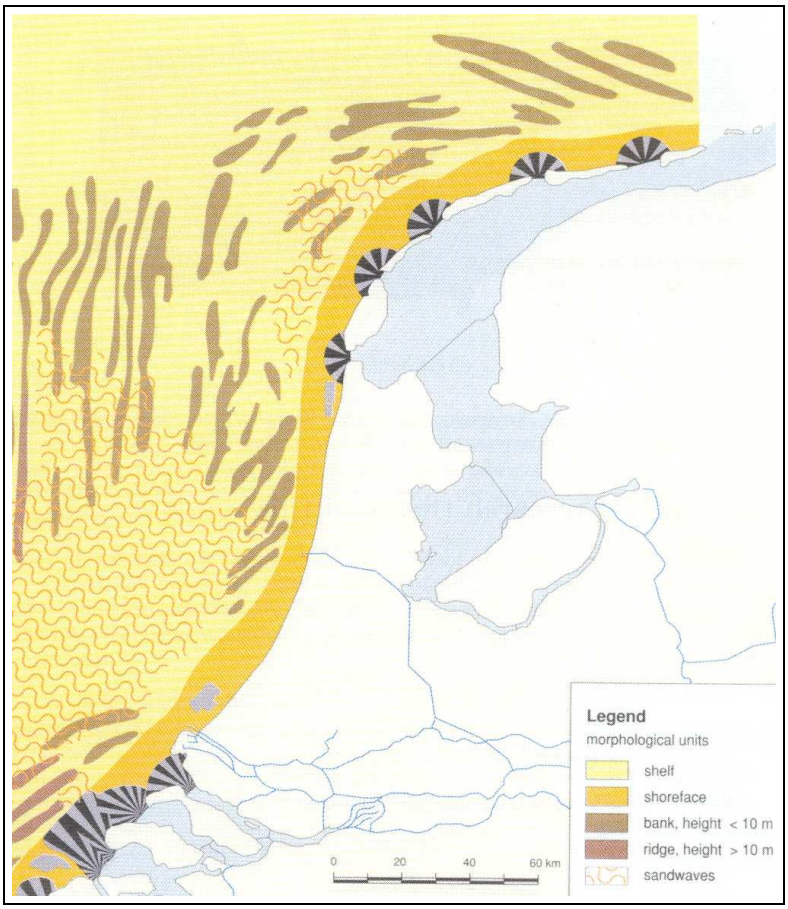

Figure 6: Location of sand waves and sand banks patterns in the North Sea in front of the Dutch coast (from Van Alphen and Damoiseaux, 1989).

As pointed by Hulscher, De Swart & De Vriend (1993), Hulscher (1996a) and Gerkema (2000) the process which leads to the formation of these bedforms is similar to that originating sea ripples under gravity waves (Sleath, 1976; Blondeaux, 1990; Blondeaux, 2001). In fact, the interaction of the oscillatory tidal flow with bottom perturbations gives rise to a steady streaming in the form of recirculating cells. When the net displacement of the sediment dragged by this steady streaming is directed toward the crests of the bottom waviness, the amplitude of the perturbation grows and bedforms are generated. On the other hand, the flat bottom configuration turns out to be stable when the net motion of the sediment is directed toward the troughs of the bottom waviness.

The appearance, growth, and migration of the sand waves have significant effects on the human activities taking place in shallow shelf seas, as in

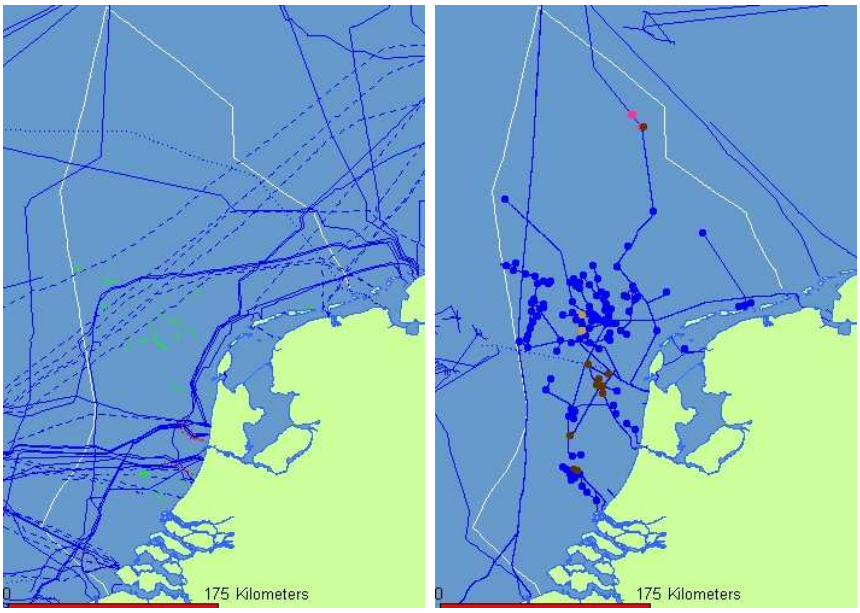

Figure 7: Networks of telecommunication and energy cables (left panel) and of pipelines, gas ducts and oil-extraction platforms (right panel) present in the North Sea in front of the Dutch coast (source: Noordzeeatlas).

the North Sea, and even in deeper waters, like the Mediterranean Sea. In recent decades, in fact, managers and engineers carrying on activities in environments where sand waves were present, needed to understand and foresee the behaviour of these bedforms. Pipelines and cables, navigability and sand mining are the main activities influenced by the presence of these bedforms.

Pipelines and Cables

Laying down a new pipeline in shallow or deep seas requires good accuracy and attention in order to position the lines in such a way that they are protected from severe stresses and forces due to the exposure to tidal currents and gravity, which could buckle or bend them. Usually the typical procedure is to bury them well below the sea bed. Obviously, the cost of the pipeline increases with the depth at which it is buried. However, if the depth at which the pipes are buried is not deep enough and sand waves appear, the pipeline will be exposed to the action of the tidal currents along its free span which will be almost the same of the wavelength of the sand waves. This situation can lead to high stresses of buckling under the action of the gravity and of the drag force of the current, but also to vibration problems due to the release of vortices.

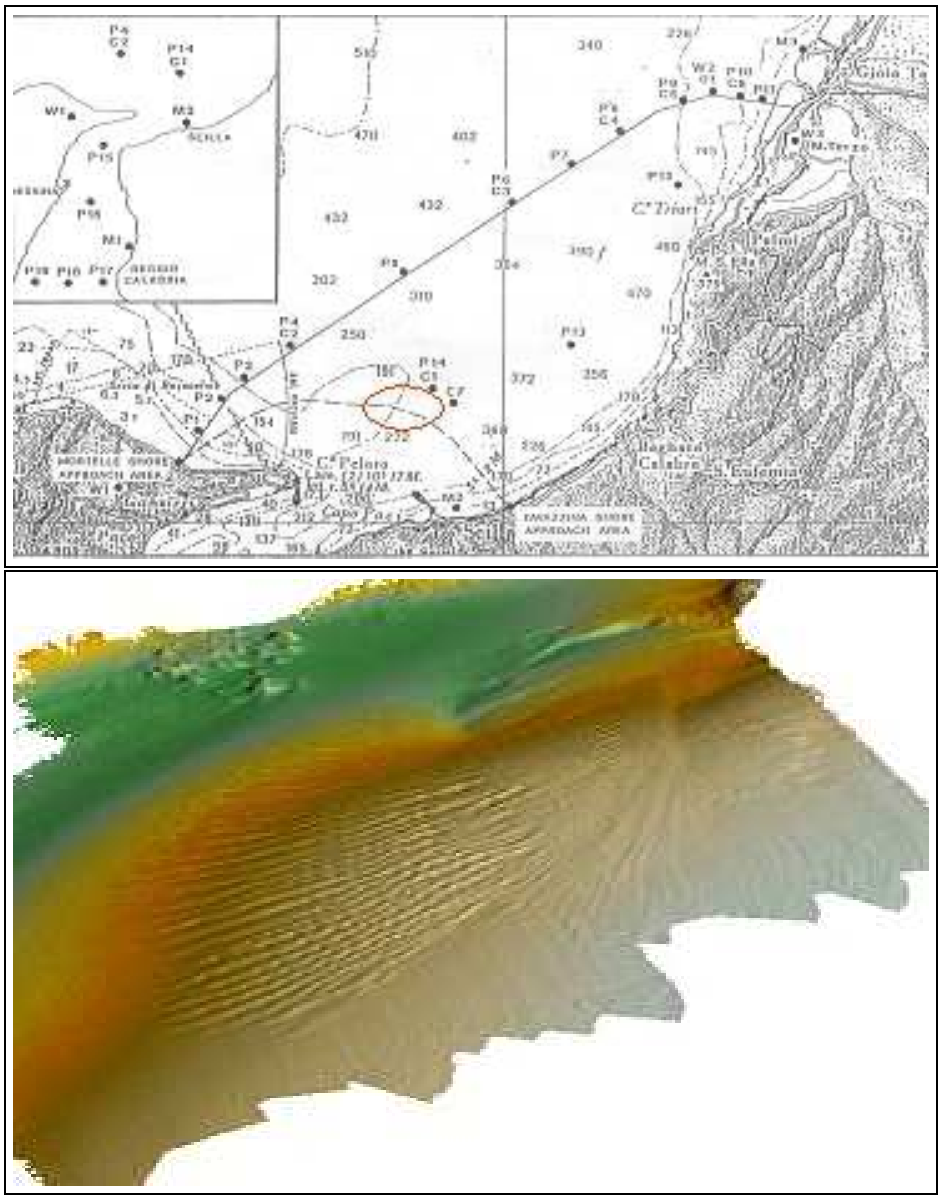

Figure 8: Top Panel - Strait of Messina (between Sicily and main land Italy): location of the surveyed area (red circle). Bottom Panel - Bottom topography; a sand waves field is clearly present in the middle of the area (adapted from Santoro et. al, 2002).

In this case, a large amount of money has to be spent in periodic maintenance work in order to protect and stabilise the lines. Even more dangerous could be the linkage by ship anchors or by fishing gear, like the ground-nets, which can lead to the fracture of the pipeline. Positioning the pipes on the

top of the profile of the sand waves does not improve the situation: changes in the shape of the bedforms or their migration can expose again the pipes to the stresses described above. A very expensive solution to overcome the problem is to position the lines around sand wave fields, instead of crossing them. This is not a very suitable option because of the significant increase of materials to be employed and because sand waves fields are not static and they could move toward the pipeline. As shown in figure 7, the presence of complicated networks of telecommunication cables (left panel) and of oil and gas pipelines (right panel) lets one imagine the problems that could be created by the interaction between these bedforms and the buried lines.

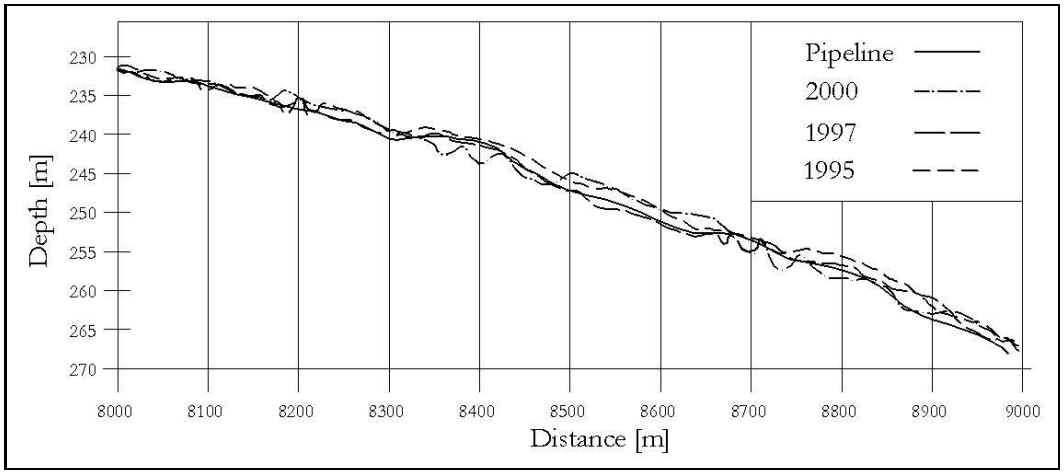

Figure 9: Surveys of the sea bed profile performed in different years in correspondence of the gas-pipeline between Sicily and Italy. Source: SNAMPROGETTI.

This problem has not been observed only in shallow seas like the North Sea, but in deeper waters like in the Mediterranean sea. In particular, after the laying of a pipeline in the Strait of Messina, located between the island of Sicily and main land Italy, the formation of several sand waves after few years has been observed. In figure **8** and **9** the location of the site where sand waves have been observed and the surveys performed along the pipeline in different years are reported. Note that the depth at which these bedforms appeared was approximately 250m.

Navigation Channels

Large ships, like container carriers or huge oil-tankers, require a minimum navigation depth, and even the width of the navigation channel is very im-

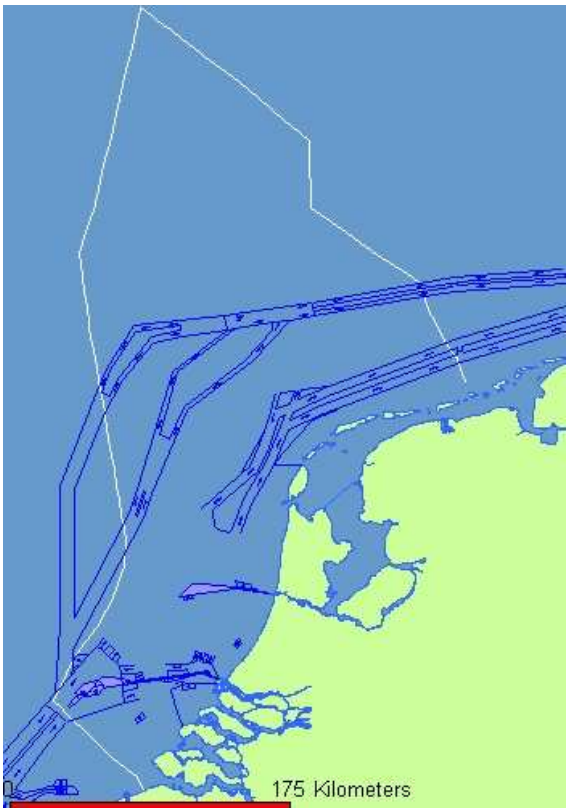

Figure 10: Navigation channels present in the North Sea along the Dutch coast. Approximatively 500,000 ships travel along these paths. More than 220,000 run through the channel leading to the Europoort of Rotterdam (source: Noordzeeatlas).

portant when the ships are manoeuvring. In shallow seas like the North Sea and in particular along the navigation route which leads to the Rotterdam harbour (EUROPOORT), the maintenance of the navigability standards is of vital importance for the economic activities of the region. To prevent any risk to shipping, the Eurochannel is frequently dredged. Nevertheless, the clearances are very marginal (in figure **10** the main navigation channels present in the North Sea are shown, most of them have to be dredged in order to reach the minimum nautical depth required by draught bulk carriers, i.e. 22-23 meters).

Both the migration and the seasonal variation in height or asymmetry of the sand waves can significantly affect the topography of the sea bed. In some cases this reduces the minimum free water depth necessary for the navigation of the vessels. Applying the knowledge concerning sand wave dynamics

(growth and migration) with analytical tools could improve the management and the planning procedures of the maintenance activities for safe navigation conditions.

Sand Mining

In the last decade the need for coastal administration to decrease the rate of erosion of the coasts, either for touristic aims, or for necessity, indicated sand extraction from the sea bed as one of the solutions to be employed. The dredged sand, in fact, can be used for beach nourishment, land reclamation and even in the construction industry. Moreover, as explained before, the dredging of these bedforms is necessary to allow safe navigation in shallow seas. For this reason it is important to understand the influence of sand wave fields on dredging and mining activities. Of particular interest is the question whether sand waves fields tend to regenerate after the sand extraction, and if so, how quickly they will reach their original size (Knaapen et a., 2002). A good knowledge of the evolution of sand waves will allow to set up optimised dredging/mining activities with respect to the environmental matters and economical costs.

Other Practical Relevances

The appearance of sand wave fields is also of interest in regards to coastal protection and dispersion of pollutants. In the first case the presence of sand waves and sand banks provides for a direct protection of the adjacent coastline because they lead to the dissipation of the wave energy by the breaking of storm waves before they reach the coast. In the second case, buried or dumped material can be incorporated in the sand waves, and depending on the specific weight of the material, it will tend to accumulate in the troughs or on the crests of the bedforms. The following migration of these patterns could lead to a dispersion of the dumped materials with potentially very negative effects on the eco-system.

Outline of the Thesis

The aim of this research thesis is to deepen the knowledge and understanding of sand wave dynamics, improving the description of the physics of the problem and introducing new elements to the analysis which were not

taken into account in previous works. The first step followed in this work is the set-up of a simple model focused on the study of the interaction between the topography of small bedforms and the surrounding flow field. In fact, the physical process leading to the formation and migration of sand waves in tide-dominated coastal areas has been investigated by means of a linear stability analysis of a flat sandy bottom subject to an oscillatory current of tidal origin. To perform the analysis the problem has been divided into a basic state and a perturbed state. The former represents an undisturbed tidal current in absence of bedforms, while the latter takes into account the introduction of bottom perturbation which trigger the rise of a perturbed flow responsible of the growth or decay of the bedforms.

In a second stage a fully three-dimensional model for the generation and evolution of sand waves and tidal sand banks from bottom perturbations of a flat seabed subject to the action of tidal currents is proposed. A horizontally two-dimensional basic flow comprehensive of Coriolis effects, forced by the local tidal currents, is considered. The basic flow is completely resolved also in the vertical direction from the sea bed up to the free surface. The flow regime is assumed to be turbulent and a Boussinesq approach is adopted to model Reynolds stresses. The eddy viscosity depends on the distance from the bed and an accurate description of the flow close to the sea bed, where sediment motion is mainly confined, is obtained. Sediment transport is modelled in terms of both suspended load and bed load. Finally, the presence of wind waves is taken into account.

The outline of the thesis is as follows:

Chapter 1

In the first chapter the model has been applied to investigate the mechanism leading to the formation of sand waves.

The conditions for the decay or amplification of small bottom perturbations are determined for arbitrary values of the typical parameters of the problem, which are r, corresponding to the ratio between the amplitude of the horizontal tidal excursion and the wavelength of the bottom perturbations, and s, which is a stress parameter necessary for the description of the partial slip condition, relating shear stress and velocity at the bottom.

According to field observations, the initial growth of sand waves requires a minimum amplitude of the tidal current, even when the critical bed shear stress for the initial motion of sediment is set equal to zero. In this first set of runs only the main tidal constituent has been taken into account, while steady currents and over-tides have been neglected. Moreover, the minimum amplitude depends on sediment characteristics. In particular, the analysis

shows that sand waves appear only on a sandy bottom and their growth does not take place when a coarse sediment covers the sea bed.

The solution procedure extends the harmonic truncation method which is often used to describe the flow generated by the interaction of bottom perturbations with the oscillatory tidal current (Hulscher, 1996a; Komarova & Hulscher, 2000; Komarova & Newell, 2000). In the present work, the problem has been solved for arbitrary values of r and s using a procedure similar to that employed by Vittori (1989) and Vittori & Blondeaux (1990) in a different context. A Fourier series in time is used to compute the stream function associated with the flow perturbations and the results show that the number of harmonics necessary to obtain an accurate description of the perturbed flow is relatively small for moderate values of r, but it increases as the parameter r is increased. Finally, the asymptotic approach proposed by Gerkema (2000) for large values of both r and s is modified in the bottom boundary layer to describe cases characterised by values of s of order one, which is the order of magnitude suggested by an analysis of field data.

Chapter 2

In the second chapter attention is focused on the mechanism of migration of sand waves and in particular the study has been devoted to the prediction of migration rates that sand waves undergo because of tidal and residual currents.

The inclusion of steady current ($Z0$) and various harmonic components ($M2$ and $M4$) of the tidal wave in the description of the phenomenon allows for the prediction of the migration speed of sand waves. In fact, if only one tidal component ($M2$) is accounted for and the residual current is neglected as done by Hulscher (1996a), Gerkema (2000), Komarova & Hulscher (2000), the flow at time $t + T/2$ (T being the tide period) is the mirror image of that at time t, the time-averaged flow is symmetric and no migration of sand waves can be induced. Although for practical problems migration is probably the most important property of sand waves, only Németh et al. (2002) modelled sand wave migration. Németh et al. (2002) investigated the phenomenon by means of a model similar to that of Hulscher (1996) and, hence, with an approach which is strictly valid only when the parameter r is moderate. Moreover, Németh et al. (2002) only considered the presence of a residual current and found that sand waves always migrate downstream, i.e. in the direction of the steady current. Field data, which will be presented in section **2.2**, show that in some cases sand waves migrate upstream, i.e. against the residual current. Even though different elements can contribute to sand wave migration (a.o. storms, wind driven currents, ...), it is possible to show that such an upstream migration can be modelled by investigating

the interaction of different tide constituents ($Z0$, $M2$ and $M4$).

The model adequately predicts migration rates even for the cases of upstream-propagating sand waves, i.e. for sand waves which migrate in the direction opposite to that of the residual current. It is shown that upstream/downstream propagation is mainly controlled by the relative strength of the residual current with respect to the amplitude of the quarter-diurnal tide constituent and by the phase shift between the semi-diurnal and quarter-diurnal tide constituents. Therefore, to accurately predict field cases a detailed knowledge of the direction, strength, and phase of the different tide constituents is required.

Chapter 3

In the third chapter attention is focused on the use of a more sophisticated and complete model capable of giving both a more reliable description of the process which leads to the formation of tidal sand banks and sand waves and more accurate predictions of their characteristics. Turbulence generated by tidal currents is described by introducing an eddy viscosity which is assumed to linearly grow with the distance from the bottom in the region close to the sea bed, to reach a maximum and to decrease and assume small values close to the free surface. Sediment is supposed to move as both bed load and suspended load since field surveys show that large amounts of sediment are put into suspension and transported by tidal currents. Moreover, the sediment motions induced by surface gravity waves are also considered. Finally, residual (steady) currents are taken into account because their presence is essential in explaining sand wave migration.

The model is based on the study of the stability of the flat bottom configuration. Small bottom perturbations are considered and a linear analysis of their growth is performed. The results show that the model can describe both the process which gives rise to sand waves and that leading to the formation of sand banks. The former bedforms have their crests normal to the direction of the tidal current and are characterised by wavelength of $O(10^2$ m). The latter bedforms have wavelengths of $O(10^4$ m) and turn out to be rotated slightly counterclockwise or clockwise with respect to the direction of propagation of the tidal current depending of the direction of rotation of the tidal wave. A comparison of the theoretical results with field observations supports the model findings. As a matter of fact, model predictions are successfully compared with field data of different sand banks (Le Bot et al., 2000) and sand waves measured at different locations in the North Sea.

Part I

A simple model

Introduction to Part I

One of the first attempts to explain the appearance of large scale bedforms is due to Huthnance (1982a). He focused his attention on sand banks and he assumed that they arise as free instabilities of the sea bottom forced by tidal currents. Further contributions to the study of sand banks formation were given by De Vriend (1990), Hulscher et al. (1993) and De Swart & Hulscher (1995). In the latter works it is also pointed out that a model based on depth averaged shallow water equations can explain formation of sand banks but is unable to predict the appearance of sand waves unless secondary circulations in the vertical plane are properly parametrized. Indeed, as pointed out in the studies of sand waves (Hulscher, 1996a; Gerkema, 2000), the process which leads to the formation of these bedforms is similar to that causing sea ripples under gravity waves (Sleath, 1976; Blondeaux, 1990; Blondeaux & Vittori, 1999; Blondeaux, 2001). Thus the interaction of the oscillatory tidal flow with bottom perturbations gives rise to a steady streaming in the form of recirculating cells. When the net displacement of the sediment dragged by this steady streaming is directed from troughs toward crests of bottom perturbation, the amplitude of the latter grows. On the other hand, the flat bottom configuration turns out to be stable when the net motion of the sediment is directed from crests toward troughs of the bottom perturbations.

Finite-amplitude sand waves were investigated by Fredsøe & Deigaard (1992) with an approach similar to that proposed by Fredsøe (1982) for dunes in fluvial environments. The approach describes the form of sand waves, but it is unable to explain the mechanism causing these bedforms and to predict the conditions which lead to their appearance. First attempts to describe sand wave appearance were made by Hulscher et al. (1993) and De Swart & Hulscher (1995) using depth averaged models with parameterisations of secondary currents in the vertical plane.

The first contribution aimed at a quantitative investigation of sand wave formation by means of a 3D approach is due to Hulscher (1996a), who formulated a model based on the three-dimensional shallow water equations. In this study turbulent stresses are handled by means of the Boussinesq hy-

pothesis and the eddy viscosity is assumed to be constant in time and over the water depth. As discussed in Hulscher (1996a) a constant eddy viscosity gives rise to an acceptable velocity profile, except in a negligible thin layer close to the wall, only when the no-slip condition at the bottom is replaced by a partial slip condition. Finally, the bottom time development is determined using the sediment continuity equation and a simple sediment transport formulation. The analysis predicts the temporal development of bottom perturbations of small amplitude (strictly infinitesimal) and determines the range of parameters for which the bottom perturbations amplify or decay.

The hydrodynamics of the problem is characterised by the presence of the parameter r, which is the ratio between the amplitude of the horizontal tidal excursion and the wavelength of the sand waves. Under field conditions r is typically large and, as discussed by Gerkema (2000), the truncation method used by Hulscher (1996a) to work out the solution, is not appropriate. By exploiting the fact that r is large, he solved the problem by using an asymptotic approach similar to that developed for the Orr-Sommerfeld equation for large values of the Reynolds number Re (Lin, 1967; Drazin & Reid, 1981). In this approach the fluid perturbation is split into two parts: an inviscid outer solution and viscous boundary layers, located at the wall and possibly corrections that are significant near 'critical' levels. Moreover, an analysis of the order of magnitude of the terms of the Orr-Sommerfeld equation shows that the wall layer has a thickness of order $Re^{-1/3}$. In closely following such approach, Gerkema (2000) assumed that the viscous wall layer has a thickness of order $r^{-1/3}$. However, the latter estimate is suitable when the no slip condition applies at the wall. In the context of the model employed by Gerkema (2000), the turbulent basic velocity distribution is approximated by a profile which does not vanish at the bottom, unless the stress parameter s, as assumed by Gerkema (2000), tends to be much larger than one and the turbulent velocity profile is almost coincident with that characterising the laminar regime. An analysis of field data and previous works on the subject (Hulscher, 1996a & 1996b) suggest that in the field s is of order one. In this case it can be shown (see section 1.3.3) that the viscous wall layer turns out to be of order $r^{-1/2}$ rather than $r^{-1/3}$ and critical layers do not exist. Gerkema (2000) also solved the problem with two alternative approaches. The first is an extension of Hulscher's (1996a) approach and it is strictly valid only for small values of the parameter r. The second uses a double series expansion and applies to values of r much larger than one. Unfortunately the method is not convergent in the case of, as pointed out by Gerkema (2000) himself, r is very large. To make an example considering sand waves characterised by a wavelength of the order of 100m and a semi-diurnal strong tide of the

order of 1m/s, it can be easily found that r attains values about 400, a value which is larger than the upper limit suggested by Gerkema (2003) for the application of the double series expansion approach (300).

In the present work, the problem has been solved with a method that is applicable for arbitrary values of r and s using a procedure similar to that employed by Vittori (1989) and Vittori & Blondeaux (1990) in a different context. A Fourier series in time is used to compute the stream function associated with the flow perturbations. The results show that the number of harmonics necessary to obtain an accurate description of the perturbed flow, for moderate values of r, is relatively small, but larger than one and increases as the parameter r is increased (see discussion in section 1.4). This finding shows that the model of Hulscher (1996a), who evaluated the perturbed flow by considering just one harmonic, describes the main qualitative features of sand wave growth, but the results might be affected by significant quantitative errors.

Chapter 1

Formation of sand waves

1.1 Formulation of the problem

The formulation of the problem does not differ from that of previous authors (see for example Hulscher, 1996a, and Gerkema, 2000). Here, it is repeated for the sake of completeness and clearness.

We consider the flow generated by a tidal wave propagating over a cohesionless bed and investigate the time development of the bottom configuration it induces. To allow an easy comparison between the results of the present analysis and that of Gerkema (2000), we use, when possible, the same notations. We consider a two-dimensional turbulent flow and, we employ a Boussineq type closure and the 'slip velocity' approach of Engelund (1964). Hence the hydrodynamics of the problem is described by momentum and continuity equations which read

$$\frac{\partial \mathbf{u}}{\partial t} + (\mathbf{u} \cdot \nabla)\mathbf{u} = -\frac{1}{\rho}\nabla p + A\nabla^2 \mathbf{u} \tag{1.1}$$

$$\nabla \cdot \mathbf{u} = 0 \tag{1.2}$$

where x denotes the horizontal coordinate in the direction of tide propagation, z is the vertical coordinate, $\mathbf{u} = (u, w)$ are the horizontal and vertical velocity components averaged over turbulence respectively and ∇ is the operator defined by $(\partial/\partial x, \partial/\partial z)$. Moreover, the density ρ and the eddy kinematic viscosity A, which is introduced to model Reynolds stresses, are assumed to be constant in space and in time. This assumption lead to a simplified formulation of the problem, advantageous in terms of analytical and numerical computations.

A constant eddy viscosity model provides an approximate but still acceptable description of the flow induced by tide propagation provided the

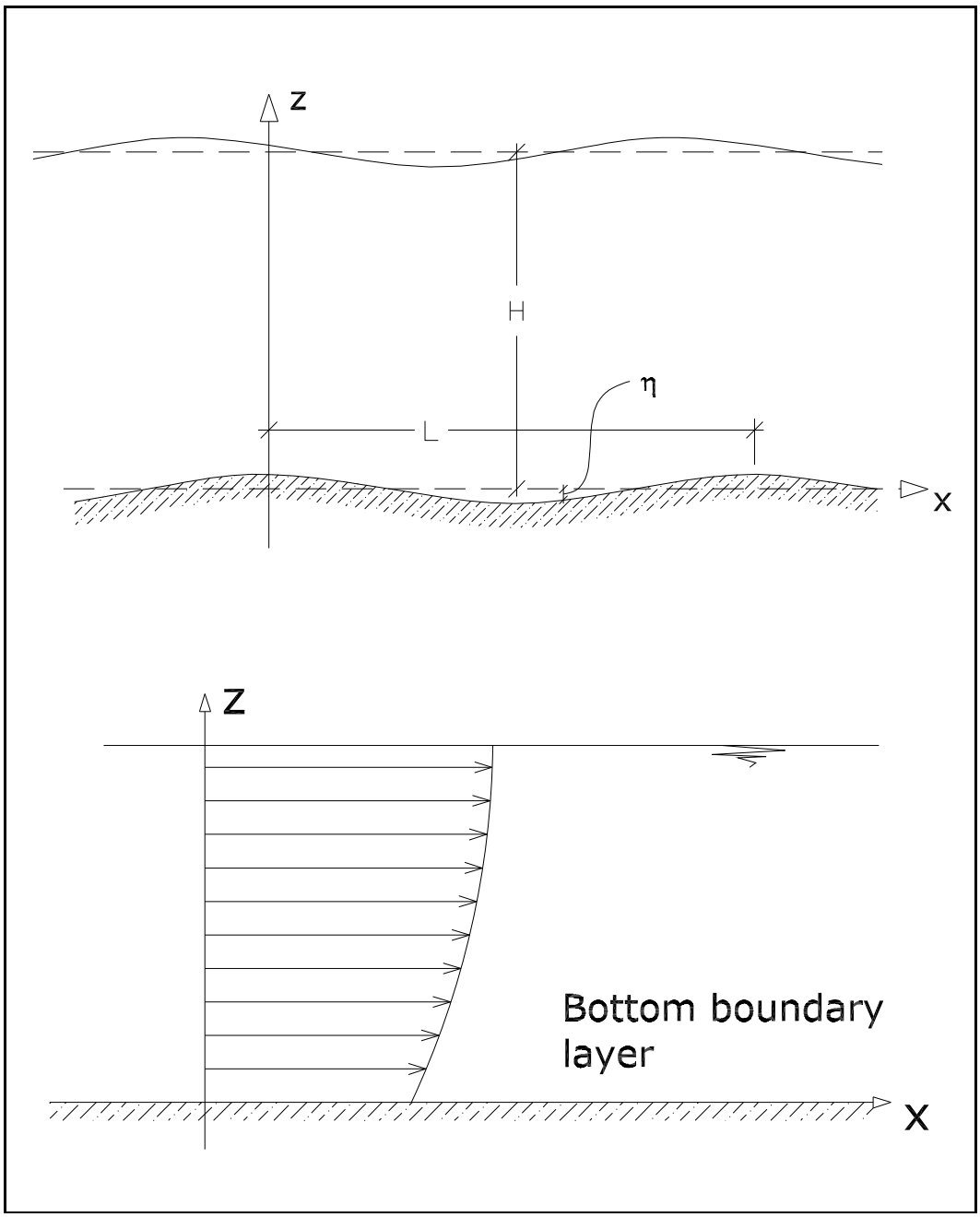

Figure 1.1: Sketch of the model geometry and of the partial slip condition. The horizontal and vertical direction are denoted by x and z.

no-slip condition at the bottom is replaced by a partial slip condition

$$\frac{\partial u_{||}}{\partial n} = \tilde{s} u_{||} \quad \text{at} \quad z = \eta(x,t) \tag{1.3}$$

where $\partial/\partial n$ denotes the derivative in the direction normal to the bottom, $u_{||}$ indicates the along-slope velocity component and $z = \eta(x,t)$ describes the bottom profile (Engelund, 1964). In (1.3) $\tilde{s}$ is a stress parameter, the value of which should be properly chosen. Moreover, at the bed the normal velocity component should vanish

$$u\frac{\partial \eta}{\partial x} - w = 0 \quad \text{at} \quad z = \eta(x,t). \tag{1.4}$$

Finally, we use the rigid lid approximation and, at the free surface ($z = H$), we force

$$w = 0, \qquad \frac{\partial u}{\partial z} = 0 \quad \text{at} \quad z = H. \tag{1.5a,b}$$

The results of the present analysis do not fully confirm the adequacy of such model. However, before improving upon the turbulent formulation, we need to investigate fully what predictions arise from the correct use of such model.

The morphodynamics of the problem is governed by the sediment continuity equation which simply states that convergence (or divergence) of the sediment flux must be accompanied by a rise (or fall) of the bed profile

$$\frac{\partial \eta}{\partial t} + \frac{\partial Q}{\partial x} = 0 \tag{1.6}$$

where Q denotes the sediment flux per unit width divided by a porosity factor. The problem is closed by a sediment transport formulation. To allow an easy comparison of present results with those of Gerkema (2000), we follow his analysis and assume that

$$Q = \alpha |u|^3 \left(\frac{u}{|u|} - \gamma \frac{\partial \eta}{\partial x} \right). \tag{1.7}$$

The above sediment transport formula is obtained by relating Q to the agitating forces which act on sediment grains. The latter move subject to the drag force and to the tangential component of gravity acting along the bed profile, other forces being negligible. The sediment transport induced by the drag force is empirically known to be proportional to the third power of the fluid velocity while that caused by gravity is known to be linearly related to the local bottom slope, at least for small values of the latter. In (1.7) α is a

constant, the value of which is of order $10^{-4}\mathrm{s}^2\mathrm{m}^{-1}$, and γ is the dimensionless bed-slope parameter which assumes typically values of order one (see Fredsøe, 1974). To estimate the constant value A of the eddy viscosity, the depth averaged value of the actual eddy viscosity profile is computed. Moreover, it is possible to obtain an estimate of the value of the parameter $\tilde{s}$ comparing the parabolic velocity profile obtained by (1.1) in steady conditions with the well known logarithmic distribution.

Using a parabolic profile to describe the z-variations of the kinematic eddy viscosity and the values of the conductance coefficient C suggested in the literature (see a.o Fredsøe and Deigaard, 1992), it turns out that

$$A = \frac{\kappa U_m H}{6C} \; ; \quad \tilde{s} = \frac{6}{H(\kappa C - 2)} \quad \text{with} \quad C = 2.5 \ln\left(\frac{H}{\epsilon}\right) + 6 \qquad (1.8a,b)$$

where $\kappa = 0.41$ is the Von Karman's constant, U_m is the depth averaged velocity defined as

$$U_m = \frac{1}{H}\int_0^H u(z)\, dz \qquad (1.9)$$

and ϵ is the bottom roughness. Similar relationships are obtained using different eddy viscosity profiles even if significant quantitative differences may be present. Since tidal currents are a slowly varying phenomenon, relationships (1.8) are expected to provide a reliable estimate also in the case under investigation. On the basis of these results it can be concluded that A ranges around 10^{-2} and 10^{-1} m^2/s and $\tilde{s}$ around 10^{-2} and 10^{-1} m^{-1},values similar to those employed by Hulscher (1996a) and discussed in Hulscher (1996b).

1.2 The basic state

In order to model the flow locally induced by the propagation of the tidal wave, we consider the flow over a flat bottom forced by an oscillatory horizontal pressure gradient of angular frequency σ and write

$$\frac{\partial p}{\partial x} = -\frac{P_{1x}}{2}\left(e^{i\sigma t} + c.c.\right), \qquad (1.10)$$

where the strength of the pressure gradient can be related to the amplitude of the tidal wave. In this first part of the work we assumed just one harmonic constituent in order to study the effect of the main semi-diurnal tidal constituent on the growth of the bedforms. The reader should notice that the form of $\partial p/\partial x$ employed herein differs from that used by Gerkema (2000). It

can be easily verified that the vertical velocity component of the basic flow vanishes identically, while the horizontal component (u_b) reads

$$u_b = \frac{P_{1x}}{2i\rho\sigma}\left[1+\tilde{c}\left(E^2 e^{-(1+i)\frac{z}{\Delta}} + e^{(1+i)\frac{z}{\Delta}}\right)\right] e^{i\sigma t} + c.c. \quad , \tag{1.11}$$

where Δ is the thickness of the viscous boundary layer

$$\Delta = \sqrt{2A/\sigma} \quad , \tag{1.12}$$

and

$$E = e^{(1+i)\frac{H}{\Delta}}; \quad \tilde{c} = -\frac{\tilde{s}}{\tilde{s}(E^2+1)+(1+i)(E^2-1)/\Delta} \quad . \tag{1.13a,b}$$

As discussed by Gerkema (2000), for moderate values of the parameter $\mu = H^2/(A/\sigma)$, which is the square of the ratio between the water depth and the thickness of the viscous boundary layer, the basic flow, given by (1.11), can also be approximated as follows:

$$u_b = \frac{U_0}{2}\left(z_c + \frac{z}{H}\right)\left(2 + z_c - \frac{z}{H}\right) e^{i\varphi} e^{i\sigma t} + c.c. \quad , \tag{1.14}$$

where z_c is a dimensionless constant defined in the form

$$z_c = -1 + \sqrt{1 + 2/(\tilde{s}H)} \quad , \tag{1.15}$$

defined as the distance below the sea bed at which the parabolic profile of the velocity vanishes, and U_0 and φ are fitting parameters which can be easily determined by comparing the depth averaged values of u_b obtained from (1.14) and (1.11). In particular, as described later in more detail, it turns out that $U_0 = [2/3 + z_c\,(2+z_c)]^{-1}\,U_m$, where U_m is the amplitude of the depth average velocity oscillations induced by the tide.

In figure **1.2** the velocity profiles (1.11) and (1.14) with optimised values of U_0 and φ are shown at different instants throughout the tidal cycle, for fixed values of the parameters and in particular for values of μ of order 1. The agreement is satisfactory even though the reader should be aware that, for increasing μ, the differences between (1.11) and (1.14) become significant.

At this stage it is worth pointing out that z_c is always positive, smaller than 1 but not close to zero if values of $\tilde{s}$, H ($\tilde{s} \sim O(10^{-1}\ \mathrm{m}^{-1})$, $H \sim O(10\mathrm{m})$) typical of the tides in the North Sea are used. For example considering a value of the bottom roughness ϵ equal to 3 cm (sea ripples are supposed to be present) and a water depth of 30 m, (1.8) and (1.15) lead to z_c equal to about 0.87. Even in the presence of megaripples, which can reach an amplitude up to 0.5m, z_c will turn out to be smaller than one, but not close to zero.

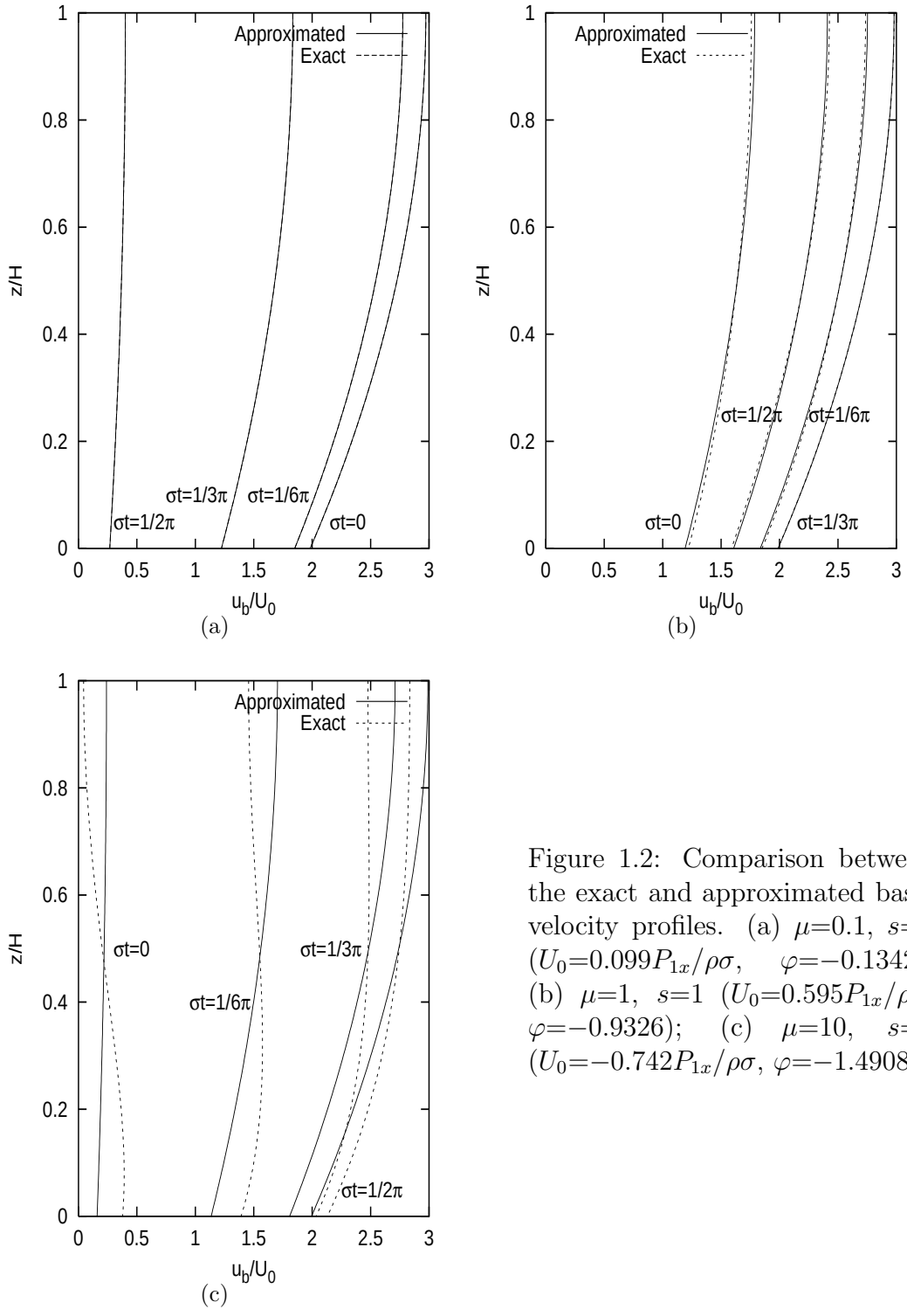

Figure 1.2: Comparison between the exact and approximated basic velocity profiles. (a) μ=0.1, s=1 (U_0=$0.099P_{1x}/\rho\sigma$, φ=-0.1342); (b) μ=1, s=1 (U_0=$0.595P_{1x}/\rho\sigma$, φ=-0.9326); (c) μ=10, s=1 (U_0=$-0.742P_{1x}/\rho\sigma$, φ=-1.4908).

1.3 The time development of bottom perturbations

We now perform a normal mode analysis to investigate the stability of the flat bottom configuration.

We consider perturbations of small amplitude (strictly infinitesimal), hence the problem can be linearised and a generic component of the bottom perturbation of the form

$$\eta(x,t) = \Pi(t)\cos(kx) = \frac{\Pi(t)}{2}e^{ikx} + c.c. \tag{1.16}$$

can be considered.

In (1.16) Π is assumed to be much smaller than H and k is the wavenumber of the perturbation that can be chosen arbitrarily.

In order to solve the mathematical problem, it is convenient to make it dimensionless by introducing the following dimensionless variables which are denoted by a prime:

$$x' = kx, \quad z' = z/H, \quad t' = \sigma t \tag{1.17a,b,c}$$

$$u_b' = u_b/U_0 \tag{1.18}$$

$$\eta' = \eta/H, \quad \Pi' = \Pi/H, \quad \psi' = \psi/(U_0 H) \tag{1.19a,b,c}$$

$$T' = t\alpha U_0^3/H^2, \quad Q' = Q/(\alpha U_0^3) \ . \tag{1.20a,b}$$

In (1.19c), ψ is the stream function associated with the velocity field induced by the bottom perturbation ($u = \partial\psi/\partial z$, $w = -\partial\psi/\partial x$), while T' has been made dimensionless using the morphodynamic time scale ($H^2/\alpha U_0^3$). The quantity U_0 has been chosen as velocity scale to allow an easy comparison between the present analysis and that by Gerkema (2000). However, the results described in the following can be easily converted into those obtainable with different choices of the scaling velocity. For example, if the amplitude U_m of the depth averaged velocity oscillations is taken as the scaling velocity, it can be easily shown that $U_m = [2/3 + z_c(2 + z_c)]U_0$. In fact operating the average of (1.11) and (1.14) over the depth we respectively obtain

$$U_m = -\frac{Pi}{2\sigma}\left\{1 + \tilde{c}\sqrt{\frac{2}{\mu}}\frac{1}{(1+i)}\left(E^2 - 1\right)\right\}e^{it} + c.c. \tag{1.21}$$

$$U_m = \frac{U_0}{2}\left[z_c\left(z_c+2\right)+\frac{2}{3}\right]e^{i\phi}e^{it}+c.c. \tag{1.22}$$

and equating the amplitudes it is straightforward to obtain the above mentioned relationship.

Using these scaled variables and taking into account that the stream function can be written in the form

$$\psi(x,z,t) = \Pi(T)\Psi(z,t)e^{ix}+c.c. \tag{1.23}$$

the hydrodynamic problem is posed by the following Orr-Sommerfeld like equation:

$$\frac{1}{r}\frac{\partial}{\partial t}(N^2\Psi)+iu_bN^2\Psi-i\Psi\frac{\partial^2u_b}{\partial z^2}=\frac{1}{\mu r}N^4\Psi \tag{1.24}$$

with the following boundary conditions

$$\Psi+\frac{1}{2}u_b=0,\quad \frac{\partial^2\Psi}{\partial z^2}+\frac{1}{2}\frac{\partial^2u_b}{\partial z^2}=s\left(\frac{\partial\Psi}{\partial z}+\frac{1}{2}\frac{\partial u_b}{\partial z}\right)\quad \text{at}\quad z=0 \tag{1.25a,b}$$

$$\Psi=0,\quad \frac{\partial^2\Psi}{\partial z^2}=0\quad \text{at}\quad z=1 \tag{1.26a,b}$$

Because the morphodynamic time scale turns out to be much larger than the hydrodynamic scale, the time derivative of Π has consequently been neglected in (1.24). Moreover in (1.24) the operator N^2 is defined by $N^2 = \partial^2/\partial z^2 - \delta^2$.

Finally, the time development of the bottom configuration is described by

$$\frac{\partial\Pi}{\partial T}+2\delta i\left\langle\mathcal{Q}\right\rangle\Pi=0 \tag{1.27}$$

$$\mathcal{Q}=i\left[3u_b^2\frac{\partial\Psi}{\partial z}-\frac{1}{2}\gamma\delta|u_b|^3\right] \tag{1.28}$$

where the $\langle\rangle$ brackets denote the time average over the tide cycle and the small oscillations of the bottom profile, which take place around its average value during the tide cycle, have been neglected. In fact, we are interested in studying the long term behaviour of the development of the bottom perturbations because the bedform's morphodynamic scale is much greater than the evolution time scale of oscillations of the bed profile. For convenience, in (1.23)-(1.28) and in the following, the prime has been dropped.

The problem is characterised by the following dimensionless parameters

$$\delta = kH, \quad r = kU_0/\sigma, \quad \mu = H^2\sigma/A, \quad s = \tilde{s}H, \quad \gamma. \tag{1.29}$$

At this stage it is useful to discuss the typical size of the parameters δ, r, μ, s, γ for field conditions. The parameter δ is the dimensionless wavenumber of the bottom perturbation. Since sand waves are characterised by wavelengths of the order of 500 m and the water depth is tens of metres, δ attains values of order one. Typical values of U_m range around 1 m/s and σ is equal to 1.4544×10^{-4} s^{-1} for a semi-diurnal tide and to 7×10^{-5} s^{-1} for a diurnal tide. Therefore r attains values ranging from 10 to 10^2. Since, as already pointed out, tidal currents are characterised by a time scale much larger than that of the turbulent eddies, an estimate of the eddy viscosity A and of the stress parameter $\tilde{s}$ can be obtained from our knowledge of turbulence structure and eddy viscosity in steady currents and by equating A to the depth averaged value of empirical relationships proposed to describe the kinematic eddy viscosity and forcing the shear stress acting on the bed to be equal to $\rho\,(U_m/C)^2$ where C is a conductance coefficient which depends on the bottom roughness. On the basis of (1.8) it follows that typical values of μ and s are of order 1. Indeed figures **5** and **6** of Hulscher (1996b) show that average conditions of the North Sea are characterised by values of s ($s = \hat{S}/E_v$) smaller than 1 while in the Middelkerke bank s can be larger than 1 but it is smaller than 2. Moreover, as discussed in Hulscher (1996a), the field data presented in Maas & van Haren (1997) show that s ranges between 0.1 and 10. Finally in (1.7) α is a constant, the value of which is of order 10^{-4}s^{2}m^{-1}, and γ is the dimensionless bed-slope parameter which assumes typically values of order one. Note that Fredsøe (1974) used $\gamma = 0.1$.

Since the morphodynamic time scale is much larger than the hydrodynamic time scale (the tide period), the problem posed by (1.24)- (1.28) can be split into two parts: the hydrodynamics governed by the equations (1.24)-(1.26), the solution of which provides Ψ, and the morphodynamics governed by the equations (1.27),(1.28), the solution of which provides the time behaviour of Π.

The hydrodynamics has been solved here following an approach which holds for arbitrary values of r and is based on a procedure similar to that employed by Vittori (1989) and Vittori & Blondeaux (1990) in a different context. A Fourier series in time has been used to compute the stream function associated with the flow perturbation. In principle this approach can be applied for any value of r, even though the evaluation of Ψ becomes difficult for very large values of r, because the number of harmonics which are necessary to obtain an accurate description of the flow increases as the parameter r increases. However, as discussed in the following, accurate results

can be obtained for any value of r of practical relevance and the results show that the harmonic truncation method used by Hulscher (1996a) and later by Komarova & Hulscher (2000) and Komarova & Newell (2000) provides a qualitative description of the phenomenon but cannot be used to obtain accurate results for any set of the parameters.

To test the present approach, results have been obtained also for small values of r and they have been compared with those derived by means of a perturbation approach based on the assumption $r << 1$. A good agreement has been found.

Finally the problem has been solved assuming that the parameter r attains large values. As pointed out in the introduction, the analysis follows closely that of Gerkema (2000). However, since a finite velocity at the bottom is required to have a good description of the velocity profile generated by tide propagation, we show that the model requires a thickness of the viscous bottom boundary layer of order $r^{-1/2}$ rather than $r^{-1/3}$. Hence our results, and in particular those concerning the growth rate of bottom perturbation, substantially differ from those described by Gerkema (2000). The results of the asymptotic analysis have been successfully compared with those of the approach which holds for arbitrary values of r.

Once Ψ is known, the solution of the morphodynamic problem (1.27), (1.28) is trivial and the growth rate of Π can be easily determined.

1.3.1 The hydrodynamic problem for arbitrary values of r and s

When r assumes finite values, the hydrodynamic part of the problem can be solved using a procedure similar to that employed by Vittori (1989) and Vittori & Blondeaux (1990). Since the basic flow is time periodic, the function Ψ can be expanded as a Fourier series in time

$$\Psi = \sum_{n=-\infty}^{\infty} \hat{\Psi}_n(z) e^{int}. \tag{1.30}$$

Then, substitution of (1.30) into (1.24)-(1.26) leads to the following system of coupled linear ordinary differential equations

$$\begin{aligned} &\frac{in}{r} N^2 \hat{\Psi}_n + i \left[\hat{U}_1 N^2 \hat{\Psi}_{n-1} + \hat{U}_1^* N^2 \hat{\Psi}_{n+1} \right] - \\ &i \left[\frac{d^2 \hat{U}_1}{dz^2} \hat{\Psi}_{n-1} + \frac{d^2 \hat{U}_1^*}{dz^2} \hat{\Psi}_{n+1} \right] = \frac{1}{\mu r} N^4 \hat{\Psi}_n \end{aligned} \tag{1.31}$$

along with the following boundary conditions

$$\hat{\Psi}_n = 0 \;\; ; \;\; \frac{d^2\hat{\Psi}_n}{dz^2} = 0 \qquad \text{at} \;\; z = 1 \tag{1.32}$$

$$\hat{\Psi}_n = 0 \qquad \text{for} \;\; n \neq \pm 1 \qquad \text{at} \;\; z = 0 \tag{1.33}$$

$$\hat{\Psi}_1 = -\frac{\hat{U}_1}{2} \;\; ; \;\; \hat{\Psi}_{-1} = -\frac{\hat{U_1}^*}{2} \qquad \text{at} \;\; z = 0 \tag{1.34}$$

$$\frac{d^2\hat{\Psi}_n}{dz^2} - s\frac{d\hat{\Psi}_n}{dz} = 0 \qquad \text{for} \;\; n \neq \pm 1 \qquad \text{at} \;\; z = 0 \tag{1.35}$$

$$\frac{d^2\hat{\Psi}_1}{dz^2} - s\frac{d\hat{\Psi}_1}{dz} = -\frac{1}{2}\frac{d^2\hat{U}_1}{dz^2} + s\frac{d\hat{U}_1}{dz} \qquad \text{at} \;\; z = 0 \tag{1.36}$$

$$\frac{d^2\hat{\Psi}_{-1}}{dz^2} - s\frac{d\hat{\Psi}_{-1}}{dz} = -\frac{1}{2}\frac{d^2\hat{U_1}^*}{dz^2} + s\frac{d\hat{U_1}^*}{dz} \qquad \text{at} \;\; z = 0. \tag{1.37}$$

In (1.32)-(1.37) the basic flow u_b has been written in the form

$$u_b = \hat{U}_1(z)e^{it} + \hat{U}_1^*(z)e^{-it} \tag{1.38}$$

where $\hat{U}_1$ and its complex conjugate $\hat{U}_1^*$ can be derived comparing (1.38) with (1.11) if the exact solution is sought or with (1.14) if the approximate solution is used.

Notice that, in order to have a better description of the solution close to the bottom, where large gradients are expected for large values of r, the numerical integration has been carried out using a constant step in the variable ζ defined by

$$\zeta = \ln(1 + r^{1/2}z) \; . \tag{1.39}$$

Hence this assumption bears

$$\frac{d}{dz} = \frac{r^{1/2}}{e^{\zeta}}\frac{d}{d\zeta} \tag{1.40a}$$

$$\frac{d^2}{dz^2} = \frac{r}{e^{2\zeta}}\left(\frac{d^2}{d\zeta^2} - \frac{d}{d\zeta}\right) \tag{1.40b}$$

$$\frac{d^3}{dz^3} = \frac{r^{3/2}}{e^{3\zeta}}\left(\frac{d^3}{d\zeta^3} - 3\frac{d^2}{d\zeta^2} + 2\frac{d}{d\zeta}\right) \tag{1.40c}$$

$$\frac{d^4}{dz^4} = \frac{r^2}{e^{4\zeta}}\left(\frac{d^4}{d\zeta^4} - 6\frac{d^3}{d\zeta^3} + 11\frac{d^2}{d\zeta^2} - 6\frac{d}{d\zeta}\right). \tag{1.40d}$$

Substituting equations (1.40a-d) in (1.32), it is possible to write the system of coupled linear ordinary differential equations in the form

$$\begin{aligned}
&\frac{in}{r}\left[\frac{1}{e^{2\zeta}}\left(\frac{d^2}{d\zeta^2}-\frac{d}{d\zeta}\right)-\frac{\delta^2}{r}\right]\hat{\Psi}_n+ \qquad (1.41)\\
&+i\left\{\hat{U}_1\left[\frac{1}{e^{2\zeta}}\left(\frac{d^2}{d\zeta^2}-\frac{d}{d\zeta}\right)-\frac{\delta^2}{r}\right]\hat{\Psi}_{n-1}+\hat{U}_1^*\left[\frac{1}{e^{2\zeta}}\left(\frac{d^2}{d\zeta^2}-\frac{d}{d\zeta}\right)-\frac{\delta^2}{r}\right]\hat{\Psi}_{n+1}\right\}-\\
&-\frac{i}{r}\left\{\frac{d^2\hat{U}_1}{dz^2}\hat{\Psi}_{n-1}+\frac{d^2\hat{U}_1^*}{dz^2}\hat{\Psi}_{n+1}\right\}=\\
&=\frac{1}{\mu}\left\{\frac{1}{e^{4\zeta}}\left[\frac{d^4}{d\zeta^4}-6\frac{d^3}{d\zeta^3}+11\frac{d^2}{d\zeta^2}-\frac{d}{d\zeta}\right]-2\frac{\delta^2}{re^{2\zeta}}\left[\frac{d^2}{d\zeta^2}-\frac{d}{d\zeta}\right]+\frac{\delta^4}{r^2}\right\}\hat{\Psi}_n.
\end{aligned}$$

Analogously the boundary conditions can be written as follows

$$\hat{\Psi}_n=0\ \ ;\ \frac{d^2\hat{\Psi}_n}{d\zeta^2}-\frac{d\hat{\Psi}_n}{d\zeta}=0 \qquad \text{at}\ \ \zeta=\zeta_{fin} \qquad (1.42)$$

$$\begin{aligned}
&\hat{\Psi}_n=0 \qquad \text{for n}\neq\pm1;\\
&\hat{\Psi}_1=\frac{\hat{U}_1}{2}\ \ ;\ \hat{\Psi}_{-1}=\frac{\hat{U}_1^*}{2} \quad \text{at}\ \ \zeta=0 \qquad (1.43)
\end{aligned}$$

$$\begin{aligned}
&\frac{d^2\hat{\Psi}_n}{d\zeta^2}-\left(1+\frac{s}{r^{1/2}}\right)\frac{d\hat{\Psi}_n}{d\zeta}=0 \quad \text{for}\ \ n\neq\pm1\ \ \text{at}\ \ \zeta=0 \qquad (1.44)\\
&\frac{d^2\hat{\Psi}_1}{d\zeta^2}-\left(1+\frac{s}{r^{1/2}}\right)\frac{d\hat{\Psi}_1}{d\zeta}=-\frac{1}{2r}\left[\frac{d^2\hat{U}_1}{dz^2}-s\frac{d\hat{U}_1}{dz}\right]\\
&\frac{d^2\hat{\Psi}_{-1}}{d\zeta^2}-\left(1+\frac{s}{r^{1/2}}\right)\frac{d\hat{\Psi}_{-1}}{d\zeta}=-\frac{1}{2r}\left[\frac{d^2\hat{U}_1^*}{dz^2}-s\frac{d\hat{U}_1^*}{dz}\right]
\end{aligned}$$

where $\zeta_{fin}=\ln\left(1+r^{1/2}\right)$.

Neglecting harmonics higher than the $\mathcal{N}th$ in the Fourier series (1.30), the functions $\hat{\Psi}_n$ can be determined numerically using a Runge-Kutta scheme of second order and a shooting procedure. More precisely, starting from $z=1$, a set of $2\mathcal{N}+1$ linearly independent solutions $\hat{\Psi}_n^{(j)}$ are obtained assuming linearly independent values for the second and third derivatives of $\hat{\Psi}_n$. Then, the solution is determined as a linear combination of $\hat{\Psi}_n^{(j)}$ which satisfies the boundary conditions at the bottom. The number $\mathcal{N}$ of harmonics retained in (1.30) has been chosen on the basis of numerical experiments.

1.3.2 The hydrodynamic problem for $r \ll 1$

While unrealistic in practical situations, the case $r \ll 1$ is the easiest to analyse and provides results which can be used to test the procedure outlined in section 1.3.1.

When $r \ll 1$ the stream function Ψ can be expanded in the form

$$\Psi = \Psi_0^{(0)} + r\Psi_1^{(0)} + h.o.t. \tag{1.45}$$

where the index (0) indicates contributions determined in the limit $r \to 0$.

Then an analysis of the problems obtained at the first and second order of approximation substituting (1.45) into (1.24)-(1.25) shows that

$$\Psi_0^{(0)} = \hat{\Psi}_{0,1}^{(0)} e^{it} + c.c. \tag{1.46a}$$

$$\Psi_1^{(0)} = \hat{\Psi}_{1,0}^{(0)} + \hat{\Psi}_{1,2}^{(0)} e^{2it} - c.c. \tag{1.46b}$$

The determination of $\hat{\Psi}_{i,j}$ is straightforward. Analysing the terms of order r^0 it's possible to write

$$N^2 \hat{\Psi}_{0,1}^{(0)} \mu i = N^4 \hat{\Psi}_{0,1}^{(0)}. \tag{1.47}$$

Therefore we obtain the following differential equation

$$\frac{d^4 \hat{\Psi}_{0,1}^{(0)}}{dz^4} - \frac{d^2 \hat{\Psi}_{0,1}^{(0)}}{dz^2} \left(2\delta^2 + \mu i\right) + \hat{\Psi}_{0,1}^{(0)} \left(\delta^4 + \mu i \delta^2\right) = 0. \tag{1.48}$$

Hence the analytical solution can be easily written as

$$\hat{\Psi}_{0,1}^{(0)} = c_1^{(0)} e^{\delta z} + c_2^{(0)} e^{-\delta z} + c_3^{(0)} e^{z\sqrt{\delta^2 + i\mu}} + c_4^{(0)} e^{-z\sqrt{\delta^2 + i\mu}} \tag{1.49}$$

where the constants $c_1^{(0)}$, $c_2^{(0)}$, $c_3^{(0)}$, $c_4^{(0)}$ are determined imposing the boundary conditions

$$\hat{\Psi}_{0,1}^{(0)} = 0 \qquad z = 1 \tag{1.50a}$$

$$\frac{d^2 \hat{\Psi}_{0,1}^{(0)}}{dz^2} = 0 \qquad z = 1 \tag{1.50b}$$

$$\hat{\Psi}_{0,1}^{(0)} = -\frac{\hat{U}_1}{2} \qquad z = 0 \tag{1.50c}$$

$$\frac{d^2 \hat{\Psi}_{0,1}^{(0)}}{dz^2} - s\frac{d\hat{\Psi}_{0,1}^{(0)}}{dz} = -\frac{1}{2}\frac{d^2 \hat{U}_1}{dz^2} + s\frac{d\hat{U}_1}{dz} \qquad z = 0. \tag{1.50d}$$

Performing the analysis for the terms of order r^1, the resulting differential equation reads

$$\frac{\partial^4 \hat{\Psi}_1^{(0)}}{\partial z^4} + \hat{\Psi}_1^{(0)}\delta^4 - 2\delta^2 \frac{\partial^2 \hat{\Psi}_1^{(0)}}{\partial z^2} - \frac{\partial}{\partial t}\left(\frac{\partial^2 \hat{\Psi}_1^{(0)}}{\partial z^2} - \delta^2 \hat{\Psi}_1^{(0)}\right)\mu = \mu i u_b \left(\frac{\partial^2 \hat{\Psi}_0^{(0)}}{\partial z^2} - \delta^2 \hat{\Psi}_0^{(0)}\right) - \mu i \hat{\Psi}_0^{(0)} \frac{\partial^2 u_b}{\partial z^2}. \tag{1.51}$$

As pointed out by (1.46b) it is possible to split $\hat{\Psi}_0^{(0)}$ into a time dependent part ($\hat{\Psi}_{1,2}^{(0)}$) and a part ($\hat{\Psi}_{1,0}^{(0)}$) which does not depend on time

$$\frac{\partial^4 \hat{\Psi}_{1,2}^{(0)}}{\partial z^4} + \hat{\Psi}_{1,2}^{(0)}\delta^4 - 2\delta^2 \frac{\partial^2 \hat{\Psi}_{1,2}^{(0)}}{\partial z^2} - 2\mu i \frac{\partial^2 \hat{\Psi}_{1,2}^{(0)}}{\partial z^2} + \mu\delta^2 \hat{\Psi}_{1,2}^{(0)} = \mu i \left(A' \frac{\partial^2 \hat{\Psi}_{0,1}^{(0)}}{\partial z^2} - \delta^2 A' \hat{\Psi}_{0,1}^{(0)} + \mu i \hat{\Psi}_{0,1}^{(0)}\right) \tag{1.52}$$

$$\frac{\partial^4 \hat{\Psi}_{1,0}^{(0)}}{\partial z^4} - 2\delta^2 \frac{\partial^2 \hat{\Psi}_{1,0}^{(0)}}{\partial z^2} + \delta^4 \hat{\Psi}_{1,0}^{(0)} = \mu i \left\{ \left[A' \frac{\partial^2 \hat{\Psi}_0^{(0)}}{\partial z^2} - \delta^2 A' \hat{\Psi}_0^{(0)} \right] + \hat{\Psi}_0^{(0)} \right\} \tag{1.53}$$

where the term A' is quantified by

$$A' = \frac{1}{2}\left(z_c + z\right)\left(2 + z_c - z\right). \tag{1.54}$$

The boundary conditions corresponding to $\hat{\Psi}_{1,2}^{(0)}$ and $\hat{\Psi}_{1,0}^{(0)}$ are

$$\hat{\Psi}_{1,2}^{(0)} = 0 \quad ; \quad \frac{\partial^2 \hat{\Psi}_{1,2}^{(0)}}{\partial z^2} = 0 \qquad \text{at} \qquad z = 1 \tag{1.55a}$$

$$\hat{\Psi}_{1,2}^{(0)} = 0 \quad ; \quad \frac{\partial^2 \hat{\Psi}_{1,2}^{(0)}}{\partial z^2} - s\frac{\partial \hat{\Psi}_{1,2}^{(0)}}{\partial z} = 0 \qquad \text{at} \qquad z = 0 \tag{1.55b}$$

$$\hat{\Psi}_{1,0}^{(0)} = 0 \quad ; \quad \frac{\partial^2 \hat{\Psi}_{1,0}^{(0)}}{\partial z^2} = 0 \qquad \text{at} \qquad z = 1 \tag{1.56a}$$

$$\hat{\Psi}_{1,0}^{(0)} = 0 \quad ; \quad \frac{\partial^2 \hat{\Psi}_{1,0}^{(0)}}{\partial z^2} - s\frac{\partial \hat{\Psi}_{1,0}^{(0)}}{\partial z} = 0 \qquad \text{at} \qquad z = 0. \tag{1.56b}$$

The solution of (1.52) and (1.53) and that of (1.55) and (1.56) has been obtained analytically. Further details are omitted and the results are directly presented in section 1.4.

1.3.3 The hydrodynamic problem for $r \gg 1$

As explained in the previous section, in order to validate the results of the model obtained by introducing the Fourier series in time, we performed an analysis for values of $r \gg 1$. Since in (1.24) the small parameter r^{-1} multiplies the highest derivative, for large values of r the flow domain can be split into an inviscid core region, where z is of order one, and a viscous boundary layer close to the bottom. In the core region, the leading order component $\Psi^{(\infty)}$ of the stream function is provided by the solution of (1.24) where both the local acceleration term and the viscous term can be neglected and a balance takes place between advective terms:

$$u_b N^2 \Psi^{(\infty)} - \Psi^{(\infty)} \frac{\partial^2 u_b}{\partial z^2} = 0 \tag{1.57}$$

with the boundary conditions

$$\Psi^{(\infty)} = 0 \qquad \text{at} \quad z = 1 \tag{1.58a}$$

$$\frac{\partial^2 \Psi^{(\infty)}}{\partial z^2} = 0 \qquad \text{at} \quad z = 1 \tag{1.58b}$$

and a matching condition with the solution in the bottom boundary layer. Hereinafter the index (∞) indicates contributions determined assuming values of r much larger than one.

For the purpose of finding $\Psi^{(\infty)}$, the basic velocity field (1.11) can be approximated by the much simpler profile (1.14), which provides a good approximation if μ is of order 1 or smaller (Gerkema, 2000)(see also figure **1.2**). If the basic flow is assumed to be accurately described by (1.14), the solution can be written in the form

$$\Psi^{(\infty)}(z,t) = c_1^{(\infty)}(t)\phi_1(z) + c_2^{(\infty)}(t)\phi_2(z) \tag{1.59}$$

where

$$\phi_1 = (z + z_c) \sum_{n=0}^{\infty} d_n (z + z_c)^n \tag{1.60a}$$

$$\phi_2 = \phi_1 \ln(z + z_c) + \sum_{n=0}^{\infty} b_n (z + z_c)^n \tag{1.60b}$$

and the constants d_n and b_n can be easily computed by means of recursive relationships:

$$d_1 = -\frac{d_0}{C}, \qquad d_2 = \frac{\delta^2 d_0}{6},$$

$$d_{n+1} = \frac{[n\,(n+1) - 2]\,d_n + C\delta^2 d_{n-1} - \delta^2 d_{n-2}}{(n+1)\,(n+2)\,C} \qquad (n \geq 2)$$

where

$$d_0 = 1, \quad \text{and} \quad C = 2\,(1 + z_c)$$

and

$$b_2 = \frac{1}{2}\left(\delta^2 b_0 + \frac{d_0}{C} - 3d_1\right)$$

$$b_{n+1} = \left\{[n\,(n-1) - 2]\,b_n + \delta^2\,(Cb_{n-1} - b_{n-2}) - (2n+1)\,Cd_n + (2n-1)\,d_{n-1}\right\}\frac{1}{n\,(n+1)\,C} \qquad (n \geq 2)$$

where

$$b_0 = -\frac{C}{2}d_0, \quad b_1 = 0.$$

If z_c was negative, the inviscid balance would produce a logarithmic singularity in ϕ_2 which should be removed by taking into account the viscous term on the right hand side of (1.24) for z falling close to $-z_c$. However, z_c turns out to be positive with values smaller than one but not close to zero. Therefore the evaluation of $\Psi^{(\infty)}$ in the core region by means of (1.59),(1.60) does not lead to any problem. Finally, the forcing of the boundary conditions at the free surface allows to find a relationship between the constant $c_1^{(\infty)}$ and $c_2^{(\infty)}$ but not to determine both of them (note that it can be easily verified that (1.58a) is equivalent to (1.58b) because of (1.57)):

$$c_1^{(\infty)} = -c_2^{(\infty)} \ln(1 + z_c) + \frac{\tilde{\phi}_2}{\phi_1} \quad \text{at} \quad z = 1 \tag{1.61}$$

where

$$\tilde{\phi}_2 = \sum_{n=0}^{\infty} b_n \tilde{z}^n \qquad \text{and} \qquad \tilde{z} = z + z_c\ . \tag{1.62}$$

The inviscid balance should be corrected near the bottom, where a boundary layer develops and viscous effects turn out to be relevant. In the classical Orr-Sommerfeld equation, the thickness of this viscous layer is proportional to the $(-1/3)$ power of the Reynolds number (if $Re >> 1$), because the basic velocity profile vanishes at the wall. In the present case the value of s has been assumed ~ 1, therefore the basic flow described by (1.14) keeps finite at the bottom and an analysis of the order of magnitude of the different terms

appearing in (1.24) suggests that the thickness of the bottom boundary layer is of $O(r^{-1/2})$.

The correct analysis requires the introduction of the variable ξ defined as follows

$$\xi = r^{1/2} z \ . \tag{1.63}$$

Then the basic flow and the stream function associated with the perturbation should be expanded in the form

$$u_b = u_{b0} + r^{-1/2} u_{b1} + r^{-1} u_{b2} + h.o.t. \tag{1.64}$$

$$\Psi = \Psi_0^{(\infty)} + r^{-1/2} \Psi_1^{(\infty)} + r^{-1} \Psi_2^{(\infty)} + h.o.t. \tag{1.65}$$

By substituting (1.64), (1.65) into (1.24), (1.27)-(1.28) and equating likewise powers of $r^{-1/2}$, the functions $\Psi_i^{(\infty)}$ are determined. Then, imposing of the boundary conditions at the bottom and the matching condition with the solution in the inviscid region leads to the following solution:

$$\Psi_0^{(\infty)} = -\frac{1}{2} z_c (2 + z_c) \cos(t + \varphi) \ \ , \ \Psi_1^{(\infty)} = c_3^{(\infty)} \xi \ \ , \tag{1.66}$$

$$\Psi_2^{(\infty)} = -\frac{c_4^{(\infty)}}{i\mu u_b(t)} e^{-\sqrt{i\mu u_b(t)}\xi} + c_5^{(\infty)} \xi + c_6^{(\infty)} \ \ ,$$

with $c_3^{(\infty)}$, $c_4^{(\infty)}$, $c_5^{(\infty)}$, $c_6^{(\infty)}$ constants to be determined. Matching $\Psi_0^{(\infty)}$ with the inviscid solution determines the value of $c_2^{(\infty)}$ while matching $\Psi_1^{(\infty)}$ determines the value of $c_3^{(\infty)}$. The constants $c_j^{(\infty)}$ $(j = 4, 5, 6)$ are determined by the matching at the next order of approximation which requires the evaluation of further terms of the stream function in the inviscid region. It is also worth pointing out that the first two terms of (1.65) correspond to the largest terms of the outer solution written using the inner variable while strong gradients of Ψ appear only considering $\Psi_2^{(\infty)}$.

As already discussed by Gerkema (2000), the whole procedure breaks down when the flow reverses, i.e. when the basic velocity profile u_b vanishes in the whole water column. The problem can be easily circumvented. Indeed during the time intervals for which u_b is close to zero, the sediment flow rate vanishes and there are no significant morphodynamic implications.

1.3.4 The morphodynamic problem

Once the stream function associated with the bottom perturbation is computed, the temporal development of the amplitude Π of the generic component of the perturbation can be easily evaluated from (1.27) and (1.28).

With some straightforward algebra, it turns out that

$$\frac{d\Pi}{dT} = \delta(\theta_0 - \hat{\gamma}\delta)\Pi = \Gamma\Pi \tag{1.67}$$

where

$$\hat{\gamma} = \gamma\langle|u_b|^3\rangle_{z=0}\,, \qquad \theta_0 = \left\langle -6iu_b^2\frac{\partial\Psi}{\partial z}\bigg|_{z=0}\right\rangle \tag{1.68a,b}$$

and in terms of the coordinate ζ defined in (1.39):

$$\theta_0 = \left\langle -6iu_b^2 r^{1/2}\frac{\partial\Psi}{\partial\zeta}\bigg|_{z=0}\right\rangle \quad . \tag{1.69}$$

1.4 Discussion of the results

In this section the results on the morphodynamic stability, obtained on the basis of the procedure outlined in the previous section will be presented. But prior to this, we compare the stream function and other relevant quantities valid for arbitrary values of r, with the results of the asymptotic analyses applying for values of r much smaller or much larger than one. This has been done to test the implementation of the numerical algorithm and to ascertain the reliability of the results. Because the asymptotic solution for large values of r is based on the approximate basic velocity profile, use is made of (1.14). In figure **1.3** the function $\Psi(z)$, computed by means of (1.30), is compared with that found for r tending to zero, for fixed values of δ, μ, s and for decreasing values of r ($r = 10, 1, 0.1$). It can be seen that, as r becomes small, expansion (1.30) provides results close to those obtained on the basis of the asymptotic analysis described in section 1.3.2 and for r equal to 0.1 the two solutions are practically indistinguishable. Of course, for small values of r the stream function is dominated by the first term in (1.45) and by the harmonics e^{it} and e^{-it} in (1.30). For an exhaustive comparison we have not only compared $\hat{\Psi}_1$ with $\Psi_{0,1}^{(0)}$ but also $\hat{\Psi}_0$ and $\hat{\Psi}_2$ divided by r with $\Psi_{1,0}^{(0)}$ and $\Psi_{1,2}^{(0)}$, respectively.

A comparison is also made between (1.30) and the asymptotic solution for large values of r. In figure **1.4** the stream function is plotted for fixed values of δ, μ, s and increasing values of r at fixed phases of the tidal cycle. As expected, for increasing values of r the agreement between (1.59) and (1.30) improves and for large values of r the two approaches provide coincident results and in particular the function Ψ becomes real as predicted by the asymptotic analysis for large values of r. Hence (1.67) shows that the real

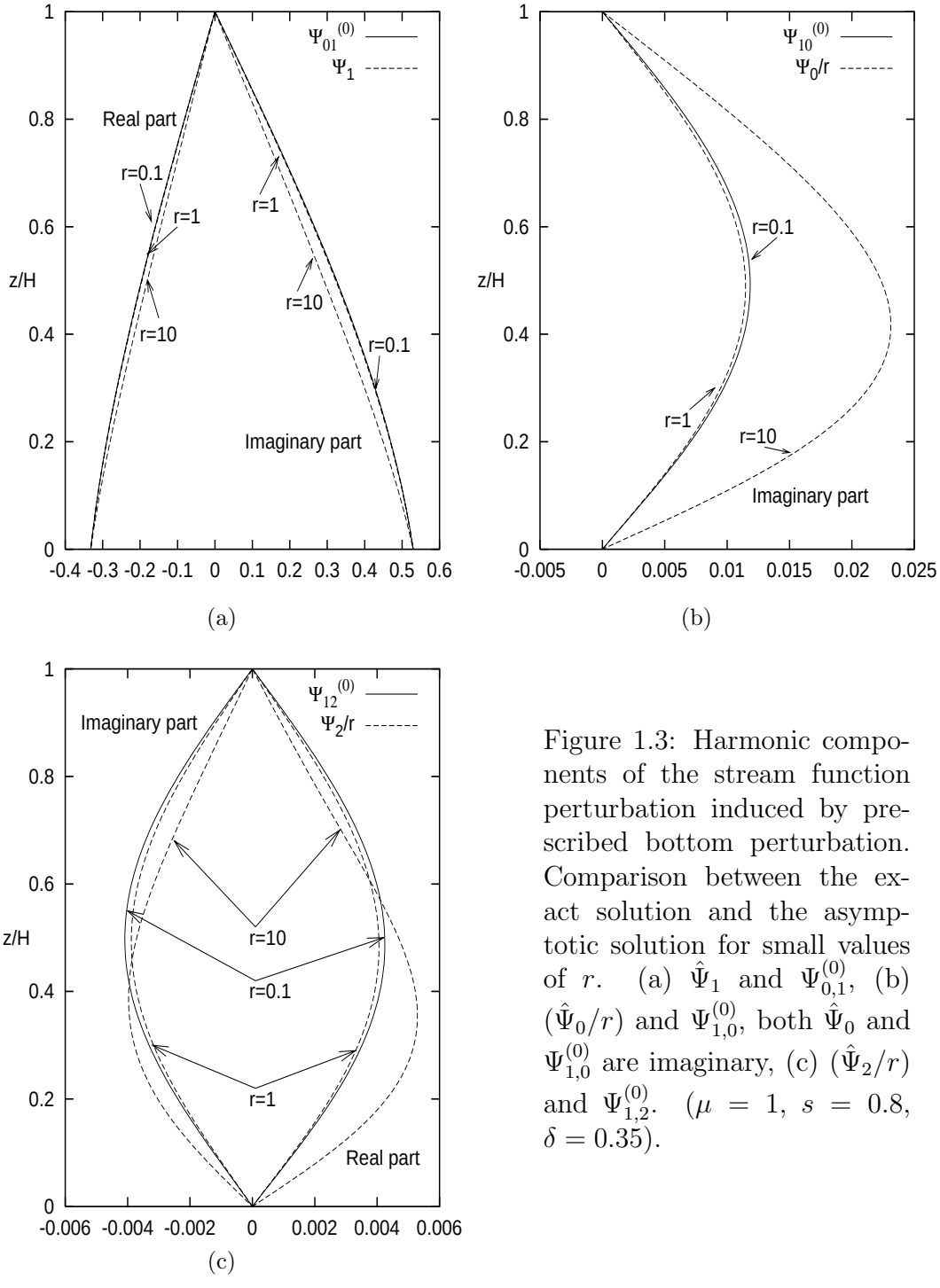

Figure 1.3: Harmonic components of the stream function perturbation induced by prescribed bottom perturbation. Comparison between the exact solution and the asymptotic solution for small values of r. (a) $\hat{\Psi}_1$ and $\Psi^{(0)}_{0,1}$, (b) $(\hat{\Psi}_0/r)$ and $\Psi^{(0)}_{1,0}$, both $\hat{\Psi}_0$ and $\Psi^{(0)}_{1,0}$ are imaginary, (c) $(\hat{\Psi}_2/r)$ and $\Psi^{(0)}_{1,2}$. ($\mu = 1$, $s = 0.8$, $\delta = 0.35$).

part Γ_r of Γ is always negative since it turns out to be equal to $\langle \gamma \delta^2 |u_b^3| \rangle$, i.e. the stabilising part related to the bed slope. Therefore for large values of r, the other parameters being fixed, no growth of the bottom perturbations takes place and the flat bottom configuration turns out to be always stable.

In figures **1.9**, **1.10**, **1.11** and **1.12**, the stream function associated with the bottom perturbation is plotted for fixed values of the parameters and for different values of truncation number $\mathcal{N}$ of the Fourier series (section 1.3.1). By looking at the results, it appears that the method of harmonic truncation used by Hulscher (1996a), in which $\mathcal{N}$ =1, can be applied only for small values of r and becomes inaccurate when r is increased.

This behaviour is clearly shown in figures **1.5**, **1.6**, **1.7** and **1.8** where the trend of the stream function Ψ is plotted against the number of harmonics used in the model, for a fixed value of z. It is evident that as r increases so has to do the number of harmonics in order to have an accurate solution.

Indeed when the horizontal tide excursion becomes significantly larger than the wavelength of sand waves (as it happens in the field), the interaction between the oscillatory flow induced by tide propagation and the bottom perturbation gives rise to a cascade process which generates many time harmonic components. For all the results described in the following, tests have been made to ensure that the results do not depend on the values of $\mathcal{N}$ and cases characterised by realistic values of the parameters can be handled without any problem.

An inaccurate evaluation of Ψ leads to errors also in the prediction of the development of the bottom perturbation as it appears in figure **1.13**, where the real part Γ_r of the correct amplification rate, obtained setting $\mathcal{N}$= 100 is plotted versus δ for realistic values of the parameters along with its value computed with $\mathcal{N}$ =1, i.e. considering just one harmonic component in the flow perturbation induced by the bottom waviness. The amplification rate obtained setting $\mathcal{N}$ =1 differs from the correct value by an amount ranging about 100%. As discussed in the introduction, this finding questions the recent results of Hulscher (1996a). Indeed significant variations of the coefficients of the amplitude equation may induce not only quantitative but also qualitative changes in the amplitude behaviour.

Once the reliability of the procedure is ascertained, to discuss the stability of the flat bottom configuration, the growth rate Γ is evaluated for different values of the parameters. Since the approach described in section 1.3.1 does not require to approximate the basic flow by (1.14), in the following the results have been obtained making use of the full solution (1.11). Both the real Γ_r and the imaginary Γ_i parts of Γ are computed. While the real part of Γ is related to the growth or decay of the amplitude of the bottom perturbations, their migration speed is controlled by the imaginary part of Γ.

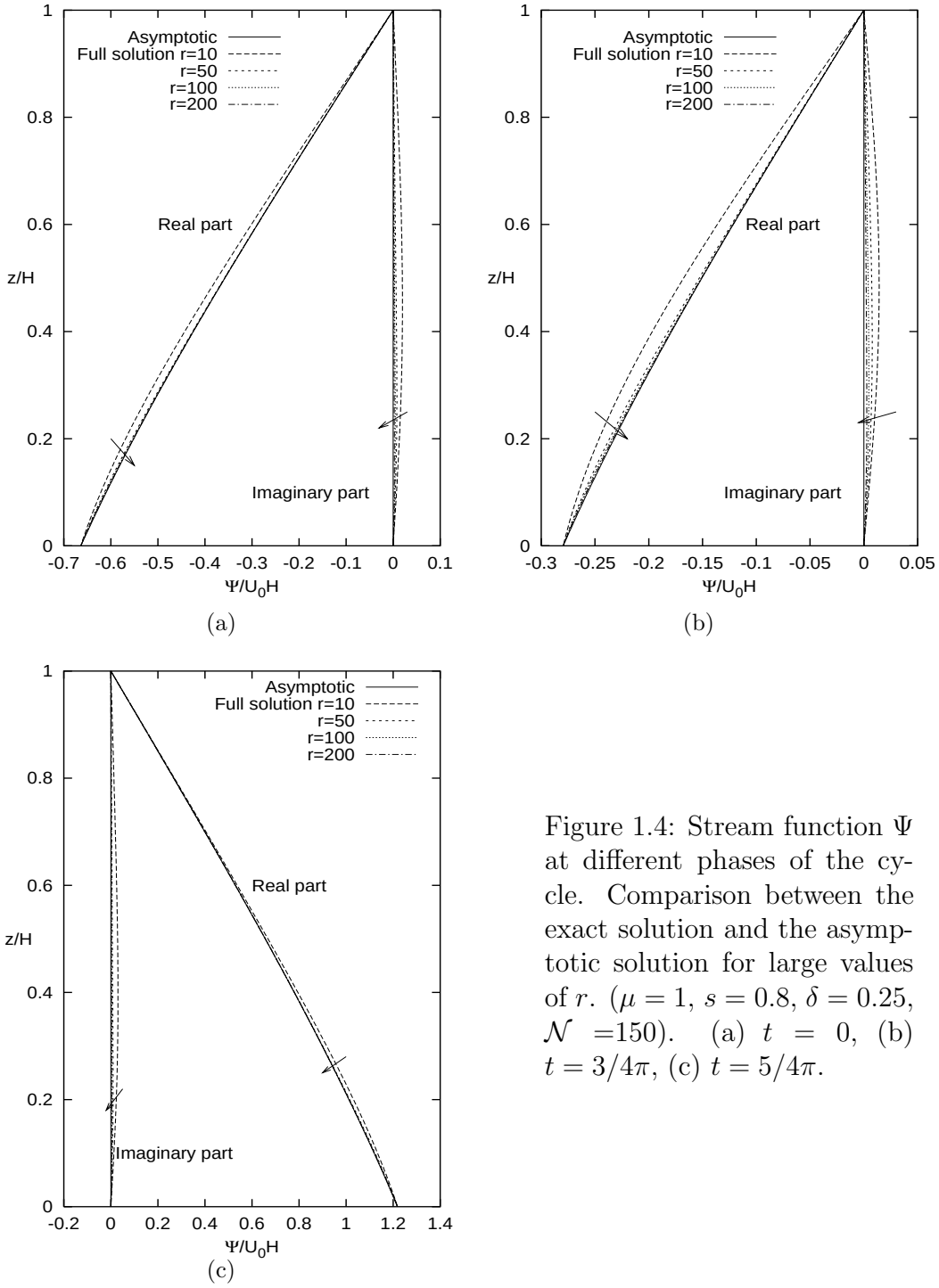

Figure 1.4: Stream function Ψ at different phases of the cycle. Comparison between the exact solution and the asymptotic solution for large values of r. ($\mu = 1$, $s = 0.8$, $\delta = 0.25$, $\mathcal{N}$ =150). (a) $t = 0$, (b) $t = 3/4\pi$, (c) $t = 5/4\pi$.

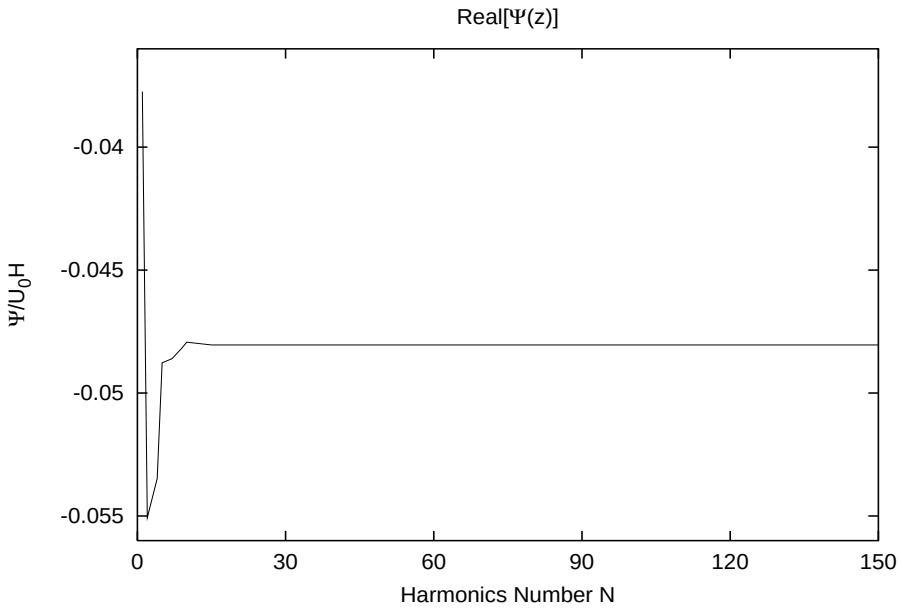

(a)

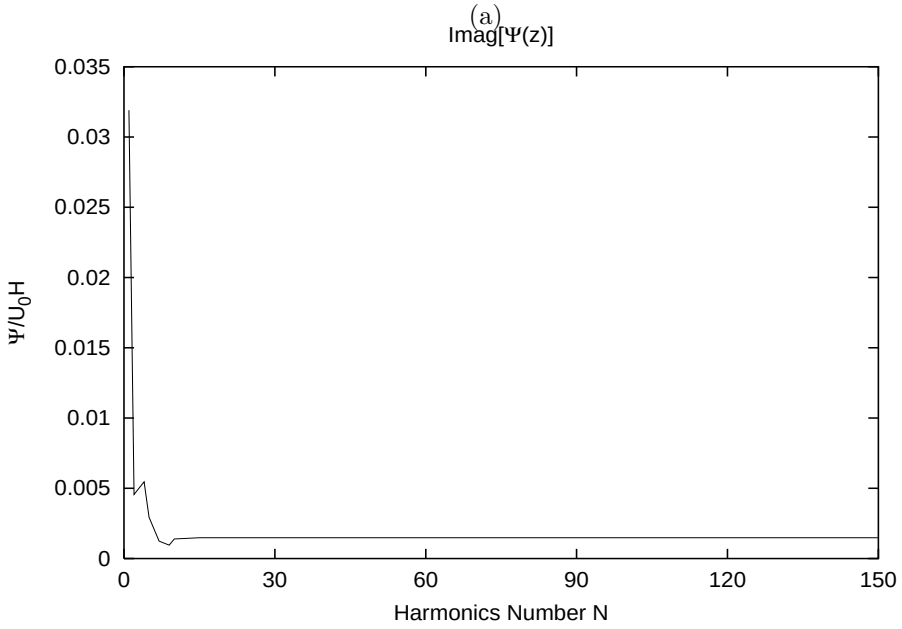

(b)

Figure 1.5: Value of streamfunction Ψ at a particular phase of the tidal cycle plotted against the number of harmonics. (μ=5, s=5, δ=0.2, t=0, z=0.5, r=10)

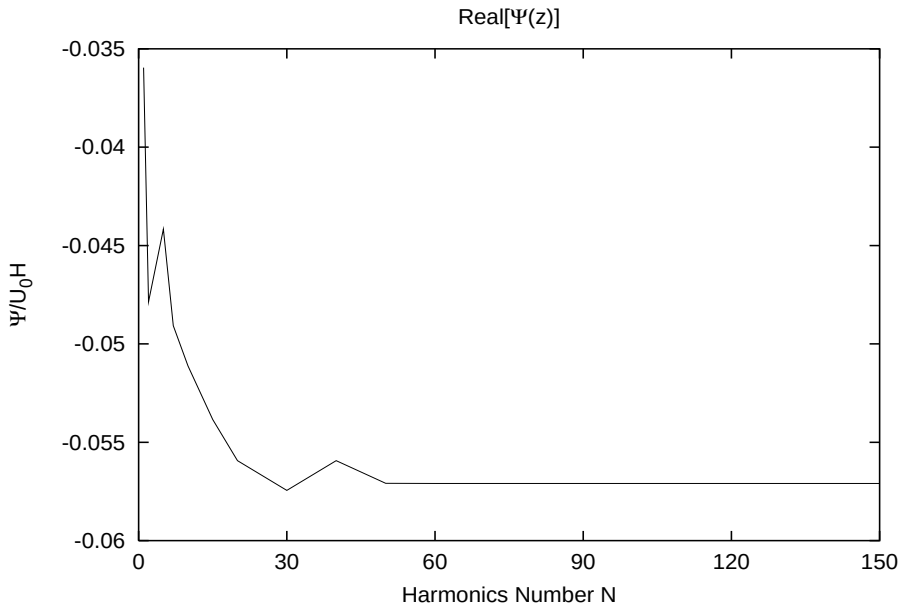

(a)

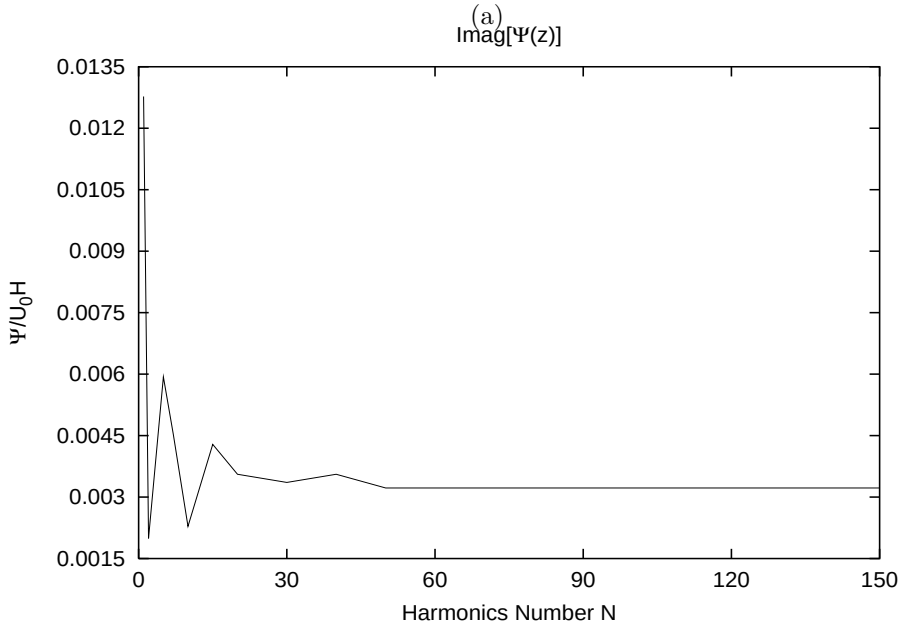

(b)

Figure 1.6: Value of streamfunction Ψ at a particular phase of the tidal cycle plotted against the number of harmonics. (μ=5, s=5, δ=0.2, t=0, z=0.5, r=50)

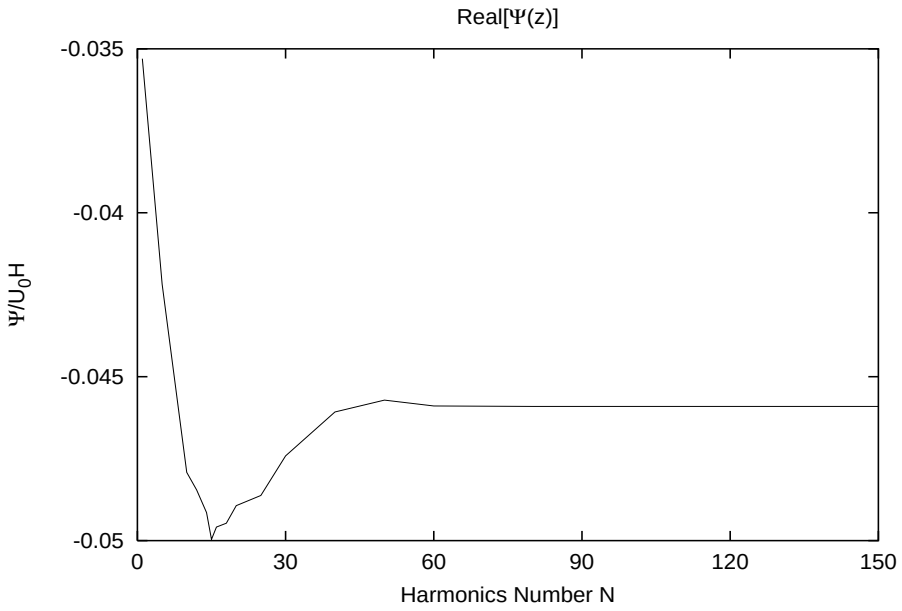

(a)

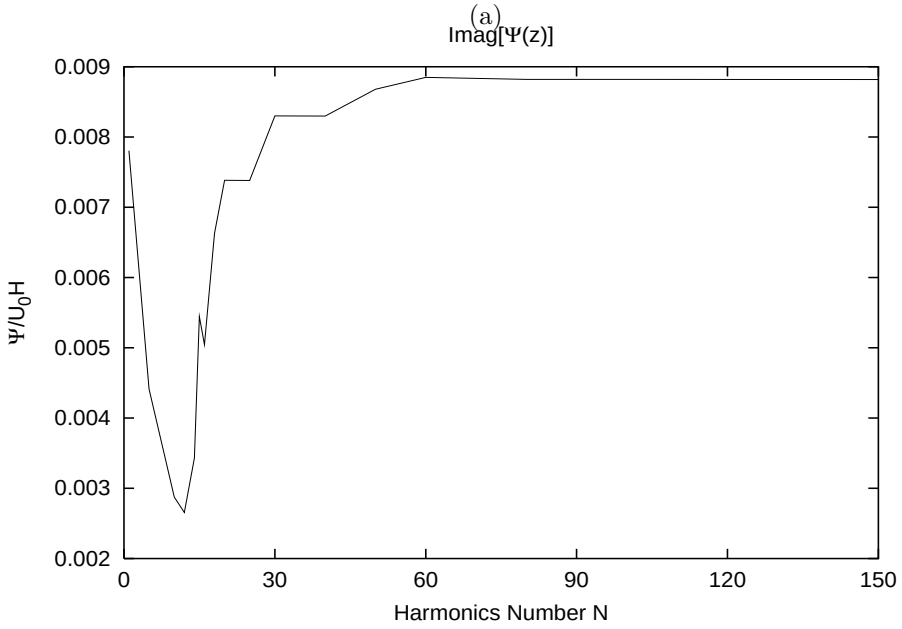

(b)

Figure 1.7: Value of streamfunction Ψ at a particular phase of the tidal circle plotted against the number of harmonics. (μ=5, s=5, δ=0.2, t=0, z=0.5, r=100)

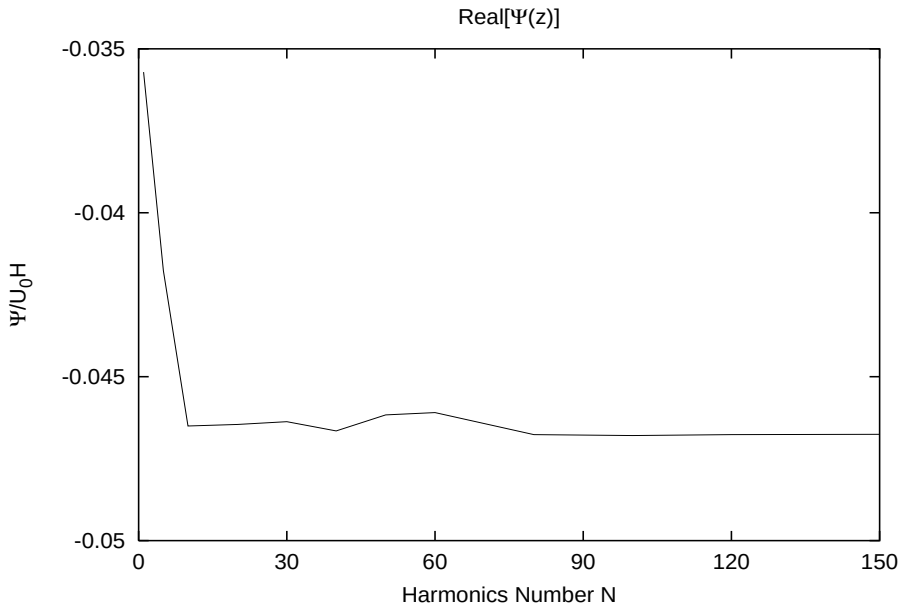

(a)

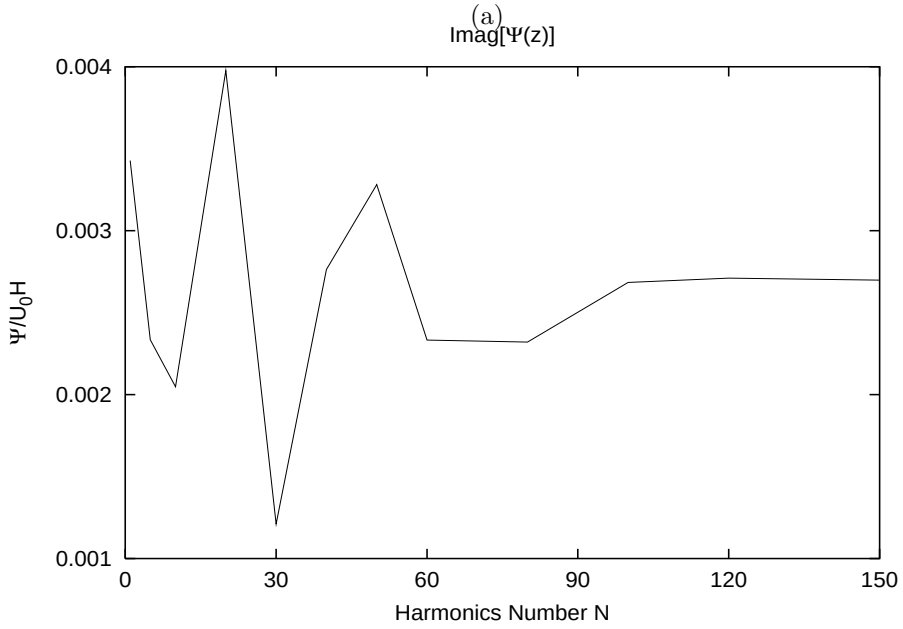

(b)

Figure 1.8: Value of streamfunction Ψ at a particular phase of the tidal circle plotted against the number of harmonics. (μ=5, s=5, δ=0.2, t=0, z=0.5, r=300)

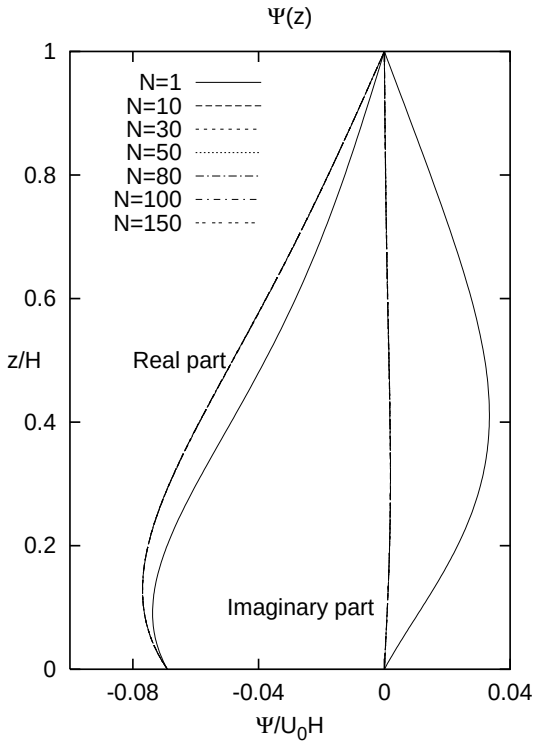

Figure 1.9: Stream function Ψ at a particular phase of the tidal cycle, computed using different values of $\mathcal{N}$. (μ=5, s=5, δ=0.2, t=0, r=10)

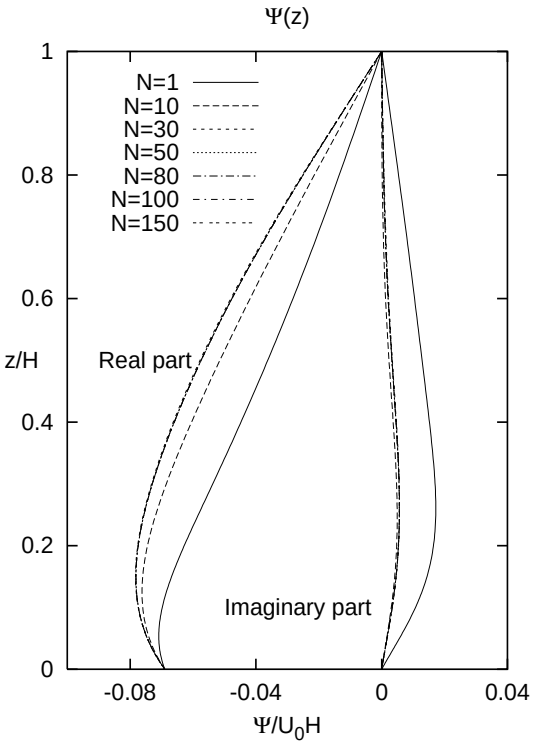

Figure 1.10: Stream function Ψ at a particular phase of the cycle, computed using different values of $\mathcal{N}$. (μ=5, s=5, δ=0.2, t=0, r=50)

A positive value of Γ_r implies a growth of the perturbation while a negative value denotes decay. Gravity, which tends to move the sediment down the slope of the bottom waviness carrying it from the crests to the troughs, has a stabilising effect. Indeed the term $-\hat{\gamma}\delta^2$ gives always a real and negative contribution to Γ.

A destabilising effect can be caused by the term $\delta\theta_0$ which describes the effect of the sediment transport induced by the steady recirculating cells originated by the interaction of the basic oscillatory tidal flow with bottom perturbations (see figure **1.14**). This mechanism, already pointed out by Hulscher (1996a) and Gerkema (2000), is similar to that giving rise to sea ripples and described for example by Blondeaux (1990). Indeed, for moderate values of r, the stream function Ψ has an imaginary part and $\delta\theta_0$ gives a contribution to the real part of Γ. An example of the steady streaming is shown in figure **1.15**. In figure **1.15b** the steady recirculating cells are shown for the same parameters as in figure **1.15a** but for a larger value of

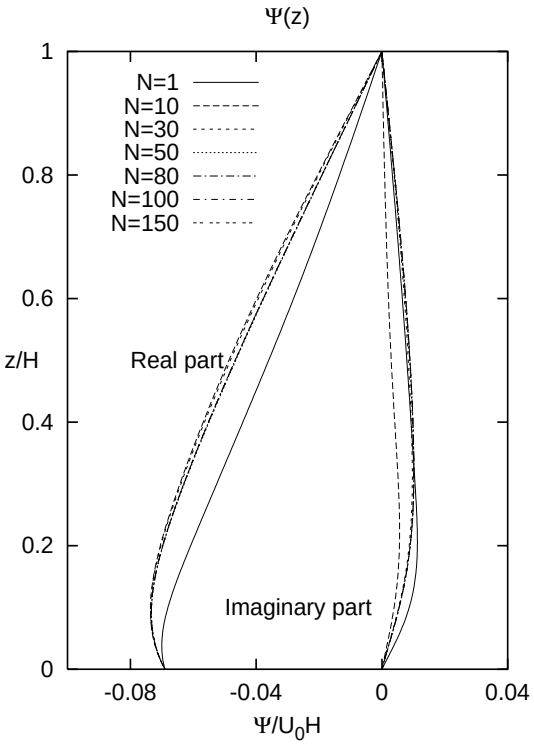

Figure 1.11: Stream function Ψ at a particular phase of the tidal cycle, computed using different values of $\mathcal{N}$. (μ=5, s=5, δ=0.2, t=0, r=100)

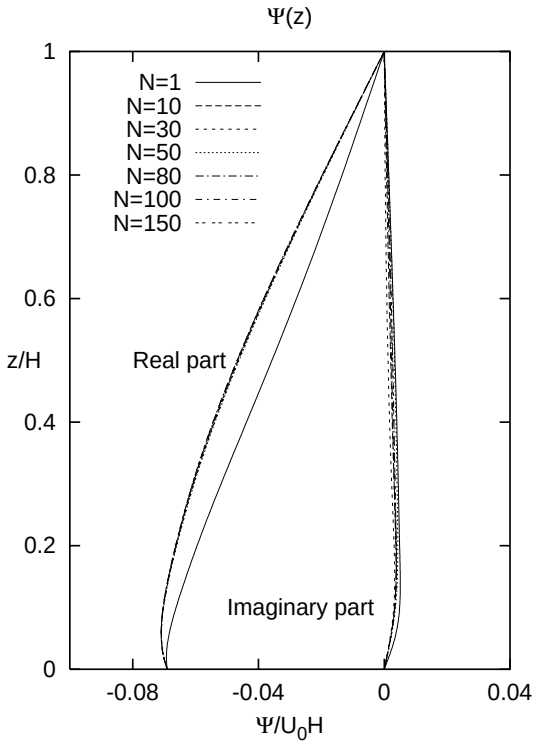

Figure 1.12: Stream function Ψ at a particular phase of the tidal cycle, computed using different values of $\mathcal{N}$. (μ=5, s=5, δ=0.2, t=0, r=300)

r. An increase of the ratio between the horizontal tidal excursion and the wavelength of sand waves leads to a shift of the centre of the cells toward the bottom and hence to stronger velocity close to the sea bed. It is interesting to point out that in the range of the parameters presently investigated the steady streaming is always directed from the troughs towards the crests of the bottom waviness.

Because of the symmetry of the problem, no migration of the bottom forms is expected to take place after a tide cycle and indeed Γ_i vanishes for whatever set of parameters is considered.

In order to allow predictions of the most unstable component of the bed perturbation, it is convenient to slightly modify the parameters defined by (1.29) and to replace r by the new parameter $\hat{r}$

$$\hat{r} = \frac{U_0}{\sigma H}. \tag{1.70}$$

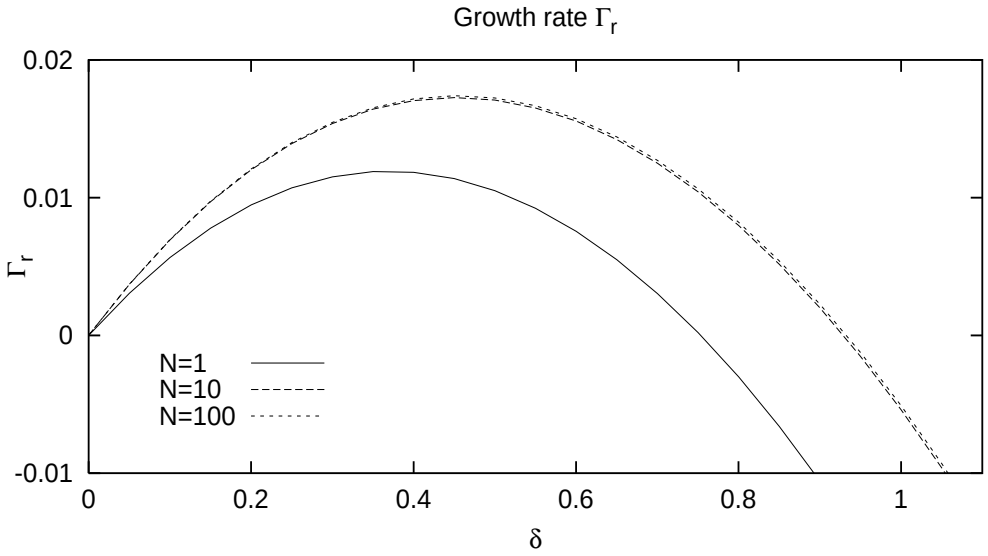

Figure 1.13: Growth rate Γ_r plotted versus δ for $\mu = 10$, $s = 5$, $r = 50$, $\gamma = 2$ and $\mathcal{N}$ =1, 10, 100. Larger values of $\mathcal{N}$ provide results practically coincident with those obtained setting $\mathcal{N}$ =100.

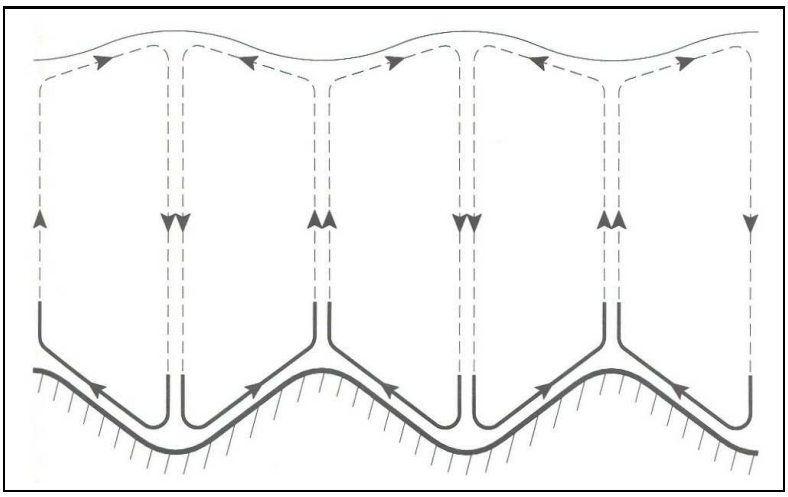

Figure 1.14: The interaction of the oscillatory tidal flow with bottom perturbations gives rise to a steady streaming in the form of recirculating cells (from Hulscher 1966).

which does not depend on the characteristics of the bottom perturbations. Introducing $\hat{r}$ allows to perform the analysis having a parameter which is related to the strength of the current and not dependent on other dimensionless

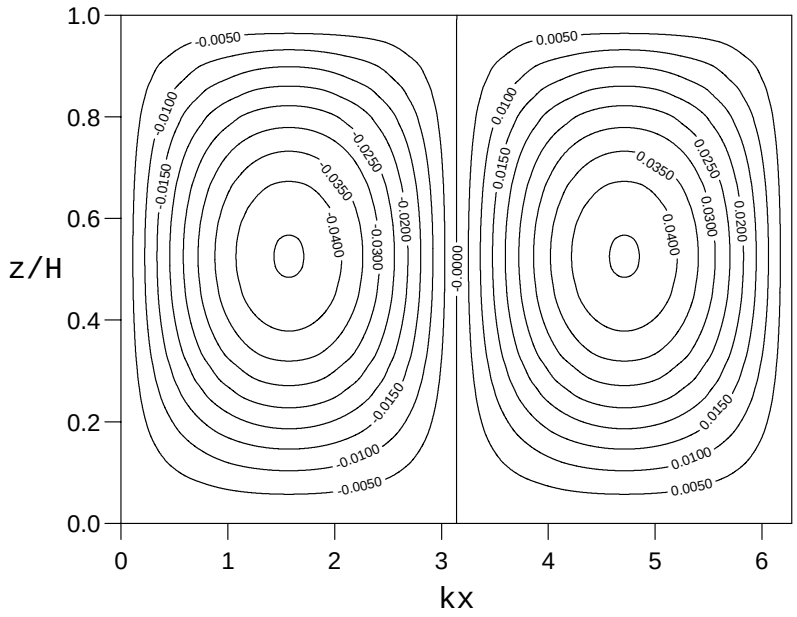

(a)

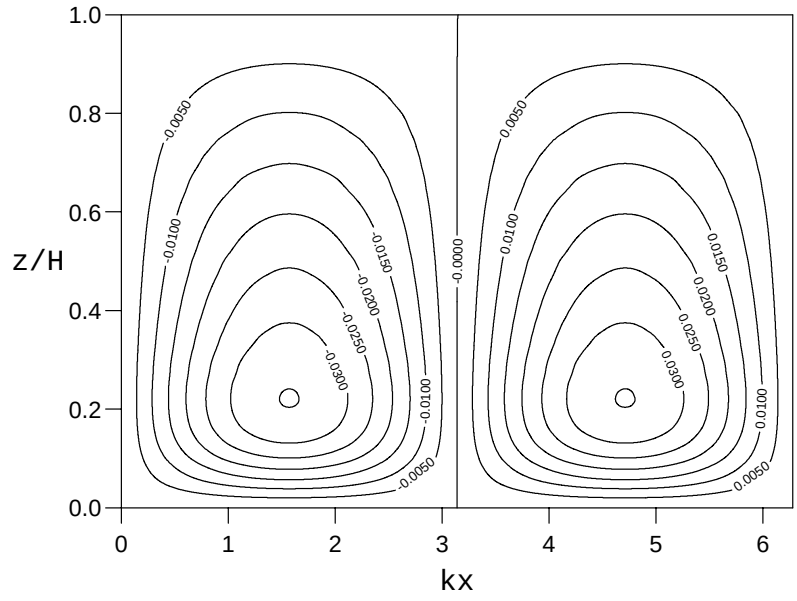

(b)

Figure 1.15: Steady recirculating cells for $\mu = 1$, $s = 10$, $\delta = 1$, $\Delta\Psi = 0.005$. (a) $r = 10$, (b) $r = 600$.

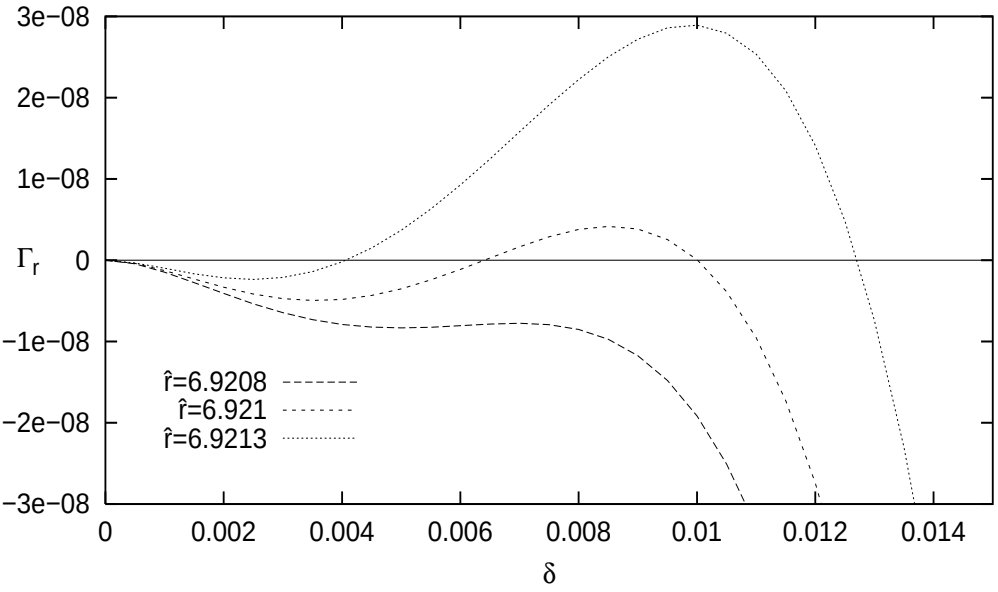

Figure 1.16: Γ_r plotted versus δ for $\mu = 1$, $s = 0.8$, $\gamma = 1$ and different values of $\hat{r}$. $\mathcal{N}$ =150.

parameter: notice, in fact, that $r = \hat{r}\delta$.

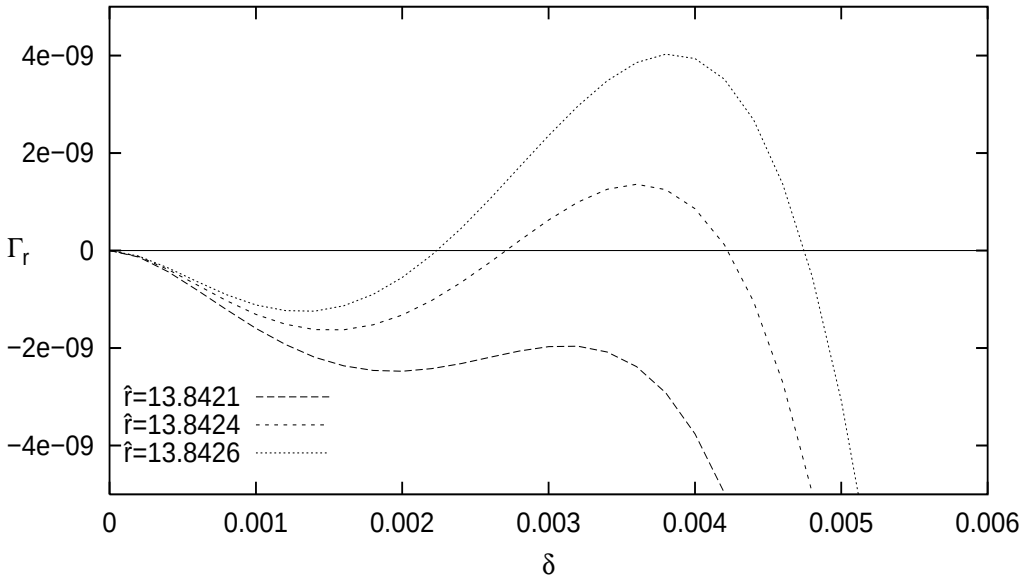

Figure 1.17: Γ_r plotted versus δ for $\mu = 1$, $s = 0.8$, $\gamma = 2$ and different values of $\hat{r}$. $\mathcal{N}$ =150.

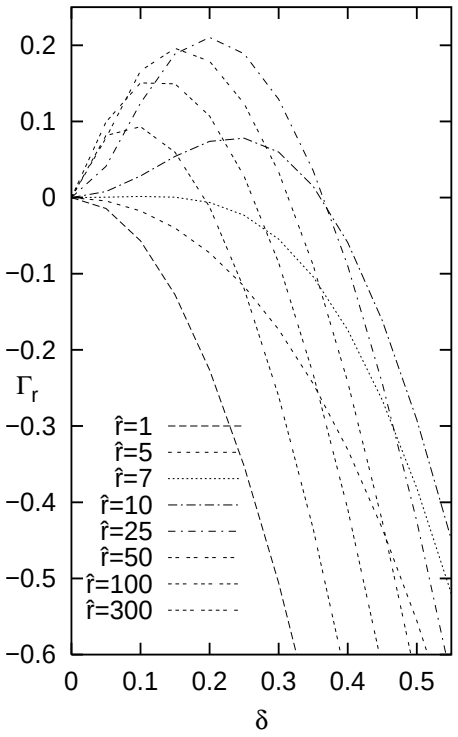

Figure 1.18: Γ_r plotted versus δ for $\mu = 1$, $s = 0.8$, $\gamma = 1$ and different values of $\hat{r}$. $\mathcal{N}$ =150.

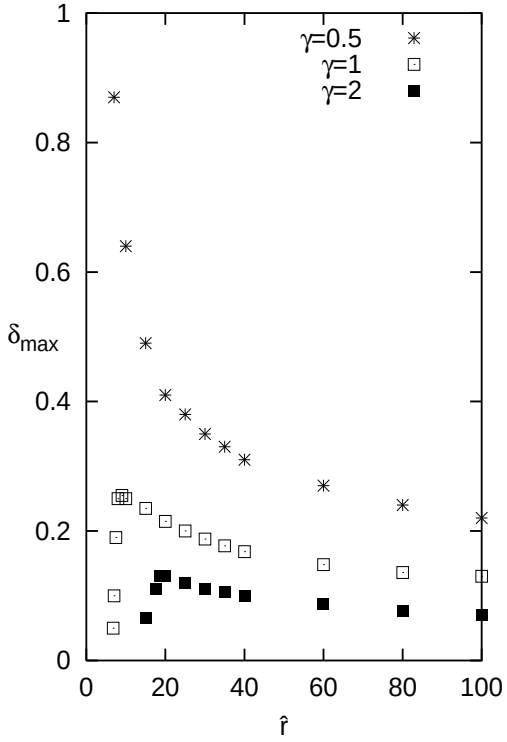

Figure 1.19: Dimensionless wavenumber δ_{max} of the most unstable perturbation plotted versus $\hat{r}$ for $\mu = 1$, $s = 0.8$, $\mathcal{N}$ =150.

In figure **1.16**, Γ_r is plotted versus δ for fixed values of μ, s, γ and different values of $\hat{r}$. For small values of $\hat{r}$, Γ_r is negative whatever value of δ is considered. When $\hat{r}$ is increased, a critical value $\hat{r}_c$ is found such that for $\hat{r}$ less than $\hat{r}_c$ bottom perturbations decay for each value of the wavenumber δ, while for $\hat{r}$ slightly larger than $\hat{r}_c$ bottom perturbations, characterised by values of δ falling within a restricted range around a critical value δ_c, experience an average amplification within a cycle. However, as soon as $\hat{r}$ is significantly larger than r_c the bandwidth of unstable modes becomes large including small values of δ, i.e. ultra-long bottom modes.

Figure **1.16** shows that $\hat{r}_c$ is about 6.92 which, for a semi-diurnal tide and a water depth equal to 40 m gives rise to a critical value of U_m equal to about 0.13 m/s. A quantitative comparison of present results with field data is difficult because of the lack of data concerning field critical conditions. Looking at figure **3.2** of Belderson et al. (1982), it appears that the critical value of U_m is certainly underestimated but not too far from the values

observed in the field which range around 0.5 m/s (incidentally sand waves have been observed also in sites characterised by much weaker tidal currents). Moreover it is worth pointing out that an increase of the value of bed slope parameter γ leads to an increase of the critical value of U_m. For example the critical value of U_m is about 0.30 m/s for $\gamma = 2$. On the other hand, the wavelength of sand waves around the critical conditions is certainly overestimated (see figure **1.17**). Therefore, in this respect, the present findings do not improve the results of previous analyses which show that, when the tidal current is strong enough to cause the instability of the flat bottom configuration, bottom perturbations characterised by wavenumbers falling between 0 and a finite value become unstable and ultra-long waves tend to growth (see Komarova & Hulscher, 2000, for a detailed discussion). However, it is worth pointing out that realistic values of the parameters lead to values of $\hat{r}$ significantly larger than $\hat{r}_c$ and in this case the most unstable perturbations have wavelengths similar to those observed in the field. In fact, figure **1.18**, where Γ_r is plotted also for large values of $\hat{r}$, shows that the maximum of Γ_r moves toward larger values of δ as soon as $\hat{r}$ becomes larger than $\hat{r}_c$, i.e. the wavelengths of the most unstable sand waves become shorter. Only further increases of $\hat{r}$ lead to decreasing value of δ, but the maximum of the amplification rate always takes place for values of δ significantly larger than δ_c. This finding is summarised in figure **1.19** where the dimensionless wavenumber δ_{max} of the most unstable perturbation is plotted versus $\hat{r}$ for fixed values of the parameters and different values of γ. The value of γ has been varied because no precise estimate is available and the value of γ should be tuned comparing theoretical results with field data. The performances of the model can be evaluated by looking at figures **1.20** and **1.21**.

Figure **1.20** shows the amplification rate Γ_r for $\mu = 1.7$, $s = 0.8$, $\hat{r} = 45$ and $\gamma = 0.28$, values of the parameters chosen to reproduce a site in the North Sea where sand waves have been observed (see figure **1.21** where the bottom topography is reproduced). Taking into account that δ_{max} turns out to be 0.5 and the local water depth is about 20 m, the model predicts the formation of sand waves characterised by a wavelength equal to about 250 m, a value quite close to the observed wavelengths ranging between 165 m and 255 m (see figure **1.21**).

As already pointed out, if $\hat{r}$ is further increased, the amplification rate tends to decrease as shown in figure **1.18** and for large values of $\hat{r}$ the model predicts the stability of the flat bottom configuration, as also shown by the asymptotic analysis for $r >> 1$. Such finding agrees with fields observations which show that sand waves are washed out when strong tidal currents are present.

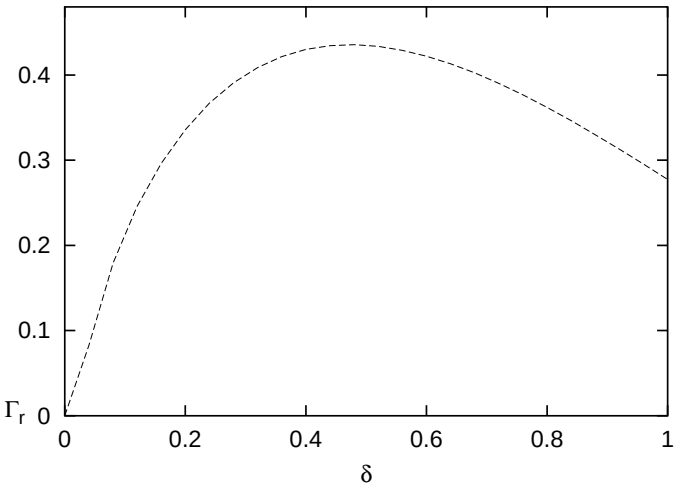

Figure 1.20: Growth rate Γ_r plotted versus δ for $\mu = 1.7$, $s = 0.8$, $\hat{r} = 45$ and $\gamma = 0.28$.

1.5 Using Meyer-Peter & Müller transport formula

Once the results of the present analysis have been qualitatively compared with those of Gerkema (2000) and Hulscher (1996a) using the same sediment transport predictor and the same parameters, a more detailed investigation of the phenomena is carried out by using the relationship proposed by Meyer-Peter & Müller (1948) to evaluate the sediment transport:

$$Q = 8\frac{\sqrt{(\rho_s/\rho - 1)\, g d^3}}{(1-p)} \left(\left| \theta - \gamma \frac{\partial \eta}{\partial x} \right| - \theta_c \right)^{3/2} \left(\theta - \gamma \frac{\partial \eta}{\partial x} \right) \left| \theta - \gamma \frac{\partial \eta}{\partial x} \right|^{-1} \quad . \tag{1.71}$$

This formulation provides values of the bed sediment transport if the value of the term $|\theta - \gamma \partial\eta/\partial x|$ is greater than the threshold value of the Shields parameter θ_c, otherwise the sediment transport vanishes.

where ρ_s, p and d are the density, the porosity and the size of the sediment respectively and θ is the dimensionless Shields parameter defined by

$$\theta = \frac{\tau}{(\rho_s - \rho)\, g d} \quad . \tag{1.72}$$

Moreover τ is the bed shear stress, which can be easily evaluated using the constitutive law and the knowledge of the kinematic eddy viscosity, and θ_c is

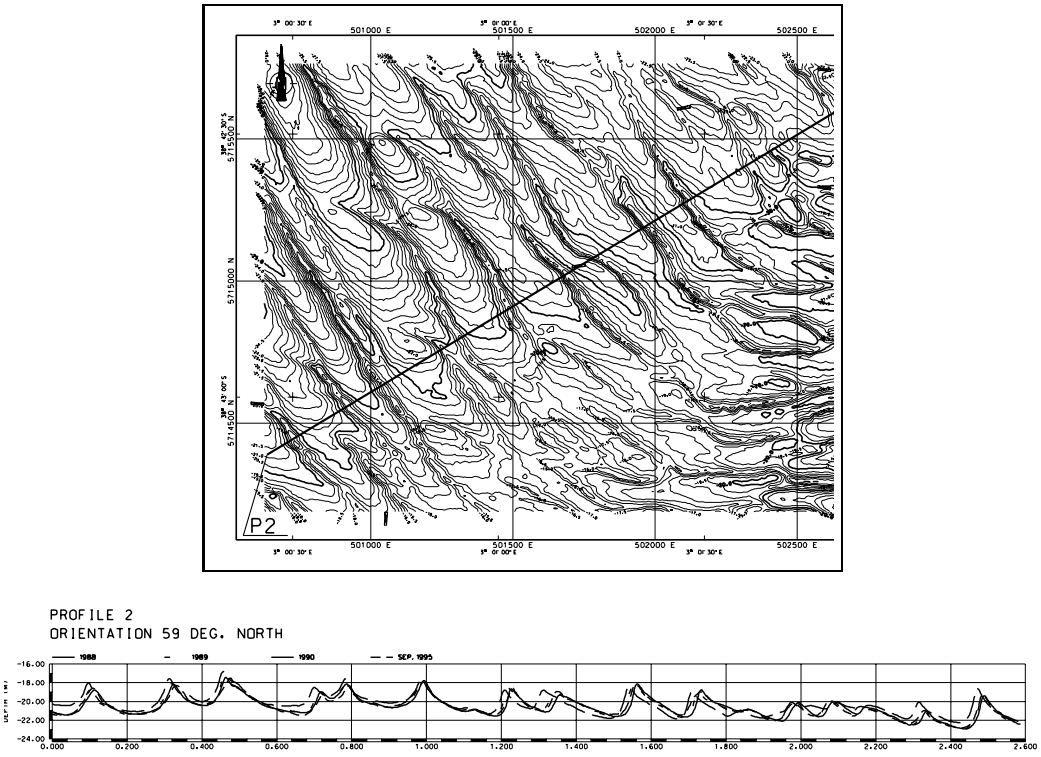

Figure 1.21: Sand waves data. Top: Contour map of the seabed at 51° 35' N and 3° 2' E with reference transect $P2$. Bottom: seabed profile along transect $P2$.

the critical value of θ for the initial motion of sediment. The term $\gamma \partial\eta/\partial x$ has been added in (1.71), as suggested by Fredsøe (1974), to take bed slope effects into account.

Introducing dimensionless variables denoted by a prime, the quantity $\sqrt{(\rho_s/\rho - 1)\, g d^3}$ scales the sediment transport rate and the dimensionless morphodynamic time scale T' is expressed by the following relationship

$$T' = t\sqrt{(\rho_s/\rho - 1)\, g d^3} / \left[(1-p)\, H^2\right]. \tag{1.73}$$

As already done in previous sections, for convenience, in the following the prime is dropped.

Therefore, the time development of the bottom configuration is described by the following expressions

$$\frac{\partial \Pi}{\partial T} + 2\delta i \langle \mathcal{Q} \rangle \Pi = 0 \tag{1.74}$$

$$\mathcal{Q} = 12 \left[\left| \frac{\delta \Psi_d}{\mu r} \frac{\partial u_b}{\partial z} \right|_{z=0} - \theta_c \right]^{1/2} \left[\frac{\delta \Psi_d}{\mu r} \left(\frac{1}{2} \frac{\partial^2 u_b}{\partial z^2} + \frac{\partial^2 \Psi}{\partial z^2} + \delta^2 \Psi \right)_{z=0} - \frac{1}{2} i \gamma \delta \right] \tag{1.75}$$

where the $\langle\rangle$ brackets denote the time average over the tide cycle and the small oscillations of the bottom profile, which take place around its average value during the tide cycle, have been neglected.

The use of Meyer-Peter & Müller transport formula leads to the definition of a new dimensionless parameter related to the sediments characteristics, defined as

$$\Psi_d = U_m^2 / \left[(\rho_s / \rho - 1)\, g d \right]. \tag{1.76}$$

The sediment mobility number Ψ_d ranges between order 10^2 for fine sand and strong currents and order 1 for coarse sand and weak currents.

Once the stream function associated with the bottom perturbation is computed, the temporal development of the amplitude Π of the generic component of the perturbation can be evaluated coupling (1.74) and (1.75), obtaining the following equation

$$\Pi = \Pi_0 \ \exp\{\Gamma T\} = \Pi_0 \ \exp\left\{ \left\langle -24 \left[\left| \frac{\delta \Psi_d}{\mu r} \frac{\partial u_b}{\partial z} \right|_{z=0} - \theta_c \right]^{1/2} \cdot \left[i \frac{\delta^2 \Psi_d}{\mu r} \left(\frac{1}{2} \frac{\partial^2 u_b}{\partial z^2} + \frac{\partial^2 \Psi}{\partial z^2} + \delta^2 \Psi \right)_{z=0} + \tfrac{1}{2} \gamma \delta^2 \right] \right\rangle T \right\}. \tag{1.77}$$

1.6 Results obtained with MPM formula

As already pointed out in section 1.4, it is convenient to replace r by the parameter $\hat{r}$ (1.70) which does not depend on the characteristics of the bottom perturbations. Moreover, in the literature (see a.o. Belderson et al., 1982) the presence of sand waves in a particular site, where the water depth and the bottom roughness are fixed, is related to the strength of the tidal current. To discuss the appearance of sand waves in terms of just one parameter containing U_0, it is convenient to introduce the new viscous parameter as

$$\hat{\mu} = \frac{U_0 H}{A} \quad . \tag{1.78}$$

In fact (1.8a,b) show that A is proportional to U_0. Then, $\hat{\mu}$ is independent of U_0 and depends only on the relative roughness size. Similarly it is

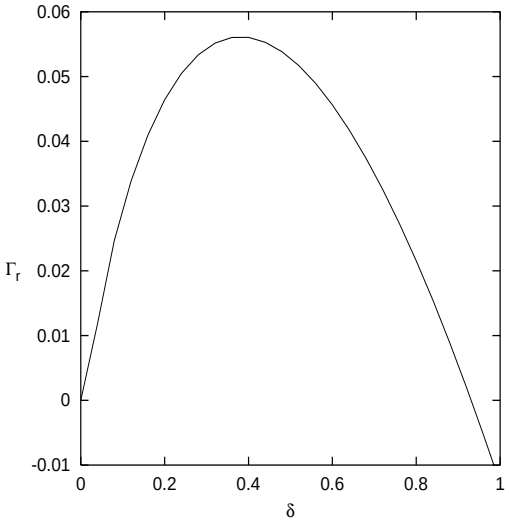

Figure 1.22: Dimensionless growth rate Γ_r plotted versus the dimensionless wavenumber δ of the bottom perturbation. Model parameters are: $\hat{\mu} = 112.5$, $s = 1.02$, $\hat{r} = 79$, $\hat{\Psi}_d = 0.0045$, $\gamma = 0.05$ and $\theta_c = 0.047$.

convenient to define the new sediment mobility number

$$\hat{\Psi}_d = \frac{(H\sigma)^2}{(\rho_s/\rho - 1)\, gd}. \tag{1.79}$$

It turns out that $\hat{\mu} = \mu\hat{r}$ and $\hat{\Psi}_d = \Psi_d/\hat{r}^2$.

The performances of the model can be evaluated by looking at figures **1.21** and **1.22**. Figure **1.22** shows the amplification rate Γ_r for $\hat{\mu} = 112.5$, $s = 1.02$, $\hat{r} = 79$, $\hat{\Psi}_d = 0.0045$ and $\gamma = 0.05$, values of the parameters which are chosen to reproduce the site SW1 located in the North Sea at $51°35'N$ and $3°2'E$ where sand waves have been observed (see figure **1.21** where the bottom topography is plotted) and tidal currents were measured. The bottom roughness has been evaluated assuming that wave ripples were present characterised by a wavelength l of about 20 cm. Their height Δ_r is assumed to be $0.17\, l$ (Sleath, 1984) and the bottom roughness is fixed equal to $3\Delta_r$ as suggested by Van Rijn (1991). If it is assumed that actual sand waves are generated by the growth of the bottom perturbations characterised by the largest amplification rate and it is taken into account that Γ_r is maximum for $\delta = \delta_{max} = 0.4$ and the local water depth is about 21 m, the model predicts the formation of sand waves characterised by a wavelength equal to about 315 m, a value close to the observed wavelengths ranging between 165 m and 255 m (see figure **1.21**).

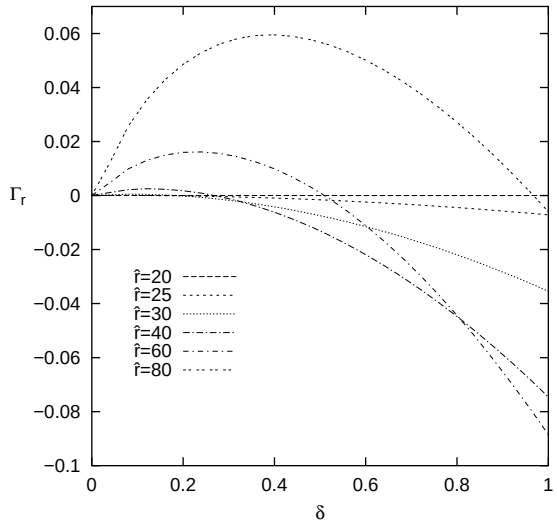

Figure 1.23: Dimensionless growth rate Γ_r plotted versus the dimensionless wavenumber δ of the bottom perturbation for different values of $\hat{r}$. Model parameters are: $\hat{\mu} = 112.5$, $s = 1.02$, $\hat{\Psi}_d = 0.0045$, $\gamma = 0.05$ and $\theta_c = 0.047$.

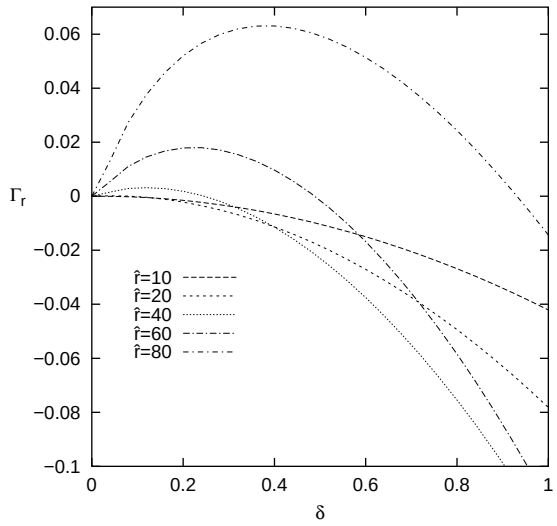

Figure 1.24: Dimensionless growth rate Γ_r plotted versus the dimensionless wavenumber δ of the bottom perturbation for different values of $\hat{r}$. Model parameters are: $\hat{\mu} = 112.5$, $s = 1.02$, $\hat{\Psi}_d = 0.0045$, $\gamma = 0.05$ and $\theta_c = 0.0$.

The data of figure **1.21** and the relationships (1.8a,b) show that field cases are characterised by a value of $\hat{\mu}$ of order 100 while s depends on the relative bottom roughness and falls in a small range around 1. Fixing $\hat{\mu} = 112.5$ and $s = 1.02$, it is interesting to look at model predictions for a fine sandy bottom ($\Psi_d = 0.0045$) and varying the parameter $\hat{r}$ which, in a particular site, is proportional to the current strength U_0. The results are shown in figure **1.23** where Γ_r is plotted versus δ. For small values of $\hat{r}$, sediment transport does not take place and the bottom configuration does not change ($\Gamma_r \equiv 0$). When $\hat{r}$ is increased, a critical value $\hat{r}_c$ is found such that the sediment starts to be transported. For $\hat{r}$ slightly larger than $\hat{r}_c$, bottom perturbations, characterised by values of δ falling within a range centred around $\delta_{c,max}$, experience an average amplification within a cycle. An analysis of the results (see figure **1.23**) shows that $\hat{r}_c$ is about 24 and $\delta_{c,max}$ is about 0.07. These values, for a semi-diurnal tide and a water depth equal to 21 m, which is the value measured at SW1, give rise to a critical value of U_m equal to about 0.2 m/s. A quantitative comparison of present results with field data is difficult because of the lack of data concerning field critical conditions. Looking at figure **3.2** of Belderson et al. (1982), it appears that the critical value of U_m is not too far from the values observed in the field which range around 0.5 m/s. Incidentally sand waves have been observed also in sites characterised by weaker tidal currents (at SW1 the semi-diurnal constituent gives rise to a tidal current equal to about 0.4 m/s). Moreover, close to the critical conditions, the wavelength of the most unstable perturbation (1900 m) is of the same order of magnitude as those observed in the field, even though it turns to be somewhat larger. The results of figure **1.23** have been obtained setting $\theta_c = 0.047$.

To compare present findings with those obtained by means of sediment transport predictors which neglect the existence of a critical bed shear stress for the erosion of sand, figure **1.24** shows Γ_r versus δ for different values of $\hat{r}$, the other parameters being equal to those of figure **1.23** but for $\theta_c = 0$. Even for a vanishing value of θ_c, the model shows the existence of a critical value $\hat{r}_c$ of $\hat{r}$ below which sand waves do not appear. For $\theta_c = 0$, $\hat{r}_c$ turns out to be about 15. For a semi-diurnal tide and a water depth equal to 21 m, this value of $\hat{r}_c$ gives rise to a critical value of U_m equal to about 0.11 m/s, a value still not far from field observations. On the other hand for $\theta_c = 0$, the wavelength of the most unstable perturbation around the critical conditions tends to infinity. This finding is not better than the results of previous analyses which show that, when the tidal current is strong enough to cause the instability of the flat bottom configuration, ultra-long waves tend to grow (see Komarova & Hulscher, 2000, for a detailed discussion). However realistic values of the parameters lead to values of $\hat{r}$ significantly larger than

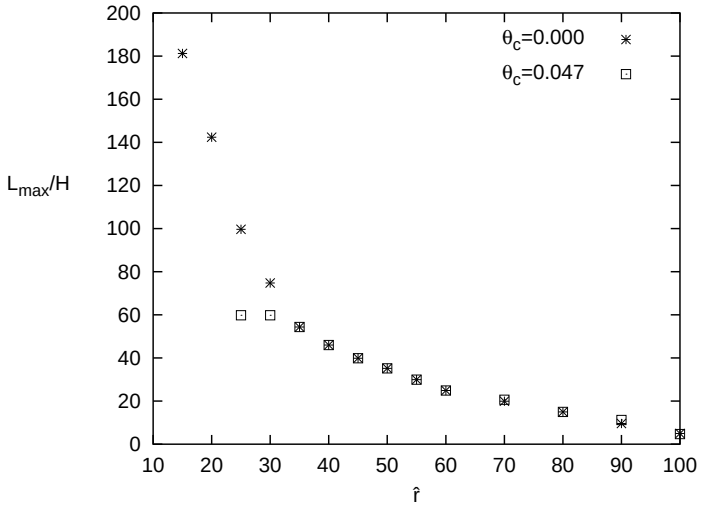

Figure 1.25: Ratio of the wavelength L_{max} of the most unstable perturbation and the water depth H plotted versus the parameter $\hat{r}$. Model parameters are: $\hat{\mu} = 112.5$, $s = 1.02$, $\hat{\Psi}_d = 0.0045$, and $\gamma = 0.05$.

$\hat{r}_c$ and in this case the most unstable perturbation has a wavelength similar to those observed in the field. Indeed figure **1.25**, where the dimensionless ratio between the wavelength L_{max} of the most unstable perturbation and the water depth H is plotted versus $\hat{r}$, shows that L_{max}/H rapidly decreases as soon as $\hat{r}$ becomes larger than $\hat{r}_c$ and the wavelength of the most unstable sand waves well agrees with field observations. In figure **1.25** the results obtained with both $\theta_c = 0.047$ and $\theta_c = 0.0$ are shown.

The results described so far have been obtained assuming that the bottom roughness is due to the presence of medium size ripples. Sometimes field surveys show that megaripples cover the sea bottom. In this case the bottom roughness is higher and relationships (1.8a,b) show that the parameter s increases. It is then interesting to look at the amplification rate Γ_r for the same values of the parameters as those of figure **1.22** but for $s = 1.5$ which is the value of the stress parameter associated to megaripples (see figure **1.26**). The value of δ_{max} turns out to be about 0.8. In this case, at SW1 where $H = 21$ m, the model predicts the appearance of sand waves characterised by a wavelength equal to 160 m. Therefore considering roughness size ranging from medium size ripples to megaripples, the predicted wavelength of sand waves falls between 160 m and 315 m, a range which well agree with field observations.

Looking at the critical conditions, it appears that the value of $\hat{r}_c$ is only slightly affected by s while the wavelength of the most unstable perturbation

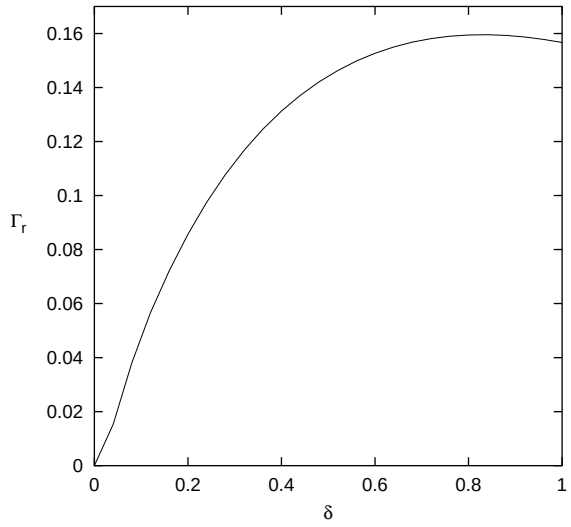

Figure 1.26: Dimensionless growth rate Γ_r plotted versus the dimensionless wavenumber δ of the bottom perturbation. Model parameters are: $\hat{\mu} = 112.5$, $s = 1.50$, $\hat{r} = 79$, $\hat{\Psi}_d = 0.0045$, $\gamma = 0.05$ and $\theta_c = 0.047$.

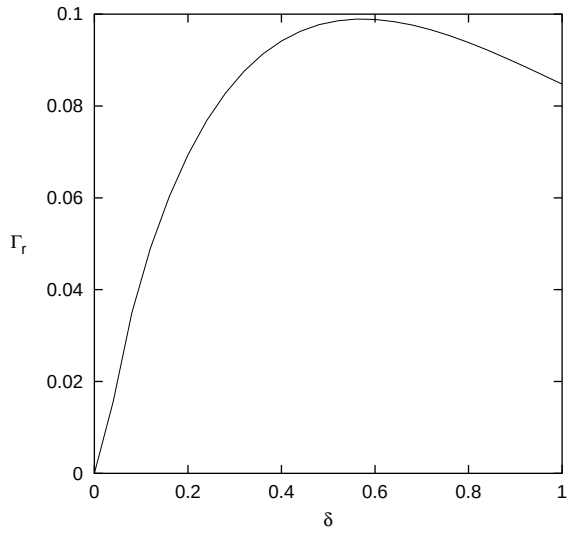

Figure 1.27: Dimensionless growth rate Γ_r plotted versus the dimensionless wavenumber δ of the bottom perturbation. Model parameters are: $\hat{\mu} = 78.1$, $s = 0.83$, $\hat{r} = 79$, $\hat{\Psi}_d = 0.0045$, $\gamma = 0.05$ and $\theta_c = 0.047$.

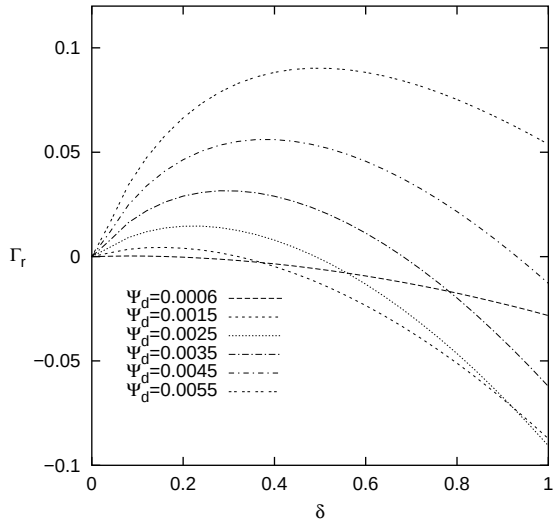

Figure 1.28: Dimensionless growth rate Γ_r plotted versus the dimensionless wavenumber δ of the bottom perturbation for different values of $\hat{\Psi}_d$. Model parameters are: $\hat{\mu} = 112.5$, $s = 1.02$, $\hat{r} = 79$, $\gamma = 0.05$, and $\theta_c = 0.047$.

for $\hat{r}$ close to $\hat{r}_c$ significantly decreases if s is increased. For example for $\hat{\mu} = 112.5$, $s = 1.5$, $\hat{\Psi}_d = 0.0045$, $\gamma = 0.05$ and $\theta_c = 0.047$, it turns out that $\hat{r}_c$ is about 24 and δ_{max} is about 0.11.

Similar results have been obtained for different values of the parameters. For example, using a different eddy viscosity profile (Van Rijn, 1991) and assuming the roughness to be induced by medium size ripples, relationships (1.8a,b) give $\hat{\mu} = 78.12$ and $s = 0.83$. With these values of $\hat{\mu}$ and s and fixing $\hat{r} = 79$, $\hat{\Psi} = 0.0045$, $\gamma = 0.05$ and $\theta_c = 0.047$, figure **1.27** shows that δ_{max} is about 0.55. For $H = 21$ m, this value of δ_{max} gives rise to a wavelength of sand waves equal to about 240 m.

At a particular site, i.e. for a fixed value of H, the conditions leading to the appearance of sand waves have been analysed also keeping fixed the value of $\hat{r}$, i.e. the strength of the tidal current, and considering different values of $\hat{\Psi}_d$, i.e. of the grain size. From the results of figure **1.28**, where Γ_r is plotted versus δ, it appears that decreasing values of $\hat{\Psi}_d$ lead to smaller values of Γ_r till for $\hat{\Psi}_d$ below a critical value $\hat{\Psi}_{dc}$, Γ_r is always negative and sand waves do not appear. Since $\hat{\Psi}_{dc}$ is equal to about 0.0006, for a semi-diurnal tide of amplitude equal to 0.43 m/s and a water depth equal to 21 m, the critical grain size above which sand wave do not appear is about 1 mm. This finding qualitatively agrees with field observations which show that sand waves develop only in sandy sea beds and they do not appear when a coarse

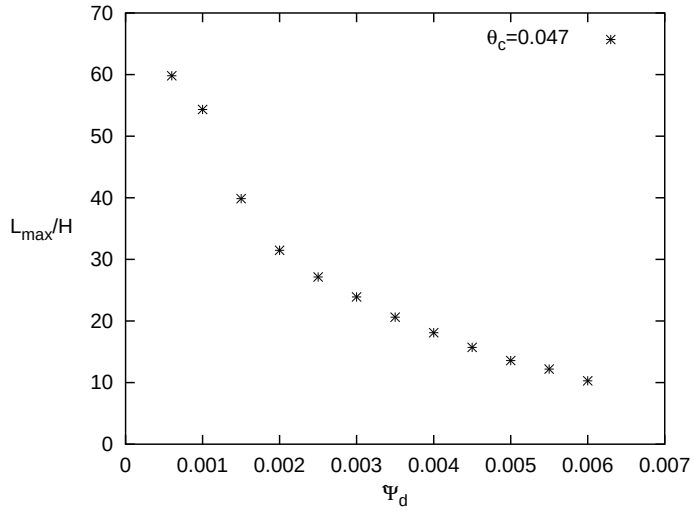

Figure 1.29: Ratio of the wavelength of the most unstable perturbation and the water depth H plotted versus the parameter $\hat{\Psi}_d$. Model parameters are: $\hat{\mu} = 112.5$, $s = 1.02$, $\hat{r} = 79$, $\gamma = 0.05$.

sediment covers the sea bottom. Finally figure **1.29**, where L_{max}/H is plotted versus $\hat{\Psi}_d$, shows that a finer sediment causes the appearance of shorter sand waves. A quantitative comparison between these theoretical findings and field observations is not possible because of the lack of the latter.

1.7 Suspended load effect

In order to have a complete description of the phenomenon the model has been improved taking into account also the effect on the growth rate coefficient caused by the suspended load. In fact rough estimates of the suspended and bed loads under field conditions show that the former is not always negligible and sometimes it can be very large. It follows that accurate quantitative predictions of sand waves characteristics (wavelength, migration speed, ...) can be obtained only considering the suspended sediment.

In a uniform steady flow the vertical distribution of sediment concentration is controlled by a balance between an upward flux of sediment induced by the turbulent mixing and a downward flux forced by gravity. When the current strength increases, sediment is entrained near the bed and sediment concentration increases close to the bottom. Then sediment diffuses over the whole depth but it takes a certain time before a steady state is reached. Similarly, when the flow decelerates, sediment particles tend to settle down

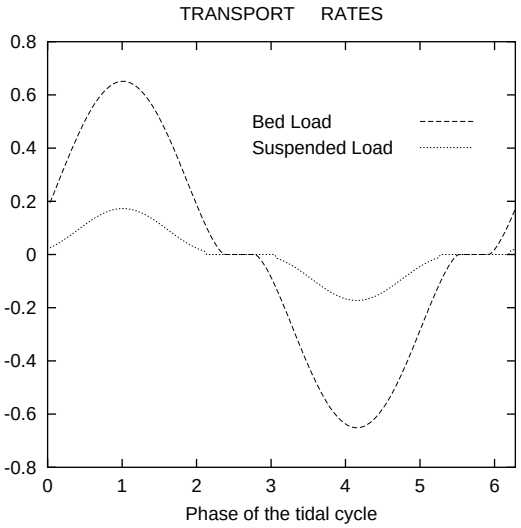

Figure 1.30: Dimensionless transport rates plotted versus the tide phase (s=1.02, $\hat{\mu}$=282, γ=0.05, $\hat{r}$=172, $\hat{\Psi}_m$=0.0026, R_p=11.4). Bedload has been evaluated by means of the Meyer-Peter & Müller formula, and the suspended by means of Rouse formulation, with Van Rijn closure.

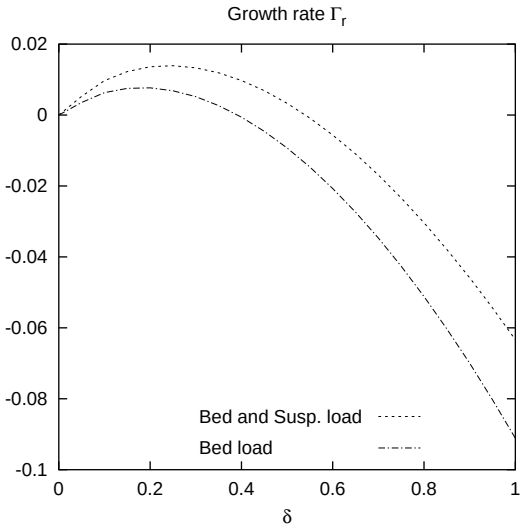

Figure 1.31: Dimensionless growth rate Γ_r plotted versus δ for s=1.02, $\hat{\mu}$=282, γ=0.05, $\hat{r}$=172, $\hat{\Psi}_d$=0.0026, R_p=11.4.

but sediment concentration takes a certain time before attaining the new steady state. Hence, the depth averaged sediment concentration responds to variations of the tidal current with a time lag which, in heuristic approach,

can be related to the quantity H/w_s where H is the local water depth and w_s is the particle settling velocity. However, it should be pointed out that other quantities like the for example the eddy diffusivity, might affect such estimate. Similarly an adaptation length, which presently scales with $U_m H/w_s$, is usually introduced in steady non-uniform flows to take into account that sediment concentration takes a certain distance to respond to local variations of flow characteristics (Armanini & Di Silvio, 1988). However in shallow waters, with the exception of a very fine sediment, the adaptation time can be assumed to be much smaller than the tidal period. Moreover sand waves are characterised by wavelengths which can be assumed to be much larger than the adaptation length. Hence, in a preliminary approach, the suspended load can be evaluated by means of a relationship which hold for steady uniform flows as specified with the actual and local values of the flow characteristics (slowly varying approach). Finally, it is worth pointing out that the mechanism which leads to the formation of sand waves is different from that giving rise to bedforms in fluvial environments (ripples, dunes, alternate bars, ...) and the adaptation length seems to play a minor role in the formation of sand waves which are induced by a steady streaming generated by the interaction of the oscillatory tidal current with the bottom waviness.

In order to have an estimate of the possible influence of the suspended load on the growth and migration of sand waves, it is worth to look at the order of magnitude of the suspended load with respect of the bed load. Plotting the dimensionless transport rates due to the bed and suspended loads versus the phase of the tide (figure **1.30**) for typical field conditions of the North Sea, it is possible to observe that the suspended load can attain values up to 30% of the bed load. These values suggest that the suspended load plays a significant role in the morphodynamic evolution of the sea bottom and, in order to have accurate predictions of sand wave characteristics, it is necessary to include the suspended load effects in the model equations.

As previously pointed out, the suspended load has been modelled and calculated by assuming that the velocity and concentrations distribution along the vertical coordinate are provided by those which are appropriate for the description of the steady state. Indeed tidal currents are slowly varying flows. Then it turns out that the suspended load for unit width can be written in the following way

$$q_{ss} = \int_a^Y c(y)\, u(y)\, dy \tag{1.80}$$

where Y is the water depth and a is a reference height at which is specified a reference value c_r of the concentration near the bed.

The velocity distribution of a turbulent plane flow has been considered,

$u = u_*/\kappa \ \ln(30Y/\epsilon)$ where u_* is the friction velocity. The concentration distribution has been evaluated by the procedure proposed by Rouse (1937), which relates the value of the sediment concentration along the vertical coordinate to a reference value c_r estimated at the height a measured from the bottom

$$c = c_r \left(\frac{Y-y}{y} \frac{a}{Y-a} \right)^Z \tag{1.81}$$

where Z is the Rouse number defined as $Z = w_s/\kappa u_*$ (w_s is the falling velocity of the sediment and κ=0.41 is the Karman constant).

Hence the dimensional suspended load can be written as

$$q_{ss} = 11.6 c_r u_* a \left[I_1 \ln\left(\frac{30H}{\epsilon}\right) + I_2 \right] \text{sign}\left(\frac{\partial u_b}{\partial z}\right) \tag{1.82}$$

where I_1 and I_2 are the Einstein integrals defined as

$$I_1 = \frac{0.216}{\xi_a} \int_{\xi_a}^1 \left[\frac{\xi_a (1-\xi)}{\xi (1-\xi_a)} \right]^Z d\xi \tag{1.83}$$

$$I_2 = \frac{0.216}{\xi_a} \int_{\xi_a}^1 \left[\frac{\xi_a (1-\xi)}{\xi (1-\xi_a)} \right]^Z \ln(\xi) d\xi \tag{1.84}$$

where $\xi_a = a/Y$.

In (1.82)-(1.84) c_r is the reference concentration at the reference height a from the bed, u_* is the bottom shear velocity which can be easily evaluated once the flow field is known, ϵ is the roughness size and Y is the local water depth.

To perform the evaluation of q_{ss} it is necessary to have an estimate of the values of a and c_r. The classic Rouse solution relies on empirical expressions and in the present contribution we adopt the relationships proposed by Van Rijn (1984)

$$c_r = 0.015 \frac{d}{a} \left(\frac{\theta}{\theta_{cr}} - 1 \right)^{1.5} R_p^{-0.2} \quad , \quad a = 0.01Y. \tag{1.85a,b}$$

In (1.85a) R_p is the particle Reynolds number defined as

$$R_p = \frac{\sqrt{(\rho_s/\rho - 1)\, g d^3}}{\nu} \tag{1.86}$$

where ν is the kinematic viscosity of the sea water.

Hence in dimensionless form we obtain

$$\mathcal{Q}_s = 11.6 \ \frac{\sqrt{\Psi_d}}{d} \ c_r^{'} \ u_*^{'} \frac{a}{H} \left[I_1 \ln\left(\frac{30H}{\epsilon}\right) + I_2 \right] \text{sign}\left(\frac{\partial u_b}{\partial z}\right) \tag{1.87}$$

where the apex denotes dimensionless quantities.

Performing a normal mode analysis to investigate the stability of the flat bottom configuration as illustrated in section 1.3 and considering bottom perturbation component (1.16), we split the suspended load into two terms: the former ($\mathcal{Q}_s^b$) is that generated by the tidal current over a flat bottom, the latter ($\mathcal{Q}_s^p$) describes the sediment transport perturbations induced by the bottom waviness. Taking into account that $Y{=}1{-}\eta$ and dropping the prime it is possible to write the two contributions in the following dimensionless forms

$$\mathcal{Q}_s^{(b)} = 0.116\ \frac{\sqrt{\Psi_d}}{d}\ \mathrm{sign}\left(\frac{\partial u_b}{\partial z}\right)(c_{r0}\ u_{*0})\left[I_{10}\ln\left(\frac{30}{\epsilon}\right)+I_{20}\right] \tag{1.88}$$

$$\begin{aligned}\mathcal{Q}_s^{(p)} = 0.116\ \frac{\sqrt{\Psi_d}}{d}\ \mathrm{sign}\left(\frac{\partial u_b}{\partial z}\right)\Bigg\{c_{r0}\ u_{*0}\left[I_{11}\ln\left(\frac{30}{\epsilon}\right)+I_{21}-\frac{I_{10}}{2}\right]+\\ +\left[I_{10}\ln\left(\frac{30}{\epsilon}\right)+I_{20}\right]\left[u_{*0}\ c_{r1}+c_{r0}\ u_{*1}-\frac{c_{r0}\ u_{*0}}{2}\right]\Bigg\}\Pi e^{ix}+c.c.\end{aligned} \tag{1.89}$$

where

$$c_{r0} = \frac{1.5}{R_p^{0.2}}\ d\ \left(\frac{|\theta_0|}{\theta_{cr}}-1\right)^{1.5} \tag{1.90}$$

$$c_{r1} = \frac{1.5}{R_p^{0.2}}\ d\ \left[\frac{1}{2}\left(\frac{|\theta_0|}{\theta_{cr}}-1\right)^{1.5}+1.5\left(\frac{|\theta_0|}{\theta_{cr}}-1\right)^{0.5}\ \theta_1\ \frac{\theta_0}{|\theta_0|}\right] \tag{1.91}$$

$$\theta_0 = \frac{\Psi_d}{\mu\hat{r}}\frac{\partial u_b}{\partial z}\quad;\quad \theta_1 = \frac{\Psi_d}{\mu\hat{r}}\left(\frac{1}{2}\frac{\partial^2 u_b}{\partial z^2}+\frac{\partial^2\Psi}{\partial z^2}+\delta^2\Psi\right) \tag{1.92a,b}$$

$$u_{*0} = \sqrt{\frac{1}{\mu\hat{r}}\left|\frac{\partial u_b}{\partial z}\right|}\quad;\quad u_{*1} = \sqrt{\frac{1}{\mu\hat{r}}}\frac{\partial u_b/\partial z}{2\left|\partial u_b/\partial z\right|^{3/2}}\left(\frac{1}{2}\frac{\partial^2 u_b}{\partial z^2}+\frac{\partial^2\Psi}{\partial z^2}+\delta^2\Psi\right). \tag{1.93a,b}$$

Moreover in the previous relationships the dimensionless parameter Ψ_d introduced in section 1.5 and the dimensionless diameter d, scaled with the water depth, have been used.

Finally the Einstein integrals become

$$I_{10} = 21.6\int_a^1\left[\frac{a\,(1-z)}{z\,(1-a)}\right]^{Z_0}dz \tag{1.94}$$

$$I_{11} = 10.8\int_a^1\left[\frac{a\,(1-z)}{z\,(1-a]}\right]^{Z_0}\left\{Z_1\ln\left[\frac{a\,(1-z)}{z\,(1-a)}\right]-Z_0\frac{1}{1-z}+1\right\}\,dz \tag{1.95}$$

$$I_{20} = 21.6a^2 \int_a^1 \left[\frac{a\,(1-z)}{z\,(1-a)}\right]^{Z_0} \ln(z)dz \tag{1.96}$$

$$I_{21} = 10.8a^2 \int_a^1 \left[\frac{a\,(1-z)}{z\,(1-a)}\right]^{Z_0} \left\{\left[Z_1 \ln\left(\frac{a\,(1-z)}{z\,(1-a)}\right) - \right.\right.$$
$$\left.\left. - Z_0 \frac{1}{1-z}\right] \ln(z) + 1\right\}\, dz \quad . \tag{1.97}$$

where

$$Z_0 = \frac{1}{\kappa} w_s \sqrt{\mu \hat{r}} \left(1/\sqrt{\frac{\partial u_b}{\partial z}}\right) \tag{1.98}$$

and

$$Z_1 = \frac{1}{\kappa} w_s \sqrt{\mu \hat{r}} \left\{-\frac{\partial u_b/\partial z}{2|\partial u_b/\partial z|^{5/2}} \left(\frac{1}{2}\frac{\partial^2 u_b}{\partial z^2} + \frac{\partial^2 \Psi}{\partial z^2} + \delta^2 \Psi\right)\right\} \quad . \tag{1.99}$$

Taking into account only the terms in which the bottom perturbation amplitude Π is present and keeping in mind relationship (1.74), we can estimate the growth rate due to the presence of the suspended load and write

$$\Gamma_s = -0.232\, \frac{\sqrt{\Psi_m}}{d}\, \delta\; i\; sgn\left(\frac{\partial u_b}{\partial z}\right) \left\{c_{r0} u_{*0} \left[I_{11} \ln\left(\frac{30}{\epsilon}\right) + I_{21} - \frac{I_{10}}{2}\right]\right.$$
$$\left. + \left[I_{10} \ln\left(\frac{30}{\epsilon}\right) + I_{20}\right] \left(u_{*0} c_{r1} + u_{*1} c_{r0} - \frac{c_{r0} u_{*0}}{2}\right)\right\} \tag{1.100}$$

while the contribution of the growth rate due to the bed load can be expressed in the form

$$\Gamma_b = -24\delta \left[|\theta_0| - \theta_c\right]^{1/2} \left(\theta_1 i + \gamma \frac{\delta}{2}\right) \quad . \tag{1.101}$$

The model hence allows for the computation the growth/decay rate of the bottom perturbations. The results described in the following have been obtained using tide characteristics and water depths which can be considered as representative of tidal currents in the North Sea and varying the sediment size considering fine, medium as well as coarse sand.

In figure **1.31** the real part Γ_r of the growth rate is plotted versus the dimensionless wavenumber δ for $s = 1.02$, $\hat{\mu} = 282$, $\gamma = 0.05$, $\hat{r} = 172$, $\hat{\Psi}_d$=0.0026 and R_p=11.4. As discussed in section 1.4, a value of δ, i.e. a value of the dimensionless wavelength of the bottom perturbation, can be identified which is characterised by the maximum amplification rate. In the framework of a linear stability analysis such wavelength can be assumed to be that of the sand waves which tend to appear. The results of figure **1.31**

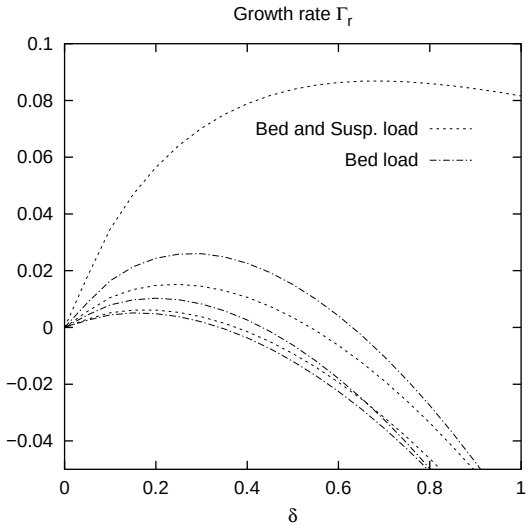

Figure 1.32: Dimensionless growth rate Γ_r plotted versus δ for s=1.02, $\hat{\mu}$=282, γ=0.05, $\hat{r}$=224. The largest value of Γ_r are for R_p=11.4, $\hat{\Psi}_d$=0.00259, the smallest values for R_p=32.2, $\hat{\Psi}_d$=0.00129, the intermediate values for R_p=20.9, $\hat{\Psi}_d$=0.00173.

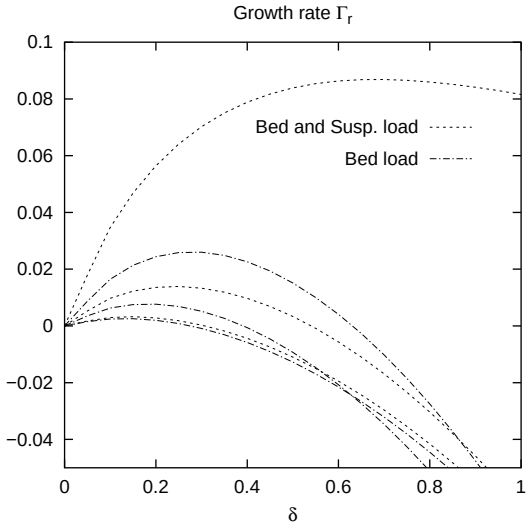

Figure 1.33: Dimensionless growth rate Γ_r plotted versus δ for s=1.02, $\hat{\mu}$=282, γ=0.05, $\hat{\Psi}_d$=0.0026, R_p=11.4. The largest values of Γ_r are for $\hat{r}$=224, the smallest values are for $\hat{r}$=137, the intermediate values for $\hat{r}$=172.

show that the suspended load destabilises the flat bed configuration and causes shorter sand waves to develop. In fact Γ_s is always positive and the

maximum of $\Gamma_b + \Gamma_s$ takes place for a value of δ larger than that of the Γ_b curve. In figure **1.32**, the tide characteristics and the water depth are fixed and different grain sizes are considered. Note that the suspended load influence on the perturbation development is strictly dependent on the value of the grain size.

For a coarse sand, the suspended load has a negligible effect on the growth rate Γ_r and the curve obtained considering only the bed load is close to that obtained adding the effects of the sediment carried into suspension. On the other hand, for a fine sand the inclusion of the suspended load induces significant variations of the growth rate. Qualitatively similar results are found for different tide characteristics as it appears in figure **1.33** where different strengths of the tidal current are considered: as the strength of the tidal current increases, the values of the growth rate Γ_r tend to increase.

Finally it could be pointed that the inclusion in the model of the suspended load does not significantly affect the qualitative behaviour of the process and the values of the real part Γ_r of the growth rate, leading to results close to those obtained considering just the effect of the bed load.

1.8 Discussion of the model findings

The present analysis supports the idea that sand waves in tide dominated coastal areas arise because of an inherent instability of the flat bottom configuration subject to tidal currents. The mechanism which leads to the growth of sand waves is that discussed by Hulscher (1996a): the interaction of an oscillatory tidal current with a bottom waviness gives rise to steady recirculating cells. When the steady streaming close to the bed is directed from the troughs toward the crests of the bottom perturbation and is strong enough to overcome gravity effects which tend to carry the sediment from the crests toward the troughs, the perturbation grows and gives rise to bottom patterns.

Present results provides a more accurate quantitative description of the phenomenon since they hold for arbitrary values of the ratio r between the horizontal tidal excursion and the wavelength of bottom perturbations. In fact for large values of r, the interaction between the flow induced by tide propagation and the bottom waviness gives rise to a perturbed flow characterised by a large number of time harmonic components (see figure **1.34**).

Notwithstanding the simplified description of turbulence and sediment transport, for realistic values of the parameters, the present results allow the prediction of patterns characterised by wavelenghts comparable with those observed in the field. However the critical conditions are somewhat underestimated and close to the critical conditions, ultra-long sand waves become

excited. A more realistic description of turbulence and sediment transport is required to significantly improve this aspect of the model predictions.

A height and flow-dependent model for eddy viscosity has been employed by Komarova & Hulscher (2000) to resolve the problem of the excitation of these very long sand waves. However in the model used by Komarova & Hulscher (2000) the eddy viscosity changes in time only for a term proportional to the amplitude of the bottom perturbation and becomes time-independent for a flat bottom configuration, i.e. the changes of turbulence structure taking place during the tidal cycle are not taken into account. This first attempt of accounting for time variations of the eddy viscosity opens the way to further investigation on the effects of temporal and spatial structure of turbulence on sand wave formation.

The asymptotic approach proposed by Gerkema (2000) for large values of $\hat{r}$ and s is modified in the bottom boundary layer to describe cases characterised by values of the stress parameter s of order one, which is the order of magnitude suggested by an analysis of field data.

The use of a sediment transport formula which takes into account the size of the sediment and the introduction of a critical bed shear stress for sediment motion allows us to predict some aspects of the phenomenon which were not considered by previous models. In fact, according to field observations, the analysis shows that a coarse sediment, even when transported by the tidal current, does not give rise to the appearance of sand waves. Moreover the introduction of a critical shear stress for sediment movement allows a more realistic evaluation of the conditions leading to sand waves appearance and give rise to a finite value of the wavelength of the most unstable perturbations when the parameters are close to their critical values.

The inclusion in the model of the suspended load does not affect significantly the qualitative behaviour of the system. For a coarse sediment the values of the real part Γ_r of the growth rate are close to those obtained considering just the effect of the bed load. However, significant quantitative differences are found when considering a fine sediment. In particular, the growth rate increases and shorter bedforms tend to appear.

Some aspects of the model can be improved. The actual value of the eddy viscosity, which is introduced to model turbulent stresses, vanishes at the bottom and increases moving far from it, before decreasing near the free surface. Since the model uses a constant eddy viscosity, the well established no slip condition at the bottom should be replaced by a partial slip condition. It follows that the model provides a fair description of the flow far from the bottom but it fails to describes the velocity profile close to the sea bed. Moreover, as already pointed out, a time independent eddy viscosity model is not accurate at flow reversal. Therefore to have a more accurate description

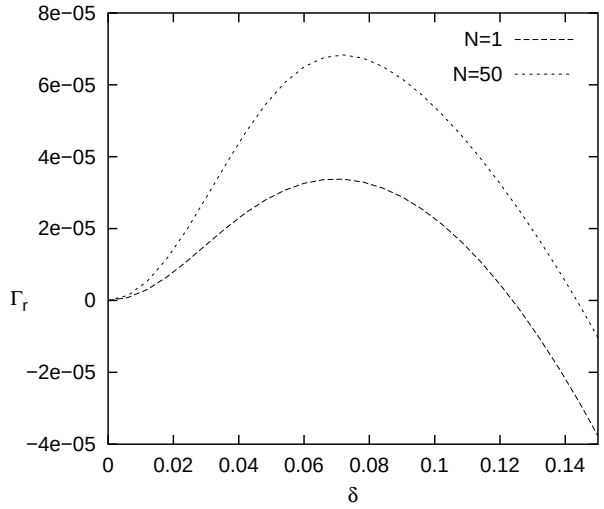

Figure 1.34: Dimensionless growth rate Γ_r plotted versus the dimensionless wavenumber δ of the bottom perturbation for $\hat{\mu} = 112.5$, $s = 1.02$, $\hat{r} = 25$, $\hat{\Psi}_d = 0.0045$, $\gamma = 0.05$ $\theta_c = 0.047$ and $\mathcal{N}$ =1, 50. Larger values of $\mathcal{N}$ provide results coincident with those obtained setting $\mathcal{N}$ =50.

of turbulence, spatial and temporal variations of the eddy viscosity should be taken into account as well as the influence of bottom perturbations on turbulent structure. Moreover the effects of wind waves are not taken into account in the model, although it is known that in shallow seas the oscillatory motion induced by wind waves close to the bottom can pick-up a lot of sediments which is then transported by the steady currents. Quite often, the local flow induced by tide propagation is not unidirectional and many tide constituents give rise to a complex time development of the actual tidal current.

Finally, being based on a linear approach, the model can predict only the initial stage of bed form growth. In order to investigate the long-term behaviour, when the amplitude of sand waves reach finite values, a nonlinear approach is required.

Chapter 2

Migration of sand waves

2.1 Introduction

As already pointed out in the section "*Introduction to Coastal Morphodynamics*", sand waves are rhythmic seabed features that occur in many shallow seas.

One of their characteristics is that their crests are almost orthogonal to the direction of the velocity oscillations induced by the tide. Furthermore they often migrate with a rate that strongly depends on the tide characteristics and in particular on the intensity of the local residual currents. Migration velocities can be up to some tens of metres per year (Terwindt, 1971; Bokuniewicz et al., 1977; Fenster et al., 1990). The sawtooth-shaped profile of sand waves is similar, but less asymmetric, to that of desert sand dunes or that of dunes observed in fluvial environments. However, they differ from bed forms induced by steady currents since the basic flow, which cause the sand waves to evolve, has an oscillatory nature. The reader interested in bedforms generated by steady currents is referred to Engelund and Fredsøe (1982), Richards (1980) and references therein.

In the section "*Introduction to Coastal Morphodynamics*" it has also been argued that knowledge about the characteristics of sand is of great practical relevance. Economical sectors that are affected by the presence and/or evolution of sand waves comprise:

i) the oil industry. Sand waves migration can represent a serious hazard to pipelines which are laid in a region of intense seabed activity. A few examples can be found of generation of large free-spans, related to sand waves migration, which led to buckling or even failure of the pipeline. On the other hand self-burial can also occur in relation with sand wave activity;

ii) the shipping industry. Intensive dredging activities may be required because of sand waves migrating into or along shipping channels and harbours, thereby reducing the local water depth and, consequently, the navigability;

iii) the fishing industry. It is well known that fields of sand waves provide an important shelter for fish stocks which find a propitious environment for growth and reproduction;

iv) coastal maintenance. It has been acknowledged that nearshore, migrating sand waves might even affect shoreline evolution (Verhagen, 1989) and hence coastal defence works.

The main objective of this section is to deepen the knowledge in sand wave migration, predicting and understanding it. This is done by extend the model proposed in chapter 1. The new aspect introduced is the incorporation of steady currents and various harmonic components of the tidal wave in the description of the phenomenon. This results in possible migration of sand waves due to time asymmetry of the tidal current. In fact, if only one tidal component is accounted for in the basic state, the flow at time $t + T/2$ (T being the component period) is the mirror image of that at time t, the time-averaged flow is symmetric and no migration of sand waves can be induced. Although for practical problems migration is probably the most important property of sand waves; only Németh et al. (2002) modelled sand wave migration. Németh et al. (2002) investigated the phenomenon by means of a model similar to that of Hulscher (1996a) and, hence, with an approach which is strictly valid only when the parameter r is moderate. Moreover, Németh et al. (2002) considered only the presence of a residual current in the basic state and found that sand waves always migrate downstream, i.e. in the direction of the steady current. As discussed in the following, field data exist which show that sometime sand waves migrate upstream. Even though different elements can contribute to sand wave migration (a.o. storms, wind-driven currents,...), we show that such an upstream migration can be modelled by investigating the interaction of different tide constituents.

2.2 Do sand waves migrate downstream or upstream?

In the literature it is usually reported that sand waves generated by tidal currents migrate downstream, i.e. in the direction of the residual steady

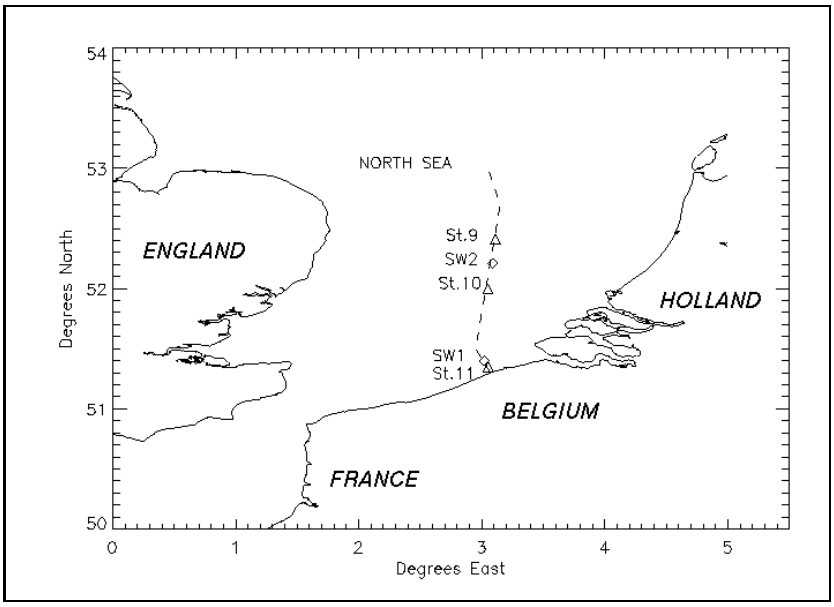

Figure 2.1: Study area (southern bight of the North Sea and position of some measurement sites for: bathymetry (diamonds) and currents (triangles).

current, at a speed of the order of several metres per year (Németh et al., 2002). However, in the following an example of a field case characterised by upstream-migrating sand waves is described. This field observation is not surprising. Indeed, the theoretical analysis described in section 2.3 shows that a simple mechanism exists able to cause the migration of sand waves in the direction opposite to that of the residual steady current.

Data concerning bathymetry, sediment properties (e.g. grain sizes, porosity, density, etc.) and current properties (i.e. tidal and residual currents characteristics) have been provided by SNAMPROGETTI S.p.A. These data were collected during a number of field surveys carried out in the North Sea (see figure **2.1**) between 1988 and 1995 for two pipeline engineering projects, namely "*ZEEPIPE*" and "*NORFRA*".

In the period August-October 1988 bathymetric surveys were performed within 28 corridors located along the path shown in figure **2.1** and progressively numbered from the coast toward the open sea. The width of the corridors is 200 metres for corridors 1-3, 5300 metres for corridors 3-16, of 4100 metres for corridors 17-20 and of 1500 metres for corridors 21-28.

Two vessels equipped with 'Simrad EM100' multibeam echo sounders were used. The ultrawide mode, covering 2.4 times the water depth, was used during the surveys. The average survey speed was 6 knots and in bad weather the velocity was reduced to about 3-4 knots. The primary positioning

systems used during the bathymetric surveys were both the 'Trinsponder' and the 'Syledis', while a differential GPS was used for control purposes. The positioning system gave a standard deviation better than +/- 3 metres. Single beam echo sounders were also used to check the depth measurements provided by the 'Simrad EM100'. The vertical datum was the Mean Sea Level. To calculate the tide and to have an accurate datum, a total of 50 tide recording stations were established along the planned route, all using concrete anchors. The concrete anchors and the recorders were retrieved by using release transponders. Data from 3 permanent stations supplied by the Dutch Hydrographic Services and Eurosense were also used. The data processing and map production were performed using a fully digital mapping system.

The surveyed area has a water depth ranging from the 7.5 metres of corridor 5 to the 50 metres of corridor 23. Sediment characteristics were obtained by analysing samples taken from the bottom surface and in boreholes reaching about 5 metres below seabed. In all the surveyed area there is a thick surface layer of sand, the mean diameter of which ranges between 0.25mm and 0.6mm. Along many corridors sand waves were observed. The typical features of the existing sand wave field were established through an analysis of the detailed bathymetric data. The sand waves present heights ranging between 2m and 10m and wavelengths varying between 120 and 500 metres. Sand waves are asymmetrical in most of the region of interest. Examples of the bathymetric data collected during the surveys are shown in figures **2.2** and **2.4** where the bottom topographies measured at the 'SW1' ($51^\circ\ 35^{'}N$, $3^\circ\ 2^{'}E$) and 'SW2' ($52^\circ\ 21^{'}N$, $3^\circ\ 9^{'}E$) sites (diamonds on figure **2.1**) are displayed. The data shown in figures **2.2** and **2.4** correspond to those measured at corridors 5 and 17, respectively.

For current data (triangle on figure **2.1**), we have used those collected at measurement sites located at ($51^\circ\ 30^{'}N, 3^\circ\ 2^{'}E$), ($52^\circ\ 0^{'}N, 3^\circ\ 5^{'}E$) and ($52^\circ\ 41^{'}N, 3^\circ\ 11^{'}E$), taken as representative of current conditions at SW1 and SW2.

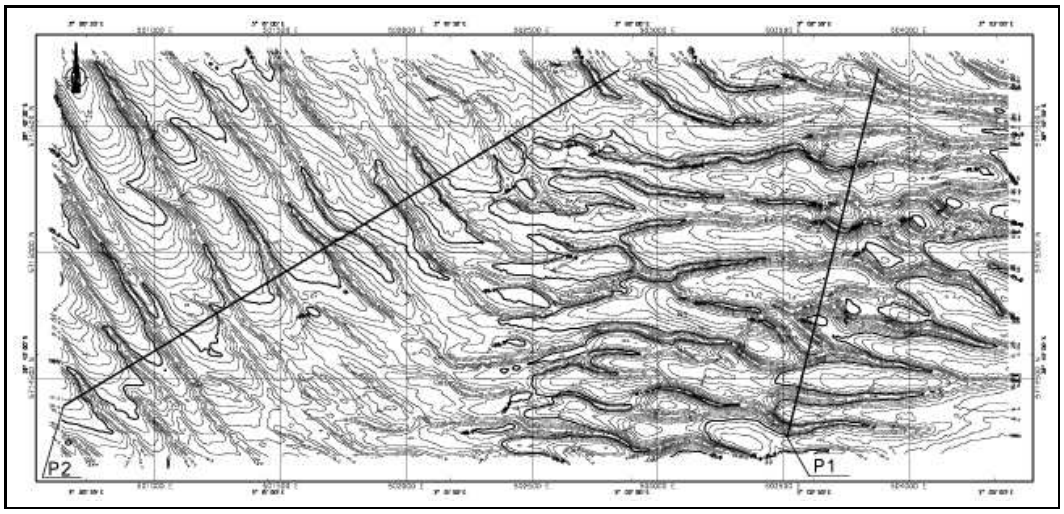

Figure 2.2: Contour map of the seabed at location SW1 with reference transects P1 and P2 showing the presence of sand waves. The black arrow indicates the north and the grid size is 500m. Courtesy of SNAMPROGETTI.

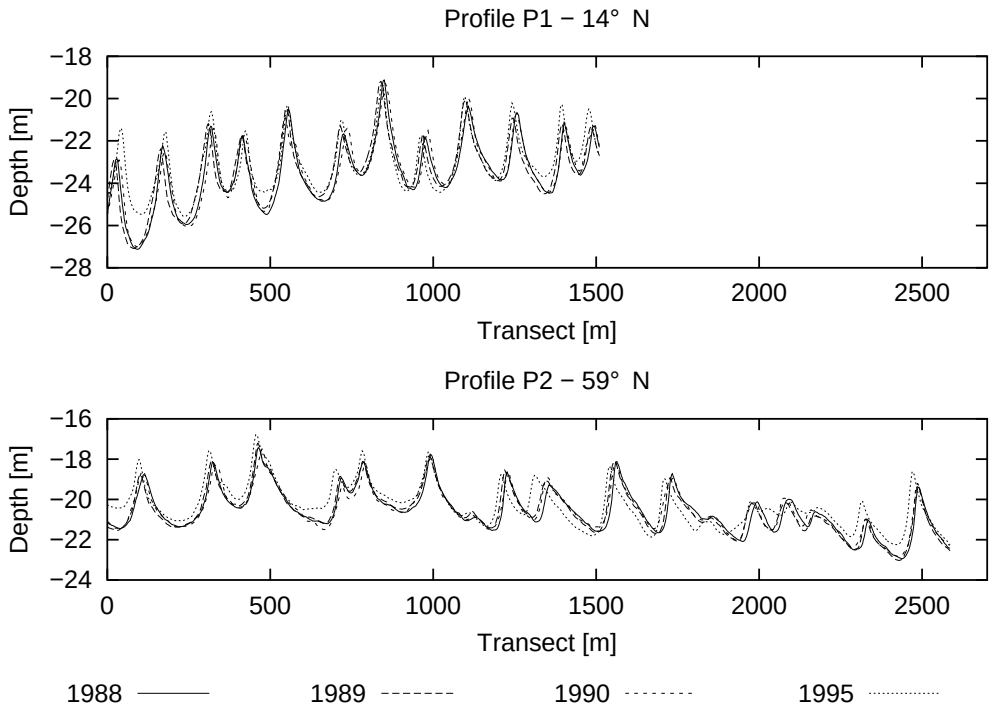

Figure 2.3: Seabed profiles at SW1 along transects P1 and P2. Distances are measured from the lower point of the transect toward the north-east. Courtesy of SNAMPROGETTI.

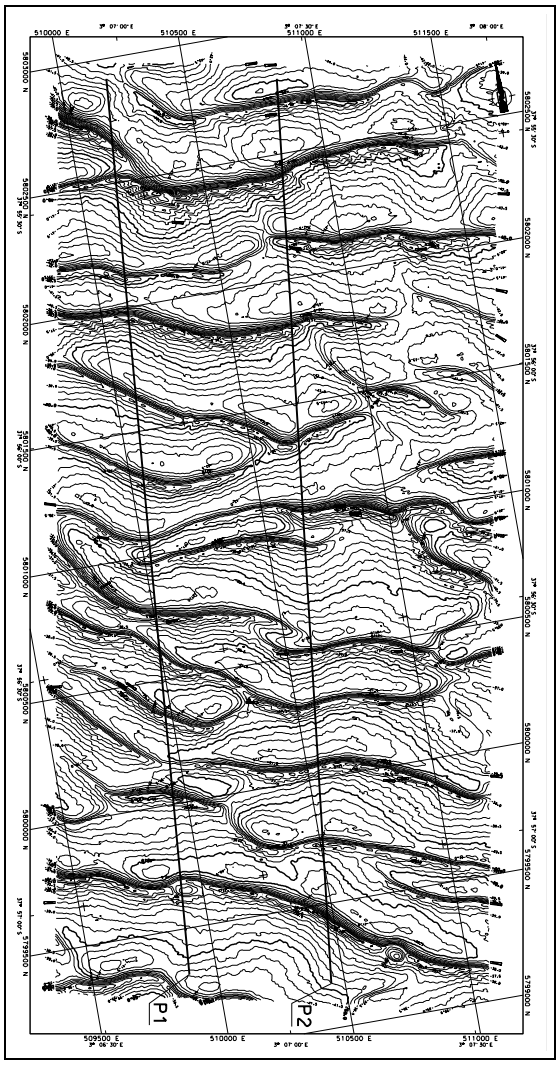

Figure 2.4: Contour map of the seabed at location SW2 with reference transects P1 and P2 showing the presence of sand waves. The black arrow indicates the north and the grid size is 500m. Courtesy of SNAMPROGETTI.

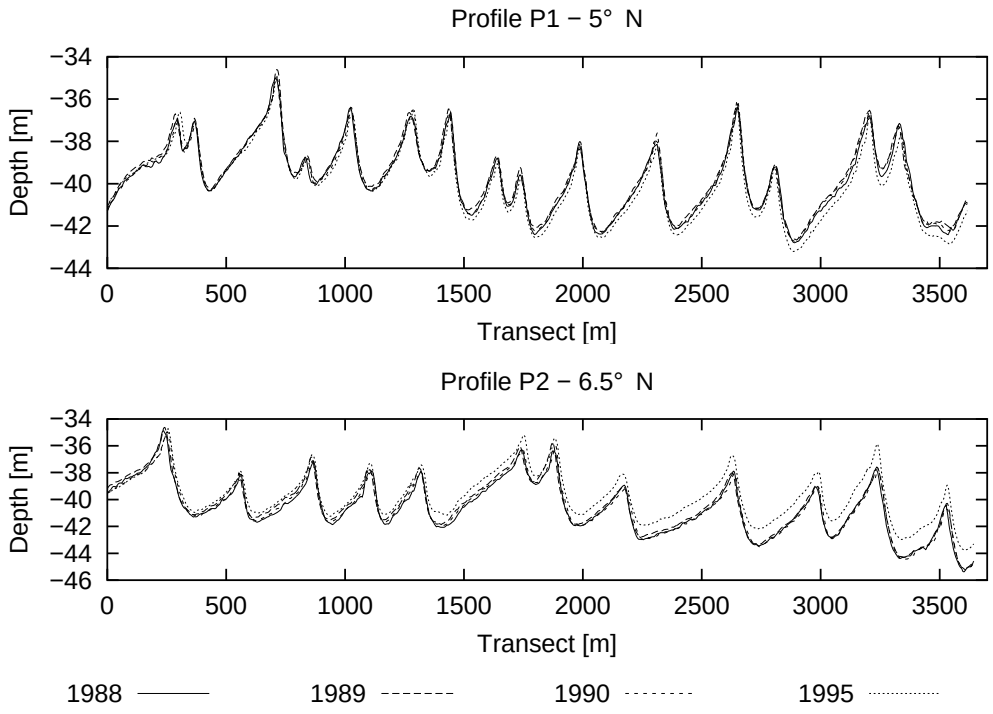

Figure 2.5: Seabed profiles at SW2 along transects P1 and P2. Distances are measured from the lower point of the transect toward the north. Courtesy of SNAMPROGETTI.

Constituent Name	Major axis [cm/s]	Minor axis [cm/s]	Inclination of major axis	phase lag ϕ
$Z0$	4.607	0.000	59.1°	360.0°
MM	0.687	-0.253	110.9°	286.5°
MSF	1.417	0.829	77.8°	32.4°
$ALP1$	0.258	0.065	155.3°	35.9°
$2Q1$	0.363	0.020	97.0°	200.0°
$Q1$	0.653	-0.010	116.9°	242.1°
$O1$	1.911	0.076	115.4°	298.0°
$NO1$	0.433	0.032	83.6°	274.8°
$K1$	1.810	-0.392	106.8°	115.5°
$J1$	0.369	-0.035	94.5°	59.6°
$OO1$	0.299	0.048	107.3°	181.4°
$UPS1$	0.101	-0.034	49.5°	184.8°
$EPS2$	1.014	-0.175	89.9°	164.6°
$MU2$	1.603	0.647	64.6°	170.5°
$N2$	7.051	-0.837	82.0°	54.0°
$M2$	43.392	-6.223	79.7°	70.9°
$L2$	4.349	0.516	76.8°	88.5°
$S2$	13.809	-2.680	79.2°	125.0°
$ETA2$	0.442	-0.112	69.6°	129.4°
$MO3$	0.703	-0.142	76.0°	155.0°
$M3$	0.231	-0.065	115.1°	102.0°
$MK3$	0.671	-0.163	77.4°	328.5°
$SK3$	0.183	0.069	97.6°	50.6°
$MN4$	1.196	0.307	163.8°	197.5°
$M4$	2.237	0.798	151.3°	192.3°
$SN4$	0.344	0.145	165.3°	296.8°
$MS4$	1.658	0.553	155.1°	254.8°
$S4$	0.233	-0.015	156.1°	355.4°
$2MK5$	0.698	-0.225	168.3°	53.4°
$2SK5$	0.155	0.060	146.2°	263.1°
$2MN6$	0.878	-0.691	65.7°	71.9°
$M6$	1.385	-1.264	178.8°	337.7°
$2MS6$	1.414	-1.198	23.1°	187.4°
$2SM6$	0.413	-0.276	128.1°	130.3°
$3MK7$	0.130	0.041	37.9°	339.4°
$M8$	0.153	-0.051	132.9°	61.0°

Table 2.1: Tidal current data at Station 9. The inclination of the major axis is measured with respect to the east axis in counterclockwise direction. Courtesy of SNAMPROGETTI.

Constituent Name	Major axis [cm/s]	Minor axis [cm/s]	Inclination of major axis	phase lag ϕ
$Z0$	5.286	0.000	70.9°	360.0°
MM	2.370	-0.695	8.8°	318.2°
MSF	1.370	-0.516	3.7°	43.9°
$ALP1$	0.461	0.018	70.8°	271.9°
$2Q1$	0.325	-0.029	64.5°	6.9°
$Q1$	0.709	-0.259	70.9°	301.5°
$O1$	1.019	-0.278	105.8°	297.3°
$NO1$	0.114	-0.002	28.8°	108.5°
$K1$	1.389	-0.534	77.0°	129.8°
$J1$	0.323	0.028	6.9°	146.3°
$OO1$	0.120	0.086	110.9°	142.2°
$UPS1$	0.102	0.036	18.0°	272.0°
$EPS2$	2.905	1.346	64.1°	200.9°
$MU2$	5.381	2.303	67.2°	181.5°
$N2$	6.057	-0.659	58.5°	9.7°
$M2$	38.699	7.547	55.8°	60.8°
$L2$	5.224	0.425	76.2°	58.3°
$S2$	10.239	1.579	47.2°	86.0°
$ETA2$	1.628	0.107	57.7°	143.0°
$MO3$	0.340	-0.011	50.2°	162.2°
$M3$	0.594	0.202	66.2°	197.8°
$MK3$	0.291	0.000	40.8°	69.7°
$SK3$	0.172	-0.119	162.7°	62.8°
$MN4$	1.337	0.171	21.8°	326.8°
$M4$	3.695	0.453	15.1°	5.3°
$SN4$	0.466	0.169	9.0°	61.3°
$MS4$	1.994	0.197	1.2°	45.4°
$S4$	0.072	0.025	115.4°	228.0°
$2MK5$	0.157	-0.100	138.3°	68.5°
$2SK5$	0.286	0.016	84.8°	137.5°
$2MN6$	0.661	-0.203	104.7°	345.9°
$M6$	1.390	0.272	85.4°	49.2°
$2MS6$	1.335	0.307	83.0°	69.1°
$2SM6$	0.174	-0.033	97.9°	125.0°
$3MK7$	0.163	0.083	101.0°	55.9°
$M8$	0.504	0.235	33.6°	344.3°

Table 2.2: Tidal current data at Station 10. The inclination of the major axis is measured with respect to the east axis in counterclockwise direction. Courtesy of SNAMPROGETTI.

Constituent Name	Major axis [cm/s]	Minor axis [cm/s]	Inclination of major axis	phase lag ϕ
$Z0$	2.377	0.000	30.2°	360.0°
MM	1.081	0.304	46.5°	221.9°
MSF	1.047	0.451	31.0°	265.4°
$ALP1$	0.104	0.085	2.9°	200.6°
$2Q1$	0.205	0.079	160.3°	243.6°
$Q1$	0.522	-0.188	37.9°	18.7°
$O1$	1.474	-0.645	36.9°	73.9°
$NO1$	0.304	-0.015	33.7°	171.1°
$K1$	1.521	-0.740	60.9°	198.5°
$J1$	0.333	0.208	80.8°	334.1°
$OO1$	0.165	-0.040	177.9°	121.2°
$UPS1$	0.190	-0.070	174.4°	16.9°
$EPS2$	0.257	-0.034	167.3°	277.1°
$MU2$	1.829	1.001	24.4°	66.4°
$N2$	8.072	2.115	61.5°	23.1°
$M2$	42.854	18.145	65.9°	35.5°
$L2$	3.814	1.888	51.0°	344.9°
$S2$	15.788	4.613	66.4°	95.1°
$ETA2$	0.255	-0.042	81.1°	31.0°
$MO3$	0.560	0.287	148.0°	163.7°
$M3$	0.264	0.144	125.5°	275.6°
$MK3$	0.665	0.286	155.7°	332.8°
$SK3$	0.404	0.007	13.3°	201.1°
$MN4$	1.664	-0.068	32.6°	320.2°
$M4$	4.137	-0.102	28.7°	330.7°
$SN4$	0.560	-0.163	100.9°	65.4°
$MS4$	2.358	0.091	23.7°	25.7°
$S4$	0.379	0.112	49.5°	131.1°
$2MK5$	0.664	0.057	54.7°	151.3°
$2SK5$	0.177	0.021	60.5°	347.7°
$2MN6$	1.694	0.266	18.2°	235.7°
$M6$	2.885	0.687	26.2°	266.4°
$2MS6$	3.086	0.799	23.5°	317.2°
$2SM6$	0.863	0.008	12.4°	12.8°
$3MK7$	0.375	0.057	37.0°	56.6°
$M8$	0.839	0.498	51.0°	256.4°

Table 2.3: Tidal current data at Station 11. The inclination of the major axis is measured with respect to the east axis in counterclockwise direction. Courtesy of SNAMPROGETTI.

Layer	**Top [m]**	**Bottom [m]**	**Soil description**	**Total unit weight [kN/m^3]**	**Friction angle undrained [deg]**	**d_{50} [mm]**
			Top of sand wave			
I	0.0	3.0 - 7.0	SAND, medium to coarse, medium dense to dense	20.0 - 21.5	35 - 43	0.60
II	3.0	>7.0	CLAY, very stiff	17.5 - 21.0	32	0.04
			Bottom of sand wave			
I	0.0	0.4 - 5.0	SAND, medium, loose to dense	19.0 - 21.0	30 - 43	0.35
II	0.4 - 5.0	>5.0	CLAY, stiff to very stiff	17.5 - 21.0	32	0.04

Table 2.4: Sediment characteristics in area SW1. Courtesy of SNAMPROGETTI.

Layer	**Top [m]**	**Bottom [m]**	**Soil description**	**Total unit weight [kN/m^3]**	**Friction angle undrained [deg]**	**d_{50} [mm]**
I	0.0	2.0 - 7.0	SAND, medium to fine, medium dense to dense	19.5 - 20.5	25 - 41	0.25
II	2.0 - 7.0	>7.2	SAND, dense and CLAY, stiff to very stiff	20.5 - 21.0 -	37 - 43 32	- -

Table 2.5: Sediment characteristics in area SW2. Courtesy of SNAMPROGETTI.

Sediment characteristics are here summarised in terms of the total unit weight, undrained friction angle and mean diameter (d_{50}) (see tables 2.2 and 2.2).

Tidal currents can be considered as a deterministic forcing and were reconstructed yielding the amplitude of the velocity oscillations $\hat{U}_n$ and the direction Θ_n of the major semi-axis of the tidal ellipses of the different tidal components (see table 2.1, 2.2 and 2.3). Similarly, the forcing due to residual currents can be given in terms of both the strength $\hat{U}_0$ and the direction Θ_0 of the steady component of the velocity field. At location SW1 an analysis of the available data shows that the ellipse of the main tide component (M2) is clockwise rotated with respect to the north by about 25 degrees, while the M4-ellipse and the steady current are clockwise rotated by about 60 degrees. The amplitude of the velocity oscillations induced by the M2 tide component is about 50cm/s while the M4 tide component has an amplitude of the velocity oscillations of about 5cm/s. Finally, the residual steady current is of the order of a few centimetres per second. The phase angle ϕ between the M2 and M4 components turns out to be $\phi = -295$ degrees. Similar values characterise tidal currents at location SW2.

To detect the presence of sand waves and determine their typical wavelengths, maps similar to those reported in figures **2.2** and **2.4** have been analysed.

As far as the SW1 area is concerned, the data reveal the presence of two different types of sand waves (refer to transects P1 and P2 of figure **2.2**). In the western part (transect P2) asymmetric sand waves are found that slowly migrate (some metres per year) toward the south-west ($240°N$) and characterised by a length of about $\mathcal{L} = 210 \pm 45$m. On the other hand, typical sand waves of the eastern part (transect P1) are shorter ($\mathcal{L} = 135 \pm 25$m), steeper, nearly symmetrical and almost stationary with the crests aligned almost perpendicular to the $20° - 200°$ N direction. Moreover, it appears that the bedforms in the eastern part have crests which are almost orthogonal to the direction of the M2 tide component while the crests of those present in the western part are orthogonal to the steady current and to the M4 tidal component. It is not simple to explain why sand waves characteristics change in such a small area (the area of SW1 is only 4×2 km^2). A careful analysis of the bathymetric data shows that the mean bottom slope in the eastern part differs from that of the western part and hence this topographic difference may trigger the appearance of different bedforms. The data also reveal that, rather surprisingly, along the P1 and P2 sections sand waves migrate in a direction opposite to that of the residual current. Besides, the migration rate along P1 is much smaller than that along P2 (see figure **2.3**).

Sand waves of the SW2 area are characterised by a more regular pattern

(see figure **2.4**). Again, field data useful for measuring migration rates are available along two transects, P1 and P2. However, contrary to what found in the SW1 area, no major differences were found by analysing properties of sand waves along these two sections. In fact, sand waves are characterised by a wavelength of about 275 ± 70m along section P1 and of about 296 ± 73m along section P2. Heights range from 3.5m to 5.5m over the whole SW2 area and the steepnesses does not vary in the domain. Moreover, bathymetric data reveal a negligible net migration over the period $1988 - 1995$ (see figure **2.5**).

The bottom configuration was measured again in March 1989, March 1990 and March 1995 only along the transects drawn in figures **2.2** and **2.4**. These transects were selected by SNAMPROGETTI because the sand waves along them are representative for sand wave fields encountered along the route of the "*ZEEPIPE*" pipeline. The bottom configuration along the transects was monitored in detail with the specific purpose of evaluating sand wave migration and mobility. The measured data are shown in figures **2.3** and **2.5**. As described in the following, an estimate of the migration speed of sand waves can be obtained using the collected data and composing the depth variations between subsequent profiles.

For current data, we have used those collected at the measurement sites (triangles on figure **2.1**) located at ($52° \; 41' N$, $3° \; 11' E$) (station 9), ($52° \; 00' N$, $3° \; 5' E$) (station 10) and ($51° \; 30' N$, $3° \; 5' E$) (station 11) and, therefore, taken as representative of current conditions at SW1 (station 11) and SW2 (stations 9 and 10), respectively. Measurements were carried out at 3 metres above the bottom. Current measurements were made by means of 'Simrad UCM-30' acoustic current meters. The instrument samples current velocity at 10 Hz and stores mean values on 10 minutes every hour. The measurement campaign was carried out in the period 15 October 1998 - 31 March 1989. The harmonic analysis of the tidal current has been performed for the current time series which have a length that is sufficient to resolve the main tidal constituents.

For each tidal constituent it was possible to obtain the amplitude of the major axis of the tidal current ellipse, the amplitude of the minor axis of the tidal current ellipse (a positive minor axis means that the vector rotates in the counterclockwise direction, a negative value indicates clockwise rotation), the inclination of the major axis, indicated as the angle from the east axis in the counterclockwise direction, the Greenwich phase lag of the constituents (in degrees). It turns out that the tidal currents at the measuring sites are mainly semi-diurnal with M2 as the dominant constituent. Weaker diurnal and quarter-diurnal contributions as well as a steady current are also evident. Tables 2.1, 2.2 and 2.3 summarise the characteristics of the tidal constituents

Site	Transect	Direction of migration		Av. migr. speed (m/year)	Stand. Dev. (m/year)
		From	To		
SW1	P1	north-east	south-west	8.0	3.2
SW1	P2	north-east	south-west	5.9	3.8
SW2	P1	south	north	1.5	5.6
SW2	P2	south	north	1.8	5.8

Table 2.6: Direction of migration, average migration speed of sand waves and standard deviation observed at SW1 and SW2 along transects P1 and P2 in the period 1988-1989.

for station 9, 10 and 11 respectively. In these table the tidal constituent Z0 represents the steady current.

At this stage it is worth providing a brief description of the procedure adopted to evaluate the tide characteristics which are used in the following to run the model. On the basis of the data shown in the previous tables, the time history of the tidal current along the transects has been reconstructed. The velocity induced by each tidal constituent was projected along each transect (accounting for its amplitude, frequency and phase) and summed up to the other contributions. Then, applying a FFT (Fast Fourier Transform) algorithm over time windows of 12 hours and 25 minutes and averaging over the total number of the windows, the amplitude and phase of the one-dimensional, representative residual (Z0), semi-diurnal (M2) and quarter-diurnal (M4) tide constituents, defined as those which best approximate the reconstructed signal, have been evaluated. This procedure has been employed since the theoretical model only accounts for the above three tide constituents.

The analysis of the data measured at SW1 reveals that, rather surprisingly, along the P1 and P2 transects during the period ranging from 1988 to 1989 sand waves migrate in a direction opposite to that of the residual current (see table 2.2). From 1989 to 1995 sand waves still migrate in the same direction. However, since current data is not available for this period and it is not possible to state that the migration is in the direction opposite to that of the residual current (see table 2.2). In the same periods at SW2, bathymetric data reveal a downstream migration.

Can these field data, and in particular the upstream sand wave migration,

Site	Transect	Direction of migration		Av. migr. speed (m/year)	Stand. Dev. (m/year)
		From	To		
SW1	P1	north-east	south-west	3.5	7.1
SW1	P2	north-east	south-west	8.8	11.4
SW2	P1	south	north	4.4	7.0
SW2	P2	south	north	6.0	5.8

Table 2.7: Direction of migration, average migration speed of sand waves and standard deviation observed at SW1 and SW2 along transects P1 and P2 in the period 1989-1995.

be explained by means of a simple model similar to that illustrated in chapter 1? In the following it is shown that the answer is positive, even though more tidal constituents must be taken into account when studying the interaction of tidal currents with the bottom waviness.

2.3 Migration of sand waves: a theoretical model

As showed in the first chapter, it has been considered the flow generated by a tidal wave propagating over a cohesionless bed and investigate the time-development of the bottom configuration it induces. Following Gerkema (2000) and Németh et al. (2002) we consider a two-dimensional flow. The hydrodynamics of the problem is described by momentum and continuity equations (see section 1.1 for details). The morphodynamics of the problem is governed by the sediment continuity equation which states that convergence (or divergence) of the sediment flux must be accompanied by a rise (or fall) of the bed profile:

$$\frac{\partial \eta}{\partial t} + \frac{1}{(1-n)}\frac{\partial Q}{\partial x} = 0 \quad . \tag{2.1}$$

Here Q denotes the sediment flux per unit width and n the bed porosity. The problem is closed by the following sediment transport predictor

$$Q = \alpha |u|^3 \left(\frac{u}{|u|} - \gamma \frac{\partial \eta}{\partial x} \right) . \tag{2.2}$$

The above sediment transport formula is obtained by relating Q to the agitating forces which act on sediment grains. The latter move subject to the drag force and to the tangential component of gravity acting along the bed profile, other forces being negligible. The sediment transport induced by the drag force is assumed to be proportional to the third power of the fluid velocity (Bailard, 1981; Bailard and Inman, 1981), while that caused by gravity is known to be linearly related to the local bottom slope when the latter is small (Fredsøe, 1974). In (2.2) the constant α has typically values of the order of $10^{-4} - 10^{-3}\mathrm{s}^2\mathrm{m}^{-1}$ while γ is the dimensionless bed-slope parameter which typically assumes values ranging from zero to order one. Relationship (2.2) can be judged to be based on an oversimplified picture of reality (for example sediment, transported by sea gravity waves is not considered by (2.2)), however the works by Gerkema (2000) and Komarova and Hulscher (2000), who used a similar sediment transport predictor, show that the use of (2.2) in the problem under consideration leads to a fair description of the phenomenon and to reliable predictions.

2.4 The basic state

In order to model the flow that is locally induced by the propagation of the tidal wave, we consider the flow over a flat horizontal bottom forced by a horizontal pressure gradient which is the sum of

i) a steady component;

ii) an oscillatory component of angular frequency σ;

iii) an oscillatory component of angular frequency 2σ:

$$\frac{\partial p}{\partial x} = -P_{0x} - \frac{P_{1x}}{2}(e^{i\sigma t} + c.c.) - \frac{P_{2x}}{2}(e^{2i\sigma t} + c.c.). \tag{2.3}$$

As shown in the following, the complex amplitudes P_{1x} and P_{2x} of the oscillatory pressure gradient can be related to the amplitude of the different tidal wave components and P_{0x} to the strength of the residual current Z0, the first two contributions can be thought of composing the M2 and M4 tidal components respectively while the steady part gives rise to the residual current. It can be easily verified that the vertical velocity component of the basic flow vanishes identically, while the horizontal component reads

$$u_b = \sum_{n=-2}^{2} \hat{U}_n e^{in\sigma t} = -\frac{P_{0x}}{\rho A}\left[\frac{z^2}{2} - zH - \frac{H}{\tilde{s}}\right] +$$

$$+\left[\sum_{n=1}^{2}\frac{P_{nx}}{2ni\rho\sigma}\left[1+\tilde{c}_n\left(E_n^2e^{-(1+i)\frac{z}{\Delta_n}}+e^{(1+i)\frac{z}{\Delta_n}}\right)\right]e^{in\sigma t}+c.c.\right] \quad . \tag{2.4}$$

Here $\tilde{s}$ is the stress parameter defined in equation (1.8b). Furthermore Δ_n is a viscous length defined in terms of the kinematic eddy viscosity A and of the angular frequency of the tide oscillations:

$$\Delta_n = \sqrt{2A/n\sigma} \tag{2.5}$$

and

$$E_n = e^{(1+i)\frac{H}{\Delta_n}}, \qquad \tilde{c}_n = -\frac{\tilde{s}}{\tilde{s}(E_n^2+1)+(1+i)(E_n^2-1)/\Delta_n}. \tag{2.6}$$

Moreover, the functions $\hat{U}_n$ can be easily by comparing the different harmonic components appearing in (2.4) and it turns out that the amplitudes $\hat{U}_{1_m}$ and $\hat{U}_{2_m}$ of the depth-averaged velocity oscillations are

$$\hat{U}_{n_m} = \frac{|P_{nx}|}{\rho\sigma}\left|1+\tilde{c}\frac{(\Delta_n/H)}{(1+i)}(E_n^2-1)\right|, \tag{2.7}$$

while the depth-averaged value of the steady current $\hat{U}_{0_m}$ is

$$\hat{U}_{0_m} = \frac{|P_{0x}|}{\rho A}\left(\frac{1}{3}H^2+\frac{H}{\tilde{s}}\right). \tag{2.8}$$

2.5 The time-development of bottom perturbations

As in Hulscher (1996a), Gerkema (2000) and as showed in section 1.3 we perform a stability analysis of the flat bottom configuration considering perturbations of small amplitude (strictly infinitesimal) and linearise the problem.

After linearising with respect to the amplitude of the initial perturbation, the hydrodynamic problem is posed by the Orr-Sommerfeld-like equation obtained in section 1.3 (see relationship (1.24)).

Expanding the stream function Ψ in equation (1.24) as a Fourier series in time we obtain the following system of coupled linear ordinary differential equations:

$$\frac{in}{\hat{r}\delta}N^2\hat{\Psi}_n+\sum_{j=-2}^{2}\hat{U}_jN^2\hat{\Psi}_{n-j}-i\sum_{j=-2}^{2}\frac{d^2\hat{U}_j}{dz^2}\hat{\Psi}_{n-j}=\frac{1}{\mu\hat{r}\delta}N^4\hat{\Psi}_n \tag{2.9}$$

supplemented with the following boundary conditions

$$\hat{\Psi}_n = 0, \qquad \frac{d^2\hat{\Psi}_n}{dz^2} = 0 \quad \text{at} \quad z = 1, \tag{2.10}$$

$$\hat{\Psi}_n = -\frac{1}{2}\hat{U}_n \quad \text{at} \quad z = 0, \tag{2.11}$$

$$\frac{d^2\hat{\Psi}_n}{dz^2} - s\frac{d\hat{\Psi}_n}{dz} = -\frac{1}{2}\frac{d^2\hat{U}_n}{dz^2} + \frac{s}{2}\frac{d\hat{U}_n}{dz} \quad \text{at} \quad z = 0. \tag{2.12}$$

The reader should notice that the presence of the terms with $\hat{U}_0$ and $\hat{U}_2$ makes (2.9) different from the equation (1.32) solved in section 1.3 and, as a consequence, the solution of (2.9) is no longer symmetric with respect to the crests and troughs of the bottom waviness. As shown in section 2.6, the loss of symmetry is the cause of sand wave migration.

Notice that, a better description of the solution is achieved close to the bottom, where large gradients are expected for large values of $\hat{r}$, if the numerical integration of equations (2.9) is carried out using a constant step in the variable ζ defined by

$$\zeta = \ln[1 + (\hat{r}\delta)^{1/2} z] \tag{2.13}$$

which corresponds to clustering the computational points close to the bottom.

2.6 Results

The model allows for the computation of both the growth/decay rate of the bottom perturbations and their dimensional migration speed C. These quantities can be computed by noticing that the bottom configuration is described by

$$\eta = \frac{\Pi_0}{2} e^{\frac{\Gamma_r \alpha \hat{U}_{1_m}^3}{H^2} t} e^{ik\left(x + \frac{\Gamma_i \alpha \hat{U}_{1_m}^3}{kH^2} t\right)} + c.c. \tag{2.14}$$

where the complex quantity Γ has been split into its real (Γ_r) and imaginary (Γ_i) parts. The real part Γ_r controls the amplification or the decay of the bottom perturbations while, as shown by (2.14), Γ_i is related to their migration speed. The dimensional migration speed is

$$C_d = \Gamma_i \left(\frac{\alpha \hat{U}_{1_m}^3}{kH^2} \right). \tag{2.15}$$

Relationships (1.68a,b) allow to evaluate the growth rate Γ of the bottom perturbations as function of the tidal currents and sediment characteristics.

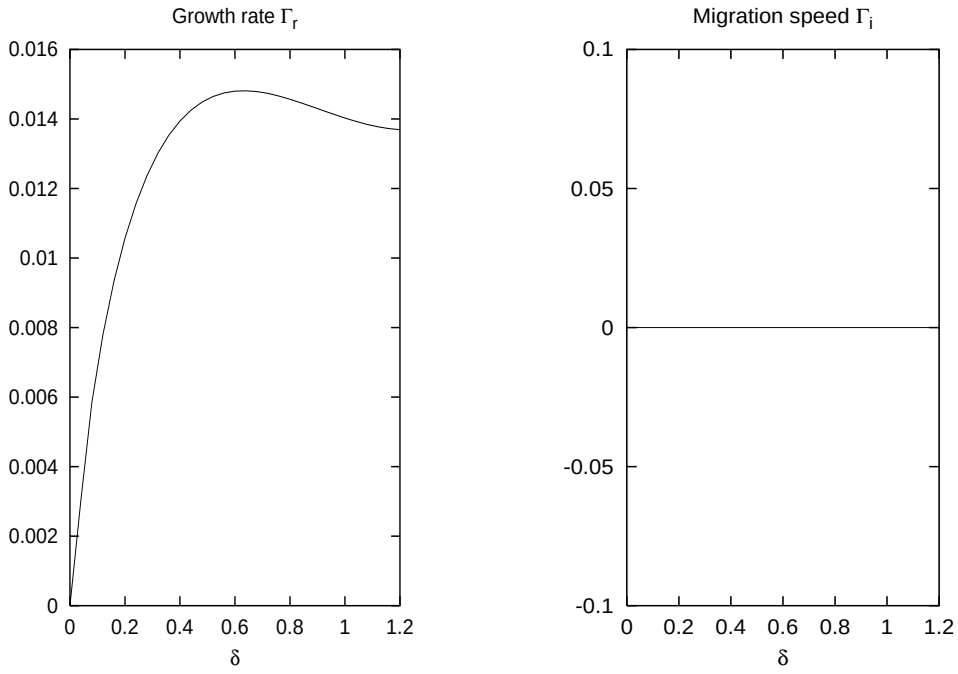

(a) (b)

Figure 2.6: Generation and migration of sand waves due to the M2 constituent only. Area SW1, transect P2: (a) dimensionless growth rate Γ_r, (b) dimensionless migration speed Γ_i. Model parameters are: $\hat{r} = 145$, $\gamma = 0.23$, $\mu = 2.25$ and $s = 0.84$ ($\hat{U}_{0_m} = \hat{U}_{2_m} = 0$).

When both P_{2x} and P_{0x} vanish, i.e. the tide has only the M2 component, the imaginary part Γ_i of Γ turns out to be identically zero and the bottom perturbations do not migrate. This finding could be expected since the flow at any phase φ of the cycle is the mirror image of that at $\varphi \pm \pi$.

In figure **2.6**, Γ_r and Γ_i are plotted for values of the parameters describing the conditions of the SW1 area that are estimated on the basis of measurements taken during the years 1988-1989. In this computation it is assumed that $\hat{U}_{0m} = \hat{U}_{4m} = 0$, and consequently the bedforms do not migrate, the predicted wavenumber of the most unstable mode is $\delta \approx 0.62$ and the dimensional wavelength turns out to be $\mathcal{L} = 2\pi H/\delta \approx 203$m, a value close to the observed sand wave size which along P2 is about 250m.

Of course a one-dimensional model like that described in the present paper does not allow for an exhaustive description of the phenomenon taking place in the area SW1, where a complex three-dimensional flow field is generated by tidal propagation. At this stage it is necessary to point out that

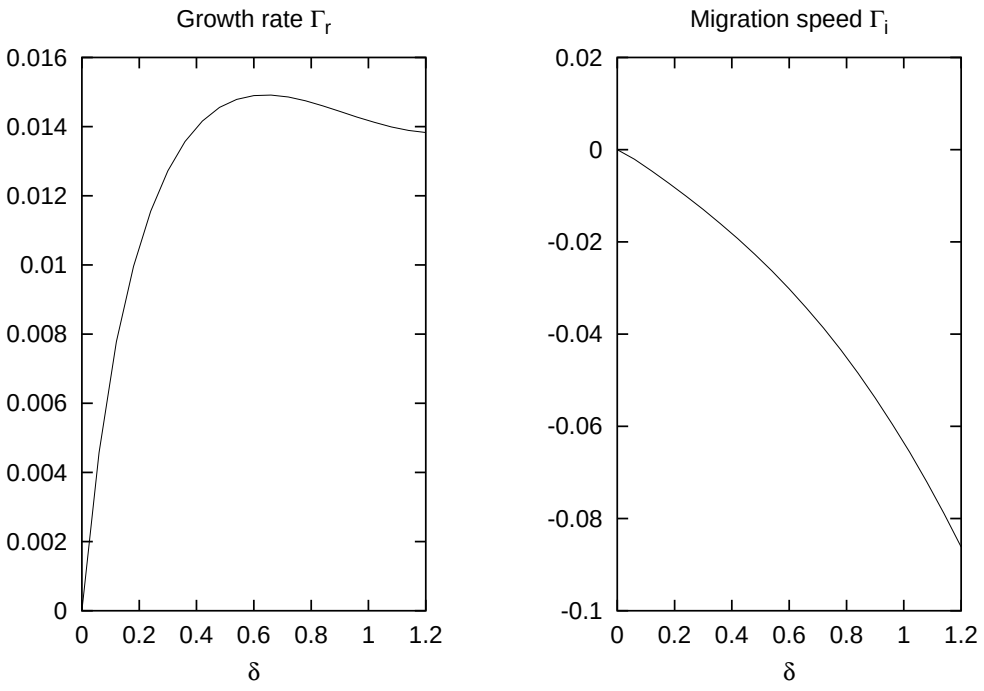

Figure 2.7: Influence of the steady component Z0 on the generation and migration of sand waves. Area SW1, transect P2: (a) dimensionless growth rate Γ_r, (b) dimensionless migration speed Γ_i. Model parameters are: $\hat{r} = 145$, $\gamma = 0.23$, $\mu = 2.25$, $s = 0.84$ and $\hat{U}_{0_m}/\hat{U}_{1_m} = 0.03$.

previous predictions (Chapter 1) have been obtained using the value of the tidal currents measured in area SW1 and projected along the P2 transect, the latter being approximately aligned with the major axis of the M4 ellipse and the Z0 direction.

When values of P_{0x} different from zero are considered, a background residual steady current is present and sand waves are found to migrate. Indeed figure **2.7** shows that the presence of a residual current makes the flow to lose its symmetry (see figure **2.8**) and it induces values of Γ_i different from zero. The results indicate that a positive value of the residual current induces negative values of Γ_i and viceversa, thus showing that sand waves always migrate in the direction of the residual current. These results qualitatively agree with those of Németh et al. (2002), even though the present analysis allows for more accurate results to be obtained. The reason is that the evaluation of the flow induced by the interaction of the bottom perturbations with the tidal currents by means of just one harmonic component in (1.30) is strictly

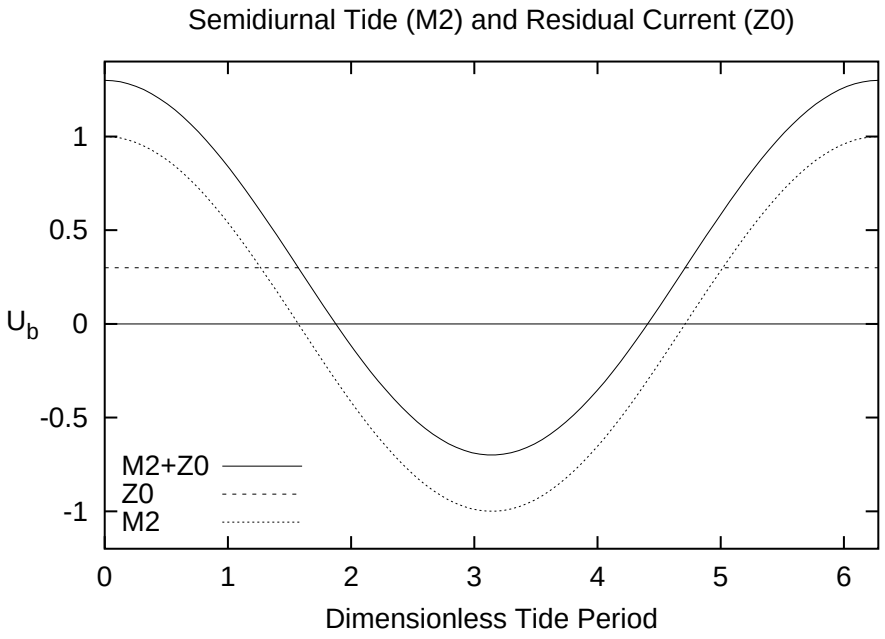

Figure 2.8: Basic flow obtained using tidal constituents M2 & Z0

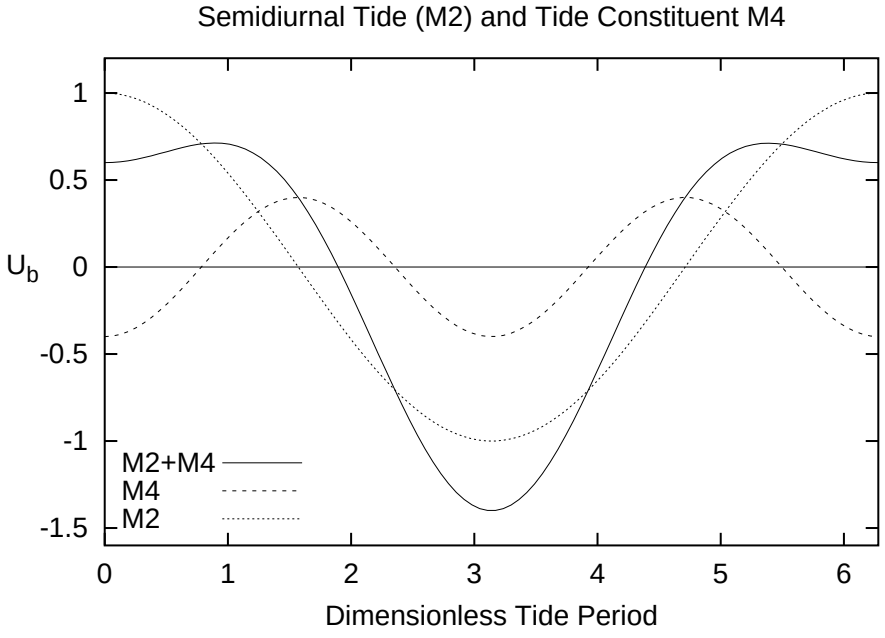

Figure 2.9: Basic flow obtained using tidal constituents M2 & M4

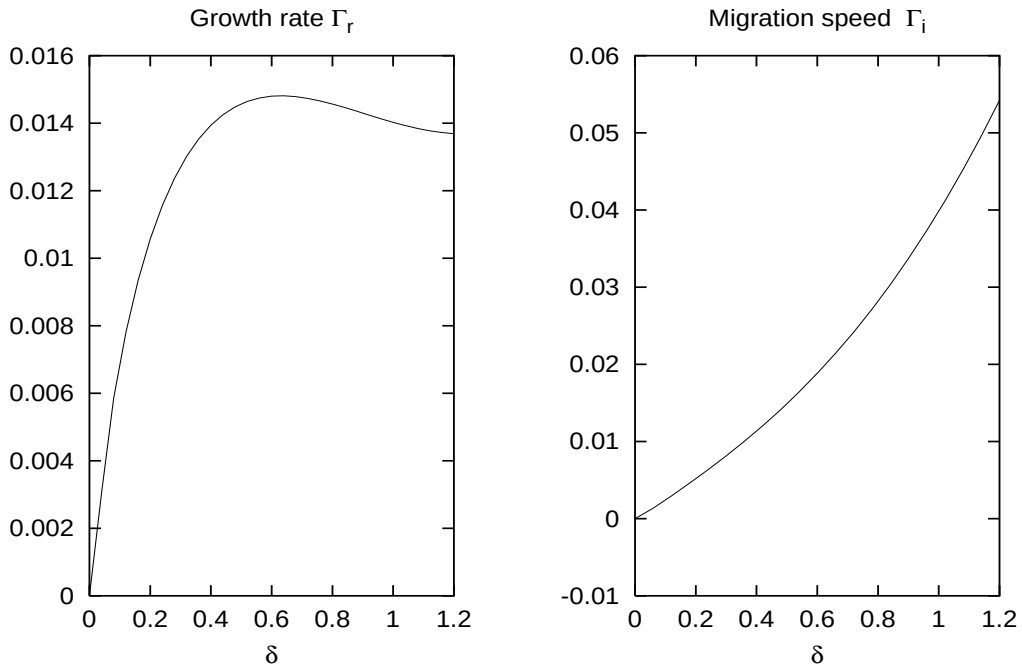

Figure 2.10: Generation and migration of sand waves in the area SW1 caused by Z0, M2 and M4. Transect P2: (a) dimensionless growth rate Γ_r, (b) dimensionless migration speed Γ_i. Model parameters are: $\hat{r} = 145$, $\gamma = 0.23$, $\mu = 2.25$, $s = 0.84$, $\hat{U}_{0_m}/\hat{U}_{1_m} = 0.03$, $\hat{U}_{2_m}/\hat{U}_{1_m} = 0.15$ and $\phi = -295°$.

appropriate only for small values of $\hat{r}$ while large values of $\hat{r}$ require values of $\mathcal{N}$ significantly larger than one. In fact, the interaction between the flow induced by tidal propagation and the bottom waviness gives rise to a perturbed flow characterised by a large number of time harmonic components, which are generated through a cascade process.

The dimensional migration rates predicted by the present analysis with appropriate values of α turn out to be of the order of few metres per year, values which are similar to those observed in the field. Indeed if α is chosen to be $1 \times 10^{-3}\mathrm{s}^2\mathrm{m}^{-1}$, i.e. a value within the range suggested by Gerkema (2000), the value of C_d for the most unstable mode is equal to about 1.6m/year and the average migration speed of sand waves observed in the period 1988-1989 along P2 is of about 6m/year.

Figure **2.10** shows the model predictions for values of the parameters characteristic of the SW1 area along transect P2; in particular the phase between the M2 and M4 component has been fixed according to the measured

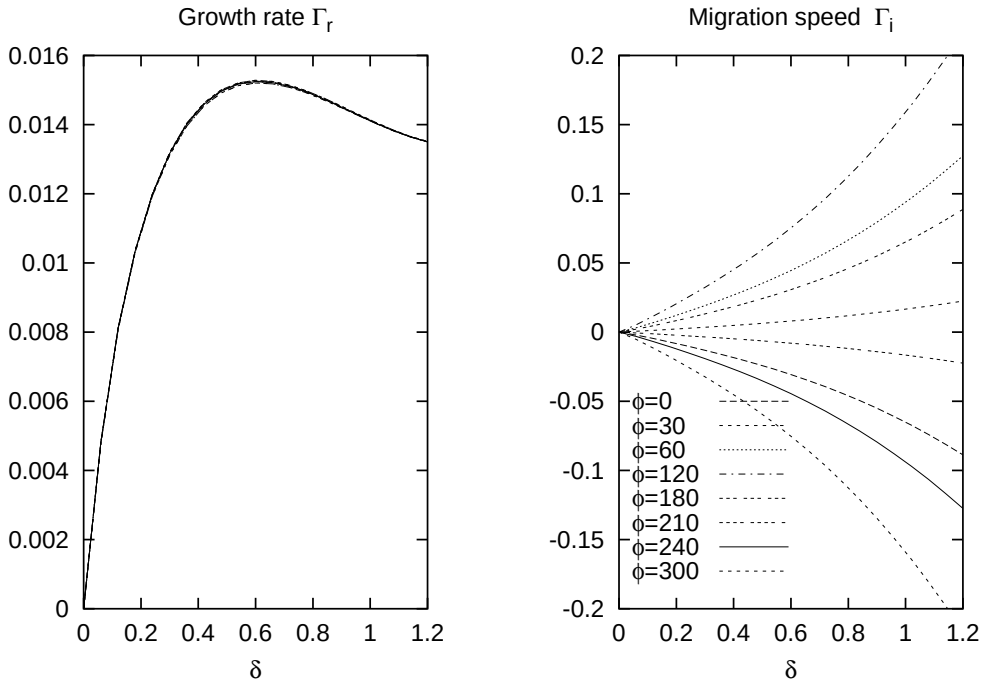

(a) (b)

Figure 2.11: Dimensionless amplification rate Γ_r (a) and dimensionless migration speed Γ_i (b) plotted versus the wavenumber δ in the case of tidal constituents M2 and M4 only; $s = 0.84$, $\mu = 2.25$, $\gamma = 0.23$, $\hat{r} = 145$, $U_2/U_1 = 0.0965$.

field values and the residual current has been added. Figure **2.10** also shows that the asymmetry in the sediment transport induced by the presence of the M4 tide component prevails on that caused by the steady residual current and sand waves are predicted to migrate in the upstream direction as shown by field surveys. The observed migration speed (of the field site) has been evaluated looking at the displacement of each crests (see figure **2.13** which shows some specific bedforms) and making the average on the observed bedforms. The standard deviation of the measured migration speed is 3.8m/year. Note that the model predictions have been made by fixing the phase between the M2 and M4 constituents according to the measured field values (remember that $\hat{U}_{1m}$ and $\hat{U}_{2m}$ are complex quantities). In fact, as shown by figure **2.11**, in which the flow only contains M2 and M4 components, the value of Γ_i is strongly affected by the phase shift ϕ between the two tidal constituents. In other words, sand waves can migrate in the upstream direction only when an appropriate phase shift exists between the M2 and M4 tidal components.

If the hydrodynamic data are projected along transect P1, which is about

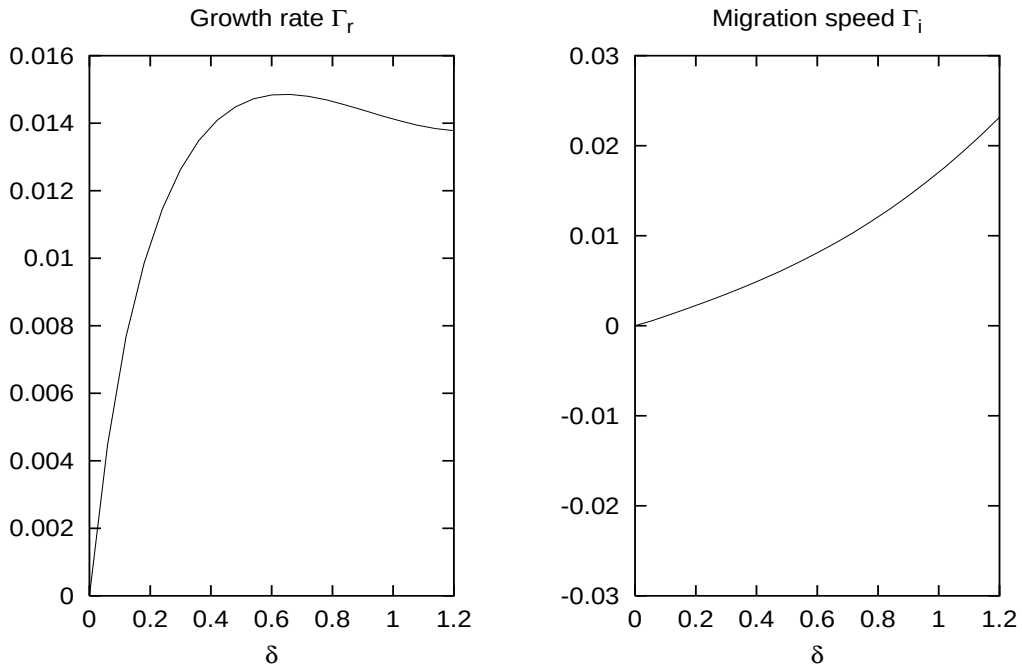

Figure 2.12: Generation and migration of sand waves in the area SW1 caused by Z0, M2 and M4. Transect P1: (a) dimensionless growth rate Γ_r, (b) dimensionless migration speed Γ_i. Model parameters are: $\hat{r} = 190$, $\gamma = 0.23$, $\mu = 1.71$, $s = 0.80$, $\hat{U}_{0_m}/\hat{U}_{1_m} = 0.017$, $\hat{U}_{2_m}/\hat{U}_{1_m} = 0.090$ and $\phi = -295°$.

the direction of the major axis of the M2 ellipse, the results of figure **2.12** are obtained. The predicted wavelength of the most unstable mode does not significantly change, while in the field the bedforms observed along transect P1 are shorter than those observed along transect P2. Moreover, the predicted migration speed (0.6m/year) slightly decreases while the field observations indicate a slight increase. The analysis of the bathymetric data along transect P1 leads to an observed migration speed equal to 8m/year with a standard deviation equal to 3.2m/year. Notwithstanding the differences between the theoretical predictions and the field data, the agreement is still satisfactory if the relative error is compared with the typical values of the relative errors provided by the existing morphodynamic stability analyses which are used to understand the characteristics of fluvial, coastal and estuarine bedforms (Blondeaux, 2001). Indeed, in the literature, relative errors equal to 100% and even larger are judged to be satisfactory (see a.o. Colombini et al., 1987; Blondeaux, 1990; Vittori & Blondeaux, 1990; Colombini,

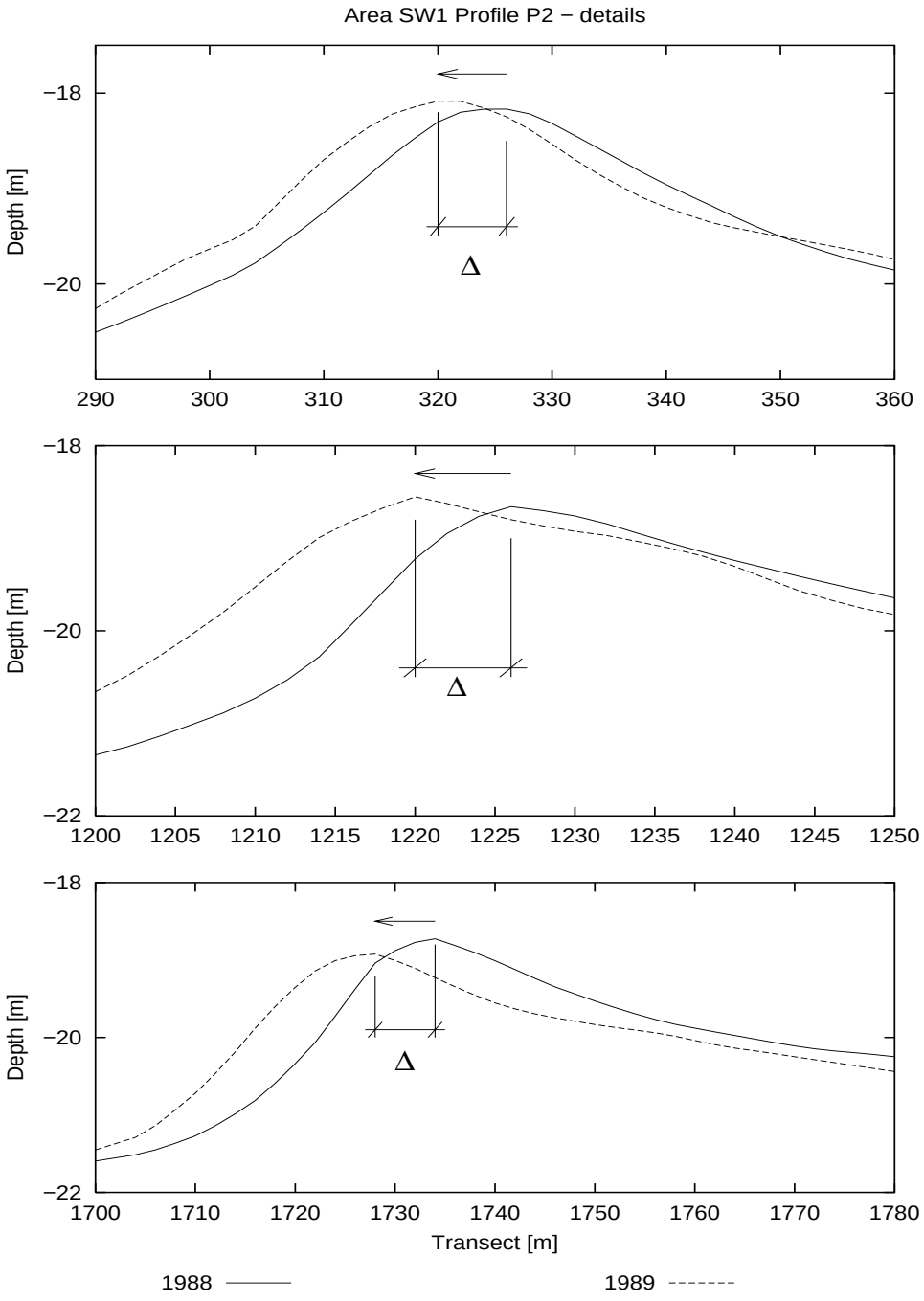

Figure 2.13: Details of sand wave profile in the area SW1 along transect P2.

1998; Calvete et al., 2001) and quite often comparisons between theoretical findings and laboratory and/or field observations are made considering just

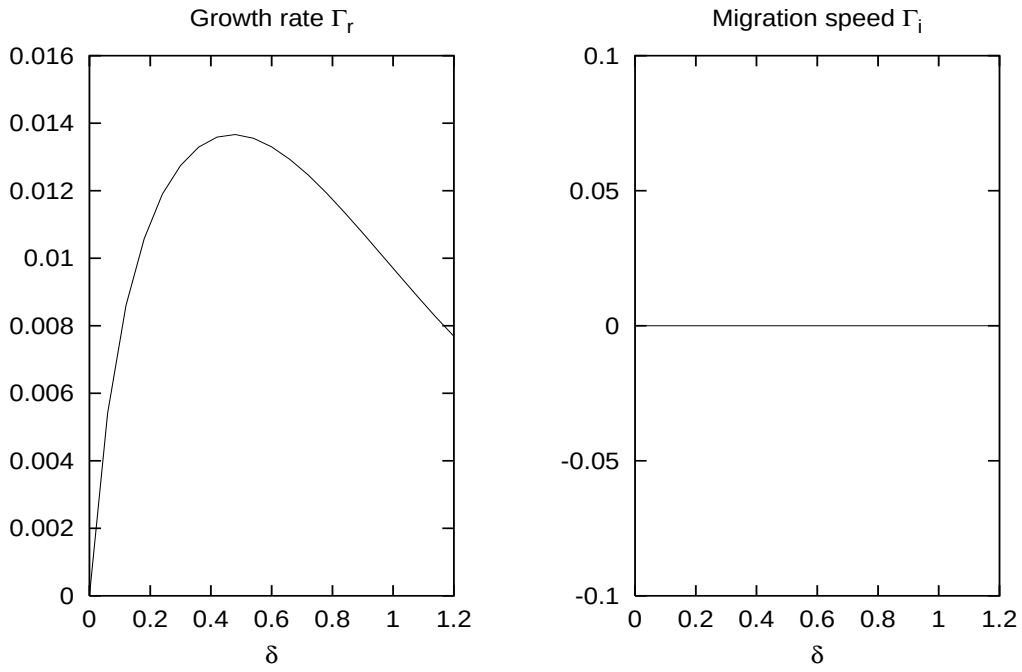

Figure 2.14: Generation sand waves in the area SW2 caused by M2 only: (a) dimensionless growth rate Γ_r, (b) dimensionless migration speed Γ_i. Model parameters are: $\hat{r} = 72$, $\gamma = 0.23$, $\mu = 4.86$ and $s = 0.77$.

the order of magnitude of the results or looking at their qualitative behaviour (see a.o. Vittori et al., 1999; Coco et al., 2000; Komarova & Hulscher, 2000; Komarova and Newell, 2000; Calvete & De Swart, 2003). In evaluating the predictions of the model, it should also be taken into account that the analysis is horizontally one-dimensional and therefore it cannot provide an exhaustive description of the phenomenon taking place in the area SW1 where a complex 2D current field is generated by tide propagation and bedforms of different characteristics are present.

A fair agreement between model predictions and field data is also found when the SW2 area is considered. The values of the model parameters are fixed, taking the average between those measured at station 9 and those measured at station 10, since SW2 is midway between the locations of the two current-metres. Figure **2.14** suggests that the most unstable mode is characterised by a wavenumber $\delta_{max} \approx 0.5$ giving a wavelength equal to $\mathcal{L} \approx$ 500m, not far from the observed value. According with field observations, the interaction between the M2, M4 and Z0 tidal constituents leads to negative

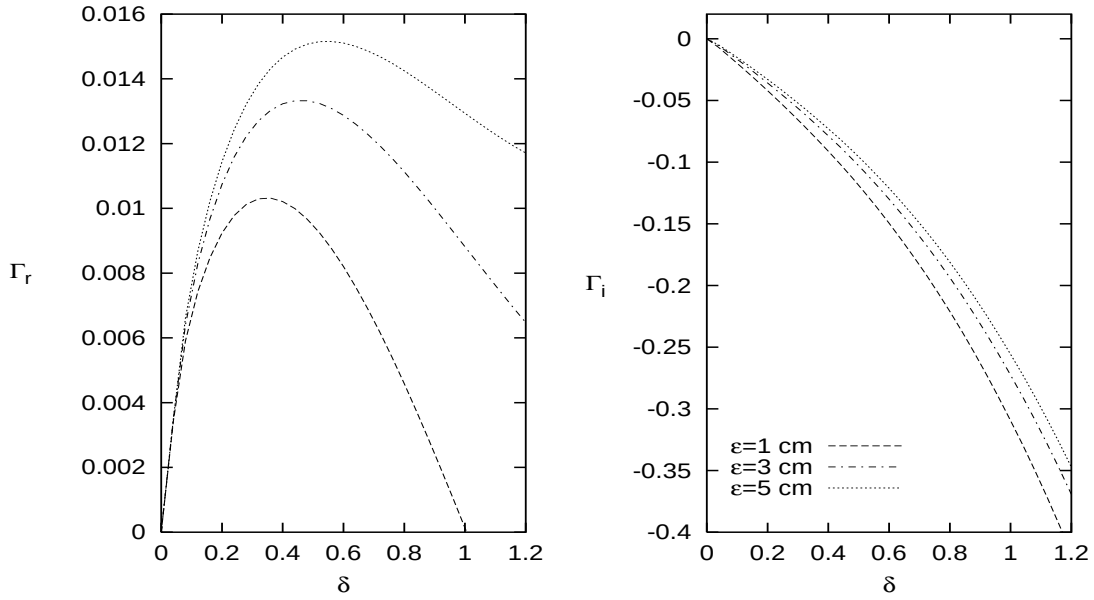

Figure 2.15: Influence of the roughness size ε on the (a) dimensionless growth rate Γ_r, (b) dimensionless migration speed Γ_i. Model parameters are: $\hat{r} = 92$, $\gamma = 0.23$, $\hat{U}_{0_m}/\hat{U}_{1_m} = 0.088$, $\hat{U}_{2_m}/\hat{U}_{1_m} = 0.072$ and $\phi = 118.5°$. The parameters s and μ vary in function of the roughness size ε, according to (1.8a,b) and (1.29).

values of Γ_i, i.e. to sand waves migration in the direction of the residual current which points from South to North. The predicted migration speed, which turns out to be of about 18m/year, overestimates the measured values which are of 1.5m/year and 1.8m/year along transects P1 and P2 respectively. The standard deviation of the measured values is about 5.7m/year along both transects.

For the sake of completeness, it is worth pointing out that both at SW1 and SW2 the bathymetric data measured from 1989 to 1995 indicate that sand waves keep migrating in the same direction as that measured from 1988 to 1989 and in particular the measured values are given in table 2.2 and 2.2. However, a comparison of these values with theoretical predictions is not possible because of the lack of hydrodynamic data for the period under consideration and in particular of the residual current data.

To conclude this section, we point out that the model requires the knowledge of the eddy viscosity A and of the stress parameter $\tilde{s}$. Presently A, and $\tilde{s}$ have been estimated using equations (1.8a,b) and assuming a roughness

height equal to 3cm which can be thought to be induced by the presence of sea ripples of medium size. Figure **2.15** shows the results analogous to those of figure **2.14** obtained for larger and smaller values of the roughness size. Quantitative differences can be observed, even though no qualitative change is present and the predicted values still fall close to the observed ones. Therefore it appears that reliable predictions of sand waves characteristics can be made without accurate information about the bottom roughness. On the other hand, notwithstanding the value of α does not affect the predicted wavelength of the most unstable sand waves, the migration rate is proportional to α (see (2.14)) and the evaluation of C_d requires reliable estimates of α.

2.7 Discussion and Conclusions

The present analysis supports the hypothesis that sand waves in tide-dominated coastal areas arise because of an inherent instability of the flat bottom configuration subject to tidal currents. The interaction of an oscillatory tidal current with a bottom perturbation gives rise to steady recirculation cells. When the steady streaming close to the bed is directed from the troughs toward the crests of the bottom perturbation and is strong enough to overcome gravity effects which tend to carry the sediment from the crests toward the troughs, the perturbation grows and gives rise to bottom patterns. The presence of a residual current induces a distortion of the spatial pattern of the recirculation cells which are no longer symmetric with respect to the crests and troughs of the sand waves. This distortion and loss of symmetry is the cause of sand wave migration. The loss of symmetry can also be caused by the presence of the M4 tide constituent. Although the current induced by the superposition of the M2 and M4 tide constituents has a vanishing time average, sediment and bedforms can be moved in a preferential direction because of the nonlinear relationship between the fluid velocity and the sediment transport. As in other theoretical analyses of the phenomenon (Gerkema, 2000; Komarova & Hulscher, 2000; Neḿeth et. al, 2002), the present model is based on the assumption of unidirectional tidal currents, even though field data show that the velocity field generated by a tidal constituent has a predominant direction but may have also a significant transverse velocity component. Moreover, the major axes of the tidal ellipses generated by different tidal constituents may have different orientations. Hence, when the model has been used to predict field conditions, the measured current data have been projected along the direction normal to the crests of sand waves. At location SW1 the direction of the transect P1 almost coincides with that of

the major axis of the M2 ellipse, while the residual current and the major axis of the M4 ellipse are rotated of about 30°. The transect P2 is almost aligned with the major axis of the M4 ellipse and the direction of the residual current while the major axis of the M2 tidal ellipse is rotated by about 30°. Similar values characterise the SW2 site. Taking into account that the direction of propagation of the tidal currents along the normal to sand waves crests differs from original value of an amount less than 15% ($\cos 30° \cong 0.87$) the use of the unidirectional model to investigate the field cases described in the paper appears appropriate.

Notwithstanding the simplified description of the hydrodynamics and of the sediment transport the present model predicts the formation of patterns characterised by wavelengths comparable with those observed in the field. Moreover, the model is able to predict the direction of sand waves migration and provides a reasonable estimate of the migration speed, even though a more refined model would be necessary to get migration speeds with an accuracy suitable for practical purposes.

Part II

A 3D model

Introduction to Part II

The bottom of shallow seas characterised by the presence of tidal currents and large deposits of sand exhibits a variety of regular morphological patterns of different length scales. The largest bedforms are the tidal sand banks described in general terms by Off (1963), Houbolt (1968) and, more recently, by Dyer & Huntley (1999). Sand banks are periodic forms with wavelengths ranging a few kilometres and heights up to one third of the water depth. The crests of the sand banks in the North Sea are usually slightly rotated counterclockwise ($10° - 30°$) with respect to the principal axis of the tidal ellipse and they hardly move. However, in the North Sea numerous examples of sand banks exist with the crests rotated clockwise with respect to the principal axis of the tidal ellipse, the Sandettie bank being a typical example (Belderson et al., 1982). At some locations smaller bedforms called sand waves are present. Wavelengths of these rhythmic features are of a few hundreds of metres while their heights are a few metres (Belderson et al., 1982). The profile of sand waves is symmetric unless either significant residual currents are present or the tidal wave itself is asymmetric. A striking characteristic of sand waves is that they are not static bed forms. Under the action of tidal currents they migrate, with their crests almost orthogonal to the direction of tide propagation, at a typical rate of about one to some tens of metres per year, (Fenster et al., 1990). This migration can be both in the direction of the residual current and against it (Besio et al., 2004). Tidal bedforms and in particular sand waves, can be classified as rhythmic features of great relevance to human activities (Dodd et al., 2003). Both the shipping industry (sand waves can migrate into shipping channels) and the oil industry (migrating sand waves can expose pipelines to both free-span generation and self-burial) are particularly interested by the presence/evolution of sand waves.

In the second part of this work a three-dimensional model is developed in order to study the appearance of both tidal sand waves and sand banks. In fact, in the study of the former, a two-dimensional model is sufficient to perform a first analysis of the growth and migration of the sand waves,

but it is not possible to get more information about the orientation of the crest in the horizontal plane. In order to investigate both the growth and the migration of the latter it is necessary to take into account the three-dimensional character of the tidal flow propagating over the bedforms due to the physical mechanism (described in the following) triggering the formation of these kinds of bedforms.

As already pointed out in part I, previous studies of the processes which lead to the formation of tidal sand banks and sand waves (Hulscher et al., 1993; Hulscher, 1996) have shown that these regular features arise as free instabilities of the system, describing the interaction between the sea bottom and the water motion induced by tide propagation.

The physical mechanism leading to the formation of tidal sand banks was first pointed out by Huthnance (1982a,b) and subsequently it was studied by Hulscher et al. (1993). As shown in these studies the Coriolis force and bottom frictional effects cause an oscillatory tidal flow, interacting with bottom forms characterised by crests rotated anticlockwise (in the Northern Hemisphere) with respect to the principal tide direction, to form clockwise horizontal residual circulation around the crests. Consequently, flow velocities on the upstream side of the crests are slightly higher than those on the downstream side. Since sediment transport increases with increasing velocities it follows that sediment will accumulate at the crests of the bottom waviness.

The formation of tidal sand waves, recently investigated by Hulscher (1996), Gerkema (2000), Komarova & Hulscher (2000), Besio et al. (2003) has strong analogies with the formation of coastal ripples (Blondeaux, 1990; Vittori & Blondeaux, 1990; Vittori & Blondeaux, 1992; Roos & Blondeaux, 2001) as tidal flows over a rhythmic sequence of sand waves produce steady streamings and a net displacement of the sediment. In this case the tidal excursion length (the distance travelled by a water particle in one tidal period) is of few kilometres, hence it is much larger than the sand wave length scale which is of the order of 100m. Furthermore, in the case of ripples, the thickness of the Stokes layer is much smaller than the water depth while in a tidal flow the effect of friction extends from the bottom up to the free surface.

Although significant progresses have been made in predicting the appearance of both tidal sand banks and sand waves, as well as in the prediction of their characteristics (see also De Vriend, 1990; Fredsøe & Deigaard, 1992; De Swart & Hulscher, 1995; Komarova & Newell, 2000), much remains to be done. In fact, to describe the tidal flow, simple hydrodynamic models are used in a manner that neglects important aspects of the phenomenon and simple sediment transport predictors are employed. One of the main limitation of the models comes from the very simple representation of the

flow close to the bottom. Turbulent stresses are usually accounted for by using Boussinesq hypothesis and by introducing an eddy viscosity which is assumed to be constant over the water depth. In actual flows, turbulent mixing tends to vanish close to a rigid wall. Hence, in the above models the wall layer is neglected and a partial slip condition at the bottom is introduced for the velocity. This approach neglects the strong velocity gradients which are present close to the bottom and are the main agents that drive the dynamics of the perturbations. Moreover, sediment transport is modelled only as bed load. In the actual phenomenon, the suspended load transport influences the process of generation and growth of tidal bedforms, particularly when the bottom is made of fine sediment.

The aim of the present contribution is to use a more sophisticated and complete model capable of giving a more reliable description of the process leading to the formation of tidal sand banks and sand waves as well as more accurate predictions of their characteristics. Turbulence generated by tidal currents is described by introducing an eddy viscosity coefficient which is assumed to increase linearly with the distance from the bottom in the region close to the sea bed, to reach a maximum and to decrease and assume small values close to the free surface. Sediment is supposed to move as both bed load and suspended load since field surveys show that large amounts of sediment are put into suspension and transported by tidal currents. In this contribution are also considered the sediment motions induced by surface gravity waves. Finally, residual (steady) currents are taken into account because their presence is essential to explain sand wave migration.

The model is based on the study of the stability of the flat bottom configuration. Small bottom perturbations are considered and a linear analysis of their growth is performed. Since the morphodynamic time scale is much longer than the hydrodynamic time scale, it is possible to decouple the problem of flow determination from that of analysing the bottom profile time development. Thus, the problem is reduced to determining the flow field induced by the interaction of the tidal wave with a bottom waviness and then studying the time development of the amplitude of a generic spatial Fourier component of the bottom perturbation which turns out to be periodic in the two horizontal directions. The results show that the model can describe both the process which gives rise to sand waves and that which leads to the formation of sand banks. The former bedforms have their crests normal to the direction of the tidal current and are characterised by wavelength of $O(10^2$ m). The latter bedforms have wavelengths of $O(10^4$ m) and turn out to be rotated slightly counterclockwise or clockwise with respect to the direction of propagation of the tidal current depending of the direction of rotation of the tidal wave. A comparison of the theoretical results with field observa-

tions supports the model findings. As a matter of fact, model predictions are successfully compared with field data of different sand banks (Le Bot et al., 2000) and sand waves measured at different locations in the North Sea.

Chapter 3

A 3D Model

3.1 Formulation of the problem

We consider a shallow sea of small depth h^* (15-70m) which extends indefinitely in the horizontal directions (herein 'indefinitely' means distances much larger than the horizontal extent of the area we are considering which scales with the typical wavelength of bottom forms under investigation): the x^*-axis is along the parallels pointing East, the y^*-axis points North along the meridian line and the z^*-axis is vertical pointing upward (see figure **3.1**). As pointed out in the Introduction, the aim of the work is to determine the time development of perturbations of the flat bottom configuration forced by tidal currents. The seabed is supposed to be made of a cohesion-less sediment of uniform size d^* and density of the water ρ_s^* (from here on, a star will denote dimensional quantities).

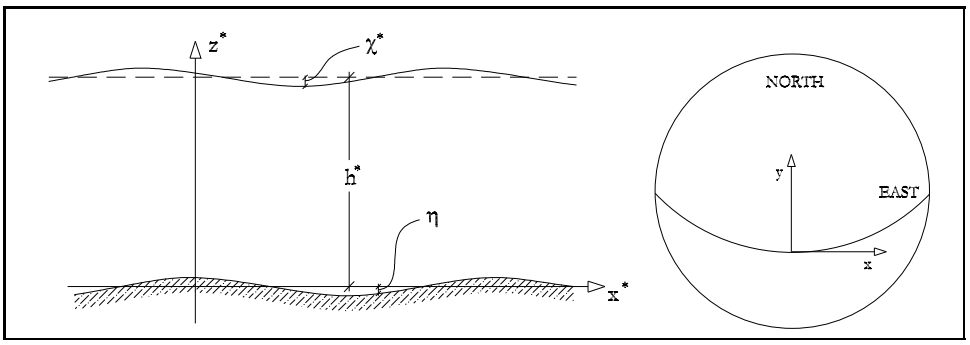

Figure 3.1: Definition sketch of the dimensional model geometry.

By using the f-plane approximation (see for example LeBlond & Mysak, 1978), the problem of flow determination is posed in terms of continuity and momentum equations where the Coriolis contributions related to the Earth's

rotation (Ω^* is the angular velocity of the Earth's rotation and φ_0 is the local latitude) are taken into account because they affect tide propagation. The flow regime is assumed to be turbulent and viscous effects are neglected. An exhaustive analysis of turbulence properties in tidal currents is provided in the review paper by Soulsby (1983). The field measurements of Heather Shaw (1979), Bowden & Ferguson (1980), Soulsby (1980), Soulsby (1981) and Soulsby & Dyer (1981) show that turbulence can be fairly assumed to be isotropic. Hence using the Boussinesq hypothesis to model Reynolds stresses, a scalar kinematic eddy viscosity ν_t^* is introduced.

3.1.1 The hydrodynamic problem

The hydrodynamics of the problem, due to the propagation of the tides, is described by continuity and momentum equations which read

$$\nabla \cdot \mathbf{u}^* = 0 \tag{3.1}$$

$$\frac{\partial \mathbf{u}^*}{\partial t^*} + (\mathbf{u}^* \cdot \nabla)\mathbf{u}^* = -\frac{1}{\rho^*}\nabla p^* + \nabla \cdot (\nu_t^* 2\mathcal{D}^*) - \mathcal{C}^* + \mathbf{g}^* \tag{3.2}$$

where $\mathbf{u}^* = (u^*, v^*, w^*)$ are the horizontal and vertical velocity components and p^* is the pressure averaged over turbulence The operator ∇ is defined by $(\partial/\partial x^*, \partial/\partial y^*, \partial/\partial z^*)$, where x^* and y^* are two horizontal axes lying on the bottom of the sea, while z^* is the vertical coordinate pointing upward. Moreover, the density ρ^* is assumed to be constant in space and in time and $\mathcal{D}^*$ is the strain rate tensor. The terms $\mathcal{C}^*$ and $\mathbf{g}^*$ represent the Coriolis and the gravity effects respectively:

$$\mathcal{C}^* = \left[2\Omega^* \left(w^* \cos\varphi_0 - v^* \sin\varphi_0\right), 2\Omega^* u^* \sin\varphi_0, -2\Omega^* u^* \cos\varphi_0\right] \tag{3.3}$$

$$\mathbf{g}^* = [0, 0, -g^*] \tag{3.4}$$

where Ω^* is the value of the angular velocity of the Earth's rotation, φ_0 is the latitude of the location we are considering and g^* is the gravity acceleration. In (3.1)-(3.2) the flow regime is assumed to be turbulent and viscous effects are neglected.

Introducing the following dimensionless variables

$$(x, y, z) = (x^*, y^*, z^*)/h_0^* \quad ; \quad (u, v, w) = (u^*, v^*, w^*)/U_0^* \tag{3.5a,b}$$

$$\Omega = \Omega^*/\sigma^* \quad ; \quad t = \sigma^* t^* \quad ; \quad p = p^*/\rho^* U_0^* \sigma^* h_0^* \tag{3.6a,b,c,d}$$

(h_0^* is the local averaged water depth, t^* is time, σ^* is the angular frequency of the tide and U_0^* is the maximum value of the depth averaged fluid velocity during the tidal cycle), it is possible to write the equations in the form

$$\frac{\partial u}{\partial x}+\frac{\partial v}{\partial y}+\frac{\partial w}{\partial z}=0 \tag{3.7}$$

$$\frac{\partial u}{\partial t}+k_c\left[u\frac{\partial u}{\partial x}+v\frac{\partial u}{\partial y}+w\frac{\partial u}{\partial z}\right]=-\frac{\partial p}{\partial x}+\frac{1}{\mu}\left\{\frac{\partial}{\partial x}\left[2\nu_t\frac{\partial u}{\partial x}\right]+\frac{\partial}{\partial y}\left[\nu_t\left(\frac{\partial u}{\partial y}+\frac{\partial v}{\partial x}\right)\right]+\frac{\partial}{\partial z}\left[\nu_t\left(\frac{\partial u}{\partial z}+\frac{\partial w}{\partial x}\right)\right]\right\}-2\Omega\left[w\cos\varphi_0-v\sin\varphi_0\right] \tag{3.8}$$

$$\frac{\partial v}{\partial t}+k_c\left[u\frac{\partial v}{\partial x}+v\frac{\partial v}{\partial y}+w\frac{\partial v}{\partial z}\right]=-\frac{\partial p}{\partial y}+\frac{1}{\mu}\left\{\frac{\partial}{\partial x}\left[\nu_t\left(\frac{\partial u}{\partial y}+\frac{\partial v}{\partial x}\right)\right]+\frac{\partial}{\partial y}\left(2\nu_t\frac{\partial v}{\partial y}\right)+\frac{\partial}{\partial z}\left[\nu_t\left(\frac{\partial v}{\partial z}+\frac{\partial w}{\partial y}\right)\right]\right\}-2\Omega u\sin\varphi_0 \tag{3.9}$$

$$\frac{\partial w}{\partial t}+k_c\left[u\frac{\partial w}{\partial x}+v\frac{\partial w}{\partial y}+w\frac{\partial w}{\partial z}\right]=-\frac{\partial p}{\partial z}+\frac{1}{\mu}\left\{\frac{\partial}{\partial x}\left[\nu_t\left(\frac{\partial u}{\partial z}+\frac{\partial w}{\partial x}\right)\right]+\frac{\partial}{\partial y}\left[\nu_t\left(\frac{\partial v}{\partial z}+\frac{\partial w}{\partial y}\right)\right]+\frac{\partial}{\partial z}\left(2\nu_t\frac{\partial w}{\partial z}\right)\right\}+2\Omega u\cos\varphi_0-\frac{g^*}{U_0^*\sigma^*} \tag{3.10}$$

where the kinematic eddy viscosity ν_t^* is written as the product $\nu_{t0}^*\nu_t$. The constant ν_{t0}^* is dimensional and provides the order of magnitude of the eddy viscosity while $\nu_t=\nu_t(x,y,z,t)$ is a dimensionless function (of order 1) describing the spatial and temporal variations of the turbulence structure. In (3.7)-(3.10) two dimensionless parameters appear which we denote by k_c and μ respectively:

$$k_c=\frac{U_0^*}{h_0^*\sigma^*}\quad,\qquad \mu=\frac{\sigma^*h_0^{*2}}{\nu_{t0}^*}\quad. \tag{3.11a,b}$$

The parameter k_c is a kind of Keulegan-Carpenter number and is the ratio between the amplitude of fluid displacement oscillations induced in the horizontal direction by the tidal wave and the local depth. Actual values of k_c are much larger than one, let us say of order 10^2. The parameter μ represents the ratio between the thickness of the viscous bottom boundary layer generated by the tidal wave and the local depth. A rough estimate of μ shows that its typical magnitude is of order one. Finally, Ω is the ratio between the angular velocity of the Earth rotation and the angular frequency of the tidal wave. For a semi-diurnal tide $\Omega\cong 0.5$ while for the diurnal tide component $\Omega\cong 1$.

The hydrodynamic problem is then closed by forcing appropriate boundary conditions and providing the function ν_t^*. The boundaries in the horizontal directions are assumed to be infinitely far away, while the dynamic boundary condition in the vertical direction forces the vanishing of the stresses at the free surface described by the equation

$$F = z - h_0 - \chi(x, y, t) = 0 \tag{3.12}$$

where χ is the free surface elevation. Hence for $z = h_0 + \chi$

$$-\frac{\partial \chi}{\partial x}\left(-p\frac{\mu}{\nu_t} + 2\frac{\partial u}{\partial x}\right) - \frac{\partial \chi}{\partial y}\left(\frac{\partial u}{\partial y} + \frac{\partial v}{\partial x}\right) + \left(\frac{\partial w}{\partial x} + \frac{\partial u}{\partial z}\right) = 0 \tag{3.13a}$$

$$-\frac{\partial \chi}{\partial x}\left(\frac{\partial u}{\partial y} + \frac{\partial v}{\partial x}\right) - \frac{\partial \chi}{\partial y}\left(-p\frac{\mu}{\nu_t} + 2\frac{\partial v}{\partial y}\right) + \left(\frac{\partial w}{\partial y} + \frac{\partial v}{\partial z}\right) = 0 \tag{3.13b}$$

$$-\frac{\partial \chi}{\partial x}\left(\frac{\partial u}{\partial z} + \frac{\partial w}{\partial x}\right) - \frac{\partial \chi}{\partial y}\left(\frac{\partial w}{\partial y} + \frac{\partial v}{\partial z}\right) + \left(-p\frac{\mu}{\nu_t} + 2\frac{\partial w}{\partial z}\right) = 0 \quad . \tag{3.13c}$$

The kinematic boundary condition forces

$$\frac{\partial F}{\partial t} = w - \frac{\partial \chi}{\partial t} - u\frac{\partial \chi}{\partial x} - v\frac{\partial \chi}{\partial y} = 0 \qquad \text{at} \qquad z = h_0 + \chi \quad . \tag{3.14}$$

Because the tidal period is much larger than the turbulence time scale, the flow induced by the tide propagation can be assumed to be slowly varying in time. Hence, as in steady flows, a boundary condition is specified at the bottom by imposing the vanishing of the velocity at a distance from the seabed equal to a fraction of the roughness z_r^*:

$$u = 0 \ , \quad v = 0 \ , \quad w = 0 \qquad \text{at} \qquad z = z_r/\mathcal{X} \quad . \tag{3.15a,b,c}$$

In (3.15) the constant $\mathcal{X}$ has been chosen equal to 29.8 by analysing data of steady velocity profiles (see a.o. Fredsøe & Deigaard, 1992). Moreover z_r is a dimensionless roughness parameter equal to z_r^*/h_0^*, z_r^* being the size of the bottom roughness.

For later convenience, the dynamic pressure P is introduced such that

$$p = P - \frac{g^*}{U_0^*\sigma^*}(z-1) + \frac{g^*}{U_0^*\sigma^*}\chi \quad . \tag{3.16}$$

When (3.16) is substituted into equations (3.7)-(3.10), the dynamic pressure P replaces p. Moreover, the extra-terms

$$-\frac{g^*}{U_0^*\sigma^*}\frac{\partial \chi}{\partial x} \quad ; \quad -\frac{g^*}{U_0^*\sigma^*}\frac{\partial \chi}{\partial y}$$

appear in the right-hand side of (3.8) and (3.9), respectively, while in (3.10) the gravitational term $-g^*/(U_0^*\sigma^*)$ disappears.

The hydrodynamic problem is finally closed providing an eddy viscosity model. The eddy viscosity ν_{tc}^*, which is assumed to be time-independent, is presently assumed to be provided by

$$\nu_{tc}^* = \kappa c_1 \frac{U_0^* h_0^*}{C} F(\xi) \quad . \tag{3.17}$$

In (3.17) κ is the Von Karman constant, being equal to 0.41, and the eddy viscosity is assumed to be proportional to the time average of the local friction velocity $\bar{u}_\tau^*$ and to the local depth h_0^*. The average friction velocity is related to U_0^* by introducing the constant c_1 which ranges between 0.65 and 1.0 (when the lower value of c_1 is chosen, the shear velocity is indeed related to the time averaged value of the tidal velocity; when the higher value is fixed, the shear velocity is related to the maximum value of the tidal velocity) and the friction factor C which only depends on the dimensionless roughness z_r, since the Reynolds number of the flow is assumed to be large. Standard formulae for steady currents can be used to evaluate C (see a.o Fredsøe and Deigaard, 1992)

$$C = 5.75 \log_{10} \left(\frac{10.9 h_0^*}{z_r^*} \right) \quad . \tag{3.18}$$

The function $F(\xi)$ describes the vertical structure of the eddy viscosity and has been chosen, as suggested by Dean (1974), such that the eddy viscosity grows linearly with the distance from the bed, when a region close to the bottom is considered, and then decreases achieving a finite small value at the free surface:

$$F(\xi) = \frac{\xi(1-\xi)}{1 + 2A\xi^2 + 3B\xi^3} \tag{3.19}$$

where A=1.84, B=-1.56 and ξ is defined as

$$\xi = \frac{z^* - \chi^*}{h^* + \chi^*} \quad . \tag{3.20}$$

A time constant value of ν_{tc}^* may appear a strong approximation. However, it is worth pointing out that, as shown by Blondeaux & Vittori (2004a) and Blondeaux & Vittori (2004b), a time independent eddy viscosity model provides a fair description of the phenomenon because it fails only around flow reversal, when tidal currents are very weak and the transport of any quantity, and in particular of sediment particles, tends to vanish. Therefore, the morphodynamic consequences of such an assumption are negligible. Finally, the eddy viscosity is written in the form $\nu_{tc}^* = \nu_{t0}^* \nu_{tc}(\xi)$ where ν_{t0}^* is

equal to

$$\nu_{t0}^* = \kappa U_0^* h_0^* \int_{-1}^{0} \frac{F(\xi)}{C} d\xi \tag{3.21}$$

and

$$\nu_{tc}(\xi) = F(\xi) / \int_{-1}^{0} F(\xi) d\xi \quad . \tag{3.22}$$

These definitions of ν_{t0}^* and ν_{tc} have been chosen in such a way that the depth average value of $\nu_{tc}(\xi)$ is equal to one.

Since (3.17) shows that ν_{t0}^* is proportional to U_0^*, for later convenience, it is useful to introduce the new viscous parameter

$$\hat{\mu} = \frac{C}{\kappa \int_{-1}^{0} F(\xi) d\xi} = \mu k_c \quad . \tag{3.23}$$

3.1.2 The morphodynamic problem

The morphodynamics is governed by the sediment continuity equation which simply states that convergence (or divergence) of the sediment flux must be accompanied by a rise (or fall) of the bed profile

$$\frac{\partial \eta}{\partial T} + \frac{\partial Q_x}{\partial x} + \frac{\partial Q_y}{\partial y} = 0 \tag{3.24}$$

where $(Q_x, Q_y) = (Q_x^*, Q_y^*) / \sqrt{(\rho_s^*/\rho^* - 1)\, g^* d^{*3}}$ are the dimensionless volumetric sediment transport rates per unit width in the x- and y-directions respectively. In (3.24) has been used the following dimensionless morphodynamic time scale

$$T = \frac{td}{\sqrt{\hat{\psi}_d}\,(1 - p_{or})} \tag{3.25}$$

in order to take into account that the time scale of the bottom configuration changes is much larger than the tide period. In (3.25) p_{or} is the sediment porosity, d is the dimensionless sediment size which, along with the mobility number $\hat{\psi}_d$ and the particle Reynolds number R_p, characterises the sediment particles:

$$d = \frac{d^*}{h_0^*} \quad , \qquad \hat{\psi}_d = \frac{(\sigma^* h_0^*)^2}{(\rho_s^*/\rho^* - 1) g^* d^*} \quad , \qquad R_p = \frac{\sqrt{(\rho_s^*/\rho^* - 1) g^* d^{*3}}}{\nu^*} \quad . \tag{3.26a,b,c}$$

The problem is closed once relationships for Q_x^* and Q_y^* are provided. Since the tide period is much larger than the turn-over time of turbulent

eddies, the sediment transport rate can be predicted by formulae proposed for steady currents specified with the actual values of the parameters.

Sediment transport is usually split into two components. The former is due to sediment which moves close to the bottom (the "bed load") while the latter is due to sediment which is carried in suspension (the "suspended load"). Presently the approach proposed by Van Rijn (1984a,b) is used to evaluate the two contributions. In particular, an empirical formula is used to quantify the bed load while the suspended load is evaluated by determining the concentration profile and then computing the sediment flux. The bed load (Q^*_{bx}, Q^*_{by}) due to the tidal current can be evaluated by means of the relationship:

$$(Q_{bx}, Q_{by}) = \frac{(Q^*_{bx}, Q^*_{by})}{\sqrt{\left(\frac{\rho^*_s}{\rho^*} - 1\right) g^* d^{*3}}} = \frac{0.25}{R_p^{0.2}} \left(\frac{\theta_{cw} - \theta_{cr}}{\theta_{cr}}\right)^{1.5} \frac{(\theta_{cx}, \theta_{cy})}{\sqrt{\theta_c}} \qquad (3.27)$$

In (3.27) θ_{cx} and θ_{cy} are the $x-$ and $y-$ components of the Shields parameter due to the tidal current defined as

$$(\theta_{cx}, \theta_{cy}) = \frac{(\tau^*_x, \tau^*_y)}{(\rho^*_s - \rho^*) g^* d^*} \qquad (3.28)$$

where (τ_x, τ_y) are the dimensional shear stress components, which can be easily evaluated by means of the constitutive law. Moreover θ_c is equal to $\sqrt{\theta^2_{cx} + \theta^2_{cy}}$ and θ_{cr} is the critical value of the Shields parameter characterising the sediment. Finally, θ_{cw} represents the algebraic sum of the dimensionless shear stress θ_c induced by the tidal current and the maximum dimensionless shear stress θ_w induced by the waves and acting along the direction of wave propagation which is assumed to form an angle β_w with the $x-$axis

$$\theta_{cw} = \theta_c + \theta_w \quad . \qquad (3.29)$$

The value of θ_w can be evaluated by the empirical relationship (Van Rijn, 1991)

$$\theta_w = 0.15 \frac{k_c^2 \hat{\psi}_d}{R_p^{2/3}} f_w \left(\frac{\hat{U}^*_\delta}{U^*_0}\right)^2 \qquad (3.30)$$

where f_w is the wave friction factor which depends on the bottom roughness size

$$f_w = \exp\left[-6 + 5.2 \left(\frac{\hat{U}^*_\delta}{U^*_0} \frac{k_c}{z_r}\right)^{-0.19}\right] \qquad (3.31)$$

and its maximum value is assumed equal to $f_w^{max} = 0.3$. $\hat{U}_\delta^*$ is the peak value of the near-bed orbital velocity induced by the waves which can be easily evaluated once the height H^* and the period T^* of the sea waves are fixed.

In the case of combined currents and waves, even when the linear theory is used to describe the wave motion and the induced oscillatory flow turns out to be symmetric, a net time average wave-related sediment transport $\boldsymbol{Q}_w^* = (Q_{wx}^*, Q_{wy}^*)$ exists which should accounted for. Following Van Rijn (1991), it can be assumed that the direction of $\boldsymbol{Q}_w^*$ is that of wave propagation, which forms an angle β_w with the x-axis, and the amount of the sediment transport rate is the difference between Q_w^{*+} and Q_w^{*-}, where Q_w^{*+} and Q_w^{*-} are the time average transport rates over half the wave period

$$Q_w^{\pm} = \frac{Q_w^{*\pm}}{\sqrt{\left(\frac{\rho_s^*}{\rho^*} - 1\right) g^* d^{*3}}} = 0.03 \frac{\sqrt{\hat{\psi}_d}}{R_p^{0.2}} \frac{\hat{U}_\delta^*}{U_0^*} \left(\frac{\theta^{\pm} - \theta_{cr}}{\theta_{cr}}\right)^{1.5} \quad . \tag{3.32}$$

The wave Shields parameters $\theta^{\pm}$ are defined by

$$\theta^{\pm} = \sqrt{(\theta_{cx} \pm \theta_{wx})^2 + (\theta_{cy} \pm \theta_{wy})^2} \quad . \tag{3.33}$$

To complete the description of the sediment transport, it is necessary to account for the weak effects associated with a slow spatial variation of the bottom topography, which affects the bed load sediment transport. Assuming that the bottom slope $\nabla\eta$ is small, simple dimensional arguments coupled with linearization lead to the following contribution

$$(Q_{px}, Q_{py}) = -(Q_b + Q_w)\boldsymbol{G} \cdot \nabla\eta \tag{3.34}$$

where $\mathbf{G}$ is a dimensionless second order 2-D tensor. Experimental observations of various authors (a.o. Talmon et al., 1995) provide estimates for the components of $\mathbf{G}$. In the intrinsic orthogonal coordinate system (s, n), with s aligned with the average bottom stress, such estimates read:

$$G_{ss} = -\frac{\theta_{cr}}{\bar{\mu}} \frac{dQ_b}{d\theta_c} \tag{3.35}$$

$$G_{sn} = G_{ns} = 0 \tag{3.36}$$

$$G_{nn} = -\frac{rQ_b}{\sqrt{\theta_c}} \tag{3.37}$$

where $\bar{\mu}$ is equal to the dynamic friction coefficient of the sediment and r is an empirical factor roughly about $0.5 - 0.6$ (Talmon et al., 1995).

Finally, the suspended sediment transport (Q^*_{sx}, Q^*_{sy}) is evaluated computing the concentration $c = c(x, y, z, t)$ by solving a standard convection-diffusion equation:

$$\frac{1}{k_c}\frac{\partial c}{\partial t} + u\frac{\partial c}{\partial x} + v\frac{\partial c}{\partial y} + w\frac{\partial c}{\partial z} - \frac{w_s}{k_c\sqrt{\hat{\psi}_d}}\frac{\partial c}{\partial z} = \frac{1}{\hat{\mu}}\left\{\frac{\partial}{\partial x}\left(\nu_t\frac{\partial c}{\partial x}\right) + \frac{\partial}{\partial y}\left(\nu_t\frac{\partial c}{\partial y}\right) + \frac{\partial}{\partial z}\left(\nu_t\frac{\partial c}{\partial z}\right)\right\} \tag{3.38}$$

where w_s is the dimensionless particle fall velocity defined by

$$w_s = \frac{w^*_s}{\sqrt{\left(\frac{\rho^*_s}{\rho^*} - 1\right) g^* d^*}} \quad . \tag{3.39}$$

The settling velocity of the sediment can be derived from a balance between the gravitational force acting on a sediment grain and the drag force exerted by the surrounding fluid. If the latter is expressed in terms of a drag coefficient, it turns out that the fall velocity depends on the sediment Reynolds number.

Suitable boundary conditions must be provided at the seabed and at the free surface. The free surface boundary condition states that the sediment flux in the normal-to-surface direction $\hat{n}$ must vanish:

$$\left(\mathcal{D}^*_t \nabla c + w^*_s c\hat{k}\right) \cdot \hat{n} = 0 \qquad \text{at} \quad z = h + \chi \tag{3.40}$$

where $\hat{k}$ is the unit vector in the vertical direction and $\hat{n}$ is the unit vector normal to the free surface. In (3.40), the diffusion coefficient D^*_t of sediment particles is assumed to be equal to the diffusion of fluid momentum. According to the data analysed by Van Rijn (1984b), in a turbulent flow the centrifugal forces on the sediment particles (which are of higher density) are greater than those on the fluid particles, thereby causing the sediment particles to be thrown to the outside of the eddies with a consequent increase of the diffusion rate. However, it is worth pointing out that other investigators have concluded that the sediment particles cannot respond fully to the turbulent velocity fluctuations and hence the diffusion rate of particles is smaller than that of fluid momentum. Therefore, because of the large uncertainty, to make morphological predictions it is possible to approximate D^*_t with ν^*_t.

A more articulated description is required for the bottom boundary condition. This is a Dirichlet-type boundary condition and prescribes a reference

concentration c_{ζ^*} at a given distance ζ^* off the seabed. Following Van Rijn (1984b) an expression for c_{ζ^*} is used which is valid for slowly-varying flows:

$$c_{\zeta^*} = 0.015 \frac{d^*}{\zeta^* R_p^{0.2}} \left(\frac{\theta_{cw} - \theta_{cr}}{\theta_{cr}} \right)^{3/2} \quad . \tag{3.41}$$

The reference distance from the sea bed is chosen to be $\zeta^* = 0.01 h_0^*$, though in general ζ^* is related also to the bottom roughness. However, ζ^* depends on the bottom roughness only when the latter is not smaller than $0.01 h_0^*$ as in the case under consideration.

Once the concentration c is obtained by solving (3.38) subject to (3.40) and (3.41), the suspended sediment transport Q_s^* is found as the integral of the horizontal flux of concentration over the water column:

$$(Q_{sx}, Q_{sy}) = \frac{(Q_{sx}^*, Q_{sy}^*)}{\sqrt{\left(\frac{\rho_s^*}{\rho^*} - 1 \right) g^* d^{*3}}} = \frac{k_c \sqrt{\hat{\psi}_d}}{d} \int_{\eta+\zeta}^{\chi} (u, v)\, c \;\; dz \quad . \tag{3.42}$$

3.2 The basic flow

The solution of the problem for arbitrary functions h^* is a difficult task. However, in the present analysis small perturbations of the flat bottom configuration are considered. Thus, the bottom configuration differs from the flat one of a small amount proportional to ϵ, this being a small (strictly infinitesimal) quantity. Therefore the bottom configuration can be thought to be given by the superposition of different spatial components which evolve one independently from the other. A normal mode analysis can be performed and the problem can be solved for the generic spatial component.

$$\eta = \epsilon \Pi(t) e^{i(\delta_x x + \delta_y y)} + c.c. + O(\epsilon^2) \tag{3.43}$$

where $\Pi(t)$ is the amplitude of the generic component which is periodic in the x- and y-directions with wavenumbers δ_x and δ_y respectively and $\epsilon << 1$. The small value of ϵ allows for the solution to be expanded in terms of ϵ. Additionally, an analysis of the order of magnitude of the different terms in continuity and momentum equations shows that it is convenient to assume

$$[u, v, w, p, \chi, c] = \left[u_b, v_b, \frac{h_0^*}{L^*} w_b, \frac{L^*}{h_0^*} P_b, \frac{a^*}{h_0^*} e_b, c_b \right] +$$
$$\epsilon \left[u_1, v_1, w_1, k_c P_1, \left(\frac{a^*}{h_0^*} \right)^2 e_1, c_1 \right] \Pi(t) e^{i(\delta_x x + \delta_y y)} + c.c. + O(\epsilon^2) \quad . \tag{3.44}$$

At the leading order of approximation, i.e. $O(\epsilon^0)$, the bottom turns out to be flat and the problem is reduced to the determination of both the flow and sediment transport induced by tide propagation over a flat seabed.

The scaling used in the previous section to define the dimensionless variables is appropriate for studying the flow induced by the interaction of a tidal wave with bedforms which are characterised by a length scale of the same order of magnitude of water depth h_0^*. In this case the three velocity components are expected to be of the same order of magnitude. When a tidal wave propagating over a flat bottom is considered, the most appropriate horizontal length scale turns out to be

$$L^* = \frac{\sqrt{g^* h_0^*}}{\sigma^*} \quad . \tag{3.45}$$

Since the ratio h_0^*/L^* is much smaller than one, an analysis of the order of magnitude of the different terms in the continuity equation suggests that the vertical velocity component is of order $h_0^* U_0^*/L^*$. Similarly, the kinematic condition at the free surface suggests that χ^* is of order a^*, where $a^* = U_0^* h_0^*/(\sigma^* L^*)$ is related to the amplitude of the tidal wave. Finally, the momentum equation shows that the dynamic pressure P^* is of order $\rho^* U_0^* \sigma^* L^*$. The above order of magnitude analysis along with the assumptions

$$\frac{h_0^*}{L^*} \ll 1 \quad , \quad \frac{a^*}{h_0^*} \ll 1. \tag{3.46a,b}$$

justify (3.44). Then, in order to determine the flow induced by tide propagation, it is appropriate to introduce the slow spatial coordinates

$$X = \frac{h_0^*}{L^*} x \ , \qquad Y = \frac{h_0^*}{L^*} y \quad . \tag{3.47a,b}$$

The solution at the leading order of approximation is supposed to be given by the sum of the main tide constituent ($n = 1$) plus super-harmonics components ($n > 1$) and a steady part ($n = 0$)

$$(u, v, w, P, \chi) = \sum_{n=0}^{N} \left(u_b^{(n)}, v_b^{(n)}, \frac{h_0^*}{L^*} w_b^{(n)}, \frac{L^*}{h_0^*} P_b^{(n)}, \frac{a^*}{h_0^*} e_b^{(n)} \right) e^{-int} + c.c. \tag{3.48}$$

Substituting (3.48) into equations (3.7)-(3.10) and into boundary conditions (3.13)-(3.15), and making the problem dimensionless, we obtain

$$\frac{\partial u_b^{(n)}}{\partial X} + \frac{\partial v_b^{(n)}}{\partial Y} + \frac{\partial w_b^{(n)}}{\partial z} = 0 \tag{3.49}$$

$$\frac{k_c}{\hat{\mu}}\frac{\partial}{\partial z}\left[\nu_{t0}\frac{\partial u_b^{(n)}}{\partial z}\right] + 2\Omega v_b^{(n)}\sin\varphi_0 + inu_b^{(n)} - \frac{\partial P_b^{(n)}}{\partial X} = \frac{\partial e_b^{(n)}}{\partial X} \quad (3.50)$$

$$\frac{k_c}{\hat{\mu}}\frac{\partial}{\partial z}\left[\nu_{t0}\frac{\partial v_b^{(n)}}{\partial z}\right] - 2\Omega u_b^{(n)}\sin\varphi_0 + inv_b^{(n)} - \frac{\partial P_b^{(n)}}{\partial Y} = \frac{\partial e_b^{(n)}}{\partial Y} \quad (3.51)$$

$$\frac{\partial P_b^{(n)}}{\partial z} = 0 \quad (3.52)$$

along with the boundary conditions at the free surface

$$P_b^{(n)} = 0 \;\;,\quad \frac{\partial u_b^{(n)}}{\partial z} = \frac{\partial v_b^{(n)}}{\partial z} = 0 \;\;,\quad e_b^{(n)} = inw_b^{(n)} \quad \text{at} \;\; z = 0 \;\; (3.53\text{a,b,c,d})$$

and close to the bottom

$$u_b^{(n)} = v_b^{(n)} = w_b^{(n)} = 0 \;\;,\quad \text{at} \;\; z = \frac{z_r}{\mathcal{X}} \quad . \quad (3.54\text{a,b,c})$$

In (3.49)-(3.52) the eddy viscosity has been split into a contribution of order one and a contribution of order ϵ as shown by (3.73).

Of course, to find the solution of the above problem it would be necessary to provide conditions at the boundary of the area of interest in the (x, y)-plane and to remove the assumption of a constant water depth. Indeed, on the length scale of the tide the bottom configuration can nearly be assumed flat. However, the horizontal structure of the tidal wave is not of interest here, as bedforms are characterised by a wavelength which is much smaller than that of the tidal wave. Hence, equation (3.49) is not considered and equations (3.50)-(3.52) are used to find the vertical structure of the velocity field for given characteristics of the tidal ellipse (orientation with respect to the $x-$axis, eccentricity, etc.). Indeed, from (3.52) $P_b^{(n)}$ is found to be constant and the first of the boundary conditions (3.53) forces $P_b^{(n)}$ to vanish. Then equations (3.50) and (3.51) can be locally solved in the vertical direction for fixed values of the complex constants

$$\frac{\partial e_b^{(n)}}{\partial X} = \varrho_X e^{i\theta_X^{(n)}} \quad , \quad \frac{\partial e_b^{(n)}}{\partial Y} = \varrho_Y e^{i\theta_Y^{(n)}} . \quad (3.55\text{a,b})$$

These quantities can be thought of as two parameters which control the orientation and the form of the local tidal ellipse. The solution of the hydrodynamic problem can be divided by $\varrho_X^{(n)} e_X^{i\theta^{(n)}}$ and hence the only parameters controlling the tidal ellipse are

$$\varrho^{(n)} = \frac{\varrho_Y^{(n)}}{\varrho_X^{(n)}} \quad , \quad \theta^{(n)} = \theta_Y^{(n)} - \theta_X^{(n)} \quad . \quad (3.56\text{a,b})$$

The solution of the ordinary differential problem posed by

$$\frac{k_c}{\hat{\mu}}\frac{\partial}{\partial z}\left(\nu_{t0}\frac{\partial \hat{u}_b^{(n)}}{\partial z}\right) + 2\Omega \hat{v}_b^{(n)} \sin\varphi_0 + in\hat{u}_b^{(n)} = 1 \tag{3.57}$$

$$\frac{k_c}{\hat{\mu}}\frac{\partial}{\partial z}\left(\nu_{t0}\frac{\partial \hat{v}_b^{(n)}}{\partial z}\right) - 2\Omega \hat{u}_b^{(n)} \sin\varphi_0 + in\hat{v}_b^{(n)} = \varrho^{(n)} e^{i\theta^{(n)}} \tag{3.58}$$

along with the following boundary conditions

$$\frac{\partial \hat{u}_b^{(n)}}{\partial z} = \frac{\partial \hat{v}_b^{(n)}}{\partial z} = 0 \qquad \text{at} \qquad z = 0 \tag{3.59a,b}$$

$$\hat{u}_b^{(n)} = \hat{v}_b^{(n)} = 0 \qquad \text{at} \qquad z = \frac{z_r}{\mathcal{X}} \quad . \tag{3.60a,b}$$

where $(\hat{u}_b^{(n)}, \hat{v}_b^{(n)}) = (u_b^{(n)}, v_b^{(n)})/\varrho_X^{(n)} e^{i\theta_X^{(n)}}$, is found with a standard shooting procedure, starting from the free surface down to the bottom profile. Equations (3.57)-(3.58) are numerically integrated by means of a Runge-Kutta method of the fourth order. In order to handle the large velocity gradients which are expected to occur close to the bottom, the vertical coordinate has been stretched, introducing the new variable ζ defined by

$$\zeta = \ln\left(\frac{z\mathcal{X}}{z_r}\right) \quad . \tag{3.61}$$

For each tide constituent, with an iterative procedure on $\varrho^{(n)}$ and $\theta^{(n)}$, it is possible to determine the values of $\varrho^{(n)}$ and $\theta^{(n)}$ which give rise to a tidal ellipse of assigned orientation and a given ratio between the major and minor axes. Then the value of $\varrho_X^{(n)}$ should be chosen in such a way that the maximum value of the dimensionless depth average velocity assumes an assigned value. Finally, it is worth pointing out that $\theta_X^{(n)}$ fixes the phases among the different tide constituents.

Once the local flow is known, the vertical distribution of sediment concentration over a flat bed can be easily computed using (3.38) and the appropriate boundary conditions which provide

$$\frac{k_c}{\hat{\mu}}\frac{\partial}{\partial z}\left[\nu_{t0}\frac{\partial c_b^{(n)}}{\partial z}\right] + \frac{w_s}{\sqrt{\hat{\psi}_d}}\frac{\partial c_b^{(n)}}{\partial z} + inc_b^{(n)} = 0 \tag{3.62}$$

$$c_b^{(n)} = c_\zeta^{(n)} \qquad \text{at} \quad z = 0.01 \tag{3.63}$$

$$\frac{k_c}{\hat{\mu}}\nu_{t0}\frac{\partial c_b^{(n)}}{\partial z}+\frac{w_s}{\sqrt{\hat{\psi}_d}}c_b^{(n)}=0 \qquad \text{at} \quad z=0 \quad . \tag{3.64}$$

The values of the reference concentration $c_\zeta^{(n)}$ come from

$$\frac{1.5}{R_p^{0.2}}\left(\frac{\theta_{cw}-\theta_{cr}}{\theta_{cr}}\right)^{3/2}=\sum_{n=0}^{N}c_\xi^{(n)}e^{-int}+c.c. \quad . \tag{3.65}$$

It is worth pointing out that, even when only the main tide constituent is considered, i.e. $N=1$, the concentration c is characterised by many harmonic components because of the non-linear relationship between the concentration and the velocity field at the bottom.

3.3 The time development of the bottom perturbations

In order to investigate the stability of the flat bottom configuration, we perform a normal mode analysis introducing perturbations of small amplitude (strictly infinitesimal), as described in section 3.2, and linearise the problem. Therefore, substituting (3.44) in equations (3.7)-(3.10), at $O(\epsilon)$, it is possible to obtain the following set of linear equations for u_1, v_1, w_1, p_1 and e_1,

$$\frac{\partial w_1}{\partial z}+i\left[\delta_x u_1+\delta_y v_1\right]=0 \tag{3.66}$$

$$\begin{aligned}&i\left[\delta_x u_b u_1+\delta_y v_b u_1\right]+w_1\frac{\partial u_b}{\partial z}=-i\delta_x\left[P_1+e_1\right]+\\&\frac{1}{\hat{\mu}}\left\{\nu_{t0}\left[\frac{\partial^2 u_1}{\partial z^2}-u_1\left(\delta_x^2+\delta_y^2\right)\right]+\frac{\partial \nu_{t0}}{\partial z}\left(\frac{\partial u_1}{\partial z}+w_1 i\delta_x\right)+\right.\\&\left.\nu_{t1}\frac{\partial^2 u_b}{\partial z^2}+\frac{\partial \nu_{t1}}{\partial z}\frac{\partial u_b}{\partial z}\right\}-2\frac{\Omega}{k_c}\left(w_1\cos\varphi_0-v_1\sin\varphi_0\right)-\frac{1}{k_c}\frac{\partial u_1}{\partial t}\end{aligned} \tag{3.67}$$

$$\begin{aligned}&i\left[\delta_x u_b v_1+\delta_y v_b v_1\right]+w_1\frac{\partial v_b}{\partial z}=-i\delta_y\left[P_1+e_1\right]+\\&\frac{1}{\hat{\mu}}\left\{\nu_{t0}\left[\frac{\partial^2 v_1}{\partial z^2}-v_1\left(\delta_x^2+\delta_y^2\right)\right]+\frac{\partial \nu_{t0}}{\partial z}\left(\frac{\partial v_1}{\partial z}+w_1 i\delta_y\right)+\right.\\&\left.\nu_{t1}\frac{\partial^2 v_b}{\partial z^2}+\frac{\partial \nu_{t1}}{\partial z}\frac{\partial v_b}{\partial z}\right\}-2\frac{\Omega}{k_c}u_1\sin\varphi_0-\frac{1}{k_c}\frac{\partial v_1}{\partial t}\end{aligned} \tag{3.68}$$

$$iw_1\left[\delta_x u_b+\delta_y v_b\right]=-\frac{\partial P_1}{\partial z}+\frac{1}{\hat{\mu}}\left\{\nu_{t0}\left[\frac{\partial^2 w_1}{\partial z^2}-w_1\left(\delta_x^2+\delta_y^2\right)\right]+\right.$$
$$\left.2\frac{\partial \nu_{t0}}{\partial z}\frac{\partial w_1}{\partial z}+i\nu_{t1}\left[\delta_y\frac{\partial v_b}{\partial z}+\delta_x\frac{\partial u_b}{\partial z}\right]\right\}+2\frac{\Omega}{k_c}u_1\cos\varphi_0-\frac{1}{k_c}\frac{\partial w_1}{\partial t} \quad (3.69)$$

along with the following boundary conditions

$$u_1=\frac{\partial u_b}{\partial z}\ ,\quad v_1=\frac{\partial v_b}{\partial z}\ ,\quad w_1=0 \qquad \text{at} \qquad z=\frac{z_r}{\mathcal{X}} \qquad (3.70a,b,c)$$

$$\frac{\partial u_1}{\partial z}+w_1 i\delta_x=0\ ,\quad \frac{\partial v_1}{\partial z}+w_1 i\delta_y=0\ ,\quad \frac{2\nu_{t0}}{\hat{\mu}}\frac{\partial w_1}{\partial z}-P_1=0 \qquad \text{at} \qquad z=1 \qquad (3.71a,b,c)$$

$$w_1-e_1 i\left(u_b\delta_x+v_b\delta_y\right)-\frac{1}{k_c}\frac{\partial e_1}{\partial t}=0 \qquad \text{at} \qquad z=1 \qquad (3.72)$$

where the eddy viscosity ν_t has been split into a contribution of order one and a contribution of order ϵ which is induced by the bottom perturbation:

$$\nu_t=\nu_{t0}+\epsilon\nu_{t1}\Pi(t)e^{i(\delta_x x+\delta_y y)}+c.c.+O(\epsilon^2)\quad . \qquad (3.73)$$

The functions ν_{t0} and ν_{t1} can be easily computed by expanding (3.19)-(3.20).

First of all, let us point out that the value of e_1 appearing in equations (3.66)-(3.69) seems to be free and the value of the boundary condition at the free surface seems to be unnecessary. However, by noticing that the term $-\partial e_1/\partial z$ can be added to (3.69) and by introducing the variable $\mathcal{P}_1=p_1+e_1$, it appears that the system can be solved without any problem. Indeed equations (3.67) and (3.68) require boundary conditions for u_1 and v_1 both at the free surface and at the bottom. Then, equation (3.66) needs one boundary condition for w_1, for example that at the bottom. The boundary condition for w_1 at the free surface can be satisfied by choosing an appropriate value of $\mathcal{P}_1=P_1+e_1$. Finally the boundary condition at the free surface involving the pressure P_1 fixes the value of the amplitude e_1 of the perturbation of the free surface elevation induced by the interaction of the tidal wave with the wavy bed. This discussion shows also that the rigid lid assumption does not introduce any approximation. Then, let us point out that those terms proportional to the time derivative of the perturbation amplitude $\Pi(t)$ are negligible with respect to the other terms. Finally, the sediment continuity equation states that $d\Pi(t)/dt$ is proportional to $\Pi(t)$ through the ratio between the hydrodynamic and the morphodynamic time scales which turns out to be much smaller than one.

Since the basic flow is time periodic, it can be written in the form

$$u_b=\sum_{n=-\infty}^{\infty}\hat{U}_n(z)\,e^{-int}\quad ,\qquad v_b=\sum_{n=-\infty}^{\infty}\hat{V}_n(z)\,e^{-int}\quad . \qquad (3.74a,b)$$

However, in the present contribution only the main tidal harmonic (n=1) and a residual steady current (n=0) have been considered and $\hat{U}_1 = \hat{U}$, $\hat{U}_0 = \hat{U}_s$.

Hence it is possible to expand all the $O(\epsilon)$ terms as Fourier series in time

$$u_1 = \sum_{n=-\infty}^{\infty} u_n e^{int} \quad , \qquad v_1 = \sum_{n=-\infty}^{\infty} v_n e^{int} \quad , \qquad w_1 = \sum_{n=-\infty}^{\infty} w_n e^{int} \quad \text{(3.75a,b,c)}$$

$$P_1 = \sum_{n=-\infty}^{\infty} p_n e^{int} \quad , \qquad e_1 = \sum_{n=-\infty}^{\infty} e_n e^{int} \quad . \qquad \text{(3.76a,b)}$$

Substitution of relationships (3.74)-(3.76) in the continuity equation (3.66) and in the momentum equations (3.67)-(3.69) leads to the following system of coupled linear ordinary differential equations

$$\frac{\partial w_n}{\partial z} + i\left[\delta_x u_n + \delta_y v_n\right] = 0 \tag{3.77}$$

$$\begin{aligned}
&\frac{\partial A_n}{\partial z} = \left\{ w_{n+1}\frac{\partial \hat{U}}{\partial z} + w_{n-1}\frac{\partial \hat{U}^*}{\partial z} + w_n \frac{\partial \hat{U}_s}{\partial z} + i\delta_x\left(p_n + e_n\right) + \right. \\
&i\left[\delta_x\left(\hat{U}u_{n+1} + \hat{U}^* u_{n-1} + \hat{U}_s u_n\right) + \delta_y\left(\hat{V}u_{n+1} + \hat{V}^* u_{n-1} + \hat{V}_s u_n\right)\right] + \\
&\left. 2\frac{\Omega}{k_c}\left(w_n \cos\varphi_0 - v_n \sin\varphi_0\right) + \frac{in}{k_c}u_n \right\}\frac{\hat{\mu}}{\nu_{t0}} + u_n\left(\delta_x^2 + \delta_y^2\right) - \\
&\frac{1}{\nu_{t0}}\frac{\partial \nu_{t0}}{\partial z}\left(A_n + iw_n\delta_x\right) - \frac{\nu_{t1}}{\nu_{t0}}\left(\frac{\partial^2 \hat{U}}{\partial z^2} + \frac{\partial^2 \hat{U}^*}{\partial z^2} + \frac{\partial^2 \hat{U}_s}{\partial z^2}\right) - \\
&\frac{1}{\nu_{t0}}\frac{\partial \nu_{t1}}{\partial z}\left(\frac{\partial \hat{U}}{\partial z} + \frac{\partial \hat{U}^*}{\partial z} + \frac{\partial \hat{U}_s}{\partial z}\right)
\end{aligned} \tag{3.78}$$

$$\begin{aligned}
&\frac{\partial B_n}{\partial z} = \left\{ w_{n+1}\frac{\partial \hat{V}}{\partial z} + w_{n-1}\frac{\partial \hat{V}^*}{\partial z} + w_n \frac{\partial \hat{V}_s}{\partial z} + i\delta_y\left(p_n + e_n\right) + \right. \\
&i\left[\delta_x\left(\hat{U}v_{n+1} + \hat{U}^* v_{n-1} + \hat{U}_s v_n\right) + \delta_y\left(\hat{V}v_{n+1} + \hat{V}^* v_{n-1} + \hat{V}_s v_n\right)\right] + \\
&\left. 2\frac{\Omega}{k_c}u_n \sin\varphi_0 + \frac{in}{k_c}v_n \right\}\frac{\hat{\mu}}{\nu_{t0}} + v_n\left(\delta_x^2 + \delta_y^2\right) - \\
&\frac{1}{\nu_{t0}}\frac{\partial \nu_{t0}}{\partial z}\left(B_n + iw_n\delta_y\right) - \frac{\nu_{t1}}{\nu_{t0}}\left(\frac{\partial^2 \hat{V}}{\partial z^2} + \frac{\partial^2 \hat{V}^*}{\partial z^2} + \frac{\partial^2 \hat{V}_s}{\partial z^2}\right) - \\
&\frac{1}{\nu_{t0}}\frac{\partial \nu_{t1}}{\partial z}\left(\frac{\partial \hat{V}}{\partial z} + \frac{\partial \hat{V}^*}{\partial z} + \frac{\partial \hat{V}_s}{\partial z}\right)
\end{aligned} \tag{3.79}$$

$$\frac{\partial p_n}{\partial z} = \frac{1}{\hat{\mu}}\left\{\nu_{t0}\left[\frac{\partial^2 w_n}{\partial z^2} - w_n\left(\delta_x^2+\delta_y^2\right)\right] + 2\frac{\partial \nu_{t0}}{\partial z}\frac{\partial w_n}{\partial z}\right\} - \frac{in}{k_c}w_n +$$
$$2\frac{\Omega}{k_c}u_n\cos\varphi_0 - iw_{n+1}\left(\hat{U}\delta_x+\hat{V}\delta_y\right) - iw_{n-1}\left(\hat{U}^*\delta_x+\hat{V}^*\delta_y\right) - iw_n\left(\hat{U}_s\delta_x+\hat{V}_s\delta_y\right) +$$
$$\frac{i\nu_{t1}}{\hat{\mu}}\left\{\left(\delta_x\frac{\partial\hat{U}}{\partial z}+\delta_y\frac{\partial\hat{V}}{\partial z}\right)+\left(\delta_x\frac{\partial\hat{U}^*}{\partial z}+\delta_y\frac{\partial\hat{V}^*}{\partial z}\right)\left(\delta_x\frac{\partial\hat{U}_s}{\partial z}+\delta_y\frac{\partial\hat{V}_s}{\partial z}\right)\right\} \qquad (3.80)$$

where the quantities A_n and B_n are defined as

$$A_n = \frac{\partial u_n}{\partial z} \quad , \qquad B_n = \frac{\partial v_n}{\partial z} \qquad (3.81a,b,c)$$

The boundary conditions (3.70)-(3.72) can be rewritten as follows

$$\text{if} \quad n \neq \pm 1 \quad \text{or} \quad 0 \qquad u_n = v_n = w_n = 0 \qquad \text{at} \quad z = z_r/\mathcal{X}$$

$$\text{if} \quad n = 1 \qquad u_I = -\frac{\partial\hat{U}^*}{\partial z} \quad , \quad v_I = -\frac{\partial\hat{V}^*}{\partial z} \quad , \quad w_I = 0$$

$$\text{if} \quad n = -1 \qquad u_{-I} = -\frac{\partial\hat{U}}{\partial z} \quad , \quad v_{-I} = -\frac{\partial\hat{V}}{\partial z} \quad , \quad w_{-I} = 0$$

$$\text{if} \quad n = 0 \qquad u_0 = -\frac{\partial\hat{U}_s}{\partial z} \quad , \quad v_0 = -\frac{\partial\hat{V}_s}{\partial z} \quad , \quad w_0 = 0 \qquad (3.82)$$

$$w_n = 0 \qquad \forall n \qquad \text{at} \quad z = 1 \qquad (3.83)$$

$$\frac{\partial u_n}{\partial z} = 0 \quad , \qquad \frac{\partial v_n}{\partial z} = 0 \qquad \text{at} \quad z = 1 \qquad (3.84a,b)$$

$$\frac{2}{\hat{\mu}}\nu_{t0}\frac{\partial w_n}{\partial z} - p_n = 0 \qquad \text{at} \quad z = 1 \quad . \qquad (3.85)$$

As was done in the solution of the basic state, the vertical coordinate has been stretched, introducing the variable ζ defined by (3.61).

Once the velocity perturbations are computed, the perturbed concentration can be evaluated by solving the following differential problem obtained by substituting (3.44) in the standard convection-diffusion equation (3.38)

$$\frac{1}{k_c}\frac{\partial c_1}{\partial t} + \left[i\delta_x u_b c_1 + i\delta_y v_b c_1 + w_1\frac{\partial c_b}{\partial z}\right] - \frac{w_s}{k_c\sqrt{\hat{\psi}_d}}\frac{\partial c_1}{\partial z} =$$

$$\frac{1}{\hat{\mu}}\left\{\nu_{t0}\left(\frac{\partial^2 c_1}{\partial z^2}-\delta_x^2 c_1-\delta_y^2 c_1\right)+\frac{\nu_{t0}}{\partial z}\frac{\partial c_1}{\partial z}+\nu_{t1}\frac{\partial^2 c_b}{\partial z^2}+\frac{\partial \nu_{t1}}{\partial z}\frac{\partial c_b}{\partial z}\right\} \quad (3.86)$$

along with the following boundary conditions

$$c_1+\frac{\partial c_b}{\partial z}=c_\zeta \qquad \text{at} \quad z=0.01 \qquad (3.87)$$

$$\frac{w_s}{k_c\sqrt{\hat{\psi}_d}}c_1+\frac{\nu_{t0}}{\hat{\mu}}\frac{\partial c_1}{\partial z}+\frac{\nu_{t1}}{\hat{\mu}}\frac{\partial c_b}{\partial z} \qquad \text{at} \quad z=1 \qquad (3.88)$$

where c_ζ is the term of $O(\epsilon)$ of the reference concentration at the bottom. Introducing the Fourier series expansion in time for the concentration, equation (3.86) reads

$$\frac{\partial^2 c_n}{\partial z^2}=\frac{\hat{\mu}}{\nu_{t0}}\left[\frac{in}{k_c}c_n+w_l\frac{\partial c_{bm}}{\partial z}-\frac{\partial c_n}{\partial z}\frac{w_s}{k_c\hat{\psi}_d}+\left(\hat{U}c_{n+1}+\hat{U}^*c_{n-1}+\hat{U}_s c_n\right)i\delta_x+\right.$$
$$\left.\left(\hat{V}c_{n+1}+\hat{V}^*c_{n-1}+\hat{V}_s c_n\right)i\delta_y\right]+c_n\left(\delta_x^2+\delta_y^2\right)-$$
$$\frac{1}{\nu_{t0}}\left(\frac{\partial \nu_{t0}}{\partial z}\frac{\partial c_n}{\partial z}+\frac{\partial \nu_{t1}}{\partial z}\frac{\partial c_{bn}}{\partial z}+\nu_{t1}\frac{\partial^2 c_{bn}}{\partial z^2}\right) \qquad (3.89)$$

where $l+m=n$. The values of the different harmonics of c_b have to be evaluated solving the problem at the leading order of approximation as explained in section 3.2. Analogously, the boundary conditions can be rewritten as

$$c_n+\frac{\partial c_{bn}}{\partial z}=c_{\zeta n} \qquad \text{at} \quad z=0.01 \qquad (3.90)$$

$$\frac{w_s}{k_c\hat{\psi}_d}c_n+\frac{\nu_{t0}}{\hat{\mu}}\frac{\partial c_n}{\partial z}+\frac{\nu_{t1}}{\hat{\mu}}\frac{\partial c_{bn}}{\partial z}=0 \qquad \text{at} \quad z=1 \quad . \qquad (3.91)$$

Hence, it is possible to evaluate the perturbations of the bottom shear stresses and those of the sediment transport rates. In particular, from the constitutive law it is possible to obtain the Shield stresses related to the action of the current:

$$\theta_{0x}^c=\frac{k_c^2\psi_d}{\hat{\mu}}\nu_{t0}\frac{\partial u_b}{\partial z} \quad , \qquad \theta_{0y}^c=\frac{k_c^2\psi_d}{\hat{\mu}}\nu_{t0}\frac{\partial v_b}{\partial z} \qquad (3.92\text{a,b})$$

$$\theta_0^c=\frac{k_c^2\psi_d}{\hat{\mu}}\sqrt{\left(\frac{\partial u_b}{\partial z}\right)^2+\left(\frac{\partial v_b}{\partial z}\right)^2} \qquad (3.93)$$

$$\theta_{1x}^c=\frac{k_c^2\psi_d}{\hat{\mu}}\left\{\nu_{t0}\left(\frac{\partial u_1}{\partial z}+w_1 i\delta_x\right)+\left(\nu_{t1}+\frac{\partial \nu_{t0}}{\partial z}\right)\frac{\partial u_b}{\partial z}+\nu_{t0}\frac{\partial^2 u_b}{\partial z^2}\right\} \qquad (3.94)$$

$$\theta_{1y}^{c} = \frac{k_c^2 \psi_d}{\hat{\mu}} \left\{ \nu_{t0} \left(\frac{\partial v_1}{\partial z} + w_1 i \delta_y \right) + \left(\nu_{t1} + \frac{\partial \nu_{t0}}{\partial z} \right) \frac{\partial v_b}{\partial z} + \nu_{t0} \frac{\partial^2 v_b}{\partial z^2} \right\} \qquad (3.95)$$

$$\theta_{1}^{c} = \frac{k_c^2 \psi_d}{\hat{\mu}} \frac{1}{\sqrt{\left(\frac{\partial u_b}{\partial z} \right)^2 + \left(\frac{\partial v_b}{\partial z} \right)^2}} \left\{ \nu_{t0} \frac{\partial u_b}{\partial z} \left(\frac{\partial u_1}{\partial z} + w_1 i \delta_x + \frac{\partial^2 u_b}{\partial z^2} \right) + \right.$$
$$\nu_{t1} \left[\left(\frac{\partial u_b}{\partial z} \right)^2 + \left(\frac{\partial v_b}{\partial z} \right)^2 \right] + \nu_{t0} \frac{\partial v_b}{\partial z} \left(\frac{\partial v_1}{\partial z} + w_1 i \delta_y + \frac{\partial^2 v_b}{\partial z^2} \right) +$$
$$\left. \frac{\partial \nu_{t0}}{\partial z} \left[\left(\frac{\partial u_b}{\partial z} \right)^2 + \left(\frac{\partial v_b}{\partial z} \right)^2 \right] \right\} \quad . \qquad (3.96)$$

Concerning the wave shear stress, expanding relationship (3.30), it is possible to obtain the following expression for the evaluation of the wave Shields stresses

$$\theta_0^w = 0.15 \frac{k_c^2 \hat{\psi}_d}{R_p^{2/3}} f_w \left(\frac{HTU}{HGT} \right)^2 \pi^2 \qquad (3.97)$$

$$\theta_{0x}^w = \theta_0^w \cos \beta_w \quad , \qquad \theta_{0y}^w = \theta_0^w \sin \beta_w \qquad (3.98a,b)$$

$$\theta_1^w = 1.5 \theta_0^w \quad , \qquad \theta_{1x}^w = \theta_1^w \cos \beta_w \quad , \qquad \theta_{1y}^w = \theta_1^w \sin \beta_w \qquad (3.99a,b,c)$$

where HTU and HGT are dimensionless parameters related to characteristics of the sea wave:

$$HTU = \frac{H^*}{T^* U_0^*} \quad , \qquad HGT = \frac{2\pi \sqrt{h_0^*}}{\sqrt{g^*} T^*} \quad . \qquad (3.100a,b)$$

Hence, remembering that $\theta_0^{cw} = \theta_0^c + \theta_0^w$ and $\theta_1^{cw} = \theta_1^c + \theta_1^w$, it is straightforward to obtain the expression for the evaluation of the sediment transport in the case of bed load, suspended load, bed slope effect and wave load:

- Bed Load

$$\left(Q_{0x}^b, Q_{0y}^b \right) = \frac{0.025}{R_p^{0.2}} \left(\frac{\theta_0^{cw} - \theta_{cr}}{\theta_{cr}} \right)^{1.5} \frac{\left(\theta_{0x}^c, \theta_{0y}^c \right)}{\sqrt{\theta_0^c}} \qquad (3.101)$$

$$\left(Q_{1x}^{b}, Q_{1y}^{b}\right) = \frac{0.025}{R_p^{0.2}} \left\{ \left(\frac{\theta_0^{cw} - \theta_{cr}}{\theta_{cr}} \right)^{1.5} \left[\frac{\left(\theta_{1x}^{c}, \theta_{1y}^{c}\right)}{\sqrt{\theta_0^c}} - \frac{1}{2} \frac{\theta_1^{cw}}{\left(\theta_0^c\right)^{3/2}} \left(\theta_{0x}^{c}, \theta_{0y}^{c}\right) \right] + 1.5 \left(\frac{\theta_0^{cw} - \theta_{cr}}{\theta_{cr}} \right)^{0.5} \frac{\left(\theta_{0x}^{c}, \theta_{0y}^{c}\right)}{\sqrt{\theta_0^c}} \frac{\theta_1^{cw}}{\theta_{cr}} \right\} \tag{3.102}$$

- Suspended Load

$$\left(Q_{0x}^{s}, Q_{0y}^{s}\right) = k_c \sqrt{\hat{\psi}_d} \int_{z_r+a}^{0} c_b \left(u_b, v_b\right) dz \tag{3.103}$$

$$\left(Q_{1x}^{s}, Q_{1y}^{s}\right) = k_c \sqrt{\hat{\psi}_d} \int_{z_r+a}^{0} \left[c_1 \left(u_b, v_b\right) + c_b \left(u_1, v_1\right)\right] dz - k_c \sqrt{\hat{\psi}_d} c_b \left(u_b, v_b\right) \mid_{z=z_r/\mathcal{X}+a} \tag{3.104}$$

- Slope Effect

$$\left(Q_{1x}^{p}, Q_{1y}^{p}\right) = Q_0^b \left[\left(\frac{\partial \eta}{\partial x} \theta_{0x} + \frac{\partial \eta}{\partial y} \theta_{0y} \right) \frac{\theta_{0x}}{\theta_0^2} \left(G_{ss} - G_{nn}\right) + \frac{\partial \eta}{\partial x} G_{nn} \quad , \left(\frac{\partial \eta}{\partial x} \theta_{0x} + \frac{\partial \eta}{\partial y} \theta_{0y} \right) \frac{\theta_{0y}}{\theta_0^2} \left(G_{ss} - G_{nn}\right) + \frac{\partial \eta}{\partial y} G_{nn} \right] \tag{3.105}$$

where

$$Q_0^b = \frac{0.25}{R_p^{0.2}} \left(\frac{\theta_0^{cw} - \theta_{cr}}{\theta_{cr}} \right)^{1.5} \sqrt{\theta_0^{cw}} \tag{3.106}$$

- Wave Load

$$\left(Q_{0x}^{w\pm}, Q_{0y}^{w\pm}\right) = 0.03 R_p^{-0.2} \sqrt{\hat{\psi}_d} k_c \frac{HTU}{HGT} \pi \left(\frac{\theta_0^{\pm} - \theta_{cr}}{\theta_{cr}} \right)^{1.5} \left(\cos \beta_w, \sin \beta_w\right) \tag{3.107}$$

$$\left(Q_{1x}^{w\pm}, Q_{1y}^{w\pm}\right) = 0.03 R_p^{-0.2} \sqrt{\hat{\psi}_d} k_c \frac{HTU}{HGT} \pi \left[\frac{3}{4} \left(\frac{\theta_0^{\pm} - \theta_{cr}}{\theta_{cr}} \right)^{1.5} + \right.$$

$$1.5\left(\frac{\theta_0^{\pm}-\theta_{cr}}{\theta_{cr}}\right)^{0.5}\frac{\theta_1^{\pm}}{\theta_{cr}}\Bigg](\cos\beta_w,\sin\beta_w) \tag{3.108}$$

where

$$\theta_0^{\pm}=\sqrt{\left(\theta_0^c\right)^2+\left(\theta_0^w\right)^2\pm 2\left(\theta_{0x}^c\theta_{0x}^w+\theta_{0y}^c\theta_{0y}^w\right)} \tag{3.109}$$

$$\theta_1^{\pm}=\frac{\left(\theta_{0x}^c\pm\theta_{0x}^w\right)\left(\theta_{1x}^c\pm\theta_{1x}^w\right)+\left(\theta_{0y}^c\pm\theta_{0y}^w\right)\left(\theta_{1y}^c\pm\theta_{1y}^w\right)}{\theta_0^{\pm}} \quad . \tag{3.110}$$

The amplitude equation which provides the time development of $\Pi(t)$ (amplitude of the bottom perturbation) follows from the sediment continuity equation:

$$\frac{d\Pi(T)}{dT}=\gamma(t)\Pi(T) \tag{3.111}$$

where γ is a periodic, complex function of t which depends on the parameters of the problem:

$$\begin{aligned}\gamma(t)&=\gamma_b(t)+\gamma_s(t)+\gamma_w(t)+\gamma_p(t)=\\&=\left\{i\left(\delta_xQ_{1x}^b+\delta_yQ_{1y}^b\right)+i\left(\delta_xQ_{1x}^s+\delta_yQ_{1y}^s\right)+\right.\\&\left.\quad i\left(\delta_xQ_{1x}^w+\delta_yQ_{1y}^w\right)+i\left(\delta_xQ_{1x}^p+\delta_yQ_{1y}^p\right)\right\}\end{aligned} \tag{3.112}$$

where

$$Q_{1x}^w=Q_{1x}^{w+}+Q_{1x}^{w-} \quad , \quad Q_{1y}^w=Q_{1y}^{w+}+Q_{1y}^{w-} \quad . \tag{3.113a,b}$$

The solution of (3.111) is clearly:

$$\Pi(T)=\Pi_0\exp\left[\int_0^T\gamma(t')dt'\right]. \tag{3.114}$$

Hence, the growth or the decay of the perturbation is controlled by the real part of the time average of γ, while the imaginary part is related to the migration speed of the perturbations. The periodic part of γ, with a vanishing time average, simply describes oscillations of the sand wave configuration around its average configuration which turn out to be quite small since the tide period is much smaller than the morphodynamic time scale. Different contributions to the amplification rate γ of the bottom perturbation can be identified according to the mechanisms of sediment transport. The most important contributions are those related to the bed load and to the slope effects, the latter always being real and negative and tending to stabilise

any bottom waviness. These two contributions are described by the first and fourth terms appearing on the right hand side of (3.111). The value of γ is also affected by the suspended load even though the latter becomes important only when the particle mobility number is large.

3.4 Results

Before discussing the results on the morphodynamic stability it is necessary to point out that for each run the model has been used in a first time neglecting the terms appearing in (3.66)-(3.69) which are proportional to the time derivative of the perturbation amplitude $\Pi(t)$ because they are smaller than the other terms, being of $O(1/k_c)$. In a second step the same runs have been obtained taking into account the time derivative in order to study its effect on the formation of sand waves and sand banks. If the parameter k_c attains large values, the influence of the time derivative is expected to be negligible. However, in the case of sand bank formation, a predominant role on the physical processes is played by the effect of the Coriolis force. An analysis of the order of magnitude of the different terms appearing in the momentum equation shows that the terms proportional to the time derivative of the perturbation amplitude $\Pi(t)$ are of the same order of those related to the Coriolis term. Hence, it is necessary to take into account the terms relative to the local acceleration in order to have a more realistic description of sand bank formation.

3.4.1 Case study

Because of the large number of parameters controlling the behaviour of the system, it is useful to start to check the capability and reliability of the model by considering specific sets of data which allow for a comparison of the theoretical results with some field observations. Subsequently, on varying the parameters, it is possible to try to identify the role of the different physical processes (tide characteristics, sediment transport, etc.) involved in the phenomenon of sand wave and sand bank formation and migration.

Let us start by considering two different locations in the North Sea, which were already considered in the previous chapters where simpler models have been used to predict the characteristics of the observed morphological patterns. Data concerning bathymetry, sediment properties and current velocities were provided by SNAM PROGETTI S.p.A.. The surveyed areas have a water depth ranging from 20 to 40m. The bathymetric data of the first site, identified as SW2 are shown in figure **3.2**, where the bottom topography

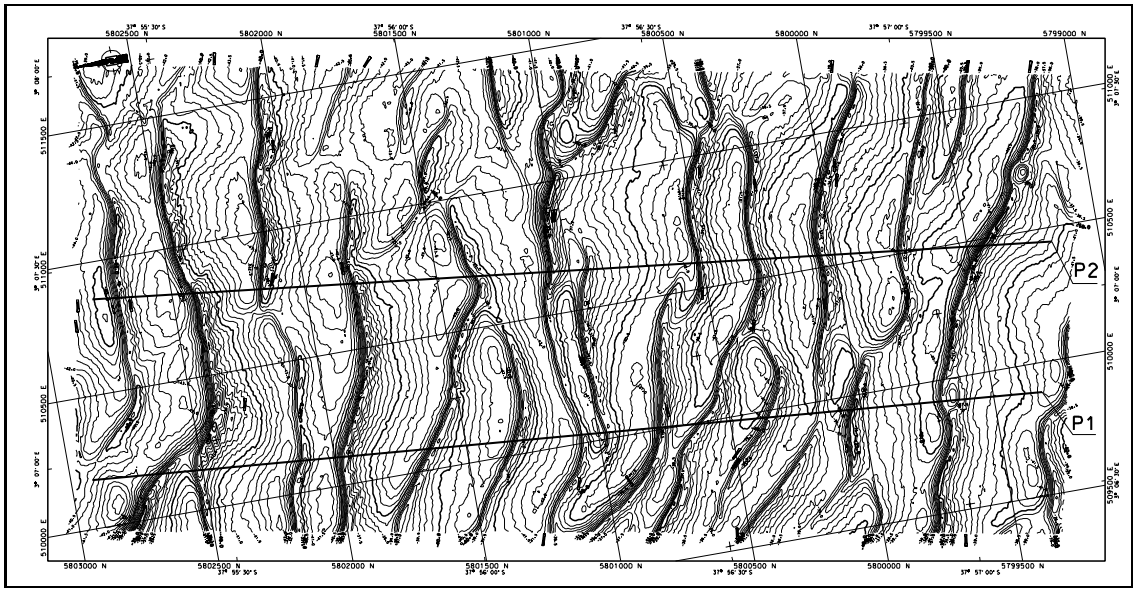

Figure 3.2: Bottom topography measured at 52° 21′ N and 3° 9′ (Area SW2) showing the presence of sand waves. The grid size is 500m. Courtesy of SNAMPROGETTI.

measured at 52° 21′ N and 3° 9′ E is displayed. The average water depth is about 40m but a wavy bed (sand waves) characterised by a wavelength of about 285 ± 85m and heights ranging between 3.5 and 5.5m is present. The harmonic analysis of the tidal current measured at two different locations close to the observed sand waves shows that the tide is mainly semi-diurnal with M2 as the dominant constituent (see analysis of chapter 2). The amplitude of the velocity oscillations induced by the M2 constituent during the measuring period (15 October 1998 - 31 March 1989) is about 0.41m/s and the direction of the velocity is almost orthogonal to the crests of the sand waves. Moreover, the ratio between the minor and major axis of the tidal ellipse, denoted in the following e_{cc}, is about 0.17. Finally, the sediment turns out to have a mean grain size equal to 0.25mm.

Even though the current measurements show the co-existence of many tidal constituents, to make the presentation of the results as simple as possible, the model has been run considering just the semi-diurnal tidal constituent. To show the model's capability of predicting the appearance of sand waves, the real part $\overline{\gamma}_r$ of the time average of the function γ is obtained as function of δ_x and δ_y for values of the parameters chosen in order to reproduce the local climate and sediment characteristics. Unfortunately, no information was available about the bottom roughness which presently is supposed to be due to sea ripples 0.3m long and 5cm high. We remind

the reader that $\overline{\gamma}_r$ is the growth rate of the bottom perturbations. Hence, positive values of $\overline{\gamma}_r$ imply the growth of the bottom perturbations while negative values of $\overline{\gamma}_r$ cause the disappearance of any initial bottom disturbance. Finally, when $\overline{\gamma}_r$ vanishes, perturbations neither amplify nor decay.

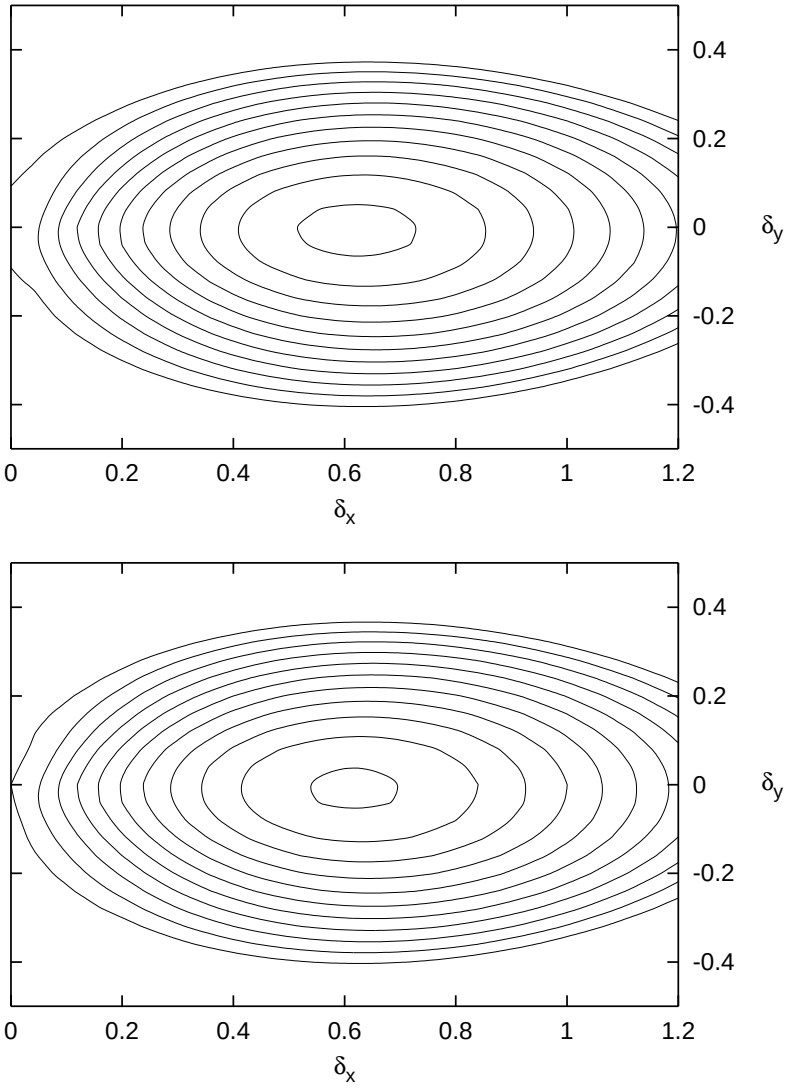

Figure 3.3: Growth rate $\overline{\gamma}_r$ plotted versus δ_x and δ_y for $k_c = 72$, $e_{cc} = 0.17$, $\hat{\mu} = 315$, $R_p = 15.9$, $\hat{\psi}_d = 0.008$, $d = 6.4\ 10^{-6}$ and no wind waves. Only positive isolines are displayed with $\Delta\overline{\gamma}_r = 0.002$. Top panel: no time derivative included. Bottom panel: time derivative included. The maximum value of $\overline{\gamma}_r$, in both cases, is located at $(\delta_x, \delta_y) \simeq (0.65, 0.0)$.

The results obtained (figure **3.3**) show that the bedforms which tend to

appear are characterised by crests almost orthogonal to the major axis of the tide since the maximum value of $\overline{\gamma}_r$ is reached for practically vanishing values of δ_y (x and y are two horizontal axes such that x is aligned with the major axis of the tidal ellipse). This theoretical prediction agrees well with the field observations (see also Belderson et al., 1982; Stride, 1982). The wavelength of sand waves predicted by the theory also falls within the range of observed values, since the perturbation component characterised by the maximum amplification rate, i.e. the component which will dominate the bottom configuration for long times, is characterised by $(\delta_x, \delta_y) \simeq (0.65, 0.0)$. These wavenumbers correspond to a dimensional wavelength of about 340m, a value similar to the observed wavelengths ranging between 200m and 370m. By taking into account the terms proportional to the time derivative of $\Pi(t)$, it is possible to note, comparing the top and the bottom panels of figure **3.3**, that the results do not change significantly from a qualitative point of view. It is noticeable when considering the full solution that the values of the growth rate $\overline{\gamma}_r$ are slightly smaller than in the previous case.

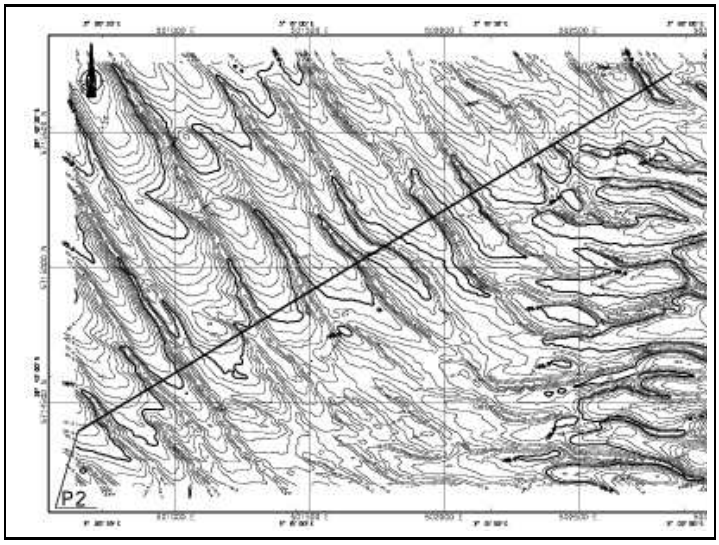

Figure 3.4: Bottom topography measured at 51° 35′ N and 3° 2′ (Area SW1) showing the presence of sand waves. The grid size is 500m. Courtesy of SNAMPROGETTI.

Sand wave appearance is investigated at a different location (51° 35′ N and 3° 2′ E), where the average water depth is much smaller (20m) and sand waves, orthogonal to the main tidal current, are characterised by a wavelength equal to 210 ± 45m (see figure **3.4**). The amplitude of the velocity oscillations induced by the M2 constituent, which is the dominant constituent, is about 0.43m/s a value close to the previous one, even though the eccen-

tricity of the tidal ellipse is larger ($e_{cc} = 0.42$). Because the site is closer to the coast, the sediment is much coarser and characterised by a value of the mean grain size equal to 0.60mm. Figure **3.5** shows the amplification rate $\overline{\gamma}_r$ provided by the model for this new data set. As in the previous case, the most unstable bottom perturbation turns out to have its crest orthogonal to the main tidal axis and a wavelength of about 300m, a value which is not too far from the observed sand wave spacing.

Because of the large value attained in this situation by the parameter k_c, the inclusion of the time derivative does not lead to significant changes neither in a qualitative nor in a quantitative sense.

The stability analysis described in section 3.3 is linear and therefore unable to provide any information on the equilibrium amplitude attained by the growing perturbation for long times. Indeed, as soon as the amplitude $\Pi(t)$ of the bottom waviness grows and reaches large values, nonlinear effects become strong and the analysis fails. However, the results which can be obtained by the linear analysis provide further information on the configuration of the sea bottom forced by a tidal wave. Indeed, Hulscher et al. (1993), using the shallow water approximation and considering the depth-averaged velocity field, showed that the interaction of tidal currents with 2D-horizontal bottom perturbations can lead to the appearance of a much longer bottom waviness which can be assumed to represent sand banks. For a unidirectional tide, the fastest growing mode determined by Hulscher et al. (1993) is characterised by crests almost aligned with the main tidal axis and wavelengths in agreement with the field values which characterise sand banks. However, very long waves are also growing exponentially. Moreover, the analysis of Hulscher et al. (1993) shows that the first mode that would become unstable, when the parameters are varied, corresponds to ultra-long waves. A better description of the phenomenon was found by Hulscher et al. (1993) by considering circular tides. In this case, the first mode to become unstable, when the parameters are varied, is characterised by a finite wavenumber but, since a circular tide has no preferred direction, the wavelength but not the orientation of the selected bedforms can be predicted. Since the depth averaged equations cannot describe the vertical recirculating cells which are the driving mechanism of sand wave formation, Hulscher et al. (1993) did not consider the conditions leading to the appearance of sand waves, even though their approach could be used to this aim with an appropriate parametrisation of the secondary currents in the vertical plane (De Swart & Hulscher, 1995).

Since the present model is based on the full three-dimensional Reynolds averaged momentum equations, it can in principle describe both the processes leading to sand waves and sand banks. Figure **3.6** shows the plot of $\overline{\gamma}_r$ versus

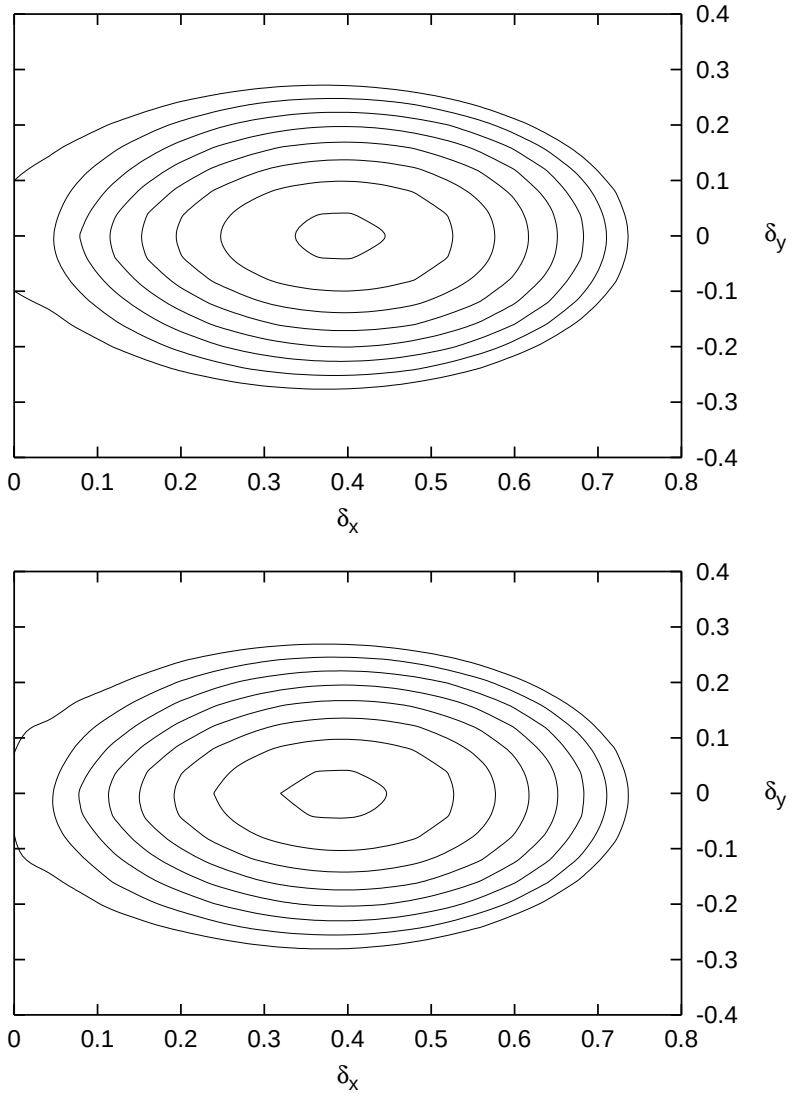

Figure 3.5: Growth rate $\overline{\gamma}_r$ plotted versus δ_x and δ_y for $k_c = 148$, $e_{cc} = 0.42$, $\hat{\mu} = 288$, $R_p = 59$, $\hat{\psi}_d = 0.00087$, $d = 3.0\ 10^{-5}$ and no wind waves. Only positive isolines are displayed with $\Delta\overline{\gamma}_r = 0.0005$. Top panel: no time derivative included. Bottom panel: time derivative included. The maximum value of $\overline{\gamma}_r$, in both cases, is located at $(\delta_x, \delta_y) \simeq (0.4, 0.0)$.

(δ_x, δ_y) for values of the parameters chosen to reproduce the site in the North Sea described by Le Bot at al. (2000). The field survey was carried out in the Calais-Dover strait midway between France and England. Both sand waves and sand banks are present on the site. Sand waves were observed with wavelength ranging between 350m and 750m and crests orthogonal to the main

tidal current which was dominated by the semi-diurnal component. Nearby (see figure 1 of Le Bot et al.'s, 2000 paper), sand banks are present and are characterised by crests almost aligned to the main tidal axis but slightly clockwise rotated (see in particular Sandettie bank, Ruytingen bank, Dyck bank) and by a mean spacing of about 6km. Unfortunately, even though accurate quantitative data concerning the local bathymetry are available, no data is given about the strength of the M2 tidal constituent, and on the bottom roughness which is presently fixed on the basis of measurements carried out in similar sites. The growth rate of the bottom perturbations predicted by the theory is characterised by the presence of two relative maxima. One of them appears close to the δ_x-axis for δ_x equal to about 0.26 (see figure **3.6**).

The second relative maximum appears more clearly in figure **3.7**, which is an enlargement around the origin of the figure **3.6**. As pointed out before, the introduction of the terms proportional to the local acceleration plays a very important role in the study of formation of sand waves. Comparing the top panel of figure **3.7** with the bottom panel it is possible to notice how the terms proportional to the time derivative more strongly enhance the formation of a maximum of the real part of the growth rate for $\delta_x = 0.015$ and $\delta_y = 0.055$.

Therefore, the theory indicates that there are two perturbation components which will tend to grow and to originate two different types of bedforms which coexist and characterise the sea-bed configuration.

The first type of bedform is characterised by crests almost orthogonal to the direction of the tidal flow and by a wavelength of about 630m. This result agrees with the data of the sand waves observed by Le Bot et al. (2000) which are characterised by a wavelength ranging between 350 and 750m. The second type of bedform has crests almost aligned to the main tidal flow direction, though slightly clockwise rotated (about 12°) and a wavelength of about 4km. These characteristics fairly agree with those of the sand banks which are observed nearby (Sandettie bank, Ruytingen bank, Dyck bank).

At this stage, we point out that the present model has no parameter which can be tuned to make the theoretical results fit the field data.

3.4.2 Sensitivity analysis

This section is dedicated to the investigation of the role of the different physical phenomena involved in the process of generation and migration of sand waves. These bedforms can affect several human activities and the understanding of their dynamics is very important from a practical point of view. Furthermore, the characteristic time of evolution of sand waves is

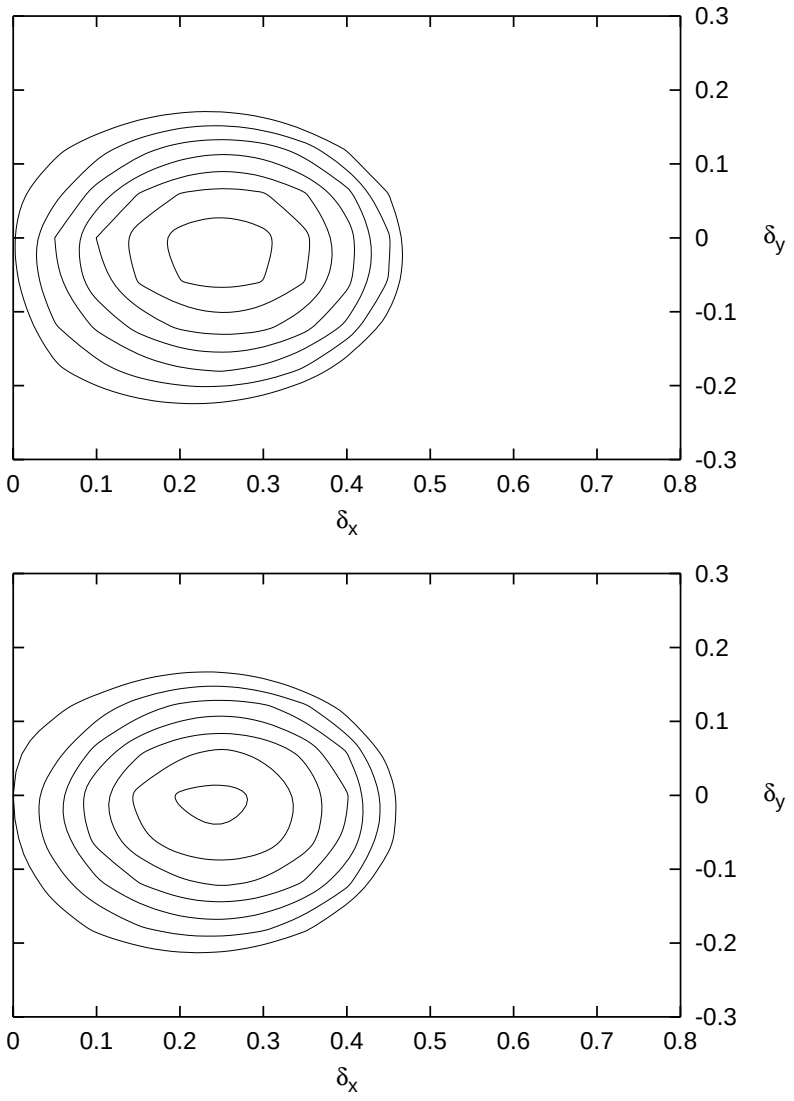

Figure 3.6: Growth rate $\overline{\gamma}_r$ plotted versus δ_x and δ_y for $k_c = 90$, $e_{cc} = 0.15$, $\hat{\mu} = 375$, $R_p = 20.9$, $\hat{\psi}_d = 0.0053$, $d = 8.6\ 10^{-6}$ and no wind waves. Only positive isolines are displayed with $\Delta\overline{\gamma}_r = 0.0005$. The maximum value of $\overline{\gamma}_r$ is located at $(\delta_x, \delta_y) \sim (0.26, 0.0)$. Top panel: no time derivative included. Bottom panel: time derivative included.

comparable to that of the economic activities interested by their appearance (migration of the order of tens of meters per year, regeneration time of sand waves after dredging of the order of a few years).

Every dimensionless parameter can be thought of as characterising the properties of the different physical dimensions of the processes. In particular

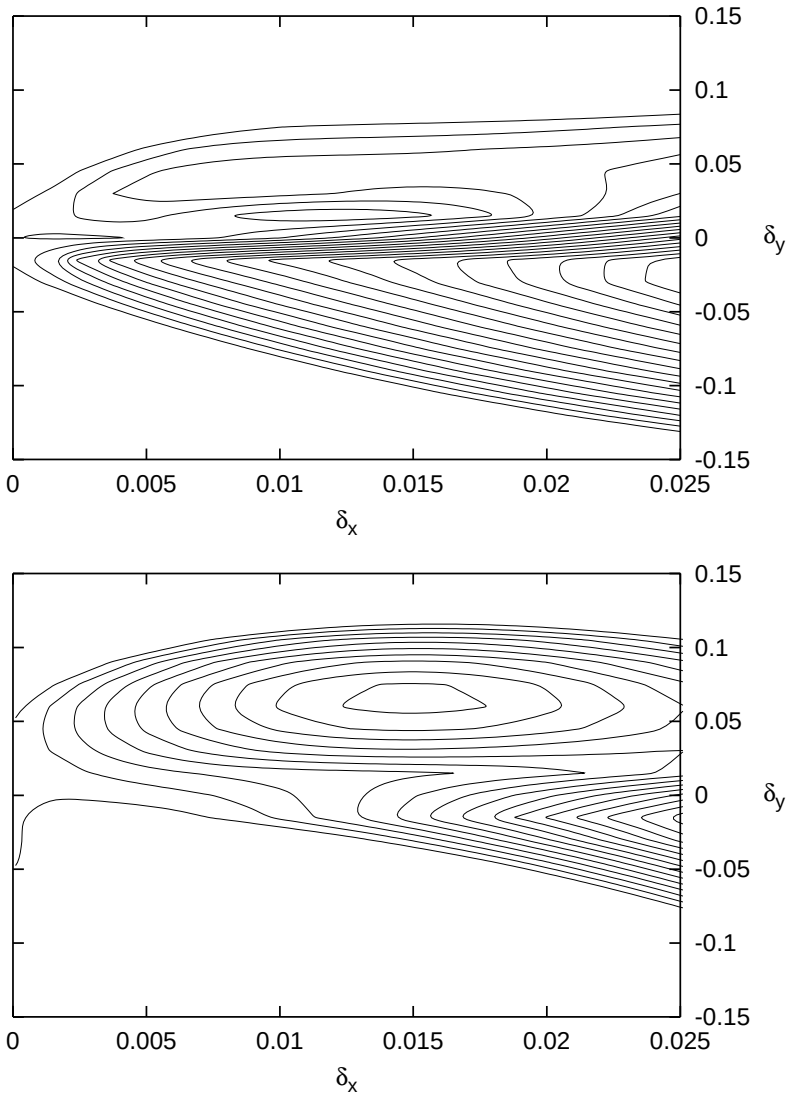

Figure 3.7: Growth rate $\overline{\gamma}_r$ plotted versus δ_x and δ_y for $k_c = 90$, $e_{cc} = 0.15$, $\hat{\mu} = 375$, $R_p = 20.9$, $\hat{\psi}_d = 0.0053$, $d = 8.6\ 10^{-6}$ and no wind waves. Only positive isolines are displayed with $\Delta\overline{\gamma}_r = 0.00003$. Top panel: no time derivative included. The maximum value of $\overline{\gamma}_r$ is located at $(\delta_x, \delta_y) \sim (0.012, 0.045)$. Bottom panel: time derivative included. The maximum value of $\overline{\gamma}_r$ is located at $(\delta_x, \delta_y) \sim (0.015, 0.06)$.

the parameter k_c is proportional to the strength of the main tidal current, $\hat{\mu}$ gives information about the roughness of the bed, $\hat{\psi}_d$, R_p and d take into account the sediment properties and finally HTU and HGT refer to the height and periods of waves generated by the wind. Considering different

values of these parameters, comprised in a range which is representative of realistic physical conditions that may occur in seas like the North Sea, it is possible to experience changes in the results from both a quantitative point of view and from a qualitative point of view.

Considering the study of sand wave formation, the obtained results show that the most unstable perturbations are characterised by almost vanishing values of δ_y. In order to investigate the relevance of the different parameters of the model on the phenomenon, a further set of model runs has been done considering only $\overline{\gamma}_r(\delta_x)$ and fixing $\delta_y = 0$. Figure **3.8** shows $\overline{\gamma}_r$ versus δ_x for different values of the parameter k_c.

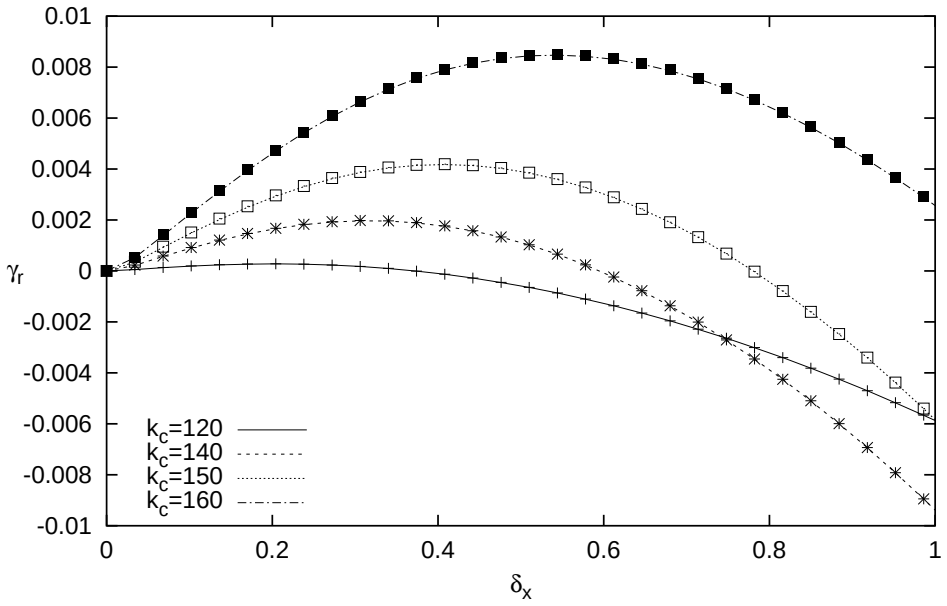

Figure 3.8: Growth rate $\overline{\gamma}_r$ plotted versus δ_x fixing $\delta_y = 0.0$ for $e_{cc} = 0.42$, $\hat{\mu} = 288$, $R_p = 59$, $\hat{\psi}_d = 0.00087$, $d = 3.0\ 10^{-5}$ and different values of k_c and no wind waves. The lines represent the solution neglecting the time derivative, the points represent the full solution.

For a semi-diurnal tide propagating over a constant water depth and a fixed sediment, different values of k_c imply different amplitudes of the depth averaged velocity oscillations induced by the tide. When the strength of the tide is increased, the values of $\overline{\gamma}_r$ grow, showing that the flat bottom configuration is more unstable. Furthermore, the full solution tends to coincide with the solution obtained neglecting the terms proportional to the time derivative of the perturbation amplitude because of the large values assumed by the parameter k_c. Moreover, the value of δ_x which gives rise to the maximum

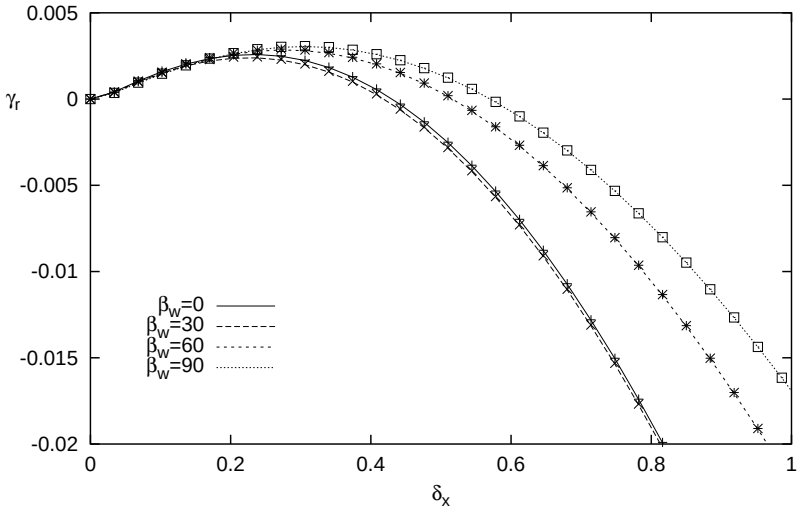

Figure 3.9: Growth rate $\overline{\gamma}_r$ plotted versus δ_x fixing $\delta_y = 0.0$ for $k_c = 150$, $e_{cc} = 0.42$, $\hat{\mu} = 288$, $R_p = 59$, $\hat{\psi}_d = 0.00087$, $d = 3.0\ 10^{-5}$, $H^* = 1.5$ m, $T^* = 5.7$ s and different values of the angle β_w between the direction of wave propagation and the major axis of the tidal ellipse.

value of $\overline{\gamma}_r$, increases, thus showing that stronger tidal currents generate shorter sand waves. On the other hand, when k_c is decreased, smaller values of $\overline{\gamma}_r$ are found until, for k_c smaller than a critical value k_c^{cr}, which at the site under consideration ranges about 110, no sediment motion takes place. Therefore, it appears that in the considered North Sea site, the flat bottom configuration is stable only when the Shields parameter is smaller than its critical value and no sediment is moved during the tidal cycle. These findings are in qualitative agreement with the results of Besio et al. (2003).

Figures **3.9**-**3.10** show the results obtained by adding the effects related to the presence of wind waves. In particular, in figure **3.9** the wave period and height are fixed equal to 5.7s and 1.5m respectively and different directions of propagation are considered. In figure **3.10**, waves propagating along the main tide axis are considered and the wave period is fixed equal to 5.7s while the height is varied. The results show that wind waves always have a stabilising effect since they produce smaller values of $\overline{\gamma}_r$. This stabilising effect increases for increasing wave height. Moreover, the strongest stabilising effect is induced by waves which propagate along the direction of the main tidal axis.

Up to now, $\overline{\gamma}_i$ vanishes and sand waves do not migrate. A significant sand wave migration is induced by the presence of a residual current. The migration speed of the bedforms is a quantity of practical relevance, since

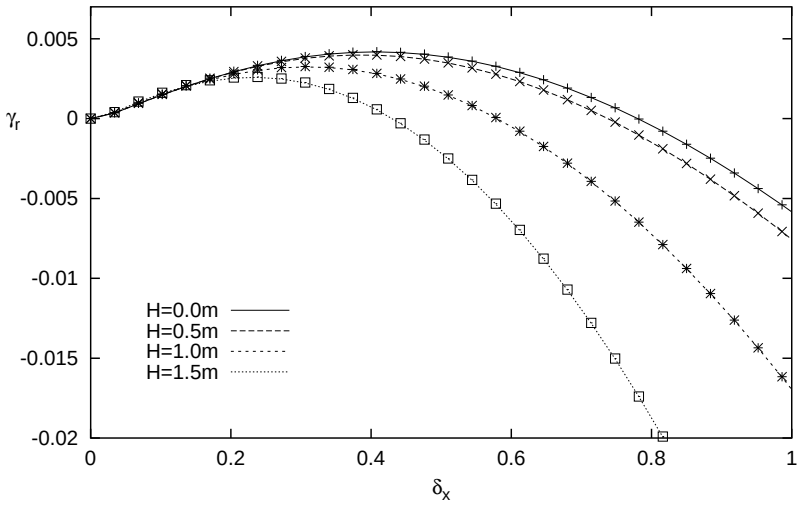

Figure 3.10: Growth rate $\overline{\gamma}_r$ plotted versus δ_x fixing $\delta_y = 0.0$ for $k_c = 150$, $e_{cc} = 0.42$, $\hat{\mu} = 288$, $R_p = 59$, $\hat{\psi}_d = 0.00087$, $d = 3.0\ 10^{-5}$, $T^* = 5.7$ s. Different values of the wave height are considered and the angle β_w between the direction of wave propagation and the major axis of the tidal ellipse is fixed equal to 0°.

migrating sand waves can expose pipelines to both free-span generation and self-burial. Moreover they can cause burial of shipping channels. Figure **3.11** shows that both the real $\overline{\gamma}_r$ and imaginary $\overline{\gamma}_i$ parts of $\overline{\gamma}$ are different from zero when a residual current aligned with the main tide axis is added to the oscillatory velocity induced by the M2 constituent, the other parameters being equal to those considered in figure **3.5**. From the results shown in figure **3.11**, it appears that the dimensionless migration speed $\overline{\gamma}_i/|\delta|$ is of order 10^{-1}, which corresponds to a dimensional migration speed of order 10 m/year. This predicted speed falls exactly in the range of the observed values (i.e. some tens of metres per year), even though no completely reliable measurements of sand wave displacement exist which allow for an accurate quantitative comparison between theoretical predictions and field values. The residual current induces not only a migration of the bottom forms but also destabilises the wavy bottom configuration.

When the residual current and the waves are aligned with the main tide axis, the maximum of $\overline{\gamma}_r$ is located at the δ_x-axis. If the residual current and/or the wind waves are orthogonal to the main tidal axis, the value of δ_y giving rise to the maximum of $\overline{\gamma}_r$ is no longer negligible even though it stays small for realistic values of the parameters.

To gain information on the relative importance of the bed and suspended

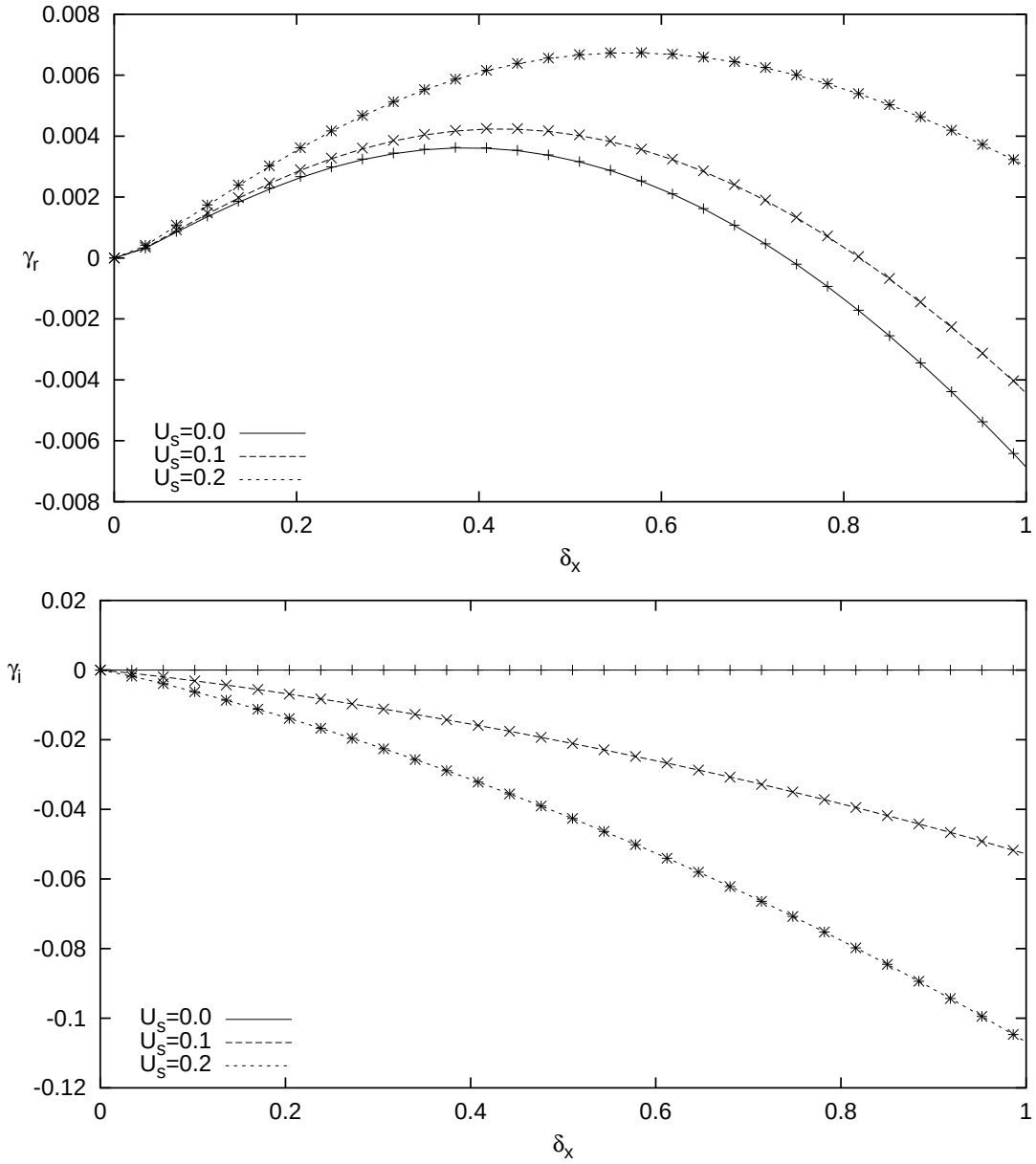

Figure 3.11: Amplification rate $\overline{\gamma}$ plotted versus δ_x fixing $\delta_y = 0.0$ for $k_c = 148$, $e_{cc} = 0.42$, $\hat{\mu} = 288$, $R_p = 59$, $\hat{\psi}_d = 0.00087$, $d = 3.0\ 10^{-5}$ and no wind waves. Top panel: real part $\overline{\gamma}_r$. bottom panel: imaginary part $\overline{\gamma}_i$. Dimensionless residual currents equal to 0.0, 0.1 and 0.2 are considered aligned with the major axis of the tidal ellipse. The lines represent the solution neglecting the time derivative, the points represent the full solution.

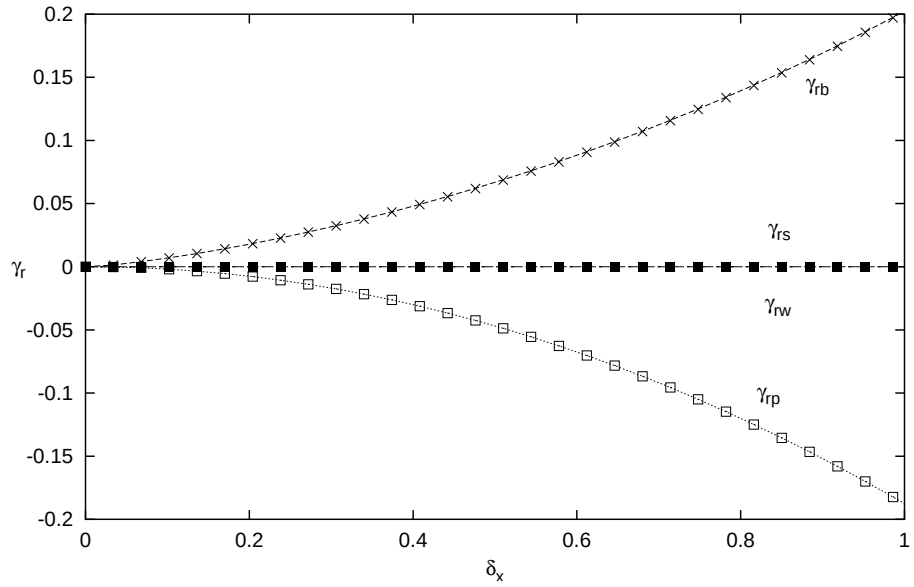

Figure 3.12: The different contributions to $\overline{\gamma}_r$ defined by (3.112) plotted versus δ_x for $\delta_y = 0.0$ and $\hat{r} = 72$, $e_{cc} = 0.17$, $\hat{\mu} = 315$, $R_p = 15.9$, $\hat{\psi}_d = 0.008$, $d = 6.4\ 10^{-6}$ and no wind waves. The lines represent the solution neglecting the time derivative, the points represent the full solution.

loads and of sediment transport due to wind waves, the different contributions to $\overline{\gamma}_r$, as defined by (3.112), are plotted in figure **3.12** for the same values of the parameters as those considered in figure **3.3** while in figure **3.13** a smaller grain size is considered. When the sand is coarse (figure **3.12**) the suspended load vanishes. Therefore, $\overline{\gamma}_{rs}$ is zero and the growth or decay of the bottom perturbations is controlled by a balance between the destabilising effect due to the bed load and the stabilising effect due to the bottom slope. When the sand is fine (figure **3.13**) the suspended load provides a significant contribution to the time development of the bottom. In particular $\overline{\gamma}_{rs}$ turns out to be negative and therefore the sediment carried into suspension provides a stabilising contribution to $\overline{\gamma}_r$ ($\overline{\gamma}_{rs} < 0$). This finding is not in agreement with the results obtained by the simplified two dimensional model employed in the first part of this work. A reason for the discrepancy between this result and the previous one can be identified in the approximation employed in the evaluation of the time lag and of the adaptation length in the first part of this work.

Both in figures **3.12** and **3.13**, no wave is considered and $\overline{\gamma}_{rw}$ vanishes. As shown in figures **3.9** and **3.10** wind waves always have a stabilising effect. As done in the previous figures, the lines represent the solution obtained

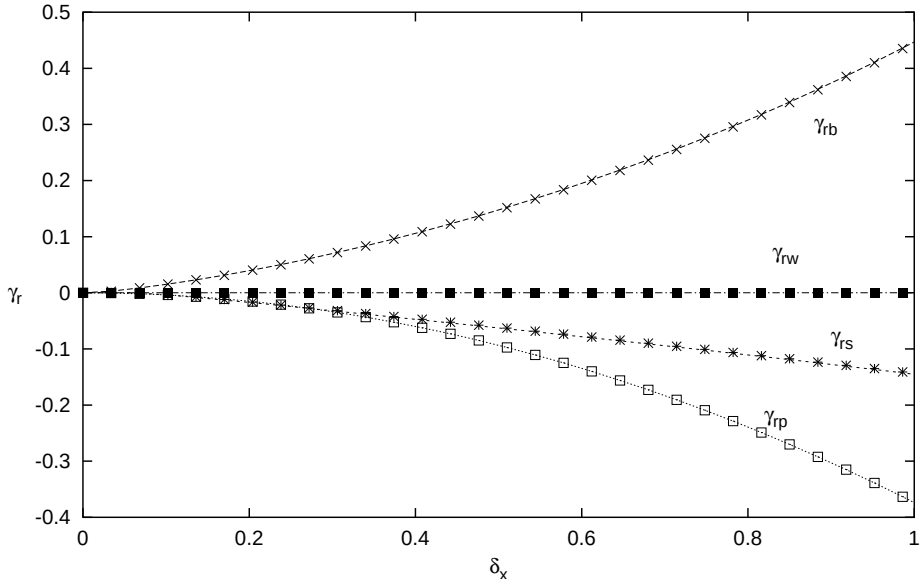

Figure 3.13: The different contributions to $\overline{\gamma}_r$ defined by (3.112) plotted versus δ_x for $\delta_y = 0.0$ and $\hat{r} = 72$, $e_{cc} = 0.17$, $\hat{\mu} = 315$, $R_p = 5.62$, $\hat{\psi}_d = 0.016$, $d = 3.2\ 10^{-6}$ and no wind waves. The lines represent the solution neglecting the time derivative, the points represent the full solution.

neglecting the time derivative proportional to the perturbation amplitude and the points represent the full solution.

3.5 Conclusions

In the second part of this work we have provided more evidence for the hypothesis that a simple model, based on the study of the time development of small bottom perturbations of a shallow sea, where the water motions are induced by tide propagation and by wind waves, can explain the formation of sand waves and tidal sand banks and can also give reliable predictions of their characteristics.

Concerning sand banks, it is worthwhile to point out that a predominant role in the process of their formation is played by the direction of rotation of the tidal wave. In fact, as pointed out by Soulsby (1983), a fixed tidal ellipse can be characterised by a clockwise rotary component of the depth average velocity or by a counter-clockwise rotary component.

Because the present model does not solve tide propagation but only describes the local structure of the tidal velocity, it cannot predict whether the

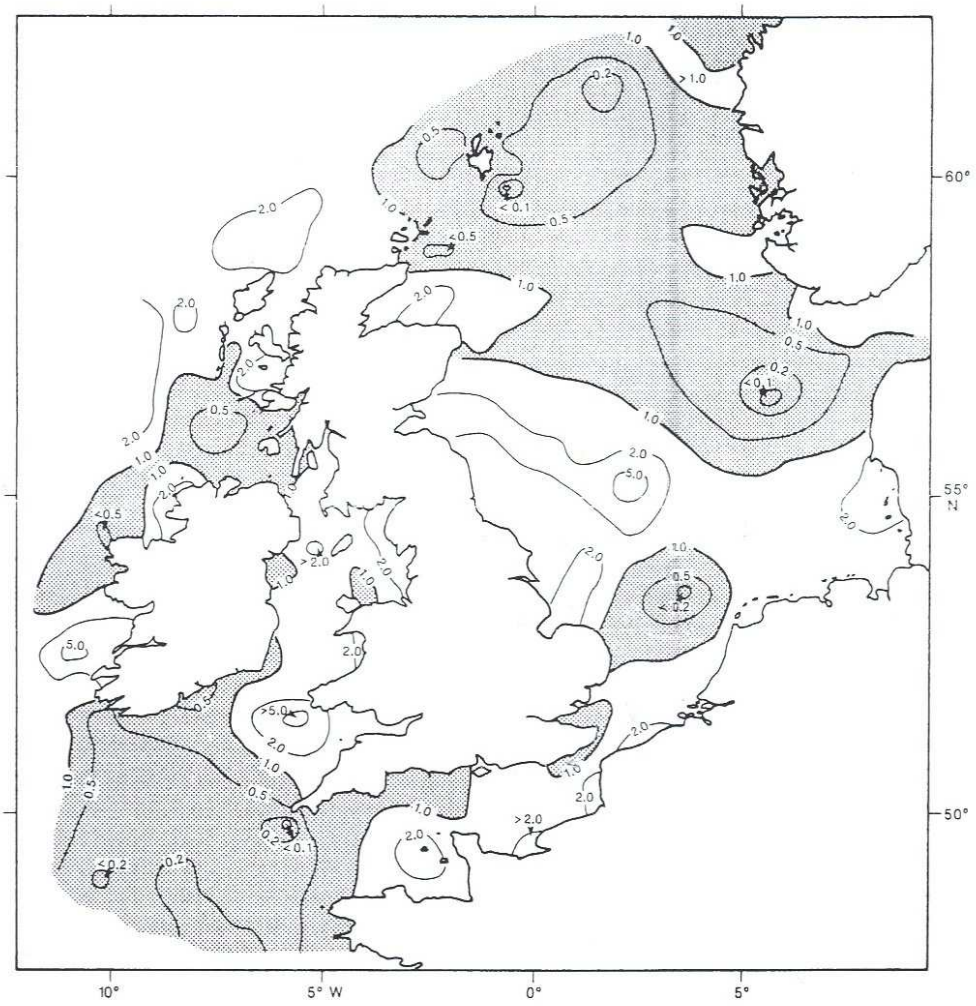

Figure 3.14: Ratio of the counter-clockwise to the clockwise rotary component of depth-average velocity of the mean spring tide in the seas around the British Isles. Shaded regions have a net clockwise rotation of the current vector. Results from the numerical model of Flather (1976). Adopted from Soulsby (1983).

tidal ellipse is clockwise or counter-clockwise. However, this information is available from numerical models of tide propagation and the proposed model can describe the vertical structure of a clockwise or of a counter-clockwise tidal ellipse (see figure **3.14**). The preliminary results we have obtained show that sand bank orientation depends on the clockwise or counter-clockwise orientation of the tidal ellipse as well as on the other parameters of the model

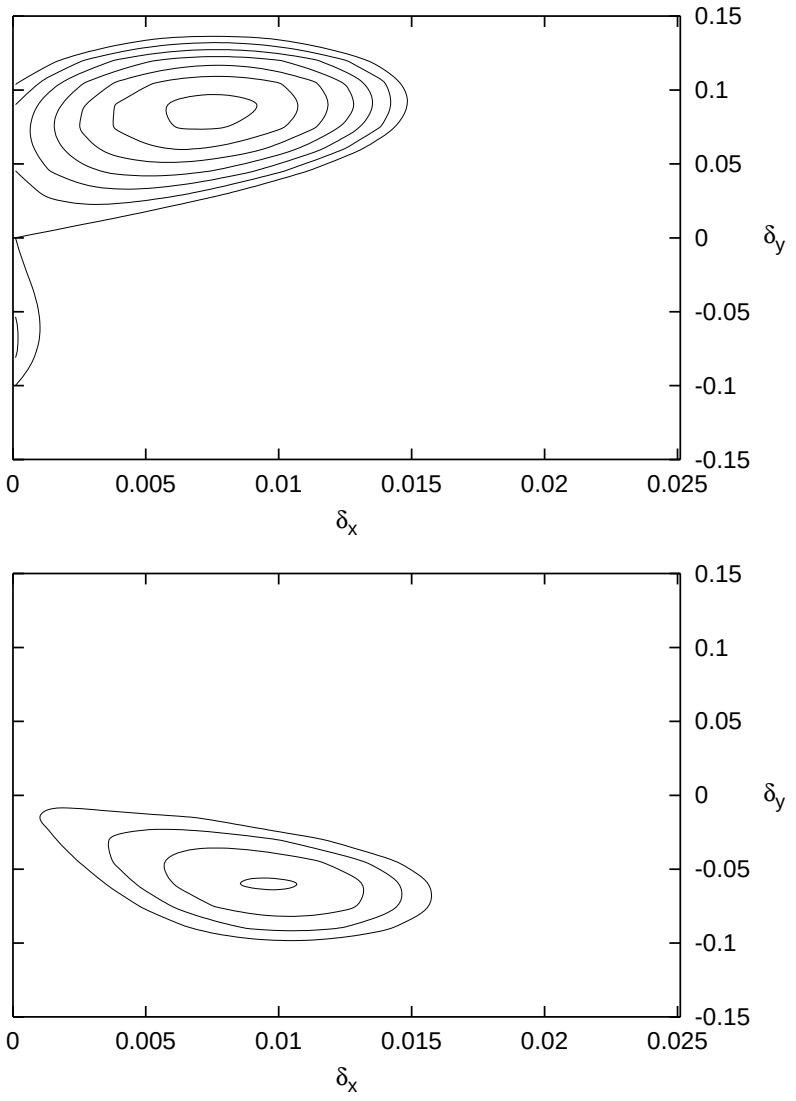

Figure 3.15: Growth rate $\overline{\gamma}_r$ plotted versus δ_x and δ_y for $k_c = 78$, $e_{cc} = 0.15$, $\hat{\mu} = 353$, $R_p = 1.99$, $\hat{\psi}_d = 0.02546$, $d = 1.8\ 10^{-6}$ and no wind waves. Only positive isolines are displayed with $\Delta\overline{\gamma}_r = 0.001$. Top panel: counter-clockwise rotating tide. Bottom panel: clockwise rotating tide.

(sediment and tidal parameters). As shown in figure **3.15** where positive isoline of the growth rate $\overline{\gamma}_r$ are plotted against δ_x and δ_y, the direction of rotation of the tide has a strong influence on the relative orientation of sand banks. In fact clockwise rotating tides (bottom panel of figure **3.15**) give rise to counter-clockwise oriented sand banks, while counter-clockwise rotating tides lead to a clockwise orientation of the bedforms with respect to the

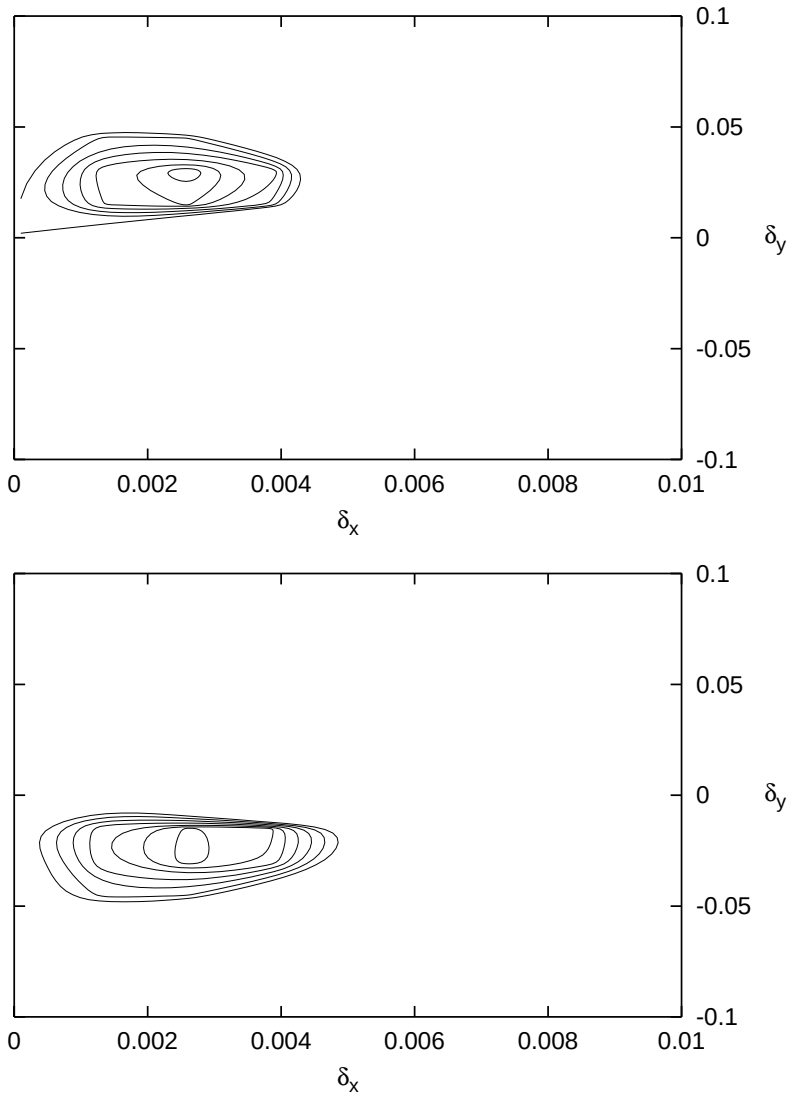

Figure 3.16: Growth rate $\overline{\gamma}_r$ plotted versus δ_x and δ_y for $k_c = 310$, $e_{cc} = 0.15$, $\hat{\mu} = 331$, $R_p = 1.99$, $\hat{\psi}_d = 0.0083$, $d = 3.1\ 10^{-6}$ and no wind waves. Only positive isolines are displayed with $\Delta\overline{\gamma}_r = 0.05$. Top panel: counter-clockwise rotating tide. Bottom panel: clockwise rotating tide.

direction of propagation of the main tidal flow. In both cases the length scale of the predicted sand banks is of the order of 3.5km and their orientation is of about 7°. The above findings have been obtained taking into account a semi-diurnal tide of about 0.4m/s propagating over a cohensionless bed with a mean diameter of 0.0625mm and an average depth of 35m. This kind of behaviour is present even if we consider different strength of the tide and

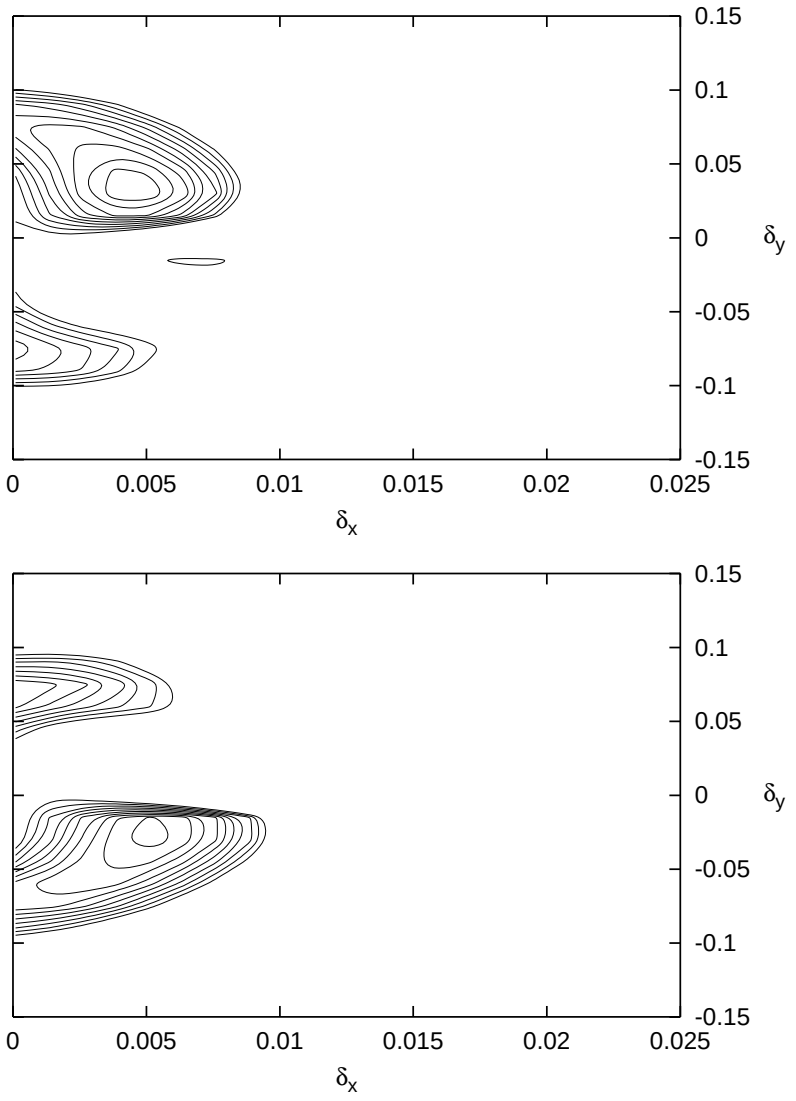

Figure 3.17: Growth rate $\overline{\gamma}_r$ plotted versus δ_x and δ_y for $k_c = 310$, $e_{cc} = 0.15$, $\hat{\mu} = 331$, $R_p = 5.62$, $\hat{\psi}_d = 0.0042$, $d = 6.2\ 10^{-6}$ and no wind waves. Only positive isolines are displayed with $\Delta\overline{\gamma}_r = 0.01$. Top panel: counter-clockwise rotating tide. Bottom panel: clockwise rotating tide.

different water depth as shown in figure **3.16** where it has been considered a stronger tide (0.9m/s) propagating over a smaller depth (20m), while the sediment mean diameter has been kept fixed. This configuration leads to the formation of bedforms with a characteristic wavelength of about 4.2km and an orientation of about 6°. Increasing the mean sediment diameter does not lead to significant qualitative changes, and the orientation of the bedforms is

still controlled by the direction of rotation of the tide (see figure **3.17** where the results obtained with the same set of the parameters of figure **3.16** are reported but the sediment mean diameter which has been assumed equal to 0.125mm). This set of the parameters leads to the formation of sand banks characterised by a wavelength of about 5km and an orientation of about 10° The reader can recognise the generation mechanism of some of the sand bank patterns observed in the field and described a.o. by Dyer & Huntley (1999).

The above findings suggest that it is necessary to have detailed information about the characteristics of the tide and of the sediment in order to be able to perform reliable predictions and analyses of these large scale bedforms. In particular the direction of rotation of the tidal waves influences directly the orientation of the bedforms.

The idea that bottom forms observed in tidal seas arise as free instabilities of a simple morphological system driven by tide propagation is due to Huthnance (1982) and refinements of Huntnance's (1982) analysis were performed by Hulscher et al. (1993), De Vriend (1990) and Hulscher (1996) and more recently by Gerkema (2000), Komarova & Hulscher (2000), Németh et al. (2003), Besio et al. (2003), Besio et al. (2004). The present analysis removes many of the assumptions and restrictions characterising previous approaches and allows for a quantitative description of the phenomenon without the need of tuning any parameter. The presence of wind waves and residual currents is also taken into account in the analysis and therefore the model is also capable of predicting the migration of bottom forms and the appearance of complex bottom topographies which arise from the simultaneous growth of different modes. Upon taking into account the effects of wind waves and residual currents it has been shown that sea bed forms generation is a more complex phenomenon than that described by previous simplified models. A limitation of the present analysis is that perturbations of small amplitude are considered and a linear approach is used. Therefore only the initial stage of bedform growth can be simulated. In order to investigate the long-term behaviour, when the amplitudes of sand banks and sand waves have reached finite values, a nonlinear approach is required. This could be based on a weakly nonlinear stability analysis by considering tidal current strengths close to the critical value. This possible analysis should also allow for both the investigation of the interaction between different modes and the prediction of the final complex configuration of the sea bottom when different types of sand waves coexist. The model formulated provides a simplified description of the actual phenomenon, but considers all the main processes affecting the growth of bottom forms (e.g. oscillating tidal currents, residual currents, wind waves, bed load, suspended load, longitudinal and transverse bottom slope effects on sediment transport). Of course, some aspects of the

model could be improved: in particular it is hoped to be able to introduce a better turbulence model capable of describing the time variation of the turbulence structure during the tidal cycle. However, we also feel that only minor changes of presently obtainable quantitative predictions would be induced at the expense of a major effort in the analysis.

Bibliography

Bailard, J.A. 1981 An energetic total load sediment transport model for a plane sloping beach. *J. Geophys. Res.* 86 (**C11**), 10938–10954.

Bailard, J.A. & Inman, D.L. 1981 An energetic bedload model for a plane sloping beach: local transport. *J. Geophys. Res.* 86 (**C3**), 2035–2043.

Belderson, R.H., Johnson, M.A. & Kenyon, N.H. 1982 in *Offshore tidal sands. Processes and deposits* , (Ed. A.H. Stride), Chapman and Hall. London.

Belderson, R.H. 1986 Offshore tidal and nontidal sand ridges and sheets: differences in morphology and hydrodynamic setting. In *Shelf Sands and Sandstones*. Ed. R.J. Knight, J.R. McLean, pp 293–301. Calgary, Alberta. Can: Can. Soc. Pet. Geol. Memoir II

Besio, G., Blondeaux, P., Brocchini, M. & Vittori, G. 2004 Migrating Sand Waves. *J. Geophys. Res.* In press.

Besio, G., Blondeaux, P. & Frisina, P. 2003 A note on tidally generated sand waves. *J. Fluid Mech* **485**, 171–190.

Blondeaux, P. 2001 Mechanics of coastal forms. *Annu. Rev. Fluid Mech.* **33**, 339–370.

Blondeaux, P. 1990 Sand ripples under sea waves. Part 1. Ripple formation. *J. Fluid Mech* **218**, 1–17.

Blondeaux, P. & Vittori, G. 2004a Flow and sediment transport induced by tide propagation. Part I: the flat bottom. *To be submitted*

Blondeaux, P. & Vittori, G. 2004b Flow and sediment transport induced by tide propagation. Part II: the wavy bottom. *To be submitted*

Blondeaux, P. & Vittori, G. 1999 Boundary layer and sediment dynamics under sea waves. *Adv. Coastal and Ocean Eng.* **4**, 133–190.

Boggs, S. 1974 Sand wave fields in Taiwan straight. *Geology* **2**, 251-253.

Bokuniewicz, H.J, Gordon, R.B. and Kastens, K.A. 1977 Form and migration of sand waves in a large estuary, Long Island Sound. *Mar. Geol.,* **24**, 185–199.

Bowden, K.F. & Ferguson, S.R. 1980 Variations with height of the turbulence in a tidally-induced bottom boundary layer. In *Marine turbulence*. Ed. J.C.J. Nihoul, pp 259–286. Elsevier. Amsterdam.

CALVETE, D. & DE SWART, H.E. 2003 A nonlinear model study on the long-term behaviour of shoreface-connected sand ridges. *J. Geophys. Res.* 108 (**C5**), 3169, doi:10.1029/2001JC001091.

CALVETE, D., FALQUES, A., DE SWART, H.E., WALGREEN, M. 2001 Modelling the formation of shoreface-connected sand ridges on storm-dominated inner shelves. *J. Fluid Mech.* **441,** 169–193.

COCO G., HUNTLEY, D.A., O'HARE, T.J. 2000 Investigation of a self-organized model for beach cusp formation and development. *J. Geophys. Res.* 105 (**C9**), 21991–22002.

COLOMBINI, M., SEMINARA, G. AND TUBINO, M. 1987 Finite-amplitude alternate bars. *J. Fluid Mech.* **181,** 213-232.

DEAN, R.B. 1974 *AERO Report* 74-11, Imperial College, London.

DE SWART, H.E. & HULSCHER, S.J.M.H. 1995 Dynamics of large-scale bed forms in coastal seas, in *Nonlinear Dynamics and Pattern Formation in the Natural Environment* (ed. A. Doelman and A. van Harten), pp. 315–331, Longman.

DE VRIEND, H.J. 1990 Morphological processes in shallow tidal seas. In *Residual Currents and Long-term Transport* (ed. R. T. Cheng), pp. 276–301, Springer.

DODD, N., BLONDEAUX, P., CALVETE, D., DE SWART, H., FALQUES, A., HULSCHER, S.J.M.H., ROZYNSKI, G. & VITTORI, G. 2003 The use of stability methods for understanding the morphodynamical behaviour of coastal systems. *Cont. Shelf Res.,* **19** (4), 849–865.

DRAZIN, P.G. & REID, W.H. 1981 Hydrodynamic Stability. *Cambridge Univ. Press.*

DYER, K.R. & HUNTLEY, D.A. 1999 The origin, classification and modelling of sand banks and ridges. *Cont. Shelf Res.,* **19**, 1285–1330.

ENGELUND, F. & FREDSØE, J. 1982 Sediment ripples and dunes. *Ann. Rev. Fluid Mech.* **14,** 13–37.

ENGELUND, F. 1964 A practical approach to self-preserving turbulent flows. *Acta Polytechnica Scandinavica.* p.6.

FENSTER, M.S., FITZGERALD, D.M., BOHLEN, W.F., LEWIS, R.S. AND BALDWIN, C.T. 1990 Stability of giant sand waves in eastern Long Island Sound, U.S.A. *Mar. Geol.,* **91**, 207–225.

FLATHER, R.A. 1976 A tidal model of the north-west European continental shelf. *Mem. Soc. R. Sci. Liège, Ser. 6* **10,** 141-164.

FREDSØE, J. & DEIGAARD R. 1992 Mechanics of coastal sediment transport. *World Scientific.*

FREDSØE, J. 1982 Shape and dimensions of stationary dunes in rivers. *J. Hydraul. Div..* ASCE **108,** (HY8), 932–947.

FREDSØE, J. 1974 On the development of dunes in erodible channels. *J. Fluid Mech.* **64,** 1-16.

GERKEMA, T. 2000 A linear stability analysis of tidally generated sand waves. *J. Fluid Mech.* **417**, 303–322.

HEATHERSHAW, A.D. 1979 The turbulent structure of the bottom boundary layer in a tidal current. *Geophys. J. R. Astron. Soc.* 58, 395–430.

HOUBOLT, J.J.H.C. 1968 Recent sediments in the Southern Bight of the North Sea. *Geology en Mijnbouw* **47** (4), 245–273.

HULSCHER, S.J.M.H., SWART, H.E. DE & VRIEND, H.J. DE 1993 Generation of offshore tidal sand banks and sand waves. *Cont. Shelf Res.* **13**, 1183–1204.

HULSCHER, S.J.M.H. 1996a Tidal-induced large-scale regular bed form patterns in a three-dimensional shallow water model. *J. Geophys. Res.* 101 (**C9**), 20727–20744.

HULSCHER, S.J.M.H. 1996b On validation of a sand waves and sand banks model. *Coastal Eng. Conf.*, September 2-6, Orlando, Vol. 3, **276**, 3574–3587.

HULSCHER, S.J.M.H. & VAN DER BRINK, G.M. 2001 Comparison between predicted and observed sand waves and sand banks in the North Sea. *J. Geophys. Res.* 106 (**C5**), 9327–9338.

HUNTLEY, D.A., HUTHNANCE, J.M., COLLINS, M.B., LIU, C.-L., NICHOLLS, R.J. AND HEWITSON, C. 1993 Hydrodynamics and sediment dynamics of North Sea sand waves and sand banks. *Phil. Trans. R. Soc. London A,* **343**, 461–474.

HUTHNANCE, J. 1982a On one mechanism forming linear sand banks. *Est. Coastal Shelf Sci.* **14**, 79–99.

HUTHNANCE, J. 1982b On the formation of sand banks of finite extent. *Est. Coastal Shelf Sci.* **15**, 277–299.

KNAAPEN, M.A.F. & HULSCHER, S.J.M.H. 2002 Regeneration of sand waves after dredging. *Coast. Eng.* **46**, 277-289.

KOMAROVA, N.L. & HULSCHER, S.J.M.H. 2000 Linear instability mechanism for sand wave formation. *J. Fluid Mech* **413**, 219–246.

KOMAROVA, N.L. & NEWELL, A.C. 2000 Nonlinear dynamics of sand banks and sand waves. *J. Fluid Mech* **415**, 285–312.

LANGERAAR, W. 1966 Sandwaves in the North Sea. *Hydrogr. Newsl.,* **1**, 243–246.

LE BOND, P.H. 1992 *Waves in the ocean.* Elsevier Scientific, Amsterdam, xiv+602.

LE BOT, S., TRENTESAUX, A. GARLAN, T., BERNE S. & CHAMLEY, H. 2000 Influence des tempetes sur la mobilite des dunes tidales dans le detroit du Pas-de-Calais. *Oceanologia Acta* **23(2)**, 129–141.

LIN, C.C. 1967 The Theory of Hydrodynamic Stability. *Cambridge University Press.*

LUDWICK, J.C. 1972 Migration of tidal sand waves in Chesapeake Bay entrance. In *Shelf Sediment Transport: Processes and Pattern.* Ed. D. Swift, D. Duane, O. Pilkey, pp 377-410. Dowden, Hutchinson and Ross. Stroudsburg, PA.

LYNE, W.H. 1971 Unsteady viscous flow over wavy wall. *J. Fluid Mech* **50**, 33–48.

MAAS, L.R.M. & VAN HAREN, J.J.M. 1987 Observations on the vertical structure of tidal and inertial currents in the central North Sea. *J. Mar. Res.* **45**, 293–

318.

Mc Cave, J.N. 1971 Sand waves in the North Sea off the coast of Holland. *Mar. Geol.,* **10**, 199–225.

Meyer-Peter, E. and Müller, R. 1948 Formulas for bedload transport. *III Conf. of Internat. Ass. of Hydraul. Res., Stockholm.* Sweden.

Németh, A.A., Hulscher, S.J.M.H. and de Vriend, H.J. 2002 Modelling sand wave migration in shallow shelf seas. *Cont. Shelf Res.,* **22** (18-19), 2795–2806.

Off, T. 1963 Rhythmic linear sand bodies caused by tidal currents *Bull. of the Am. Ass. of Petroleum Geologists* **47,** 324–341.

Richards, K. 1980 The formation of ripples and dunes on an erodible bed. *J. Fluid Mech.* **99**, 597–618.

Roos, P. & Blondeaux, P. 2001 Sand ripples under sea waves. Part 4. Tile ripple formation. *J. Fluid Mech.* **447**, 227–246.

Santoro, V., Amore, E., Cavallaro, L., Cozzo, G., Foti, E. 2002 Sand-waves in the Messina Strait, ICS Proceedings *J. Coast. Res.* Spec. Issue **36**.

Seminara, G. & Blondeaux, P. 2001 Perspectives in morphodynamics. *River, coastal and estuarine morphodynamics* , (Eds. G. Seminara & P. Blondeaux), Springler & Verlag.

Sleath, J.F.A. 1984 Sea bed mechanics. (Ed. M.E. McCormick), John Wiley & Sons.

Sleath, J.F.M. 1976 On rolling grain ripples. *J. Hydraulic Res.* **14**, 69–81.

Soulsby, R.L. 1980 Selecting record length and digitization rate for near-bed turbulence measurements. *J. Phys. Oceanogr.* **10**, 208–219.

Soulsby, R.L. 1981 Measurement of the Reynolds stress components close to a marine sand bank. *Mar. Geol.* **42**, 35–47.

Soulsby, R.L. 1983 The bottom boundary layer of shelf seas. In *Physical Oceanography of Coastal and Shelf Seas*, Ed B Johns, Elsevier, Amsterdam, 1983.

Soulsby, R.L. & Dyer, K.R. 1981 The form of the near-bed velocity profile in a tidally accelerating flow. *J. Geophys. Res.* **86**, 8067–8074.

Stride, A.H. 1970 Shape and size trends for sand waves in a depositional zone of the North Sea. *Geol. Mag.,* **107**, 469–477.

Stride, A.H. 1982 in *Offshore tidal sands. Processes and deposit* , (Ed. A.H. Stride), Chapman and Hall. London. 222pp

Talmon, A.M., Struiksma, N. & Van Mierlo, M.C.L.M. 1995 Laboratory measurements of the direction of sediment transport on transverse alluvial bed slopes. *J. Hydraul. Res.* **33**, 495–517.

Terwindt, J.H.J. 1971 Sand waves in the Southern Bight of the North Sea. *Mar. Geol.,* **10**, 51–67.

Van Alphen, J.S.L.J. & Damoiseaux, M.A. 1989 A geomorphological map of the Dutch shoreface and adjacent part of the continental shelf. *Geologie en*

Mijnbouw, **68**, 433-444.

Van de Meene, J.W.H. 1994 The shoreface-connected ridges along the central Dutch coast. *PhD thesis,* Univesiteit Utrecht, 222pp.

Van Rijn, L.C. 1991 Sediment transport in combined current and waves. *Proc. Euromech 262*, Sand transport in rivers, estuaries and the sea. (Eds. Soulsby, Bettes) Balkema.

Van Rijn, L.C. 1984a Sediment transport, part I: bed load transport. *J. Hydr. Engng* **110**, 1431–1456.

Van Rijn, L.C. 1984b Sediment transport, part II: suspended load transport. *J. Hydr. Engng* **110**, 1613–1641.

Van Veen, J. 1935 Sandwaves in the Southern North Sea. *Hydrogr. Rev.,* **12**, 21–29.

Verhagen, H.J. 1989 Sand waves along the Dutch Coast. *Coast. Engng.* **13**, 129–147.

Vittori, G. & Blondeaux, P. 1992 Sand ripples under sea waves. Part 3. Brick-pattern ripple formation *J. Fluid Mech.* **239**, 23–45.

Vittori, G. & Blondeaux, P. 1990 Sand ripples under sea waves. Part 2. Finite-amplitude development. *J. Fluid Mech.* **218**, 19–39.

Vittori, G. 1989 Nonlinear viscous oscillatory flow over a small amplitude wavy wall. *J.Hydraul. Res.* **27**, 267–280.

Wright, L.D. & Short, A.D. 1984 Morphodynamic variability of surf zones and beaches: a synthesis *Marine Geol.* **56**, 93–118